



DEVELOPMENT OF A TOMOGRAPHIC ATMOSPHERIC MONITORING SYSTEM BASED ON DIFFERENTIAL OPTICAL ABSORPTION SPECTROSCOPY

RUI FILIPE CANTARINO VALENTE DE ALMEIDA

Master in Biomedical Engineering

BIOMEDICAL ENGINEERING

NOVA University Lisbon
(month), (year)



NOVA

NOVA SCHOOL OF
SCIENCE & TECHNOLOGY

DEPARTMENT
OF PHYSICS

DEVELOPMENT OF A TOMOGRAPHIC ATMOSPHERIC MONITORING SYSTEM BASED ON DIFFERENTIAL OPTICAL ABSORPTION SPECTROSCOPY

RUI FILIPE CANTARINO VALENTE DE ALMEIDA

Master in Biomedical Engineering

Adviser: Mary Doe Adviser Name
Full Professor, NOVA University Lisbon

Co-advisers: John Doe Co-Adviser Name
Associate Professor, NOVA University Lisbon
John Doe other Co-Adviser Name
Full Professor, NOVA University Lisbon

BIOMEDICAL ENGINEERING

NOVA University Lisbon
(month), (year)

Development of a Tomographic Atmospheric Monitoring System based on Differential Optical Absorption Spectroscopy

Copyright © Rui Filipe Cantarino Valente de Almeida, NOVA School of Science and Technology, NOVA University Lisbon.

The NOVA School of Science and Technology and the NOVA University Lisbon have the right, perpetual and without geographical boundaries, to file and publish this dissertation through printed copies reproduced on paper or on digital form, or by any other means known or that may be invented, and to disseminate through scientific repositories and admit its copying and distribution for non-commercial, educational or research purposes, as long as credit is given to the author and editor.

To my parents.

Acknowledgments

I know the pieces fit, 'cause I watched them fall away.

ABSTRACT

Regardless of the language in which the dissertation is written, a summary is required in the same language as the main text and another summary in another language. It is assumed that the two languages in question are Portuguese and English.

The abstracts should appear first in the language of the main text and then in the other language. For example, if the dissertation is written in Portuguese the abstract in Portuguese will appear first, then the abstract in English, followed by the main text in Portuguese. If the dissertation is written in English, the abstract in English will appear first, then the abstract in Portuguese, followed by the main text in English.

In the L^AT_EX version, the NOVAtesis template will automatically order the two abstracts taking into account the language of the main text. You may change this behaviour by adding

```
\abstractorder(<MAIN_LANG>) := {<LANG_1>, ..., <LANG_N>}
```

to the customization area in the document preamble, e.g.,

```
\abstractorder(de) := {de, en, it}
```

The abstracts should not exceed one page and, in a generic way, should answer the following questions (it is essential to adapt to the usual practices of your scientific area):

1. What is the problem?
2. Why is this problem interesting/challenging?
3. What is the proposed approach/solution?
4. What results (implications/consequences) from the solution?

Keywords: Keyword 1, Keyword 2, Keyword 3, Keyword 4, Keyword 5, Keyword 6, Keyword 7, Keyword 8, Keyword 9, ...

RESUMO

Independentemente da língua em que a dissertação esteja redigida, é necessário um resumo na mesma língua do texto principal e outro resumo noutra língua. Pressupõe-se que as duas línguas em questão sejam o português e o inglês.

Os resumos devem aparecer primeiro na língua do texto principal e depois na outra língua. Por exemplo, se a dissertação for redigida em português, o resumo em português aparecerá primeiro, seguido do resumo em inglês (*abstract*), seguido do texto principal em português. Se a dissertação for redigida em inglês, o resumo em inglês (*abstract*) aparecerá primeiro, seguido do resumo em português, seguido do texto principal em inglês.

Na versão L^AT_EX o template NOVAthesis irá ordenar automaticamente os dois resumos tendo em consideração a língua do texto principal. É possível alterar este comportamento adicionando

```
\abstractorder(<MAIN_LANG>) := {<LANG_1>, ..., <LANG_N>}
```

à zona de customização no preâmbulo do documento, e.g.,

```
\abstractorder(de) := {de, en, it}
```

Os resumos não devem ultrapassar uma página e, de forma genérica, devem responder às seguintes questões (é essencial adaptá-los às práticas habituais da sua área científica):

1. Qual é o problema?
2. Porque é que é um problema interessante/desafiante?
3. Qual é a proposta de abordagem/solução?
4. Quais são as consequências/resultados da solução proposta?

Palavras-chave: Palavra-chave 1, Palavra-chave 2, Palavra-chave 3, ...

CONTENTS

List of Figures	xi
List of Tables	xvi
Acronyms	xvii
1 Introduction	1
1.1 Background, Motivation and Starting Points	1
1.1.1 Introduction	1
1.1.2 Context	1
1.2 Problem Introduction	2
1.3 Literature review	3
1.3.1 Tomography	3
1.3.2 Differential Optical Absorption Spectroscopy (DOAS)	5
1.3.3 DOAS Tomography	5
1.4 Research Questions	6
1.5 Hypothesis	7
1.6 Methods and Findings	8
1.7 Layout	8
2 Literature Review	10
2.1 Air Pollution	10
2.1.1 Criteria Pollutants	11
2.1.2 Air Pollution Effects on Human Health	11
2.1.3 Air Pollution effects on ecosystems	17
2.1.4 Air Pollution Sources	18
2.1.5 Detecting and Monitoring Air Pollution	26
2.2 DOAS	28
2.2.1 Types of DOAS experiments	31
2.3 Important Notes on DOAS in practice	36
2.3.1 Cross section conditioning	36
2.3.2 Spectral Calibration	37
2.4 Tomographic algorithms and reconstruction techniques	39
2.5 DOAS Tomography	45

CONTENTS

3 Methods	49
3.1 Tomosim	49
3.1.1 Discretisation	51
3.1.2 Phantoms	56
3.1.3 Error Estimation	57
3.1.4 Reconstruction Results	59
3.2 The Experiment	62
3.2.1 Protocol and conduction	63
3.2.2 First Run	65
3.2.3 Second run	67
3.2.4 Data Processing	70
3.2.5 The DOAS Library	71
4 Discussion	77
4.1 First Hypothesis	77
4.2 Second Hypothesis	78
5 Conclusions	82
5.1 TomoSim	82
5.2 Lambertian Absorption Experiment	83
5.3 Research Questions Summary	84
Bibliography	85
Appendices	
A Systematic Review of DOAS Tomography	94
B Forest Fire Finder: DOAS application to long-range forest fire detection	117
C TomoSim: a tomographic simulator for Differential Optical Absorption Spectroscopy	131
D Testing Lambertian Absorption - handout protocol for the experiment of Section 3.2	152
Annexes	

LIST OF FIGURES

1.1	A schematic representation of a projection acquisition. In this image, taken from [42], the clear line that comes down at a diagonal angle is a projection.	4
2.1	Annotated anatomy of the respiratory system [85].	12
2.2	Possible abnormalities caused by Air Pollution (AP) exposure <i>in utero</i> . Notice that time of exposure is of critical importance [85].	15
2.3	Developmental stages of the lung throughout life vs the risks of AP exposure in each stage [85].	16
2.4	Dramatic photograph depicting the Capelinhos' lighthouse, half a kilometer from the eruption site, surrounded by a cloud of ash Particulate Matter (PM), volcanic gas and water vapor with more than 1km in height[82]. .	20
2.5	House almost completely buried by the Black Sunday dust storm. Several houses were entirely swallowed during this storm, trapping people inside, as if a big blizzard had hit them. Unlike a blizzard though, there was nothing anyone could do to keep the dirt outside, and all surfaces were covered black [73].	21
2.6	Carbon Dioxide (CO ₂) atmospheric concentrations since the year 1000. Note the seemingly exponential increase since the 1800s. Plotted and published by the 2 Degrees Institute [1] with data from ice cores [30] and in situ monitors [81].	22
2.7	Schematic presentation on the sources of anthropogenic pollution and its categorisation according to the IPCC. Adapted from [15]	23
2.8	Chinese energy production, Gross Domestic Product (GDP) and CO ₂ emissions. Data collected from the World Bank and International Energy Agency websites [90, 44]	24
2.9	General trends for European emissions. Data presented in % emissions of year 2000. Note the downward global trend in pollutant emissions, and its decoupling with the European GDP [29].	25
2.10	European emissions divided by activity sector. The global decreasing trend is confirmed, as industries all around are producing less and less AP with the passing years [29].	26
2.11	Semiconductor electrochemical sensor basic structure. There are many examples of this type of sensors, but in general they follow this architecture [20].	28

LIST OF FIGURES

2.12 Simplified schematic flowchart of the DOAS algorithm, including the non-linear part	32
2.13 Active DOAS schematic.	32
2.14 Passive DOAS schematic.	33
2.15 Several examples of possible passive DOAS experiment geometries. All these examples use only the light from an astronomical source to detect many atmospheric trace gases. All these examples were taken from [66].	34
2.16 Occultation measurement schematic representation [66]	34
2.17 Schematic representation of the limb satellite measurement geometry. .	35
2.18 Schematic representation of the nadir satellite measurement geometry.	35
2.19 Before being used in DOAS calculations, literature trace gas cross section spectra must undergo a conditioning process to make sure they are compatible with the current experiment's instruments. Figure adapted from [5]	37
2.20 This figure, taken from [5], shows the difference between NO ₂ cross sections. The red line comes from the literature, and has been conditioned to the experiment spectrometer. The blue line was actually collected with that device. The slight discrepancies that can be observed are calibration defects.	38
2.21 High resolution solar spectrum commonly used to calibrate the various spectral signals in DOAS experiments [19].	39
2.22 Schematic representation for coordinate setting. The image depicts a parallel projection setting [48].	41
2.23 The Fourier Slice Theorem (FST), a schematic representation [4].	42
2.24 Schematic representation of an equiangular fan-beam projection, taken from [47].	44
2.25 Simplified diagram of the Systematic Mapping Study (SMS) method. This type of study is focused on registering every step of the search and the reading of the retrieved material, in an effort to make the process completely repeatable. Adapted from [50].	46
2.26 BABII assembly geometry. In this experiment campaign, the telescopes illuminated retroreflecting targets that were positioned in two steel towers on both sides of a busy motorway in Germany, connecting Heidelberg to Mannheim [70].	46
2.27 Erna Frins's paper [33] proposes a very relevant passive DOAS application that can conceptually be employed in a DOAS tomography scenario. In this 2006 paper, the authors use multi-axis measurements of sun-illuminated targets to estimate absorption paths without using radiative transfer models.	48
3.1 Hexacopter in flight. Image taken from LevelFiveSupplies[53], for illustration purposes only.	50

3.2 Illustration of the projection gathering algorithm based on the assembly of groups of acquisitions as fanbeam projections. The lines presented on the drawing come from the right to the left. Each is a ray in fan, corresponding to one stop of the drone. In the second measurement moment, the drone moves to the exit point on the left and repeats the first moment collection. Here, both fans and rays are separated by 5 degrees and there are 6 rays within each fan. A "real life" acquisition would feature a lot more rays, but that would be graphically complicated for the reader. Both ray and fan angular distance are customisable at runtime. Map taken from Google Maps in 2019. ©Google.	51
3.3 Grid and pixel definition, as they appear in the original article by Robert Siddon [76]. Pixels are "formed" by intersecting the ray (here going from point 1 to point 2) with the superimposed grid.	52
3.4 P_2 Calculation. The software uses the position of the drone, as defined by the vertical angle, β , and the distance between the drone and the centre of the trajectory, D , to determine P_2 through the solution of a second degree equation.	55
3.5 A graphical representation of the new spectral phantom, custom built for the TomoSim application.	57
3.6 Error estimation graphical representation. Note errors are extremely exaggerated for visualisation purposes.	58
3.7 Sinogram examples: the new spectral phantom projection data at a projection interval of 1 degree. On the left, the projection data before resorting; on the right, the parallel projection data obtained after resorting the fan-beam line integrals.	60
3.8 Tomographic reconstruction results, projection interval of 1 degree. From left to right: original phantom, FBP reconstruction, SART reconstruction, MLEM reconstruction	60
3.9 Tomographic reconstruction errors. Each one of these images was constructed by subtracting the respective reconstruction matrix, displayed in Figure 3.8, from the original phantom matrix. Error value is normalised to the pixel values, i.e., 32 bit floating point numbers with values between 0 and 1.	60
3.10 Reconstruction degradation: the projection interval was crucial for reconstruction. Note the image degradation going from a projection interval of 1 degree to 5 degrees (left to right). Images reconstructed using the FBP algorithm.	61
3.11 Location of observer points for the physical experiment.	63
3.12 Published spectrum of the CREE XHP50.2 LED light. The LED that was used in this experiment corresponds to the blue line [21].	64
3.13 Spectrum measured with the experiment spectrometers, at a distance of approximately 50 m from the torchlight.	64
3.14 View from West Bank assembly at sunrise during the first run of the experiment. Note that even with the sun appearing in the back, the light from the torch is perfectly visible at this distance.	66

LIST OF FIGURES

3.15	Passive DOAS fits for the first run of the experiment, collected at the West Bank assembly	68
3.16	Passive DOAS fits for the first run of the experiment, collected at the East Bank assembly	68
3.17	Nitrogen Dioxide (NO_2) density values, in number of molecules, for the first run of the experiment. Note that the calculated value is the subtraction between the density found for the East Bank and the density found at the West Bank	69
3.18	This image, built using Google Maps, illustrates the East Bank relocation that took place in the second leg of the experiment. The first location is presented as EB ₁ , while the second is naturally EB ₂ . The West Bank is also presented for some geographic reference, and identified by WB.	69
3.19	Active DOAS molecular density for NO_2 , varying with the measurement number	71
3.20	Passive DOAS molecular density for NO_2 , varying with the measurement number. Note that this is the difference between the density obtained at the two experiment assemblies, as per hypothesis 2 (see 4.2).	71
3.21	Active DOAS fit results. Each plot corresponds to one measurement moment.	72
3.22	Passive DOAS fit results, from the system on the East Bank. Each plot corresponds to one measurement moment.	73
3.23	Passive DOAS fit results, from the system on the West Bank. Each plot corresponds to one measurement moment.	73
3.24	The Avantes ASCII file format. This is a screenshot of a file of this type opened in the VIM text editor. Note its particular structure, around which the file / folder parsing objects described by Figure 3.26 and Figure 3.27 are constructed.	74
3.25	The Data processing. The Object Oriented Programming (OOP) approach that was taken attempts to take advantage of the organisational structure of the spectral data, by modelling it into Python objects.	74
3.26	The file loading process. An Avantes ASCII file originates an AvantesASCII object, which besides a series of string-parsing operations stores the data in a Pandas DataFrame, for easy access and control.	75
3.27	The folder loading process. Each folder can have many files. The way in which the data is gathered (described in Subsection 3.2.2) requires some global operations performed on groups of files, like summation and normalisation (with reference to the integration time). The AvantesASCIIFolder object provides such operations.	75
3.28	UML diagram for the DOAS library. The OOP approach that was followed allows for an instrument-oriented experiment parametrisation, which is not available in any other software	76
4.1	QualAR chart for the NO_2 concentration at the closest monitoring station from the experiment site [3]. 07 June 2021.	79
4.2	Cross section for NO_2 , cut to the analysis window described in Table 3.7.	80

LIST OF FIGURES

4.3 Cross section for Tetraoxygen (O_4), cut to the analysis window described in Table 3.7.	80
4.4 QualAR chart for the NO_2 concentration at the closest monitoring station from the experiment site [3]. 23 June 2021.	81

LIST OF TABLES

1.1	Main research question	7
1.2	Secondary research questions	7
2.1	Global energy production, divided according to the fuel used to obtain it and the production country	24
3.1	Table summarising the new phantom's construction details, as a sum of 5 Gaussian profiles and an ellipse designed using TomoPhantom. In this table, Co is the object's amplitude, Xo and Yo are its center coordinates, and a and b are the objects half-widths. The table is constructed using TomoPhantom's particular syntax and more information can be obtained at [49].	56
3.2	Reconstruction error table for the new spectral phantom at several projection intervals. The MLEM routine used pure fan-beam data while the other two used resorted parallel information. Errors presented were calculated using the Root Mean Square Errors, normalised to the range of the reconstructed image.	59
3.3	Summary table for the two experiment assemblies. Note the difference in terms of material, due to the two different roles both assemblies play during the experiment. This is translated into not having the need of an artificial light source in the West Bank's assembly.	64
3.4	Actions are the indivisible unit upon which each capture is built. The prescribed actions for this experiment are described in this table.	65
3.5	Captures are particular sets of actions that are conducted according to a specific order, depending on the time of day on which the capture is run. This table describes the prescribed captures on which this experiment consisted.	65
3.6	First run: measurement table.	66
3.7	Parameters for the DOAS measurements relative to the first run of the experiment.	67
3.8	Second run: time of measurements table.	70
3.9	Parameters for the DOAS measurements relative to the second run of the experiment.	70
5.1	Summary table for the research questions presented in Section 1.4.	84

ACRONYMS

ALRI	Acute Lower Respiratory Infections i, 13
ANS	Autonomic Nervous System i, 13, 14
AP	Air Pollution i, ix, xi, 1, 2, 3, 6, 10, 11, 12, 13, 14, 15, 16, 17, 18, 19, 21, 22, 23, 24, 25, 26, 27, 28
API	Application Programming Interface i, 56
ART	Algebraic Reconstruction Technique i, 4
ASCII	American Standard Code for Information Interchange i, 64, 70
BAEP	Brainstem Auditory-Evoked Potentials i, 15
BTU	British Thermal Unit i, 22
CEM	Continuous Emission Monitoring i
CNS	Central Nervous System i, 16
CO	Carbon Monoxide i, 25, 27, 35
CO₂	Carbon Dioxide i, xi, 22, 24, 27, 35
COPD	Chronic Obstructive Pulmonary Disease i, 13, 16
CT	Computed Tomography i, 3, 4, 39
CVD	Cardiovascular Disease i, 13
CVM	Cardiovascular Mortality i, 13, 14
DIAL	Differential Absorption LIDAR i
DOAS	Differential Optical Absorption Spectroscopy i, ix, xii, xiv, 2, 5, 6, 7, 8, 11, 28, 29, 30, 31, 32, 33, 34, 35, 36, 37, 38, 39, 40, 45, 46, 47, 48, 49, 50, 62, 67, 68, 70, 71, 72, 73, 76, 78, 79, 83
EEA	European Environmental Agency i, 10, 11, 25
EPA	Environmental Protection Agency (United States) i, 10
ESCAPE	European Study of Cohorts for Air Pollution Effects i, 13
FBP	Filtered BackProjection i, 4, 41, 42, 43, 44
FFF	Forest Fire Finder i, 1, 2
FP7	European Union's Seventh Framework Programme i, 13

ACRONYMS

FST	Fourier Slice Theorem i , xii , 41 , 42
FT	Fourier Transform i , 41 , 42
FWHM	Full Width at Half Maximum i , 36
GDP	Gross Domestic Product i , xi , 22 , 24 , 25
H₂O	Water i , 35
H₂S	Hydrogen Sulfide i , 19
ICE	Internal Combustion Engine i
ICE	Internal Combustion Engine i , 24 , 25
IEP	InfraEstruturas de Portugal i , 63 , 65
IFT	Inverse Fourier Transform i , 42 , 43
IOT	Internet Of Things i , 2
LPG	Liquefied Petroleum Gas i , 25
MAX-DOAS	MultiAxis-DOAS i , 5 , 6 , 34
ML	Machine Learning i
MLEM	Maximized Likelihood Expectation Maximization i , 4
MSE	Mean Squared Error i , 58 , 59
NH₃	Ammonia i , 26
NO₂	Nitrogen Dioxide i , xiv , xv , 6 , 11 , 13 , 15 , 17 , 27 , 67 , 69 , 70 , 71 , 79 , 80 , 81
NO_x	Nitrogen Oxides i , 25
O₃	Ozone i , 11 , 15 , 18
O₄	Tetraoxygen i , xv , 79 , 80
OECD	Organisation for Economic Cooperation and Development i , 6
OOP	Object Oriented Programming i , xiv , 71 , 74 , 76
PAH	Polycyclic Aromatic Hydrocarbons i , 15
PICOC	Population Intervention Context Objective Comparison i
PM	Particulate Matter i , xi , 11 , 13 , 14 , 15 , 19 , 20 , 21
Project ATMOS	ATmosphere MOnitoring System Project i , 1 , 2
PT2020	Portugal2020 i , 1 , 2
ROI	Region Of Interest i , 3 , 8 , 49 , 50 , 51 , 52
RQ	Research Question i , 7 , 8 , 49
RTK GPS	Real Time Kinematic Global Positioning System i , 57
SART	Simultaneous Algebraic Reconstruction Technique i , 4
SGA	Small for Gestation Age i , 14 , 15
SLR	Systematic Literature Review i
SLR	Systematic Literature Review i

SMS	Systematic Mapping Study i , xii , 45 , 46
SO₂	Sulfur Dioxide i , 15 , 17 , 19
TDL	Tunable Diode Laser i
UAV	Unmanned Aerial Vehicle i , 1 , 8 , 50 , 81 , 83 , 84
UML	Unified Modelling Language i , 71
USB	Universal Serial Bus i , 64
VOC	Volatile Organic Compound i , 21
WFM-DOAS	Weighting Function Modified Differential Optical Absorption Spectroscopy i , 34 , 35
WHO	World Health Organization i , 2

TODO LIST

INTRODUCTION

1.1 Background, Motivation and Starting Points

1.1.1 Introduction

This thesis describes the work that I have done in the past 4 years on the design and development of a miniaturized system for atmospheric monitoring based on optical spectroscopy. The project itself was the major part of the [ATmosphere MOnitoring System Project \(Project ATMOS\)](#), an initiative that was contemplated with European funding through a [Portugal2020 \(PT2020\)](#) initiative and came as a response to the growing weight that [AP](#) has in the whole Western world.

The potential impact of [AP](#) on human health is amply documented. Numerous papers have, for decades, established many links between air quality and several common ailments like respiratory syndromes and cardiovascular diseases. Similar connections have also been found regarding the probability of gestational malformations and several types of cancer. On a different level, and of perhaps less immediate concern, are the effects that have been observed on ecosystems. Many times these effects are difficult to predict (and timely mitigate) and in some cases have been known to interfere with people's livelihood. In time, and if not addressed, these interferences will certainly hinder economies and limit the quality of life of populations globally. The severity of this problem makes it clear that we need to tackle it intelligently, and this approach requires that we can measure, trace and track [AP](#) effectively, which beckons engineers and scientists to create more technology for this specific purpose.

Answering this call, with this work I have tried to create a reply to the question of whether it would be possible to develop a two-dimensional pollutant mapping tool, small enough to be fitted onto a [Unmanned Aerial Vehicle \(UAV\)](#), which came to be a to-morphographically enabled design. To this end, I have developed a simulation platform that computationally proves the method's feasibility and confirmed through experiments that the hypothesis on which the solution is based, regarding the use of sequentially measured scattered sunlight as analogous to an artificial light source is valid.

1.1.2 Context

The idea behind this thesis was born in 2015, at NGNS-IS (a Portuguese tech startup). At the time, the company's flagship product was the [Forest Fire Finder \(FFF\)](#). The

FFF was a forest fire detection system, capable of mostly autonomous and automatic operation. The system was the first application of **DOAS** for fire detection, and for that it was patented in 2007 (see [87, 86]). The **FFF** is a remote sensing device that scans the horizon for the presence of a smoke column, sequentially performing a chemical analysis of each azimuth, using the Sun as a light source for its spectroscopic operations [84].

The **FFF** was deployed in several "habitats", both nationally (Parque Nacional da Peneda-Gerês and Ourém) and internationally (Spain and Brazil). One of the company's clients at the time was interested in a pollution monitoring solution, and asked if the spectroscopic system would be capable of performing such a task. The challenge resonated through the company's structure and the idea that created this thesis was born. The team then started reading about the concept of **AP** and how both populations and entities were concerned about it. It became clear that, while there were already several methods to measure **AP**, there was a clear market drive for the development of a system that could leverage the large area capabilities of a **DOAS** device while being able to provide a more spatially resolved "picture" of the atmospheric status. With this in mind, the company managed to have the investigation financed through a **PT2020** funding opportunity. This achievement was a clear validation of the project's goals and of the need there was for a system with the proposed capabilities. It was, however, not enough. **FFF** was a very good starting point, but there was still a lot of continuous research work needed before any of the goals that had been set were achieved. This led to the publication of this PhD project, in a tripartite consortium between FCT-NOVA, NGNS-IS and the Portuguese Foundation for Science and Technology. Its main goal was to develop an atmospheric monitoring system prototype that would be able to spectroscopically map pollutant concentrations in a two-dimensional way.

In April 2017, NGNS-IS was integrated in the Compta group, one of the oldest IT groups operating in Portugal. Despite its age, this company is one of the main presences in some of the most modern industrial fields, like **Internet Of Things (IOT)** applications. **Project ATMOS**'s pollutant tracing capabilities made it an almost perfect fit in one of **IOT**'s most resounding niches, the *Smart Cities* trend. Unfortunately, the transition between one company and the other, regardless of the project's adequacy, was anything but smooth. Almost two years later, in the beginning of 2019, engulfed in a sea of endless bureaucracy and ill intent on behalf of the managing governmental authorities (who seemed always more interested in seeing the project fail than anything else), **Project ATMOS** was terminated and financing was cut.

1.2 Problem Introduction

Air Pollution poses an important threat to the human way of life. The **World Health Organization (WHO)** have estimated that 1 out of each 9 deaths in 2012 were **AP**-related and of these, 3 million were directly attributable to outdoor **AP** worldwide, most of which in developing countries (87% vs 82% population). Although the European picture is not so dire as this, the topic does cause concern. In 2016, there were an estimated 400.000 deaths due to **AP** in Europe, 391.000 of which in the EU-28

space [37]. An increased number of premature deaths is sufficiently bad for treating this issue seriously, but the problems brought forth by [Air Pollution](#) do not end here. Not only are people dying more, disabilities (namely respiratory) are more frequent, and so are hospital visits. These two factors represent a decrease in productivity and an increase in medical costs, which accrue to the huge burden that [AP](#) already represents to any society. In Europe, health impacts of diesel emissions were estimated to be in the region of 60 billion euros [18] for the year of 2016.

These impressive numbers have perspired onto the public opinion, which is (now more than ever) concerned with the whole problem of [AP](#). In fact, the subject is considered by the public the second most important environmental threat (after Climate Change, which is a very related topic), and citizens throughout Europe have been partaking in initiatives which aim to aid and incentivize air quality monitoring, as well as raising awareness to the necessity of paying attention to this issue and for behavioral changes. As tackling [Air Pollution](#) and its causes grows ever more popular, so does the political weight associated with the subject, which in turn results in an increased number of measures destined to improve air quality. However, effective actions against [AP](#) require the approach to be intelligent and knowledgeable, for the more we know, the better we can handle it. It is thus the role of technology and technologists, to develop new ways in which to measure, map, track and trace [AP](#), leveraging the power of human intellect and ingenuity to combat this impending threat that is upon us.

1.3 Literature review

1.3.1 Tomography

Tomography is the cross-sectional imaging of an object through the use of transmitted or reflected waves, captured by the object exposure to the waves from a set of known angles. It has many different applications in science, industry, and most prominently, medicine [23]. Since the invention of the [Computed Tomography \(CT\)](#) machine in 1972, by Hounsfield [38], tomographic imaging techniques have had a revolutionary impact, allowing doctors to see inside their patients, without having to subject them to more invasive procedures [47].

Mathematical basis for tomography were set by Johannes Radon in 1917. At the time, he postulated that it is possible to represent a function written in \mathbb{R} in the space of straight lines, \mathbb{L} through the function's line integrals. A line integral is an integral in which the function that is being integrated is evaluated along a curved path, a line. In the tomographic case, these line integrals represent a measurement on a ray that traverses the [Region Of Interest \(ROI\)](#). Each set of line integrals, characterized by an incidence angle, is called a projection (see Figure 1.1). To perform a tomographic reconstruction, the machine must take many projections around the object. To the set of projections arranged in matrix form by detector and projection angle, we call sinogram. All reconstruction methods, analytical and iterative, revolve around going from reality to sinogram to image [11, 47, 43, 41, 42, 25].

There are two broad algorithm families when it comes to tomographic reconstruction, regarding the physics of the problem. It can involve either non-diffracting sources



Figure 1.1: A schematic representation of a projection acquisition. In this image, taken from [42], the clear line that comes down at a diagonal angle is a projection.

(light travels in straight lines), such as the X-Rays in a conventional [CT](#) exam; or diffracting sources, such as micro-waves or ultrasound in more research-oriented applications [47]. In this document, I will not address the latter family, since I will not be applying them in my work.

In any tomographic procedure, the first step is to gather information from the target object. The first concept one requires for this is to determine the problem's geometry. There are many different possible geometry, however, there are two that are more important for this thesis: parallel and fan-beam geometries. In the parallel case, there are as many light sources as there are detectors. Light travels between the source and the detector in straight lines, and the whole set rotates around the object's location. Fan-beam geometries are characterized by having only one light source which rotates around the target object. In this geometry, a set of detectors are placed on the other side of the object, and the lines (rays) between the source and the detectors describe a fan, thus the name of the technique [42, 47].

As far as algorithms are concerned, there are two main types: analytical and iterative. The first family includes the most famous algorithm for these applications, the [Filtered BackProjection \(FBP\)](#). Iterative algorithms work by iteratively searching for a solution to the reconstruction equation, which is basically an underdetermined system of equations (far less equations than unknowns). There are numerous algorithms that work in this way, but in my work, I have identified three that are extensively used, both in the field of atmospheric tomography and in medicine: [Algebraic Reconstruction Technique \(ART\)](#), [Simultaneous Algebraic Reconstruction Technique \(SART\)](#), and [Maximized Likelihood Expectation Maximization \(MLEM\)](#). The simulator that was developed as part of this project uses the last two and [FBP](#). All these techniques are further discussed and presented in Chapter 2.

1.3.2 DOAS

Since the beginning of the 20th century, scientists have been using spectroscopy to measure reactive trace gases in the atmosphere, especially ozone. The basis for these applications were set by Bouguer, Lambert and Beer, which have separately presented the law (Lambert-Beer's) that determines the relationship between light extinction and the concentration of an absorber, when it must traverse a medium in which this absorber is present. DOAS is one of the methods that is applied for this purpose. It was developed in 1976, by Perner and his colleagues [65], to detect and quantify the hydroxyl radical in the atmosphere. The book by Jochen Stütz and Ulrich Platt [66] is considered by most researchers one of the most important references in the field and is present in most bibliographies of the literature in this subject (it is also one of the main references in this thesis). Platt, in particular, has been working with the technique since its beginning, as one of the elements of Perner's team that published the article about the hydroxyl radical mentioned some lines above [65].

Besides DOAS, Lambert-Beer's law is the basis of many quantitative spectroscopy applications. However, most of these techniques are used in a laboratory context, in which conditions are controlled and very well known. Atmospheric studies do not have this luxury. In the open atmosphere, there are a number of factors, like Mie and Rayleigh scattering, atmospheric turbulence or thermal fluctuations in the optical path that make outdoor spectral measurements more complicated. DOAS is able to circumvent these difficulties by measuring differential absorptions, which is to say the difference in absorption between two different wavelengths [66, 56].

There are two modalities for DOAS experiments, Active and Passive, which differ mainly on the use of artificial or natural light sources, respectively. Both methods have their advantages and disadvantages. Active systems are more similar to a bench spectroscopy experiment. Conditions are more controlled (starting with the light source) and therefore, results are usually more reliable and precise, not to mention simpler to reach, since there is no need to account for complex physical phenomena, like radiative transfer [66]. However, these systems do require additional material, and many times entire infrastructures have to be built around them [69]. Passive systems, on the other hand, can be comprised of just a computer, a spectrometer and a telescope, making them instrumentally much simpler than their active counterparts. This flexibility also comes with the possibility to develop new interesting sub-techniques, like MultiAxis-DOAS (MAX-DOAS), which allows (for instance) the determination of the stratospheric contribution of a certain trace gas (in opposition to its tropospheric contribution). The mathematical processing of the acquired spectra, nonetheless, is much more complex.

1.3.3 DOAS Tomography

DOAS tomography is a relatively new subject within the realm of DOAS. It consists in the application of tomographic methods to reconstruct a two-dimensional or three-dimensional *map* of the concentrations of trace gases in study. The seminal paper that originated this and other remote sensing tomographic techniques was published by Byer and Shepp in 1979 [14]. It is not by any means a very populated literary space. In a systematic review that was performed as part of a course I took during

the development of this PhD thesis (see Section 2.5), I managed to identify a total of 13 papers that were clearly about DOAS tomography. In doing this review, I have also found that the largest DOAS tomography study was performed in Germany, during the first years of the 21st century. This research campaign, called BAB-II [52], aimed to measure and map traffic-related concentrations for NO₂ in the motorway that goes between Heidelberg and Mannheim. A more recent effort that is mention worthy is the paper by the Stutz [80], in which the group created a tomographic system that was able to perform as a fence line monitor for a refinery in Houston, Texas. In between the two studies, and right after BAB-II, Erna Frins published her paper [33], in which she described the use of a MAX-DOAS system alternately pointed towards sun-illuminated and dark targets in a tomographic manner.

Besides the birds eye view of the literary panorama of the DOAS tomography field, this systematic review allowed me to understand two important gaps in the technology being employed for this research. The first is that all of the studies that were featured in my review used a very low number of tomographic projections (some dozens of line integrals). This is a problem because it is the single most important factor for the resolution of any tomographic procedure, and although resolution is not an absolutely critical factor in atmospheric analysis (because the sizes of the target objects - gas plumes - are very large and diffuse), it is an important system feature that should be improved. Moreover, the second important pattern that was clear from my research was that all but one of the described systems were fixed, and the one that was mobile was composed of a minimum of two spectral acquisition devices and had one of the lowest numbers of projections in all papers. This is a very important gap. DOAS tomography has the ability not only to measure but also to map pollutant concentrations and can be an invaluable technique in the fight to understand and track the movement of pollutant plumes, but the fact that the available systems require dedicated infrastructure to operate and have no mobility at all may be the most important factor leading to the almost non-existing investment DOAS tomography systems.

More than half of the world's population is expected to be living in cities by the year 2050, and in the next 10 years we will see an increase in the number of so-called mega cities of more than 30% [15]. This puts a lot of pressure on governmental agencies and municipalities (specially in the West) to "smarten up" their urban infrastructures, so that cities can harbour their inhabitants with reasonable quality of life for everyone. In fact, a recent report by Organisation for Economic Cooperation and Development (OECD) concluded that in 2010, estimated costs due to AP were around 1.7 trillion American dollars, just in OECD countries. The flexibility and mobility that the system I am developing brings to the table are two very heavy points in its favour as a pollution mapping tool which is unobtainable with the traditional methods, whether *in-situ* or remote.

1.4 Research Questions

In Section 1.1.2, I have introduced the reasons which led NGNS-IS to pursue the development of an atmospheric monitoring system, and that what set it apart from other systems was the ability to spectroscopically map pollutants concentrations using

tomographic methods, thus defining a primary objective for this thesis.

Two secondary objectives were born from the necessary initial research, which had a very heavy influence over the adopted methods:

- To use a tomographic approach for the mapping procedure;
- To ensure the designed system would be small and highly mobile;
- To use a single light collection point, minimizing material costs.

Taking all the above into account, we arrive at the main Research Question ([Research Question \(RQ\)](#)), presented in Table [1.1](#).

Table 1.1: Main research question.

RQ1	<i>How to design a miniaturized tomographic atmosphere monitoring system based on DOAS?</i>
------------	---

This is the main research question. It gave rise to four other more detailed research questions. These secondary questions allow a better delimitation of the work at hand and are important complements to RQ1. This questions are presented in Table [1.2](#).

Table 1.2: Secondary research questions.

RQ1.1	<i>What would be the best strategy for the system to cover a small geographic region?</i>
RQ1.2	<i>What would be the necessary components for such a system?</i>
RQ1.3	<i>How will the system acquire the data?</i>
RQ1.4	<i>What should the tomographic reconstruction look like and how to perform it?</i>

1.5 Hypothesis

As stated in Section [1.4](#), the main goal of my work was to provide an answer to the question of how to design a miniaturized tomographic atmosphere monitoring system, based on [DOAS](#). This sentence is the most important point of the project. Every development from this point forward stems from it and is motivated by it. It also requires some deconstruction in order to understand the true scope of the matter. First, it is a miniaturized device. This means that besides all the habitual requirements (performance, function, adequacy, compatibility with the other components, safety and security) in defining components in an engineering project, one must also keep in mind the footprint of each component, and how much it weighs. Second, it is a tomographic system, which means that not only the device must be able to take line integrals from some kind of medium, it must also be able to describe a predefined trajectory, with admissible levels of geometric error, which complies to a certain projection geometry. Otherwise, one would not be able to apply a tomographic reconstruction routine to

obtain the map of the target species concentrations. Finally the system is supposed to monitor the atmosphere in some way. Now, as implied in the same sentence, **DOAS** is the technique that I am trying to apply in this system. But as I point out in Section 1.3.2 and with more depth in Section 2.2, there are two families of **DOAS**, and within them, many sub-techniques. This system which I am developing is based on the hypothesis that we can use an almost hybrid approach to **DOAS**: passive **DOAS** instrumental simplicity and active **DOAS** retrieval simplicity. One could use a scattered sunlight measurement as a light source for a **DOAS** analysis, provided distances between the two points are kept small, optical densities are low (clear atmosphere), and both spectral measurements are taken in the same angle. With this process, we would only effectively be using as projections the spectral measurements of the **ROI**. This hypothesis, while not being mentioned in the library directly, has already been hinted at in several papers, namely references [33, 17, 46].

1.6 Methods and Findings

The **Research Question** were used to guide the conduction of this thesis' work. This has led to a natural two side division: on the one hand, there was the need to algorithmically define projections for tomographic reconstruction of a trace gas concentration field; on the other hand, physical tests had to be conducted to ensure that the idealised projections were feasible. These were the two hypothesis that had to be verified.

The first hypothesis was addressed by the construction of a software simulation system based on several projection and backprojection matrix operators. This system is based on one of the main novelties involved in this project: a high degree of geometric measurement freedom. This is achieved by assuming that our tomographic acquisition system is mounted on a custom-built **UAV**, which carries specific spectroscopic equipment and is programmed using ArduCopter's SITL software suite [**arducopter**] for full autonomous operation. Spectral acquisition takes place using a set circular trajectory that implies the acquisition of a higher-than-usual projection number in comparison with traditional DOAS-tomography operations. After simulating the spectral projection information, according to a number of parameters that are input at runtime, the system calculates their backprojection and assembles a simulated concentration map for the selected trace gases.

The second hypothesis is addressed by means of the physical acquisition of spectral data between two relatively close points in Almada, Portugal. By comparing spectral information retrieved by two different sets of equipment in said geographical points, we should be able to establish that current day equipment is able to measure trace gas concentrations in this kind of distances and that it is possible to make these measurements through the difference of two passive **DOAS** measurements.

1.7 Layout

After this introduction, in Chapter 2, we can find a more thorough literature review than the one presented in Section 1.3. After that, I have included the chapter in which I present the methods employed in this project's development (Chapter 3), and discuss

them in Chapter 4. Finally, in Chapter 5, I present what could be concluded as a result of this project and some of the future developments that might be pursued.

LITERATURE REVIEW

2.1 Air Pollution

Daniel Vallero, in his book "Fundamentals of Air Pollution" [85] makes a very important observation: Air Pollution has no universal definition. Its meaning is intertwined with the context with which it is measured and observed, with the ecosystem in which it is perceived and even with the pollutant concentration (not every toxic compound is toxic at every concentration). The [Environmental Protection Agency \(United States\) \(EPA\)](#) defines Air Pollution as the following:

Air Pollution is the presence of contaminants or pollutant substances in the air that interfere with human health or welfare, or produce other harmful environmental effects.

He then analyzes this definition through two possible lenses, the one that comes with the interference produced by air contaminants; and the one that comes from the harm they may cause. He notes that both points of view come with a heavy burden of ambiguity, incompatible with a scientific definition. We can thus observe that preferable to address the issue through its measurable effects and consequences. These are well-established and well known, and scientists all around the world have been publishing extensively about them for some decades now. The correlation between Air Pollution and an increased mortality in heavily industrialized areas was first established in Europe, in the 19th century, but the first time it was taken seriously was during the 1952 killer-smog incidents, in London [66]. At the time, a combination of very cold weather, an anticyclone and fireplace emissions caused a thick smog to fall over London, directly causing thousands of deaths and indirectly many more [6, 62]. The disastrous consequences of this incident had a huge impact in the civil society, resulting in a series of policies and laws, among which the Clean Air Acts of 1956 and 1968, which are broadly considered to be some of the first actions to decrease pollution in human societies. Much work has been done, and it has resulted in remarkable progress since the definition of those two policies. We are in fact in a much better place than we were some years or decades ago, but pollution is still a part of everyday reality for the whole of civilization. In the current day and age, both European and American regulatory and surveillance bodies (the [European Environmental Agency \(EEA\)](#) and the [EPA](#), respectively) have identified a group of six *criteria pollutants* that need to be monitored effectively.

2.1.1 Criteria Pollutants

Description of criteria pollutants and an explanation of their chemistry and atmospheric cycles.

2.1.2 Air Pollution Effects on Human Health

Arguably, there is no medium in which it is more important to consider AP by its effects than in the human body. However, even this has its caveats. The body's response to any given substance changes with the dose that is administered to it, something which has been known to us for centuries:

What is it that is not poison? All things are poison and nothing is without poison. It is the dose alone that makes a thing not poison.

– Paracelsus

This quote, originally in the writings of one of the fathers of modern medicine, the Swiss Paracelsus, was taken from Patricia Frank's book called *The Dose Makes The Poison* [32] and is one of the core tenets of toxicology even today. There are, however, some substances which do not need anything close to a high dose to cause harm to human health, and in general, atmospheric pollutants fall in that category. According to the EEA, heart disease and stroke are the most common causes of premature death due to Air Pollution. The same organization states that the most prominent atmospheric pollutants in terms of the effects they have on human health are PM, NO₂ and Ozone (O₃) [28, 27]. In this thesis, I will focus mostly on them, not only because of their health importance, but also because of their spectral nature, which allows us to detect them using DOAS [66]. Of course, a complete description of how AP affects the human body is a colossal task which is well beyond the scope of this thesis. Therefore, I will focus my attention on the more prominent symptoms that are results of these chemicals: respiratory syndromes, cardiovascular diseases, problems during gestation and finally, neurologic consequences of AP.

2.1.2.1 Respiratory effects of Air Pollution

The respiratory system's main functions are the delivery of oxygen into the blood stream and the removal of carbon dioxide from the body. Air enters the body from the upper airways and flows to the alveolar region, where oxygen diffuses across the lung wall into the blood stream, from which it is transported to the tissues where it diffuses yet again and is made available to the mitochondria in the cells, that use it for cellular respiration [59]. The whole system is in permanent interaction with the atmosphere, and is therefore exposed to all kinds of air pollutants and trace gases, and therefore it is only natural that respiratory effects are among the most direct health complications originating in AP [85].

The region in which a given pollutant is, within the respiratory system (see Figure 2.1), is of great importance. After the air is inhaled through the nose, the air is heated or cooled to body temperature, as well as humidified, in the upper airways. The trachea leads the air into the bronchi, where flow is divided several times before reaching the alveoli, where oxygen is supposed to enter circulation. Since air flows within

CHAPTER 2. LITERATURE REVIEW

the different regions of the pulmonary system are completely different, AP is also handled differently among them. Moreover, it is also important to consider that pollutants also vary according to their own physical properties, and pollutant absorption is also a function of this. Particles' absorption depends on their aerodynamic characteristics, as well as soluble fraction and density. Gaseous pollutants are dependent exclusively on their vapor pressure, solubility and density [59, 85].

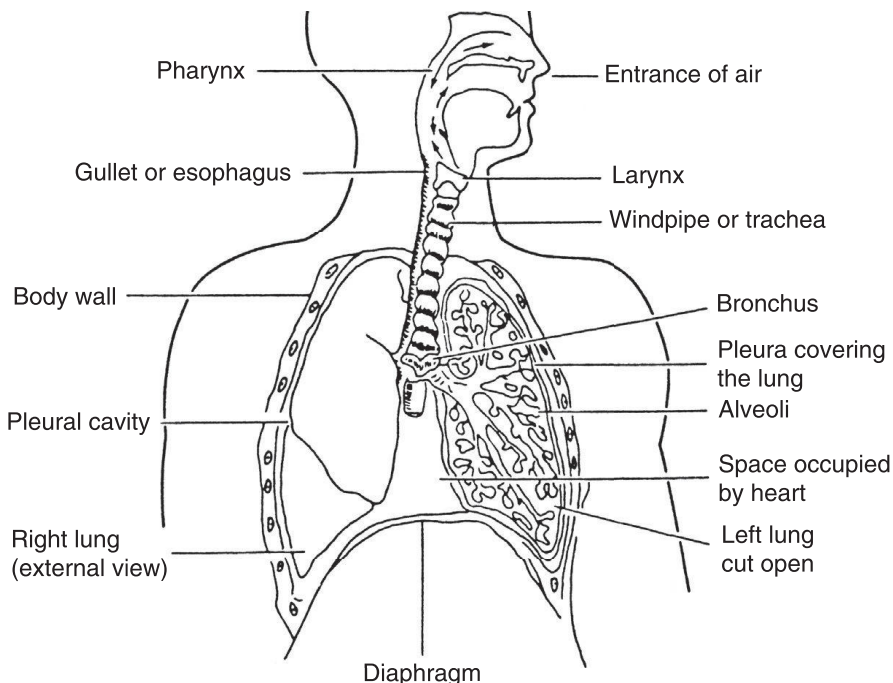


Figure 2.1: Annotated anatomy of the respiratory system [85].

The respiratory system has several (imperfect) mechanisms in place to prevent particles from reaching the blood stream. Larger particles are deposited in the nose, by impaction on the hairs and bends of the nose. Smaller particles are immune to this first barrier, and manage to get to the trachea and bronchi, where they are filtered also by impaction, this time on the walls of the innumerable bifurcations of the bronchial tree. The smallest particles are removed through Brownian motion, which ends up pushing them against the alveolar membrane. Deposited substances are then removed through the action of cilia in the pulmonary system's walls or by coughing, sneezing or blowing one's nose [85].

While the body is quite efficient at filtering out particles from the respiration process, the same cannot be said about gaseous pollutants. Removal of these compounds can only be achieved through absorption, which depends almost exclusively in the gases' solubility. High solubility compounds are absorbed directly in the upper airways (SO_2 , for instance), while less soluble gases (such as O_3 and NO_2) are absorbed in the lungs themselves. Irritant gases trigger a variety of responses, in which one can include sneezing, coughing or bronchoconstriction. These gaseous compounds are then diffused through to the bloodstream or the lungs themselves try to convert them into other substances via biochemical processes. In some cases, this attempt to detoxify a pollutant can lead to much more problematic circumstances. For instance, the lung is

known to active procarcinogens, substances that are only carcinogenic after being metabolized in a certain way [85].

Acute symptoms of AP exposure are very varied, and range from mild irritation to complete respiratory failure, depending mostly on level of exposure and individual sensitivity to the chemical compound. One of the most important acute manifestations of AP exposure are encompassed within the **Acute Lower Respiratory Infections (ALRI)** group. There are several studies in which the relationship between this issue and AP is deducted and explained, mostly in developing countries, and it remains as one of the major causes for infantile death [15, 83]. Children are one of the most affected demographics by AP [28], and one of the chief reasons for this is that the human respiratory system is till developing in this stage of life.

In a 2016 review [35], the authors searched the literature for childhood adverse effects of AP, with a particular focus on respiratory problems. They have found evidence for a number of respiratory complications and diseases that were previously reported in the literature caused or exacerbated by AP. Effects are many, and vary immensely in nature, severity and affected populations. Short term effects, like coughing and wheezing were found for the three types of major pollutant and several others; several papers mention an association between the occurrence of respiratory infections and exposure to AP, namely concerning PM and NO₂. The same review found reports of decreased lung function in children and asthma exacerbation in children due to Air Pollution. Moreover, a person exposed to high levels of AP during childhood are also more likely to develop syndromes like **Chronic Obstructive Pulmonary Disease (COPD)**, and to have exacerbated symptoms of this disease. Finally, and perhaps more concerning, the carcinogenic nature of several of the constituents of AP leads to findings relating the appearance of respiratory cancers to exposure levels during childhood. Many of the conclusions of this review come from a large-scale European effort called **European Study of Cohorts for Air Pollution Effects (ESCAPE)**, that intended to investigate long-term health effects of AP in Europe. ESCAPE was an European Union's Seventh Framework Programme (FP7) initiative that ended in 2014.

2.1.2.2 Air Pollution and cardiovascular issues

After being absorbed by the respiratory system, oxygen is distributed to all cells of the body through the cardiovascular system. Air pollutants, like particles and trace gases, are also capable of penetrating the lung barrier and therefore share the same fate. There are several pathways with which AP and negatively affect the cardiovascular system. The most immediate of which is probably an imbalance in the **Autonomic Nervous System (ANS)** caused by direct inflammation and oxidative stress in the respiratory system. The second most immediate pathway is systemic inflammation caused by Air Pollution. Finally, soluble AP compounds in the bloodstream also contribute to **Cardiovascular Disease (CVD)** by increasing inflammation and oxidative stress in the cardiovascular system [10, 85].

The link between Air Pollution and cardiovascular effects started being made during the twentieth century, given a series of incidents (like London's 1952 killer-smog) that happened in the urban areas of industrialized countries. Nowadays, **Cardiovascular Mortality (CVM)** has been shown to be intricately connected to AP. In fact, in a

2013 review indicated that an annual increase of $10\mu\text{g}/\text{m}^3$ in fine PM and NO₂ led to an increase of 11% and 13% respectively in terms of CVM and premature atherosclerosis, in spite of absolute AP concentrations were maintained below the European policy-recommended thresholds. Road traffic exposure studies have reported similar findings, with subjects having increased coronary calcium scores [8].

Arrhythmia is one of the other cardiovascular issues that might be caused by AP. There is still some debate regarding whether or not there is a causal relationship between the two, but there have been several studies in which increased levels of Air Pollution were correlated with arrhythmia-related hospital admissions. Moreover, there seems to be a correlation between low heart rate variability and AP, which is considered a marker for ANS imbalance and an important risk factor for CVM[8].

The risk of stroke is also clearly exacerbated by the presence of increased levels of AP. In fact, it is currently thought that AP is responsible for about 29% of the burden of stroke, globally. Studies have shown that an increase of $5 \mu\text{g}/\text{m}^3$ in the annual PM_{2.5} concentration leads to a remarkable 19% increase in the risk of stroke, which was found to be more significant in non-smokers. A positive correlation was also found between gaseous pollutants (NO₂, CO and SO₂) concentration and the risk of stroke or stroke mortality.

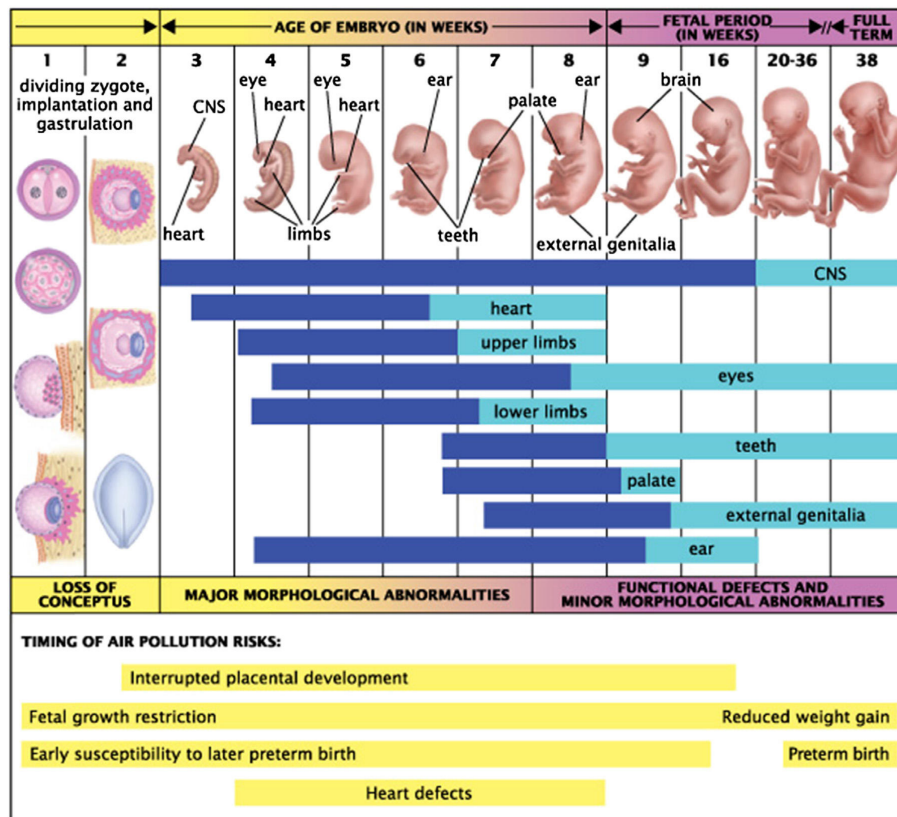
Short term effects of AP on the cardiovascular system seem to be predominantly the triggering acute coronary incidents. For instance, a positive correlation was found between short term increases in AP and non-fatal myocardial infarctions.

2.1.2.3 Gestational and developmental complications

Mammals are in their life's most vulnerable stage while they are still developing inside their mother's womb. This is the time when there is a greater rate of tissue expansion and creation, creating an enormous need for nutrients. These are supplied by the mother's blood, crossing the placenta and reaching the fetus through its umbilical cord. High rates of tissue formation and proliferation render the forming being unstable and therefore more susceptible to the appearance of some kind of morphological abnormality. At this time, there is no separation between the mother's blood and the fetus, meaning that whatever chemical reaches the progenitor's bloodstream also reaches the growing fetus. If the mother is exposed, so is the fetus [85].

There are numerous chemicals that can affect the female reproductive system, of which some are habitual components of AP. They have been associated to several highly adverse affects, and interfere with such things as the processes by which the body is able to produce eggs, or other processes that enable the formation of a single cell by the union of the sperm and the egg (the zygote). After conception, AP has been known to reduce uterine nurturing capabilities, and hinder the new being's development. Some of them are even teratogens, meaning that they induce birth defects. Figure 2.2 illustrates the kind of defects that come with exposure, according to the time at which the mother was exposed.

There are already several studies that correlate higher AP exposure levels to birth defects or the probability of negative outcomes. For instance, in [54], researchers have studied the association between AP exposure levels (for the mother) and the appearance of premature Small for Gestation Age (SGA) by collecting more than 40000 births



Note: Blue bars indicate time periods when major morphological abnormalities can occur, while light blue bars correspond to periods at risk for minor abnormalities and functional defects.

Figure 2.2: Possible abnormalities caused by AP exposure *in utero*. Notice that time of exposure is of critical importance [85].

in Changzhou Maternity (China) and studying the mother's typical environment. This study has found a positive association between SGA and exposure to PM_{2.5} in two or three pollutants models of AP (with NO₂ and Sulfur Dioxide (SO₂)), during the third trimester of gestation. Another, perhaps more comprehensive study, was performed using Swedish data from 1997 to 2007, and found that there was a positive association between O₃ exposure and the appearance of pre-eclampsia (a potentially deadly complication of pregnancy), estimating that about 1 in 20 pre-eclampsia cases were caused by AP [63].

Besides uterine development compromises, birth defects and reproductive difficulties, Air Pollution has also been associated with hindrances to the child's neurodevelopment. In a New York study was able to associate lower levels of mental development at age 3, in African-American children with valid prenatal Polycyclic Aromatic Hydrocarbons (PAH) exposure data. In another study from the neighboring Boston, AP was associated with generally lower cognitive test scores, even when correcting for several influencing factors. On a different level, AP was shown to produce significant delays in the central conduction times of Brainstem Auditory-Evoked Potentials (BAEP) tests in children, indicating that there might be important repercussions of AP to vestibular and auditory development.

Although most other systems are affected by AP, it does have a particularly heavy

toll on the respiratory development. This is because the lungs are not completely developed at birth, and are only finished in the late teens. The level to which AP affects the respiratory system development varies greatly with the stage of life in which the effect is produced, and severity is also very varied. Acute negative effects range from respiratory death to chronic cough [85]. Moreover, childhood (and prenatal) exposure to AP has been associated with the emergence of conditions such as COPD and asthma.

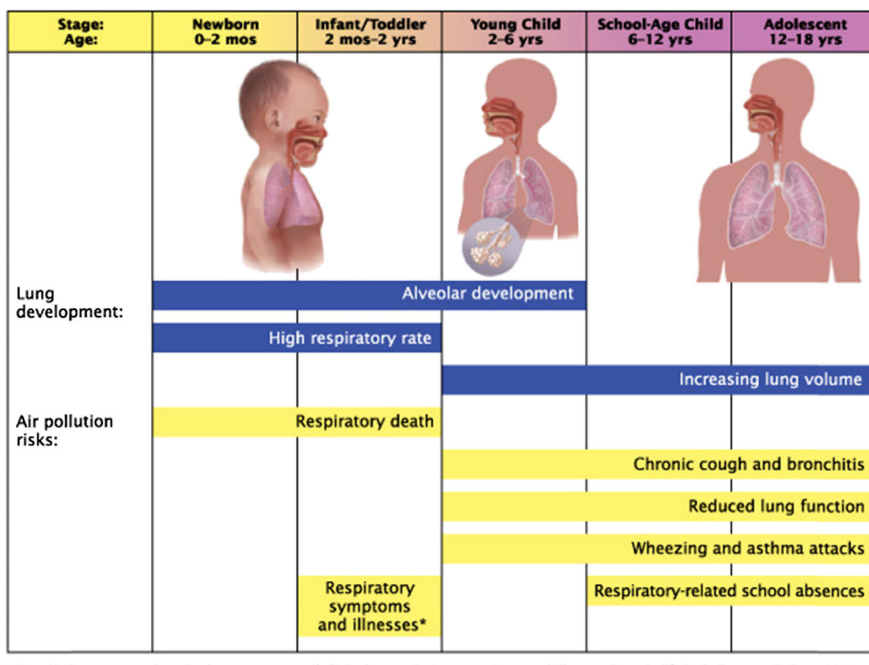


Figure 2.3: Developmental stages of the lung throughout life vs the risks of AP exposure in each stage [85].

2.1.2.4 Neurological disorders

The brain and the **Central Nervous System (CNS)** were one of the last to be included in the range of organs that are affected by AP. While the effects of AP on the respiratory and cardiovascular systems are quite broad and include some "surprises", the fact that these systems were affected by **Air Pollution** was evident and expectable, given the type of exposure these systems endure. The **CNS**, on the other hand, has a more difficult to express relationship with AP, and has required more sophisticated methods to detect [85, 34]. It was in the beginning of this century that the first connections between AP and the emergence of neurological disorders started to be made, and from then on, we have progressed into thinking that not only are they related, but also that AP might be one of the key driving forces in the onset of certain neurological diseases, including the most dreaded of them all, Alzheimer's and Parkinson's [34, 24, 16].

The reason why AP is able to reach and damage the CNS is a continuation (or even an extension) of the ways in which it affects the cardiovascular system. By crossing the alveolar barrier into the bloodstream, AP acts as an oxidative stress source. As

it can also do in lung tissue, **Air Pollution** creates some local proinflammatory effects in the cardiovascular system, affecting the vascular endothelium cells. This can lead to a systemic inflammatory status, which is accompanied by the production of proinflammatory cytokines (a type of message-protein that is used by organisms to trigger certain types of response, like inflammation [92]). Now, since blood vessels in the brain are extremely responsive to this kind of message, their presence can activate cerebral endothelial cells and disrupt the blood-brain barrier [34].

In 2018, a consortium of several Spanish universities and researchers wrote a review detailing the until-then-published articles dealing with the neurological implications of **AP** [24]. This review identifies several articles that connect the long-term exposure to **Air Pollution** with adverse impacts on the brain and brain structures. *In vitro* and *in vivo* studies, focusing on traffic related emissions and their effect on gray matter cells, have found that these display significant alterations. On other studies identified by the review, it was shown that white matter, the myelinated part of the brain, is particularly sensitive to **AP** and its volume is significantly decreased both in the elderly and children, as consequence of prolonged exposure to it.

There are also several articles that show that there is an association between exposure to air pollutants and impairments on brain function. In Section 2.1.2.3, I have already mentioned a study that was conducted in New York, and that found that the children that they were using as subjects were found to have measurable cognitive deficits in comparison with children of the same age living in less polluted areas which are compatible with the affected areas of the brain that were detected through neuroimaging studies [24].

2.1.3 Air Pollution effects on ecosystems

The Earth is home to an almost unbelievable number of different ecosystems. The ubiquitousness of **AP** means that all of them are in some way or another affected by this problem. In general terms, the threat posed by **AP** to any given habitat is a function of its biodiversity, defined as the number of different living beings that inhabit a certain environment (in all biological kingdoms) [64]. Living beings within an ecosystem are like nodes in a graph, with many connections to any particular node. More biodiversity corresponds to a greater number of nodes and an even larger number of links, which means that there is a greater probability that some of those links become disrupted by **Air Pollution** in some way.

Water based environments are greatly affected by **AP**. Material deposition on the surface of the water can have serious consequences in terms of habitat conditions for holding life. In this regard, the most important air pollutants are **NO₂** and **SO₂**, which significantly decreases the water's pH. On its own, this represents a major problem. The acidifying effects of nitrogen and sulfur deposition became very pronounced in Scandinavia (among other places). Thousands of this territory's lakes, once teeming with wildlife, became effectively lifeless. Those that did not reach this point, have seen the number of fish living on their waters dwindle to numbers from which there may be no return [89]. Sulfur and nitrogen depositions also enrich surface waters, altering the solubility and other physical aspects on the surface of the water, which in turn inevitably leads to disruptions in species abundance and diversity. Moreover, indirect

effects may also take their tolls. For instance, O_3 does not play any significant role in the chemical behavior of a water body, but it can influence the number of predators around this habitat, which will compromise the predator-prey balance of the aquatic environment [85, 55].

In terrestrial ecosystems, AP effects are not smaller in importance or complexity, and they are different for each type of being. To the Flora, AP can have a subtle to deadly effect, depending on variables like pollutant chemical species, exposure time, or plant life stage in which exposure happens. For instance, O_3 is especially poisonous to plants. Even small concentrations of this gas will cause plant growth to decrease significantly. It enters the plant through the stomata and reduces photosynthesis through increased oxidative stress. Many times, although concentrations are not enough to outright kill the plant, they are enough to make them more susceptible to other attacks like pathogens, insects or environmental conditions. Ozone is commonly responsible for huge financial losses that come from the diminished agricultural yields. And while it is true that due to several policies, AP is in a clear downward trend since the 1980s in urban regions, it is also true that in many rural areas, these changes have been smaller or non-existent, making these losses even more relevant [55, 85].

Forests are among the most susceptible environments to AP. They suffer from the previously described mechanisms of AP damage, like acidic deposition, but also suffer from other, less direct pollution risks. Emission of greenhouse gases can induce changes in humidity, temperature, and general climate profile of a forest. The combination of direct and indirect risks result in an exacerbation of both, leading to more and more forest losses due to Air Pollution. The damage done to forests all around the world is especially problematic given the biodiversity that these ecosystems contain within themselves. Rainforests in particular are thought to contain more than half of the world's terrestrial species. These species have many times adapted to a particular kind of microhabitat which only exists in the specific rainforest in which it lives. Changes in these specific conditions, whether caused by Air Pollution or any other cause, are leading to alarming extinction rates in forests and rainforests globally [85, 55].

Of course it is not only the flora that suffers with Air Pollution. Direct implications of AP on animals approximate those that fall upon humans. We are an animal species, after all. Our main difference is the adaptation capabilities that our superior intellect grants us, which allows us to escape more or less unscathed for a longer period of time, and to combat what we cannot escape from in ways which are simply unaccessible to other animal species. So, although AP has direct effects on all animals that are exposed to it, ecosystem damage and eventual destruction remains the most perilous factor for this biological realm [85, 55].

2.1.4 Air Pollution Sources

There are almost as many AP sources as there are pollutants. The first major division between these sources is whether they are natural or anthropogenic. However, this separation is not always clear, as one source can lead to another and boundaries become fuzzy within their own context. The most prominent example of such is the case of accidental fires. While they are most of the times classified as a natural source of AP,

their origin lies most of the times in human activities. In this section, I will present a selection of the most important naturally occurring air pollutants and examples of how they have affected human lives throughout the times. The selection itself does not intend to be complete description of pollution sources, but rather paint a general picture of the subject.

2.1.4.1 Natural Sources of Air Pollution

Although people, governments and institutions tend to speak far more seldomly of them than of their man-made counterparts, natural sources of air pollutant are not only abundant, but also important. One of the main natural sources of AP are volcanic eruptions. These phenomena are responsible for the emission of immense quantities of PM and gases such as SO₂, Hydrogen Sulfide (H₂S) and methane. Depending on the type of volcanic eruption, the emitted cloud of gas and PM can remain airborne for long periods of time, even disrupting modern life at times, namely in what concerns air travel. The last eruption to happen in Portuguese soil took place in the remote Azorian island of Faial. In September 1957, the Earth shook almost continuously for around two weeks. Finally, on the 27th, 100 m Northeast the Capelinhos islands, the sea was seen to boil and project vapor and volcanic material hundreds of meters into the air. In the following hours, the underwater volcano finally exploded, emitting large quantities of volcanic ash and gases into the atmosphere. The phenomenon lasted for more than a year, and the final ejection of lava took place in October 1958 (see Figure 2.4). The eruption had a significant social impact, in addition to its ecologic importance. In the end, 40% of Faial's population left the island as a result [85, 82].

Oceans are also a significant source of AP. Aerosol particles of salt are continuously emitted from these large masses of salt water, which damage many human created structures, namely metallic constructions. In certain parts of the world, another important source of Particulate Matter (especially because of its consequences in the inhabitants' daily life) are dust storms. The most famous of these events, and one of the most deadly storms in the recorded history of the US territory was the infamous *Black Sunday* dust storm. Starting on Palm Sunday, 14 April, this sky-blackening dust storm punished the peoples from the panhandles of Texas and Oklahoma, burying entire houses (see Figure 2.5) under the dust and destroying the livelihoods of thousands of Americans. Dust storms were an important part of the US history during the 1930s and led to the creation of the Soil Conservation Service, a branch of the US Department of Agriculture [85, 2, 73].

Fires are also one of the largest sources of natural air pollution in the world. The uncontrolled burning of organic matter that is a large forest fire creates a large quantity of air pollutants that range from smoke to unburned (or partially burned) hydrocarbons, nitrogen and carbon oxides, and ash particles. Besides the obvious dangers of this kind of burnings for human life and activities, forest fires can also cause indirect damages, such as disruptions in supplies and travel due to reduced visibility [85].

Trees and forests in themselves are also responsible for a certain quantity of air pollution. Although they have the main part in the carbon dioxide conversion into oxygen, through photosynthesis, plants and trees are still the largest emitters of hydrocarbons in the planet, as attested by the blue haze that is visible on top heavily



Figure 2.4: Dramatic photograph depicting the Capelinhos' lighthouse, half a kilometer from the eruption site, surrounded by a cloud of ash PM, volcanic gas and water vapor with more than 1km in height[82].



Figure 2.5: House almost completely buried by the Black Sunday dust storm. Several houses were entirely swallowed during this storm, trapping people inside, as if a big blizzard had hit them. Unlike a blizzard though, there was nothing anyone could do to keep the dirt outside, and all surfaces were covered black [73].

forested areas, resulting from chemical reactions between [Volatile Organic Compound \(VOC\)](#)s produced by the trees. This counter-intuitive fact was in the origin of the infamous Ronald Reagan speech in which he "blamed" trees for much of [AP](#), in a time when anthropogenic [AP](#) was at its apogee in the US and Europe. Plants are also the emitters of another kind of [PM](#), which is of particular importance both to themselves and humans, which are the pollens. This is a bio-aerosol - a type of aerosol that is or was part of a living being - associated with a number of diseases [85].

Finally, I will discuss Radon gas. This is a natural occurring radioactive gas that is part of the radiative decay of Uranium present in all rocks. Although chemically inert, Radon is radioactive and, as all radioactive substances, emits particles when it decays. Although present virtually everywhere, outdoor concentrations of Radon are typically too small to cause any problems. The problem with this gas comes essentially from indoor concentrations, namely at home. Being a gas, Radon is able to enter people's houses, exposing the inhabitants. Prolonged exposure to Radon gas is the second biggest cause of lung cancer and authorities estimate that between 3 and 14% of lung cancer cases are caused by this gas. In Portugal, Radon concentrations were found to be below the European prescribed limit in two thirds of the houses in a 2001 study, but in 17% of the cases, concentrations were not only above this limit, but also over the highest tolerable limit [85, 91, 68].

2.1.4.2 Anthropogenic Sources of Air Pollution

Air Pollution that originates from human activities is called anthropogenic. Since the first industrial revolution, mankind has been using more and more resources to fuel our progress and continuously improving way of life. Of course, the consumption of natural resources has some unpleasant and sometimes dangerous consequences. The most important of which, looking from the lens of this thesis, is the incredible increase in the levels of AP. If one had any doubts whatsoever, all it would take would be a look into the atmospheric CO₂ concentration chart (Figure 2.6) from a few centuries back to the current day to completely dissipate them.

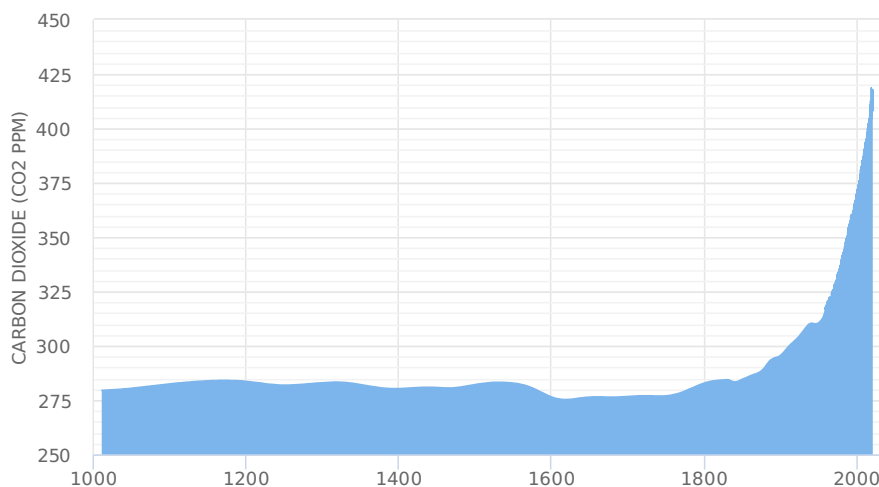


Figure 2.6: CO₂ atmospheric concentrations since the year 1000. Note the seemingly exponential increase since the 1800s. Plotted and published by the 2 Degrees Institute [1] with data from ice cores [30] and in situ monitors [81].

There are literally hundreds of sources of AP, but it is possible to categorize them into 4 main *families*: industrial processes, energy (includes transportation), agriculture and forestry, and waste. Of these 4 broad categories, as displayed in Figure 2.7. The most prominent is without a doubt the energy sector, although we also have to bear in mind that any and all combustion used in the other sectors is counted as energy production [45, 15].

From 2002 to 2011, fossil fuel combustion has been responsible for an average of 8.3 petagrams of carbon per year. This truly gigantic carbon footprint is in its majority explained by the worlds energy needs, which are ever increasing up to now. In 1990, total energy demand was situated at 356 quadrillion British Thermal Unit (BTU), having grown to 410 quadrillion BTU in 2010. In 2020, energy demand estimates are located at 600 quadrillion BTU, of which almost a quarter was expended by China [15].

It is important that we focus a little bit more on the Chinese case. It is now somewhat near commonsense to regard China as the factory of the world, and this of course is tied to Chinese energy consumption and production. On the same line of reasoning, this must mean that in some way, the country's energy expenditure is connected to the amount of financial resources that it produces, the GDP. Looking at the plots in Figure 2.8, one can see that all these numbers are highly correlated. When we ponder on the case of Chinese AP, and wonder why has this problem not been addressed

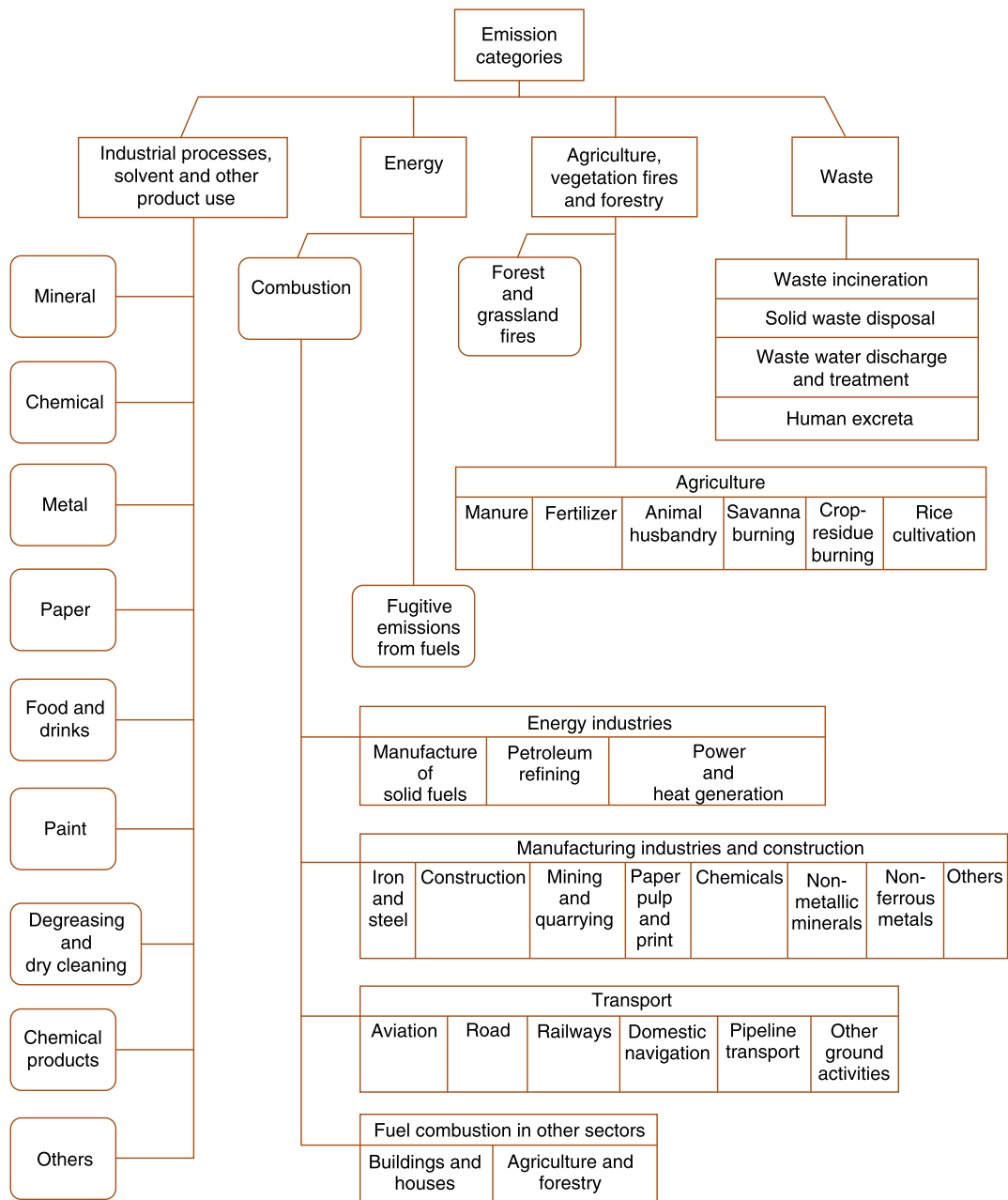


Figure 2.7: Schematic presentation on the sources of anthropogenic pollution and its categorisation according to the IPCC. Adapted from [15]

CHAPTER 2. LITERATURE REVIEW

previously, given its imposing dimensions and growing importance, one must take into account that, given the indirect importance of AP on Chinese people's gains, it is highly likely that the country's governments will be reluctant to decrease it in any expedient form [15, 44, 90].

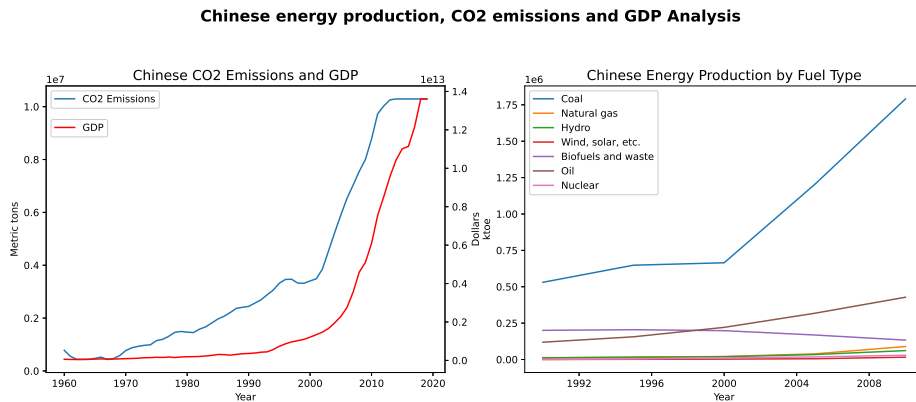


Figure 2.8: Chinese energy production, GDP and CO₂ emissions. Data collected from the World Bank and International Energy Agency websites [90, 44]

Another important conclusion that we can take from the plot in Figure 2.8 is that China has a large and historical dependence on the use of coal as fuel for energy production. This adds to the problem described in the above paragraphs, as coal is the single most damaging fossil fuel available. Not only does China get most of its energy from coal burning, but is also responsible for more than half of the world's production and consumption of this substance (see Table 2.1).

Table 2.1: Global energy production, divided according to the fuel used to obtain it and the production country.

Country	Liq. Fuel (M barrels / day)	Coal (BTU)	Nat. Gas (T cu. ft)	Renew. (BTU)	Nuc. (b kWh)
China	10,6	80,6	5,1	10,6	93
USA	18,5	17,3	25,5	7,8	769
Europe	14,4	12,5	17,9	11,7	837
Middle East	16	0,1	14,8	0,2	1
India	3,6	12,6	2,1	3,5	30
Russia	3,4	4,5	15,7	1,7	166
Africa	3,5	4,3	2,7	4,7	12
Brazil	3,3	0,5	1,1	6,8	15
World	91,4	153,9	120,8	63,7	2345

Internal Combustion Engine (ICE) are the single most important means for powering human transportation. Almost every vehicle in the world uses a kind of ICE. These motors operation is an application of the Otto cycle, in which the chemical energy in the fuel is converted to mechanical energy. These engines are as ubiquitous as the fossil fuels that have powered them since the beginning of the automobile revolution, in the early 20th century. Fossil fuels have several features that make them ideal to power our vehicles. Their energy density is high, they are incredibly safe to manipulate and use, and fossil fuel infrastructure can be found in almost every far

corner of the Earth. However, using them releases a number of gaseous and particle-condensed side products into the atmosphere, and this makes traffic one of the most important sources of AP. For instance, traffic pollution is the main responsible for human exposure to Nitrogen Oxides (NO_x) gases. Without countermeasures, gasoline ICE equipping passenger vehicles emit around 1.8 g/km of these gases, while diesel emits 2.8 g/km and Liquefied Petroleum Gas (LPG) around 2.1 g/km. On heavy duty engines, like on trucks and tractors, these figures skyrocket to 14.7 g/km for diesel engines and around 5.1 g/km for LPG [15].

Energy production (including transportation) is clearly the single largest contributor to global AP. This does not mean that other human activities do not pollute or produce air pollutants. Pollutant contributions from the industry, the agricultural activities and waste disposal are also non-negligible. In fact, industries around the world are responsible for the production and emission of all the criteria pollutants. It is important to single out one particular activity, which is the burning of forest for land-use changes. Carbon Monoxide (CO) emissions for this purpose are very high due to the nature of the burning material, which emits more than 50 times more CO than fuel or coal [15].

2.1.4.3 The European Case

Europe has for long been on the forefront of the fight against AP emissions. The European Union has put in place a number of policies aiming at cutting (or even eliminating) emissions of human health compromising pollutant components. Few places in the world have been so demanding regarding their environmental practices, and numbers are a clear reflection of these adaptation efforts. In their 2019 report, the EEA state that European emissions have globally declined, and have been declining since at least the year 2000. Moreover, and in contrast with China's case, the GDP does not seem to be connected to AP emissions. As can be seen in Figure 2.9, emissions are decoupled from economic growth, as there are now less emissions per GDP unit than before [29].

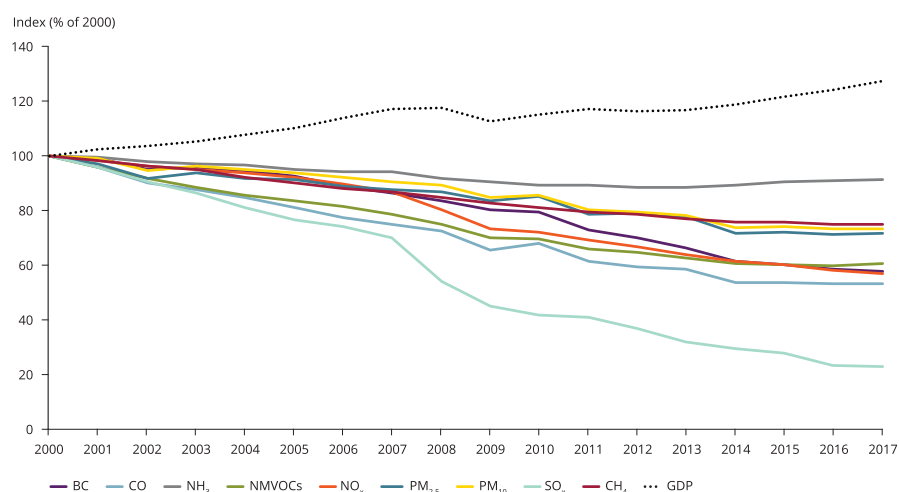


Figure 2.9: General trends for European emissions. Data presented in % emissions of year 2000. Note the downward global trend in pollutant emissions, and its decoupling with the European GDP [29].

CHAPTER 2. LITERATURE REVIEW

If one extends this analysis further, and separates emissions by using their origin, the trends are approximately the same: except for Ammonia (NH_3) (a side product of agricultural activities) a clear reduction is present in all sectors. These results can be seen in Figure 2.10 and were presented in [29].

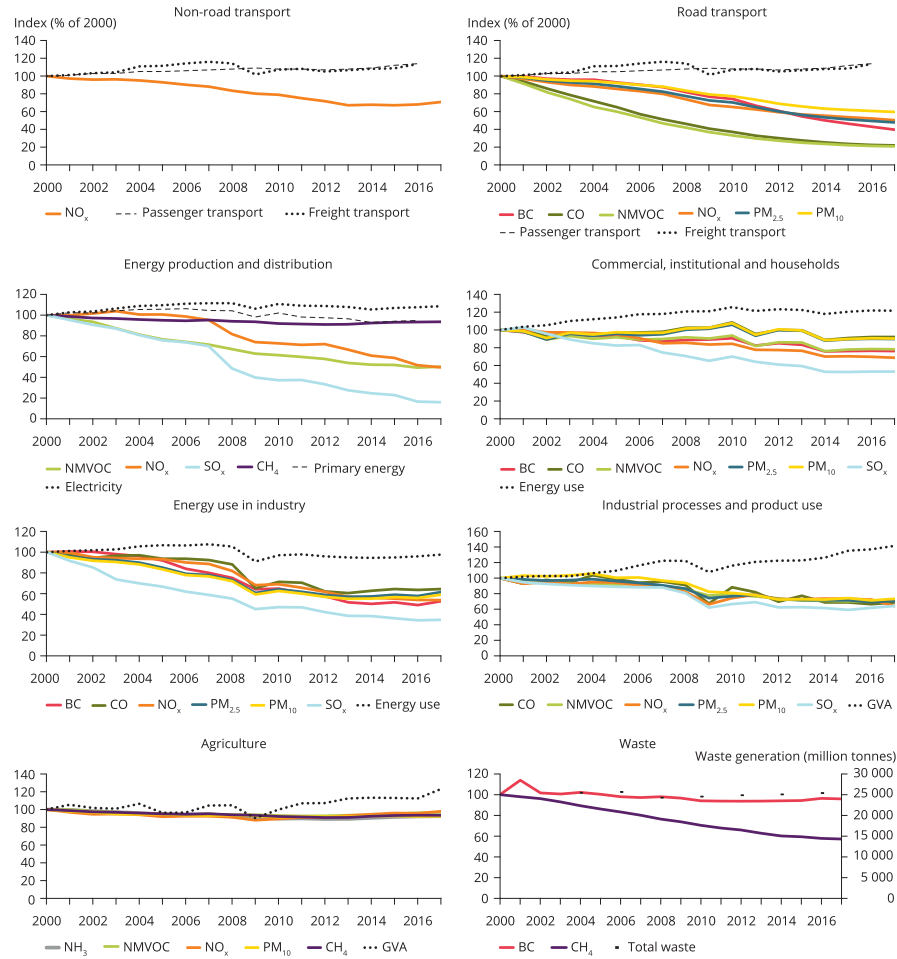


Figure 2.10: European emissions divided by activity sector. The global decreasing trend is confirmed, as industries all around are producing less and less AP with the passing years [29].

2.1.5 Detecting and Monitoring Air Pollution

There is no doubt that AP is a global threat that affects everyone, both in personal terms (through the degradation of their health) and in societal terms, through the investments and limitations that we as a whole have to commit to in order to prevent larger, unmanageable problems. Reducing AP is a priority and a requirement for today's modern societies. This demands immediate and effective actions, which in turn imply that we have a solid and profound understanding of how pollutants are created, transported and transformed in the atmosphere. The scale on which these interventions must be conducted requires them to be made on a concerted and collaborative manner, and always leveraged by technological development [29]. Many of the air pollutants cannot be detected solely by our senses, or even if they can is at already

dangerous concentrations. Technology is therefore a prerequisite to our fighting the problem of [Air Pollution](#) [85].

Pollution monitoring is itself based on the ability of a given measurement method to determine concentrations for trace gases, aerosols or radiation quantities. As with many other test techniques, in various fields, pollution monitoring techniques have three very important aspects to verify. The first of which is sensitivity, and also the most demanding. Important trace gases in atmospheric chemistry have sometimes vestigial concentrations, and the ability to correctly detect them is many times a technical challenge. The second most important is specificity, which is the ability of an atmospheric measurement to measure each compound independently, without a component influencing another component's measurement either positively or negatively. Finally, any usable monitoring technique must be sufficiently precise as to provide valid measurements.

[Air Pollution](#) monitoring techniques and devices are too many to address them all in this document. Besides, the physical principles involved are completely different from one to another, making it very difficult to make a broad generalization, other than the fact that they can be divided into local and remote sensing devices. The gold standard for air quality measurements remains those techniques in which a sample is collected in the field and then taken to the laboratory to be analyzed by very powerful analytical methods such as chromatography or mass spectroscopy. While undoubtedly providing the most accurate representation of the air composition at the time and place the sample was collected, it is also true that this method's results are too slow to use regularly in the field [85, 20, 7].

Another very important air quality monitoring method is the use of electrochemical sensors. The first variants (wet cells) of this kind of sensor became very popular in the field of industrial hygiene, where they were applied in many portable flue gas analyzers. They were very attractive to companies worldwide given their potential for very low costs in comparison to optical or other more complex techniques. Apart from the oxygen wet cell sensor, that has a slightly different configuration, these electrochemical devices are comprised of three electrodes - a sensing electrode, a counter electrode and a reference electrode - separated by a thin layer of electrolyte. The gas that is diffused to the surface of the electrode is either oxidized or reduced, thus changing the systems electrical properties, in a way that is then captured by an amplification circuit [20].

Wet cell electrochemical sensors were the precursors of the now more common solid state sensors. These sensors are the ones that we see in every subterranean parking lot, measuring several traffic related gases such as CO , CO_2 or NO_2 . In general semiconductor gas detectors are comprised of two modules: a receptor and a transducer (see Figure 2.11). The receptor has in its composition a material (or set of materials) that, in contact with the target gas, induces a change in the systems inherent properties (work function, dielectric constant, resistance, etc.) or emits heat or light. The transducer is a device or circuit that converts the receptor's changes into an electrical signal [20, 7, 85].

Optical (spectroscopic) systems are fundamentally different from the other techniques that have already been presented. They can be used to perform remote sensing measurements (as far as being used for measurements aboard satellites). In the last few decades, these techniques have gained a lot of ground in atmospheric research,

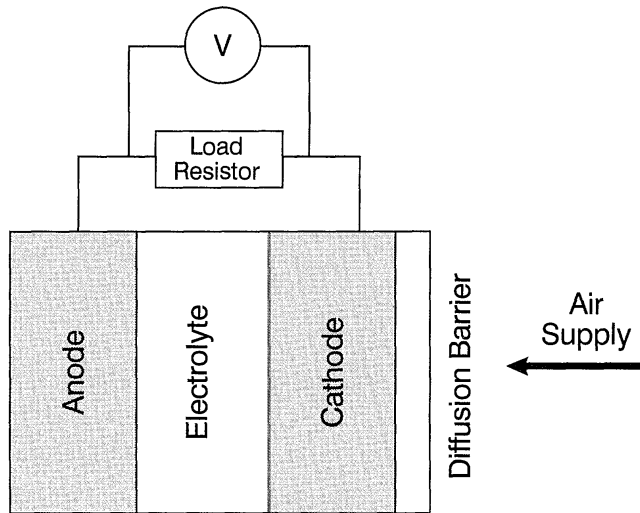


Figure 2.11: Semiconductor electrochemical sensor basic structure. There are many examples of this type of sensors, but in general they follow this architecture [20].

due to their high sensitivity and specificity and the universality of their applicability. Spectroscopic methods are based on Lambert-Beer's law (see Section 2.2 for a more thorough explanation), and make use of the fact that the way in which gases interact with light is well known and follows an exponential expression. There are many spectroscopic techniques for measuring AP. One of the most important atmospheric analysis methods, and especially in what concerns this document, is DOAS. While it is based on the same mathematical formulation as the other spectroscopic methods, it is also based on other factors, which shall be discussed in Section 2.2.

2.2 DOAS

Differential Optical Absorption Spectroscopy is a well established absorption spectroscopy technique that is widely used in the field of atmospheric studies [66]. In this section, I present a short introduction to the field. The first part of this introduction is based on [84], an article we have published in 2017, marking the conclusion of the initial studies for this PhD thesis. The second and last part refers to additional research that I have conducted since then.

DOAS itself is based on Lambert-Beer's law, which can be written as [66]

$$I(\lambda) = I_0(\lambda) \cdot \exp(-\sigma(\lambda) \cdot c \cdot L), \quad (2.1)$$

Where λ is the wavelength of the emitted light; $I(\lambda)$ is the light intensity as measured by the system; $I_0(\lambda)$ is the intensity of the light as emitted by the source; and $\sigma(\lambda)$ is the absorption cross section of absorber, which is wavelength dependent; c is the concentration of the absorber we want to measure.

This law allows the definition of optical thickness (τ) [66]:

$$\tau(\lambda) = \ln \left(\frac{I_0(\lambda)}{I(\lambda)} \right) = \sigma(\lambda) \cdot c \cdot L. \quad (2.2)$$

In a laboratory setting, Eq. (2.1) or (2.2) can be used to directly calculate an absorber's concentration, provided there is knowledge of its cross section. In the open atmosphere, however, absorption spectroscopy techniques are far more complex. On one hand, $I_0(\lambda)$ is not accessible since we measure from inside the medium we want to measure. On the other hand, there are several environmental and instrumental effects that influence measurement results. These effects include the following [66].

- Rayleigh scattering is due to small molecules present in the atmosphere and is heavily influenced by wavelength (hence the blue colour of the sky).
- Mie scattering is caused by particles and larger molecules suspended in the atmosphere and is not very dependent on the wavelength (hence the white colour of clouds).
- Instrumental and turbulence effects are the instrument's transmissivity and atmospheric turbulence in the optical path also limit light intensity.

In addition, we also have to take into account that, in the atmosphere, there are a number of trace gases that interfere with passing light. Another aspect worth mentioning is that our device is never pointed directly at the light source (the Sun) but always processes light that has been scattered at some unknown point in the optical path. This means that the light that reaches our detector is only the scattered fraction of the sunlight, depending on the system's position and geometry, as well as wavelength. The expansion of Lambert–Beer's equation to include all these effects results in Eq. (2.3).

$$\begin{aligned} \epsilon_{TG}(\lambda, s) &= \sum_i \sigma_i(\lambda, s) \cdot c_i(s) \\ I(\lambda) &= I_0(\lambda) \cdot A(\lambda, \dots) \cdot S(\lambda) \cdot \\ &\quad \cdot \exp \left[- \int [\epsilon_{TG}(\lambda, s) + \epsilon_M(\lambda, s) + \epsilon_R(\lambda, s)] ds \right] \end{aligned} \quad (2.3)$$

Where $A(\lambda, \dots)$ is the fraction of scattered light that reaches the device, $S(\lambda)$ represents instrumental and turbulence effects, $\sigma_i(\lambda, s)$ is the absorption cross section of absorber i , c_i is the concentration of absorber i . $\epsilon_{TG}(\lambda, s)$ is the absorption by the i trace gases, $\epsilon_R(\lambda, s)$ represents Rayleigh's extinction coefficient and $\epsilon_M(\lambda, s)$ represents Mie's extinction coefficient. The interest of this equation lies within the retrieval of c_i , a given absorber's concentration. Since the integral is taken along the total atmospheric path of the measured photons, and considering that their cross sections do not vary significantly in atmospheric conditions, it is possible to define the concept of slant column, which is of great importance [56].

$$SC_i = \int c_i(s) ds \quad (2.4)$$

This quantity, as Eq. (2.4) shows, equals the integral of an individual absorber's concentration along the atmospheric optical path of relevance. Now, without knowledge of $I_0(\lambda)$, these equations cannot give us absolute concentration values. We can, however, use another scattered light spectrum as reference in Eq. (2.2). Instead of absolute densities, this will yield relative changes in the atmosphere. We thus arrive at Eq. (2.5).

$$\begin{aligned} \ln\left(\frac{I_{\text{ref}}}{I}(\lambda)\right) &= \ln\left(\frac{A_{\text{ref}}}{A}(\lambda, \dots)\right) + \ln\left(\frac{S_{\text{ref}}}{S}(\lambda)\right) \\ &\quad + \sum_i (\sigma_i(\lambda) \cdot \Delta \text{SC}_i(\lambda)) + \Delta \tau_M(\lambda) \end{aligned}$$

Where ΔSC_i is the relative slant column of absorber i ; $\Delta \tau_M$ is the relative Mie scattering term, integrated to its optical thickness; and $\Delta \tau_R$ is the relative Rayleigh scattering term, integrated to its optical thickness. This is where the principle of DOAS is applied. Instrument features, scattering and other atmospheric effects have broad absorption spectral profiles, which vary slowly with wavelength. Several trace absorbers have narrow and rapidly varying spectral signatures in at least a small section of the spectrum. By using Eq. (2.5), we can separate these contributions [22].

$$\sigma(\lambda) = \sigma'(\lambda) + \sigma_0(\lambda) \quad (2.5)$$

Here, the broad part of the optical thickness ($\sigma_0(\lambda)$) can be separated from the narrow part ($\sigma'(\lambda)$ – differential) by approximating it by a low-order polynomial, resulting in Eq. (2.6).

$$\ln\left(\frac{I_{\text{ref}}}{I}(\lambda)\right) = \sum_{i=1}^n \sigma'_i(\lambda) \cdot \Delta \text{SC}_i + \sum_{j=0}^m a_j \cdot \lambda^j \quad (2.6)$$

Where $\sum_{i=1}^n \sigma'_i(\lambda) \cdot \Delta \text{SC}_i$ is the differential part (narrowband, rapidly varying with wavelength) and $\sum_{j=0}^m a_j \cdot \lambda^j$ is a low-order polynomial, used to remove the broadband spectral features resulting from atmospheric and instrumental phenomena.

In practice, the mathematical solving of Eq. (2.6) is not enough since it does not account for the Ring effect or the non-linearities that result from stray light and wavelength shift in measured and cross-section spectra.

The Ring effect is a consequence of rotational Raman scattering: molecules in the atmosphere do not absorb photons in a purely elastic (Rayleigh scattering) fashion. A small portion of the light–matter interaction is in fact inelastic [9, 56]. This changes the light source frequencies as seen from the detector. This phenomenon was first noticed by Grainger and Ring in 1962. At the time, they noticed that the well-known Fraunhofer lines would slightly change when one observed them by using moonlight instead of scattered daylight [36]. Mathematically, the Ring effect is introduced into the DOAS expressions as a synthetically produced pseudo-absorber.

Up until this point, the DOAS problem can be solved by a system of linear equations of the form displayed in Equation 2.7.

$$\tau = A \cdot X \quad (2.7)$$

A is an $m \times n$ matrix. Its columns are the differential cross-sections for the measurement target gas, $\sigma'_i(\lambda)$, and the wavelength powers ($\lambda, \lambda^2, \lambda^3, \dots$) according to the polynomial used for the broadband extraction described above, $P(\lambda) = \sum_{j=0}^m a_j \lambda^j$. The lines of matrix A are the wavelength window of study, as seen by the spectrometer used in the experiment. This leads to there being many more lines than columns in A . The system is thus overdetermined. Solving it requires the use of numerical approximations, and the most common approach is a least-squares approximation, in which the best solution minimises $\chi^2 = [\tau - A \cdot X] [\tau - A \cdot X]^T$. The upper script T used in this expression denotes the transpose of the preceding matrix [56, 66].

A crude DOAS algorithm might not go any forward. In effect, this is precisely the approach followed in [84] for smoke detection using machine learning techniques. A more refined measurement, aimed at quantification of the target trace gases and not at determining the presence of a particular type of atmospheric event requires an additional consideration, and some more algorithmic steps. There are in fact some nonlinearities in the complete retrieval process. These non-linearities are not retrievable through linear algorithms alone. These non-linear effects present themselves as shifts, stretches and offsets in the measured signal. They do not directly change the dependent variable values (i.e., the radiance), but instead "move" the scale of the independent variable (i.e., the wavelength). Therefore, linear approximations such as least-squares minimisation are not sensitive to them. A non-linear approximation algorithm such as Levenberg–Marquardt [67] can be used, and the expression that is being solved is presented in Equation 2.8.

$$\ln \left(\frac{I_{\text{ref}}(\lambda)}{I(\lambda + \text{shift}) + \text{offset}} \right) = \sum_{i=1}^n \sigma'_i(\lambda) \cdot \Delta S C_i + \sum_{j=0}^m a_j \cdot \lambda^j \quad (2.8)$$

Programming-wise, solving these equations is an iterative two-stage process, which runs until one of the following typical stop criteria are met.

Maximum iteration number: This is a self-explanatory criterion. It limits the number of times the algorithm's cycle can run;

Minimum improvement threshold: As the algorithm proceeds, this criterion ensures that it progresses in the correct direction, i.e., minimising χ^2 ;

Minimisation target: If χ^2 becomes lower than this given threshold, the cycle is terminated.

The cycle begins by the determination of the concentration values of the target trace gases and the χ^2 score is calculated. The wavelength window is shifted, stretched and offset according to the initial conditions. The χ^2 is re-calculated and compared to the previous value. This cycle is iteratively repeated in the best minimisation direction until any of the stop criteria are met and the cycle is terminated. The algorithm is illustrated (simplified) in Figure 2.12.

2.2.1 Types of DOAS experiments

There are two main families of DOAS assemblies, with different goals and capabilities:

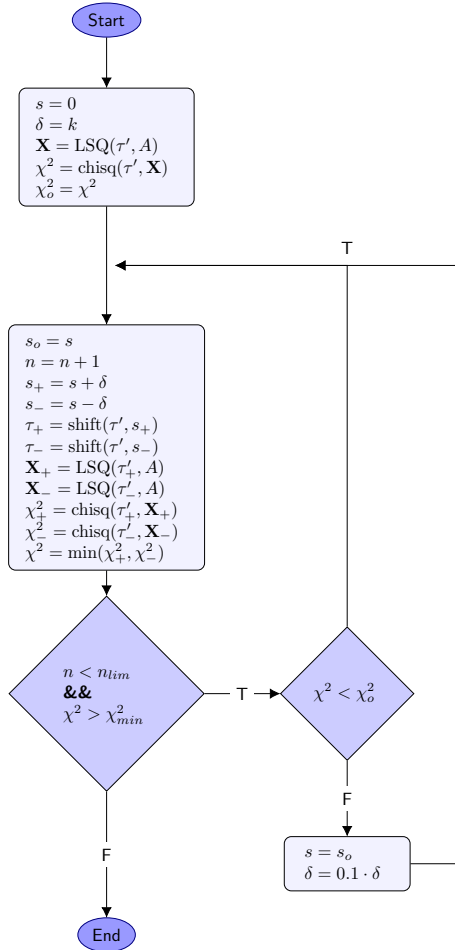


Figure 2.12: Simplified schematic flowchart of the DOAS algorithm, including the non-linear part.

- Active systems, of which a simple illustration is presented in Fig. 2.13, are characterized by relying on an artificial light source for their measurements. A spectrometer at the end of the light path performs spectroscopic detection. Active DOAS techniques are very similar to traditional in-lab absorption spectroscopy techniques [66];

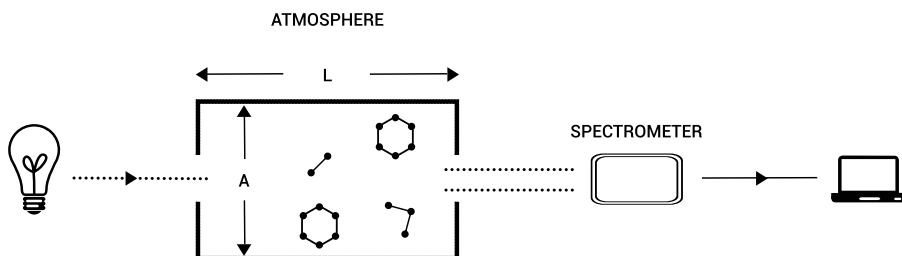


Figure 2.13: Active DOAS schematic.

- Passive DOAS techniques, illustrated in Fig. 2.14, use natural light sources, such as the Sun and the moon, in their measurement process. An optical system is pointed in certain elevation and azimuth angles and sends the captured light

into a spectrometer, connected to a computer. The system returns the total value of the light absorption in its path [66, 56].

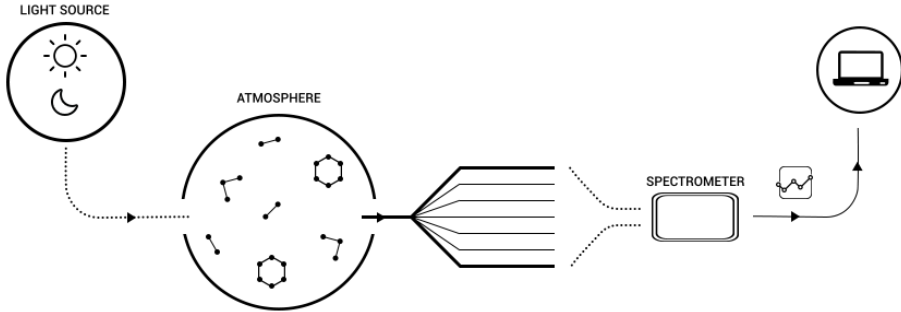


Figure 2.14: Passive DOAS schematic.

Within the two main **DOAS** families, there are several types of possible experiment. Differences in the design of these assemblies originate from a number of different target requirements. Active or passive applications can differ with relation to their intended spectral range, light throughput or resolution, among others.

In active experiments, the choice of the light source is the most critical aspect of the whole experimental design. Active **DOAS** light sources must be stable, have a very high throughput (these experiments are often conducted over long optical paths) and must have an adequate cost to purchase, maintain and operate. This is especially true in long-running experiments, which must remain working for months or even years. Moreover, the spectral range of the emitted light is also of central importance, because most trace gases have very particular spectral cross sections. The spectral structure of the emitted light is also an important feature to consider, for similar reasons.

The sun and the moon are the two most important light sources when it comes to passive **DOAS** applications. Sunlight can be used directly or after a scattering event, the latter being the more common. In these experiments, instead of pointing directly at the sun, the collector is pointed at a certain point in the atmosphere, entering the system after it has been scattered. There are many possible geometries to a scattered sunlight **DOAS** experiment. Some of them are schematically represented in Figure 2.15.

Although instrumentally simpler than their active counterpart, passive **DOAS** applications require more care in the retrieval process. In this kind of application, light sources are extremely far away. Additionally, they are normally highly structured. This means that one has to be extremely mindful when using it for the retrieval of small concentration changes. In addition to this, there is always the need to convert the system's direct measurement, a column density, into vertical densities. Since in scattered sunlight measurements, the optical path is impossible to calculate in a precise manner, this requires the use of complex radiative transfer models [66, 33].

2.2.1.1 Satellite Measurements

One particularly interesting use of passive **DOAS** are satellite measurements. There are three types satellite **DOAS** experiments:

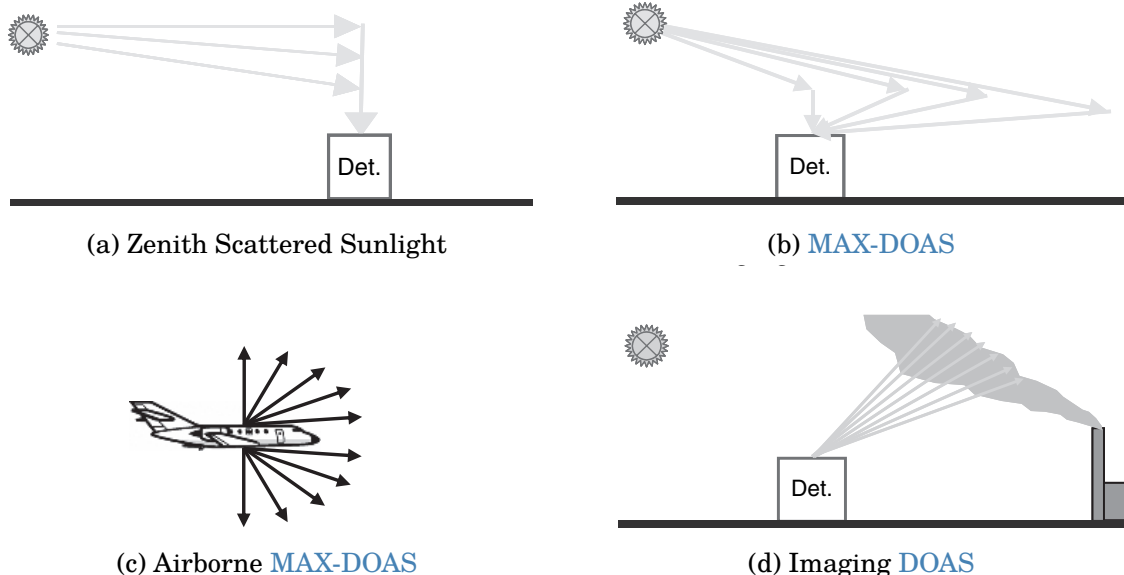


Figure 2.15: Several examples of possible passive DOAS experiment geometries. All these examples use only the light from an astronomical source to detect many atmospheric trace gases. All these examples were taken from [66].

Occultation measurements: this is a direct sunlight measurement. Light comes from the sun and traverses the Earth's atmosphere in a tangential manner before entering the satellite's light collector;



Figure 2.16: Occultation measurement schematic representation [66]

Limb: a scattered sunlight measurement, in which the collector is pointed towards the Earth, at an angle. Light reaches the detector after being scattered in the atmosphere, the ground, or both;

Nadir: this is the most common measurement geometry for satellite experiments. In this mode, light that gets reflected off the Earth's surface is captured by the collecting device, while it is pointing directly down.

Satellite based DOAS measurements have also been important because they have given rise to new trace gas retrieval techniques. Through them, new trace gases, previously unreachable through DOAS have been quantified on a global level, such as carbon monoxide through Weighting Function Modified Differential Optical Absorption Spectroscopy (WFM-DOAS) [13, 12].

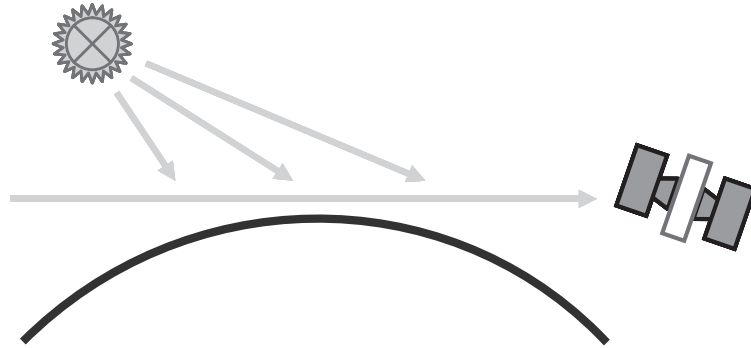


Figure 2.17: Schematic representation of the limb satellite measurement geometry.

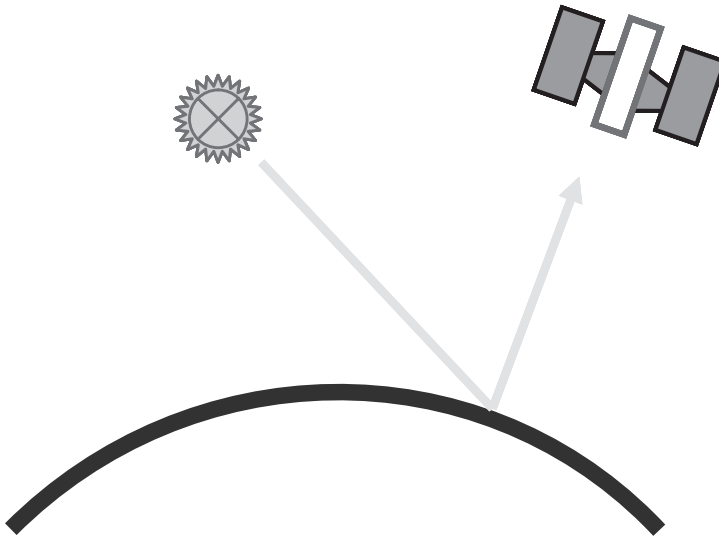


Figure 2.18: Schematic representation of the nadir satellite measurement geometry.

WFM-DOAS is a trace gas column retrieval algorithm, developed in the beginning of the 21st century, with the main goal of determining the total columns of gases such as CO, Water (H₂O) or CO₂ from satellite nadir data [12]. Instead of using literature-obtained cross-section data for each target trace gas, the **WFM-DOAS** approach uses weighing functions, calculated through the application of a radiative transfer model, such as SCIATRAN [74]. Still, the retrieval is based on a fitting process. Equation 2.9, adapted from [13, 12] can be called the **WFM-DOAS** equation.

$$\left\| \ln I_i^{obs}(\mathbf{V}^t) - \left[\ln I_i^{mod}(\bar{\mathbf{V}}) + \sum_{j=1}^J \frac{\partial \ln I_i^{mod}}{\partial V_j} \Bigg|_{\bar{V}_j} (\hat{V}_j - \bar{V}_j) + P_i(a_m) \right] \right\|^2 = \|RES\|^2 \rightarrow min \quad (2.9)$$

In Equation 2.9, I_i^{obs} is the observed sun-normalised radiance (the ratio between a nadir radiance measurement and solar irradiance) for the center wavelength λ_i of detector pixel number i . \mathbf{V} are the vector that have vertical columns as their components. These can be true, V^t , modelled, \bar{V}_j , or approximated, \hat{V}_j . The true columns

are unknown as we only have the radiance value and not the things on which it depends, modelled vertical columns are taken from the literature (they are climatological values) and \hat{V}_j are one of the fitting parameters. The other being a_m , the low order polynomial (P) coefficients. RES is the fit residuum, which is minimised for the fitting.

2.3 Important Notes on DOAS in practice

Theoretically, the procedure described in Section 2.2 would be enough to obtain the target trace gas concentrations. In practice, this is an over-simplification. There are several additional required steps, most of them concerning a certain conditioning that one has to apply to both the collected and literature spectral signals.

2.3.1 Cross section conditioning

Unless conditions are absolutely stable, and one is able to record all data with the same device, which is impractical to the point of infeasibility, external literary sources are required for the DOAS analysis. These data are obtained with standardised trace gas sampling, extremely high resolution spectrometers and in carefully designed laboratory experimental setups.

To use external cross sections in one's own experiments, these data must be adapted to one's equipments. The very high resolution spectra coming from the literature are convolved with the instrument function of the real experiment's spectrometer. This function can be thought of as the device's impulse response. Since the spectrometer is inevitably imperfect, this response is not nearly as sharp as the impulse itself, and is normally modelled as a Gaussian curve fitted to a known source's well defined, impulse-like narrow structures. An Hg-Cd lamp was used in Merlaud's 2013 work, for instance [56]. For most spectrometers, this step is not actually required, as manufacturers already provide a very accurate spectral resolution value.

After calculating or fetching this value from the device's manual, it is a matter of creating a Gaussian kernel that can be used to filter the high resolution spectra through convolution. The **Full Width at Half Maximum (FWHM)** of the Gaussian kernel is equal to the spectrometer's resolution. One can ensure this by using the formula in Equation 2.10 which relates the width of the kernel with the standard deviation used to create it. The signal that results from the convolution of the literature cross sections and the gaussian kernel can be thought of as how the cross section would look if it had been acquired using the experiment's spectrometer.

$$FWHM = 2\sqrt{2\sigma^2 \ln 2} \rightarrow FWHM \approx 2.355 \cdot \sigma \quad (2.10)$$

The final step in this process of conditioning high resolution literature cross sections to the experiment that one is conducting is the discretisation of this signal. Physically, spectra are continuous signals. In practice, they were all captured using finite-resolution devices, and therefore are a digital signal. However, the resolution of the literature cross sections is so high in comparison to the usual resolution of a DOAS experiment spectrometer that one can think of this signal as being *quasi-continuous*. In order for them to be used in DOAS calculations, they have to be "re-discretised" onto the experiment's spectrometer sensor resolution. Since it is seldom the case (if ever)

that the literature and the low resolution pixels coincide, a mathematical routine is used to interpolate the former onto the latter. The most commonly used routine is the cubic spline interpolation, widely regarded as the best compromise between computational expense and accuracy [5]. Overall, cross sections used in DOAS undergo a process illustrated in Figure 2.19 [22, 5].

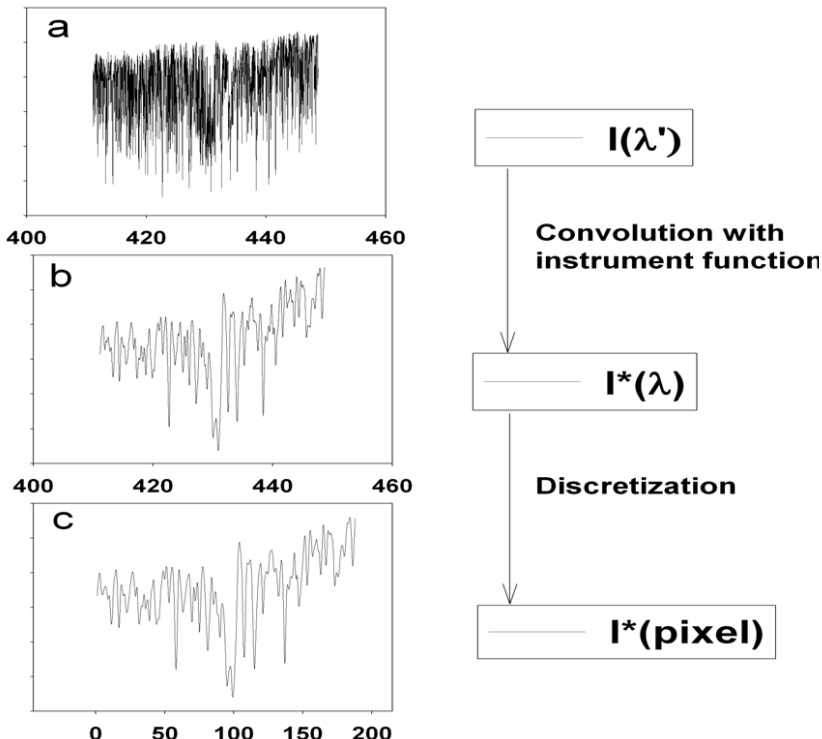


Figure 2.19: Before being used in DOAS calculations, literature trace gas cross section spectra must undergo a conditioning process to make sure they are compatible with the current experiment's instruments. Figure adapted from [5]

2.3.2 Spectral Calibration

One other small but important correction that can bias results is the lack of proper calibration between cross sections and collected spectra. Figure 2.20 shows how a conditioned cross section present slight wavelength related discrepancies.

These small nonconformities are caused not only because both types of data were captured by different spectrometers, but also because conditions most certainly changed. This means that situations in which calibration must be handled with care are the norm. This is done by running an iterative process that makes slight adjustments to the function mapping wavelength to pixel number, as explained in the next few paragraphs.

The light that enters the spectrometer is scattered by the diffraction grating before reaching the device's sensor, which is divided into pixels. These pixels have a well defined and finite width. At the centre of each one of them, the signal's intensity can

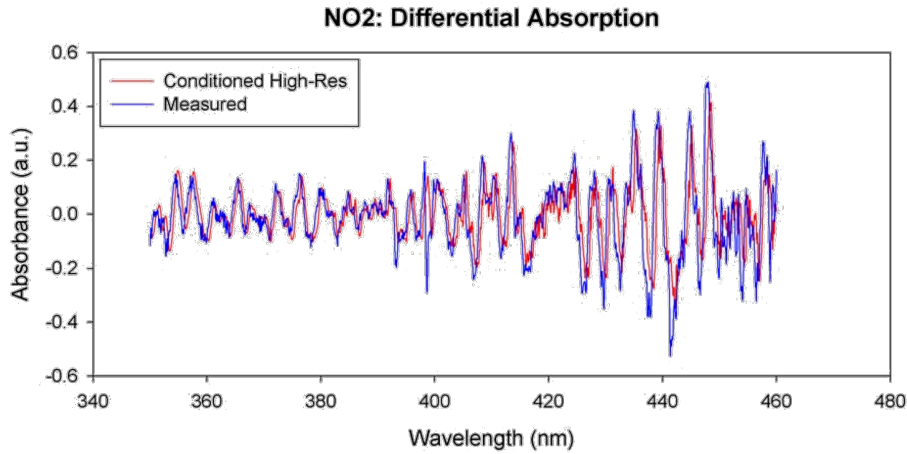


Figure 2.20: This figure, taken from [5], shows the difference between NO_2 cross sections. The red line comes from the literature, and has been conditioned to the experiment spectrometer. The blue line was actually collected with that device. The slight discrepancies that can be observed are calibration defects.

be described by Equation 2.11, in which I is the intensity, i the pixel number and λ the wavelength.

$$I(i) = \int_{\lambda(i)}^{\lambda(i+1)} I(\lambda) d\lambda \quad (2.11)$$

The expression in Equation 2.11 assumes that the signal has been conditioned properly, as described in Section 2.3.1, through the convolution of the cross section data with the instrument function and adequate discretisation. The smaller $\Delta\lambda = \lambda(i+1) - \lambda(i)$, the finer the instrument's resolution. This is, of course, inherent to the system and cannot be changed. What can and should be changed during analysis is the central wavelength assigned to each pixel. This assignment is in fact what constitutes the instrument's calibration.

The most common way of conducting said calibration is by introducing a polynomial describing wavelength to pixel relationship. This polynomial is the wavelength-pixel mapping function, and can be written as in Equation 2.12.

$$\lambda(i) = \sum_{k=0}^q \gamma_k \cdot i^k \quad (2.12)$$

In Equation 2.12, γ_k determines how the pixels are mapped to the wavelength (λ), and the type of mapping effect depends on k . Changing γ_0 shifts the signal left or right; changing γ_1 introduces linear distortions to the pixel mapping, i.e., stretching or squeezing of the signal. One can fit this polynomial up towards $k = \infty$, in theory, but normal spectrometer calibrations are only run up to the second or third degree. The Avantes spectrometers that were used in this dissertation are factory-calibrated to a fourth order polynomial.

The non-linear portion of the DOAS algorithm, described in Section 2.2, is indeed a wavelength calibration. However, it is important to previously calibrate every spectral signal before actually running the DOAS fitting process. This is because the types of

2.4. TOMOGRAPHIC ALGORITHMS AND RECONSTRUCTION TECHNIQUES

optimisation algorithm used in this technique, such as Levenberg–Marquardt, tend to find local minima or to not converge if there is significant misalignment between the spectra.

For passive applications using the sun as the light source, one can use a high resolution solar spectrum (see Figure 2.21), and the Fraunhofer bands in it (which have a very well defined wavelength that can be used as ground truth) to align the various spectra. For active applications, one can use the light source's own spectrum, either provided by the manufacturer or previously collected in the absence of atmospheric or other effects.

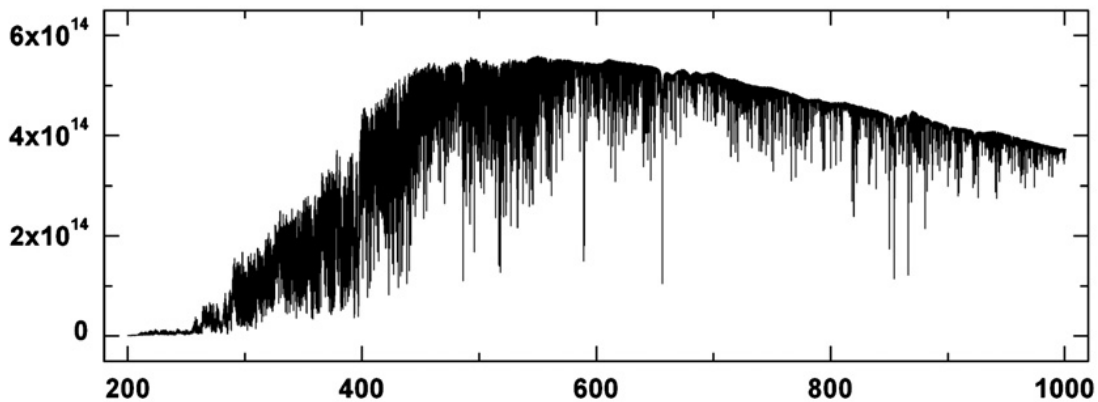


Figure 2.21: High resolution solar spectrum commonly used to calibrate the various spectral signals in DOAS experiments [19].

2.4 Tomographic algorithms and reconstruction techniques

Tomography is the cross-sectional imaging of an object through the use of transmitted or reflected waves, captured by the object exposure to the waves from a set of known angles. It has many different applications in science, industry, and most prominently, medicine. Since the invention of the Computed Tomography (CT) machine in 1972, by Hounsfield [38], tomographic imaging techniques have had a revolutionary impact, allowing doctors to see inside their patients, without having to subject them to more invasive procedures [47].

The central thought around tomographic image reconstruction is to recreate the information contained inside a target physical body, without having to cut it or open it in any way. The theory is based on Radon's idea that it is possible to "*represent a function written in \mathbb{R} in the space of straight lines (\mathbb{L}) through its line integrals*" [72].

Say we have a body that we want to fully characterise without cutting open or destroying in any way. Now imagine we can traverse it with some kind of radiation, ray by ray, and that we are able to measure the rays after they traverse the target. What we would capture would be relative to the emitted radiation, of course, but it would also contain information on how that ray had interacted with the target body's matter. In the case of the ubiquitously used X-Ray radiation, the measurement would

be one of the total attenuation "imprinted" onto the ray by the target body's molecules, in the ray's particular direction. If said body is heterogeneous, the total attenuation can be derived by the infinitesimal sum of all different attenuation phenomena caused by the object's several different constituents (the same can be said of a homogeneous object, but in that case there is only one type of attenuation present). This means that each one of the rays contains information regarding the constitution of said body.

The question that arises is thus "*how we can use this information to create a spatially accurate representation of this target's interior composition?*". The answer to this question lies on many factors, but the most prominent of which are surely choosing the quantity that we are trying to find (that characterises the object) and assembling the projections (that is what we call the line integrals in tomographic imaging) in a way that allows solving an equation system for the aforementioned quantity. This assembly, a matrix of projections organised by their angles and position within the detector, is called sinogram. All tomography methods revolve around finding the relationship between it and the system's geometrical description [11, 47, 43, 41, 42, 25].

Let's consider the case in which we deal with a single ray of solar light entering the atmosphere at a given point. Since the atmosphere contains numerous absorbers and comparable atmospheric effects, the ray changes from the point where it enters the atmosphere to the point at which it is measured by a detector. Total absorption will depend on the pollutant species, their cross-section and their concentration, since it obeys Lambert-Beer's law. Looking from another angle, this absorption is also the line integral that we will use to reconstruct our image. With DOAS, it is possible to measure several pollutants at the same time, but for simplicity (and since it is one of the most studied compounds in the field), let's consider that the single pollutant in our atmospheric mixture is NO₂.

The problem of tomographic reconstruction can be approached in a number of ways, depending mostly on the authors. In my literary search, I have found that Kak and Slaney [47] have certainly explained this problem in one of the clearer ways available. Therefore, I shall base the rest of my presentation in their writings, and complement with other authors' notes wherever necessary.

Considering the coordinate system displayed in Figure 2.22. In this schematic, the object is represented by the function $f(x, y)$. The (θ, t) parameters can be used to define any line in this schematic. Line AB in particular can be written:

$$x \cdot \cos(\theta) + y \cdot \sin(\theta) = t \quad (2.13)$$

And if we were to write a line integral along this line, it would look like Equation 2.14, the Radon transform of function $f(x, y)$:

$$P_\theta(t) = \int_{-\infty}^{\infty} f(x, y) \cdot \delta(x \cdot \cos(\theta) + y \cdot \sin(\theta) - t) dx dy \quad (2.14)$$

Where δ , the delta function, is defined in Equation 2.15.

$$\delta(\phi) = \begin{cases} 1, & \phi = 0 \\ 0, & \text{otherwise} \end{cases} \quad (2.15)$$

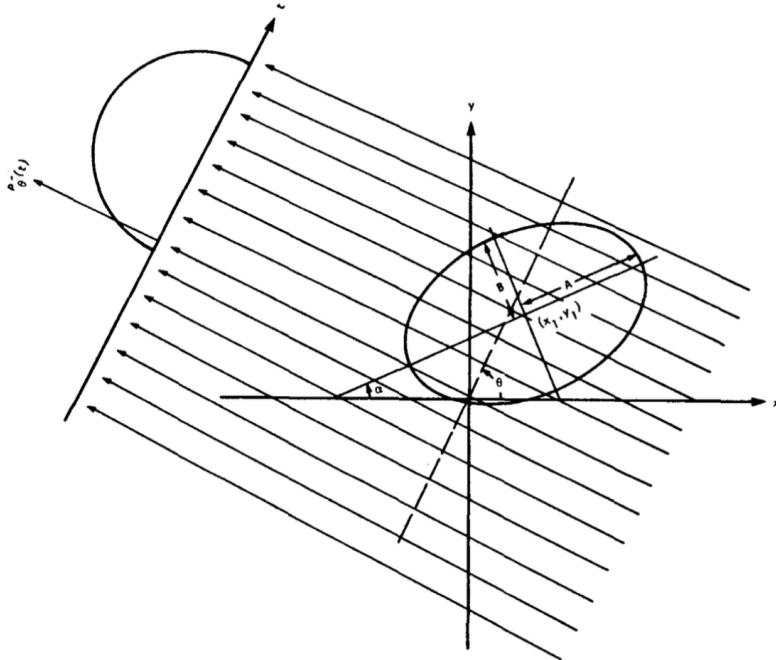


Figure 2.22: Schematic representation for coordinate setting. The image depicts a parallel projection setting [48].

As I have mentioned previously, a projection is a set of line integrals such as $P_\theta(t)$. Geometry plays a very important role in how the integrals are written and solved for reconstruction. The simplest case is the one where the set is acquired in a row, describing what is called a parallel geometry. Another more complex case is when a single point source is used as origin for all rays, forming a fan. This is called a fan-beam array. There are other possible geometries, but they fall out of the scope of this work and will therefore not be addressed any further.

The Fourier Slice Theorem (**FST**) is the most important component of the most important algorithm in tomographic inversion, the Filtered BackProjection algorithm (**FBP**). **FST** is based on the equality relation between the two-dimensional Fourier Transform (**Fourier Transform (FT)**) of the object function and the one-dimensional **FT** of the object's projection at an angle θ . Let's start by writing the 2D **FT** for the object function, Equation 2.16, and the 1D **FT** of projection P_θ , in Equation 2.17.

$$F(u, v) = \int_{-\infty}^{\infty} \int_{-\infty}^{\infty} f(x, y) \cdot \exp [-j2\pi(ux + vy)] dx dy \quad (2.16)$$

$$S_\theta(\omega) = \int_{-\infty}^{\infty} P_\theta \cdot \exp [-j2\pi\omega t] dt \quad (2.17)$$

For simplicity, let's consider the 2D **FT** at the line defined by $v = 0$ in the frequency domain. We rewrite the 2D **FT** integral as:

$$F(u, 0) = \int_{-\infty}^{\infty} \int_{-\infty}^{\infty} f(x, y) \cdot \exp [-j2\pi\omega ux] dx dy \quad (2.18)$$

Notice that y is not present in the phase factor of the **FT** expression anymore, and this means we can rearrange the integral as:

$$F(u, 0) = \int_{-\infty}^{\infty} \left[\int_{-\infty}^{\infty} \mathbf{f}(\mathbf{x}, \mathbf{y}) d\mathbf{y} \right] \cdot \exp [-j2\pi\omega ux] dx \quad (2.19)$$

Now, the **bold** part of Equation 2.19 is similar to Equation 2.14. It is precisely that equation, considering $\theta = 0$ and a constant value of x , as in Equation 2.20.

$$P_{\theta=0}(x) = \int_{-\infty}^{\infty} f(x, y) dy \quad (2.20)$$

This in turn can be substituted in Equation 2.19, finally arriving at:

$$F(u, 0) = \int_{-\infty}^{\infty} P_{\theta=0}(x) \cdot \exp [-j2\pi ux] dx \quad (2.21)$$

And this is the one-dimensional **FT** for the projection at angle $\theta = 0$. Finally, the enunciation of the Fourier Slice Theorem:

The Fourier Transform of a parallel projection of an image $f(x, y)$ taken at angle θ gives a slice of the two-dimensional Fourier Transform, $F(u, v)$, subtending an angle θ with the u -axis (see Figure 2.23)

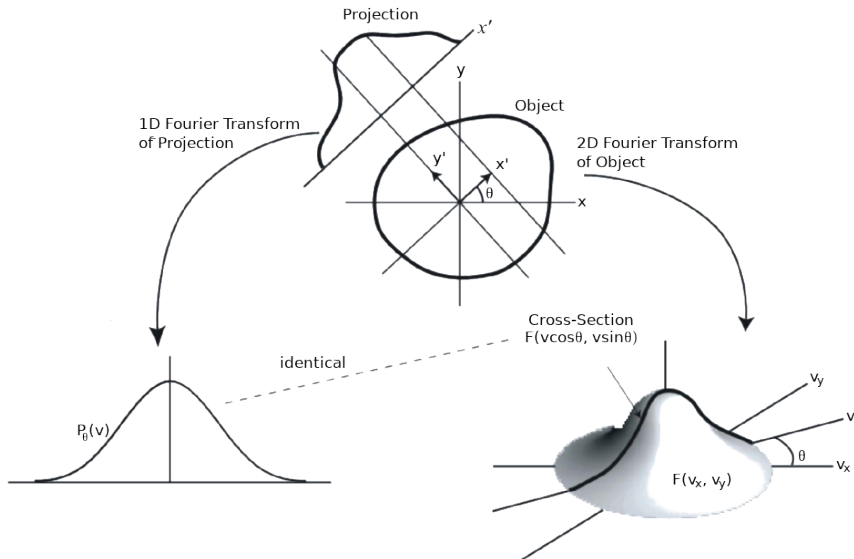


Figure 2.23: The **FST**, a schematic representation [4].

If one takes the **FST** into account, the idea behind the **FBP** seems to appear almost naturally. Say one has a single projection and its Fourier transform. From the **FST**, this projection is the same as the object's two-dimensional **FT** in a single line. A crude reconstruction of the original object would result if someone were to place this projection in its right place in the Fourier domain and then perform a two-dimensional **Inverse Fourier Transform (IFT)**, while assuming every other projection to be 0. The

2.4. TOMOGRAPHIC ALGORITHMS AND RECONSTRUCTION TECHNIQUES

result, in the image space, would be as if someone had smeared the object in the projections direction.

What is really needed for a correct reconstruction is to do this many times, with many projections. This brings a problem with the method: smearing the object in all directions will clearly produce a wrong *accumulation* in the center of the image, since every projection passes through the middle (remember we are still talking about parallel geometry projections) and are summed on top of each other, but on the outer edges, this does not occur. If one does not address this, the image intensity levels in the reconstructed image will be severely overestimated in the center and underestimated in the edges (due to normalization). The solution is conceptually easy: we multiply the Fourier transform by a weighting filter proportional to its frequency (ω) and that encompasses its relevance in the global scheme of projections. If there are K projections, then it is adequate for this value to be $\frac{2\pi|\omega|}{K}$. As an algorithm, **FBP** can be written as in Algorithm 1.

Algorithm 1: The Filtered BackProjection Algorithm

Result: A reconstructed image of the projected object.
for $\theta \leftarrow 0$ **to** 180 **by** $\frac{180}{K}$ **do**
 measure projection $P_{\text{theta}}(t)$;
 $\text{FT}(P_\theta(t))$, rendering $S_\theta(\omega)$;
 Multiply by $\frac{2\pi|\omega|}{K}$;
 Sum the **IFT** of the result in the image space;
end

Parallel projections, in which the object is scanned linearly from multiple directions, have the advantage of having a relatively simple reconstruction scheme. However, they usually result in acquisition times which are in the order of minutes. A faster way of collecting the data is one where all radiation emanates from a single point-source, which rotates around the target object (as well as the detectors). There are two types of fan-beam projections: equiangular and equally spaced. In this project, I have only worked with equiangular processes, so I will not include an explanation for equally spaced fan-beam projections. The reader may find this well described (much better than I would be able to) in [47] and [43].

Consider Figure 2.24. If our projection data were acquired through a parallel ray geometry, we would be able to say that ray SA belonged to a projection $P_\theta(t)$, in which θ and t would be written:

$$\theta = \beta + \gamma \quad \text{and} \quad t = D \cdot \sin \gamma \quad (2.22)$$

In Equation 2.22, D is the distance between the source S and the origin O ; γ is the angle of a ray within a fan and β is the angle that the source S makes with a reference axis. Through these relationships one can *translate* the parallel projection's FBP algorithm to the fan-beam case, which involves several complex geometric transformations, although the overall rationale is exactly the same.

Another particularity of fan-beam projection data is the fact that they can be sorted into a parallel projection. For that, one starts with the premise that if one were to

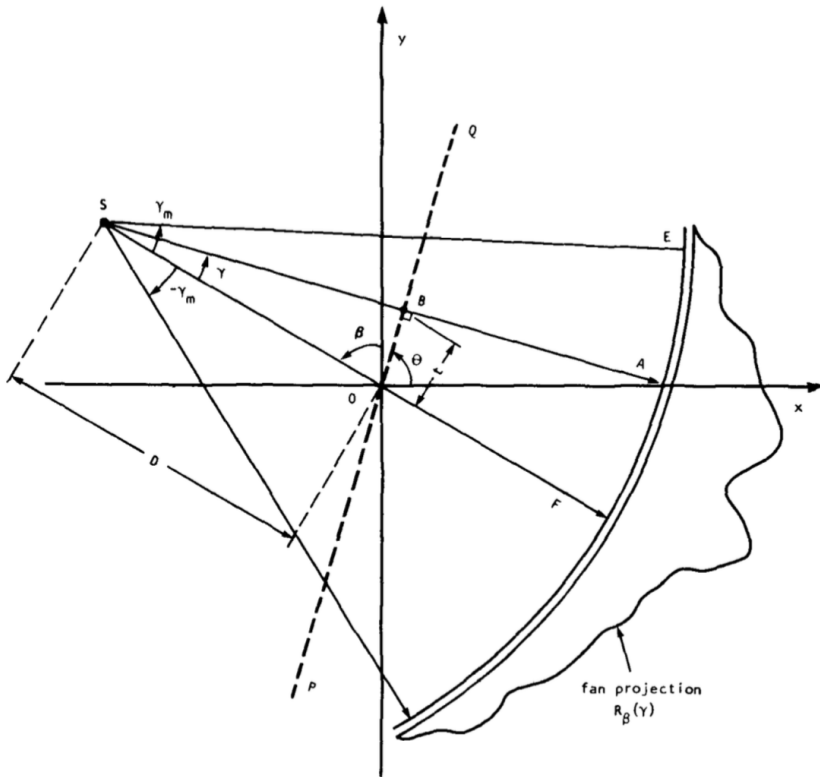


Figure 2.24: Schematic representation of an equiangular fan-beam projection, taken from [47].

substitute the fan geometry for parallel beams, most of the fan-beam rays would also appear in some projection of the parallel setup. This re-sorting algorithm starts with Equation 2.22. Now, if we call a fan-beam projection taken at angle β $R_\beta(\gamma)$, and a parallel projection taken at angle θ $P_\theta(t)$, one could thus write Equation 2.23, which can already be used to re-sort any fan-beam projection into parallel beam geometry.

$$R_\beta(\gamma) = P_{\beta+\gamma}(D \cdot \sin \gamma) \quad (2.23)$$

Let's call the angular interval between fan-beam projections can be written $\delta\beta$, and the angular interval of rays within each fan is written $\delta\gamma$. In the case that they are the same ($\beta = \gamma = \alpha$), then it is the case that they can both be replaced by multiples of that interval in Equation 2.23, which becomes Equation 2.24.

$$R_{m \cdot \alpha}(n \cdot \alpha) = P_{m \cdot \alpha + n \cdot \alpha}(D \cdot \sin n \cdot \alpha) \quad (2.24)$$

Or, in non-mathematical notation, the n^{th} ray of the m^{th} radial projection (R) is the same as the n^{th} ray in the $(m+n)^{\text{th}}$ parallel projection. Although being much simpler than directly applying the FBP algorithm to the fan-beam projection data, this method has a limitation, which is the non-uniformity of the generated parallel projections. This can usually be corrected through interpolation [48].

2.5 DOAS Tomography

In previous sections (Section 2.2) we have established that DOAS is a widespread spectroscopic technique with particular usage in the atmospheric research community. This technique uses either artificial or natural light to retrieve slant column densities, the number of molecules that interact with the said light in a given optical path. These values are described by Equation 2.4, and are indeed line integrals.

Also in a previous but different section (Section 2.4), we have seen that with enough of these integrals (which we can call projections), we can gather enough information to depict the interior structure of an object that we make traverse with radiation of some kind, as long as it is measurable and its behaviour is well known.

Joining the two notions, we can get to the idea that it would be possible to use DOAS in a tomographic manner, so long as we use sufficient light collection points. This has been proposed by Byer and Shepp [14] in 1979. At the time the authors did not mention specifically the DOAS technique, but the assembly they propose is essentially equivalent to one that would use this method. DOAS tomography was also mentioned in one of the main pieces of literature in the field, [66], as one of the most promising avenues available for DOAS progress in the future.

As a requirement for one of the courses that I chose to pursue during the curricular part of my doctorate, I had to complete an assignment that consisted in writing a Systematic Mapping Study on the subject of DOAS tomography. The study is included in full in Appendix A. It aims at characterising the literary panorama regarding the subject and tries to arrive at a standard application with respect to software, algorithms and instrumentation.

This type of study has a particular methodology focused on repeatability. Its complete explanation is out of scope of this section and even this document, but a simplified schematic is included in Figure 2.25. A more detailed and extensive description of this method can be found in several works available in the literature, namely [50, 51, 77].

After defining search terms and conducting the actual search, we arrived at a total of 9 relevant papers. These were analysed under the light of the study's main goal, which was to identify a standard DOAS tomography device and application.

The first identifiable pattern is the marked prevalence of active DOAS systems. 11 out of the 13 retrieved papers describe or consider an active DOAS system of some kind. As stated in Section 2.2, active DOAS systems do have better analytical capabilities than their passive counterparts, although that comes at the cost of increased instrument complexity and operational costs.

Another immediate conclusion is that there is a "dominant" study. Almost half of the papers found originated from the BABII campaign, in which a group of researchers set out to quantify pollution through DOAS tomography along a busy German motorway, in the beginning of the 21st century [40, 39, 52, 69, 71, 70, 57].

All of the active DOAS systems were purposely built for their corresponding experiment (or group of experiments). BABII researchers used two telescopes with around 200mm diameter and 1m focal length to simultaneously illuminate 8 retroreflectors that were assembled onto two towers located on each side of the road. In one of the papers associated with this initiative, the same telescope instrumentation was used

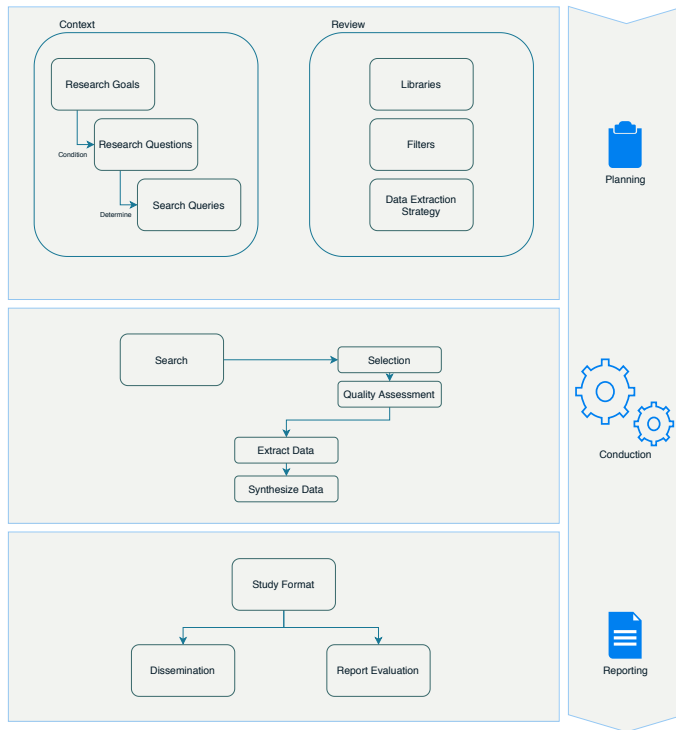


Figure 2.25: Simplified diagram of the **SMS** method. This type of study is focused on registering every step of the search and the reading of the retrieved material, in an effort to make the process completely repeatable. Adapted from [50].

to validate the 2D reconstruction technique that was going to be used in the other papers. The campaign's main assembly is illustrated in Figure 2.26.

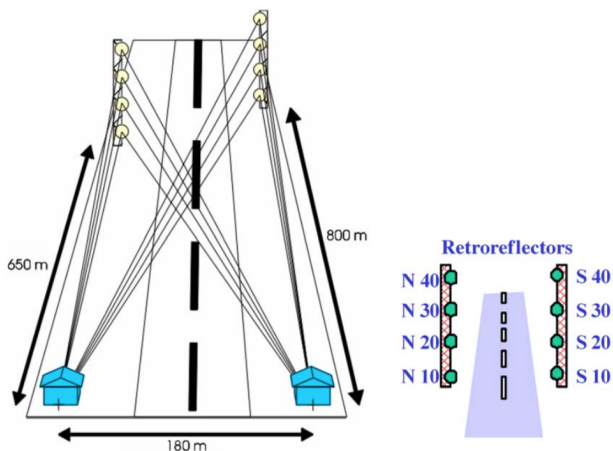


Figure 2.26: BABII assembly geometry. In this experiment campaign, the telescopes illuminated retroreflecting targets that were positioned in two steel towers on both sides of a busy motorway in Germany, connecting Heidelberg to Mannheim [70].

Another important initiative with respect to **DOAS** tomography was the study conducted in 2016 by Stutz et al [80]. The approach in this case was to use a similar telescope to detect the light emitted by a narrow interval UV LED light source (290nm) to create a fence line monitoring system for Benzenes, Toluene and Xylene. The team

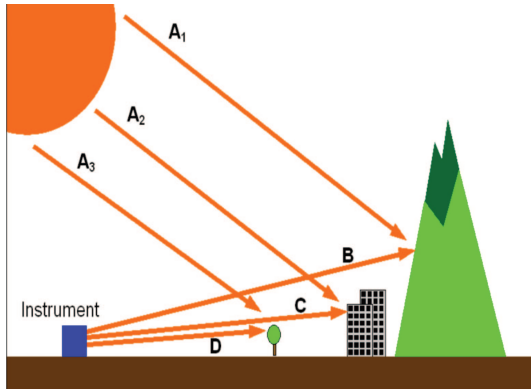
managed to apply this system in a successful manner in refineries in Los Angeles and Houston. One of the most interesting aspects of this study is that it details a tomographic system that could easily be commercially deployed.

Another type of DOAS tomography system was proposed by researchers in the Cork Institute of Technology [60, 61, 58]. In their three papers, the authors describe 1) a new multipath instrument that significantly increases the amount of projection information in this kind of application; 2) a tomographic reconstruction algorithm based on evolutionary algorithms; and 3) the application of DOAS tomography to a simulated urban canyon scenario. Although all three papers present technological innovation, it would not be fair not to say that from a strictly literary point of view, these were among the weakest retrieved by the search process.

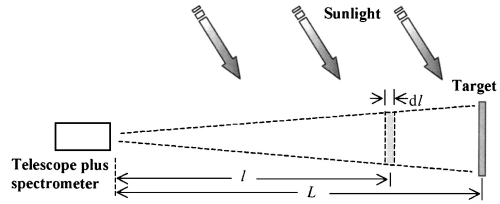
Regarding passive DOAS applications, the two papers we have found come with two completely different paradigms. The first article [46] was written in 2009 and details the application of a tomographic inversion algorithm to a scanning DOAS application, designed to work with trace gas plumes like the ones above volcanoes or power stations. The team present a system composed of two DOAS devices, with sufficient distance with themselves as to allow tomographic reconstruction, but sufficiently small to allow the light path to be considered a straight line from the point of last scattering to the detector. The authors applied an adapted version of the Lower Third Derivative (LTD) algorithm to the projections obtained by pointing the set of fixed DOAS apparatus towards the plume in different angles. Besides simulations for their proposed method, the authors have also conducted practical experiments, both over a power plant in Spain and a volcano in Italy. Results from these experiments display a good agreement between reality and simulation results, proving the technique's validity.

The second Passive DOAS application is a paper published by Frins et al. [33]. In this study, the researchers detail a particular application in which they measure light coming from bright and nonreflecting sun-illuminated objects in their field of view. They use this light to retrieve column density values for a number of trace gases. The proposed method also includes a way with which to remove the stratospheric contribution that appears in the measured light besides the target column. The authors discuss how radiative transfer can influence measurements, but they also present a number of approaches to mitigate this problem, ensuring the validity of their approach. Besides presenting the method, the authors also describe an experiment they conducted by assembling and manoeuvring a DOAS system on top of a building in Heidelberg, Germany.

In summary, the search has found that active tomographic DOAS is far more common than the passive counterpart (11 out of 13 articles discussed this method). This preference can be explained by the fact that the results produced by this kind of system are generally superior to those obtained by passive methods. However, passive applications are normally much less demanding on a technical level, and are simpler to run and assemble. Much as a result of this, we have also identified that the systems used in the literature were not mobile or had a very low mobility level which in turn caused that all the systems were working with low projection numbers. This should be taken into account in future research on the topic. As a final note, we would also like to point out that there is no commercially available systems for this kind of application, although some of the articles, like the one by Stutz in 2016 [80] detail systems which



(a) Schematic representation of Frins's assembly [33].



(b) The physical principle behind Frins's paper [33].

Figure 2.27: Erna Frins's paper [33] proposes a very relevant passive DOAS application that can conceptually be employed in a DOAS tomography scenario. In this 2006 paper, the authors use multi-axis measurements of sun-illuminated targets to estimate absorption paths without using radiative transfer models.

could easily be adapted to that end.

METHODS

Macroscopically, the approach to the **RQ** was conducted by working with two hypothesis:

First Hypothesis: The definition of a particular set of algorithmically defined projections in such a manner that they might be used for tomographic reconstruction of column densities of trace gases in the atmosphere, in a given **ROI**;

Second Hypothesis: We can retrieve the column density for a given trace gas (or set of trace gases) between two points by performing a spectral measurement in both of these points in the same direction and subtracting them one from the other.

To test the first hypothesis, I have used a number of computational methods to define and create projection and backprojection matrix operators, resulting in a dedicated simulation software tool that proves without a doubt that the devised projection gathering strategy is able to produce projection information in sufficient quantity as to perform tomographic reconstruction. This procedure is detailed in Section [3.1](#).

The second hypothesis was experimentally tested, by the conduction of a number of field experiments designed to determine the validity of measurement hypothesis with the equipments to which I have current access. The experiment and the protocol that was followed is detailed in Section [3.2](#). This chapter is heavily based on one of the two articles generated by the work of this thesis.

3.1 Tomosim

Tomosim was the (somewhat unoriginal) name given to the tomographic simulation software tool that was designed and built as part of this project. It was created to tackle the trajectory-related hypothesis, briefly described in this chapter's introduction.

The final system must be able to gather projection information by reading spectral information, in this case the **DOAS**-retrieved column density for an atmospheric trace gas (or several) from a set of predetermined directions. In "normal"tomographic **DOAS** application, these directions are fixed and depend on the experiment infrastructure's geometry (see Section [2.5](#)). One of the main novelties that I am trying to create with this project is a very high degree of geometric freedom. A mobile system has no

custom infrastructure, and therefore has no fixed positions to which it is tied. Instead its ability measure and monitor its atmospheric surroundings relies on its movement.

A ground-based mobile DOAS-tomography system would have too strong a dependency on open spaces and the topography of its ROI to be useful in any *real world* scenario. A much more interesting and feasible approach would be to use some kind of flying machine that could carry spectroscopic equipment, and that could be programmed to fly in a precise manner. Fortunately, current day technology provides a very strong immediate candidate: a UAV of the n-copter type, such as the one in Figure 3.1.



Figure 3.1: Hexacopter in flight. Image taken from LevelFiveSupplies[53], for illustration purposes only.

A natural choice as it may seem as means for the measurements I am describing in this document, its programming is almost as important as the hardware itself (if not more). The vehicle must be programmed to describe a very precise (taking into account the type of operation we are proposing) trajectory. In flight, the drone should be able to carry and point an optical system towards any direction and in a short time. Said optical system should be attached to a computer-controlled spectrometer. This would allow the whole system to determine target trace gas concentration on demand and programmatically.

The programmed trajectory should make use of these capabilities and gather enough information for tomographic reconstruction. This also means that the trajectory must be comprised of a sufficient number of spectral projection acquisition opportunities.

Of the several geometries that are described in the literature for tomographic reconstructions, the one that seemed to be more promising in terms of the balance between reconstruction complexity and the information / flight time ratio was the fanbeam assembly (described in Section 2.4). It was the feasibility of this trajectory for the proposed purposes that this simulation aimed to prove.

In essence, the drone's trajectory (illustrated in Figure 3.2) is a horizontal circle which is parametrised to be at a certain height and to have a certain diameter. Both of these dimensions are set at experiment / measurement time. The drone stops on this circle at regular angular intervals, say α degrees. Each one of these stops ($360 / \alpha$ stops) will generate a fanbeam projection, by pointing the optical system inwards (with respect to the circular macro-trajectory) and performing a series of spectroscopic measurements in different directions and also at regular intervals, say γ degrees. The

particular case in which $\alpha = \gamma$ is very interesting, because it then opens the possibility for resorting the fanbeams into parallel virtual-projections that are much easier to reconstruct tomographically, as introduced in Section 2.4.

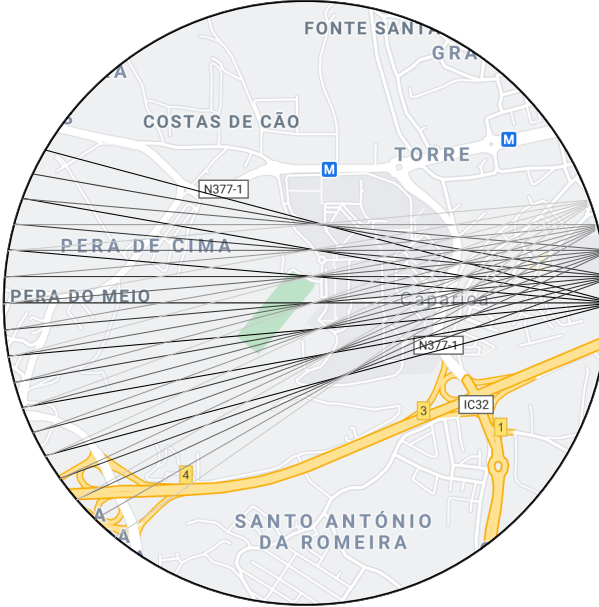


Figure 3.2: Illustration of the projection gathering algorithm based on the assembly of groups of acquisitions as fanbeam projections. The lines presented on the drawing come from the right to the left. Each is a ray in fan, corresponding to one stop of the drone. In the second measurement moment, the drone moves to the exit point on the left and repeats the first moment collection. Here, both fans and rays are separated by 5 degrees and there are 6 rays within each fan. A "real life" acquisition would feature a lot more rays, but that would be graphically complicated for the reader. Both ray and fan angular distance are customisable at runtime. Map taken from Google Maps in 2019. ©Google.

3.1.1 Discretisation

Discretisation is the process by which the **ROI** is digitised into a computational platform. There are several algorithms designed for this effect that are available in the literature. One of the easiest to implement that is also adequate to this application (unsurprisingly) comes from the medical imaging field. It was published in 1985 by Robert Siddon [76].

The Siddon algorithm is one of the foremost path calculation algorithms in the medical field of radiology. It is not only used for the discretisation of tomographic fields, but also in the dose calculation process of radiation therapy patients. The idea behind the algorithm is that the total dose of a radiation ray, i.e., its path, is given by the sum of the length within each pixel that this ray traverses multiplied by the density of said pixel. In mathematical notation, one can write this as in Equation 3.1.

$$d = \sum_i \sum_j \sum_k kl(i, j, k) \cdot \rho(i, j, k) \quad (3.1)$$

In Equation 3.1, d is the radiological path (the projection value), i, j, k are the coordinate vectors, l is the length within a pixel and ρ is the pixel density. In our case, this last value is the trace gas column density for that pixel.

The main reason for Siddon's algorithm being easy to implement is its treatment of pixels (or voxels if in 3D). Instead of considering pixels as *atomic*¹ units, it defines them as the intersections of orthogonal sets of equally spaced lines (planes in 3D). Pixel lengths are determined by the looking at the intersections between the orthogonal lines and the radiation ray.

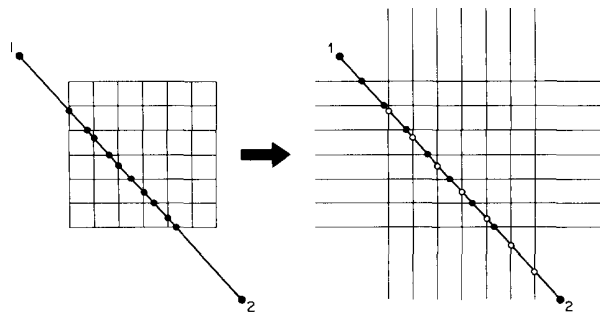


Figure 3.3: Grid and pixel definition, as they appear in the original article by Robert Siddon [76]. Pixels are "formed" by intersecting the ray (here going from point 1 to point 2) with the superimposed grid.

Since lines are orthogonal and equally spaced, all intersections can be calculated recursively after knowing where the first intersection is located. The calculation of the radiologic path is achieved by determining the subset of the intersections between the orthogonal lines and the light ray that identifies individual pixels.

If $P_1 \rightarrow (X_1, Y_1)$ and $P_2 \rightarrow (X_2, Y_2)$ are the start and end of the radiologic path within the ROI, the line between them can be parametrically written as in Equation 3.2.

$$\begin{aligned} X(\alpha) &= X_1 + \alpha \cdot (X_2 - X_1) \\ Y(\alpha) &= Y_1 + \alpha \cdot (Y_2 - Y_1) \end{aligned} \tag{3.2}$$

In Equation 3.2, α is 0 at P_1 and 1 at point P_2 . Values of α within the ROI vary according to the positions of P_1 and P_2 with respect to the ROI. By determining α values of each intersection (in both directions), one can determine the length of the ray within the pixel by the difference of adjacent intersections. The whole algorithm

¹In their undivisible sense.

can be written as in Algorithm 2.

Algorithm 2: Siddon's algorithm's procedural steps. After running this algorithm, one is able to represent any continuous ray through the analysis field as a sum of discrete lengths

Result: Discretised ROI space.

- calculate range of parametric values;
 - calculate range of pixel indices;
 - calculate parametric sets;
 - merge sets;
 - calculate pixel(or voxel) lengths;
 - calculate pixel indices;
-

Detailing the two-dimensional case² should start by the definition of the discretisation grid itself, as in Equation 3.3. The equation reflects the recursive nature of the grid definition. In it, d_x and d_y are the distances between the x and y planes, which correspond to the lengths of the pixels in those coordinates. N_x and N_y are the number of pixels in x and y that are contained in the grid.

$$\begin{aligned} X_{\text{plane}}(1) &= X_{\text{plane}}(1) + (i - 1) \cdot d_x \\ Y_{\text{plane}}(1) &= Y_{\text{plane}}(1) + (j - 1) \cdot d_y \end{aligned} \quad (3.3)$$

The parametric values α_{\min} and α_{\max} are given by the intersections of the ray with the sides of the grid ($i = 1$ and $i = N_x$) and can be written as in Equation 3.4.

$$\begin{aligned} \alpha_{\min} &= \max \{0, \min [\alpha_x(1), \alpha_x(N_x)], \min [\alpha_y(1), \alpha_y(N_y)]\} \\ \alpha_{\max} &= \min \{1, \max [\alpha_x(1), \alpha_x(N_x)], \max [\alpha_y(1), \alpha_y(N_y)]\} \end{aligned} \quad (3.4)$$

Not all line intersections have a corresponding parametric value. The ones that do are comprised within index ranges that are defined by Equation 3.5. This equation presents the case for the first coordinate (x), with the second coordinate having an identical expression.

$$\begin{aligned} i_{\min} &= N_x - \frac{X_{\text{plane}}(N_x) - \alpha_{\min}(X_2 - X_1) - X_1}{d_x} \\ i_{\max} &= 1 + \frac{X_1 + \alpha_{\max}(X_2 - X_1) - X_{\text{plane}}(1)}{d_x} \end{aligned} \quad (3.5)$$

Equation 3.5 defines a range of possible indices for the pixels, in parametric fashion. We can use this range to construct the set of used parametric indices, given in Equation 3.6 for the x coordinate.

$$\{\alpha_x\} = \{\alpha_x(i_{\min}), \dots, \alpha_x(i_{\max})\} \quad (3.6)$$

Although Equation 3.6 only presents the expression for the first coordinate, there are similar expressions for the other coordinates at play. After determining the set of possible indices for x and y , these sets must be arranged in ascending order, creating

²A three-dimensional case would be just the same but with an additional coordinate.

an index superset. To this the minimum and maximum values, calculated in Equation 3.4, are appended. The resulting and final set of parametric values is presented in Equation 3.7.

$$\begin{aligned}\alpha^* &= \text{merge}(\alpha_x, \alpha_y) \\ \{\alpha\} &= \{\alpha_{min}, \alpha^*, \alpha_{max}\} \\ &= \alpha(0), \dots, \alpha(n)\end{aligned}\tag{3.7}$$

Where the last term, n , is given by the sum of all index range numbers, as in Equation 3.8, again for the two-dimensional case.

$$n = (i_{max} - i_{min} + 1) + (j_{max} - j_{min} + 1)\tag{3.8}$$

Each element of the array defined in Equation 3.7 is an intersection between the ray and a given pixel. Since they are ordered, it is possible to calculate the array of pixel lengths for each ray, using the expression in Equation 3.9.

$$l_m = d_{12}[\alpha(m) - \alpha(m - 1)] \quad (m = 1 \dots n)\tag{3.9}$$

With d_{12} being the distance between P_1 and P_2 , calculated through the Euclidean formula for distance between two points. In Tomosim, this distance is always equal to the trajectory's diameter.

Pixel $[i(m), j(m)]$ is located in the midpoint between the m^{th} and the $(m-1)^{\text{th}}$ intersections. It is given by the expression in Equation 3.10.

$$\begin{aligned}\alpha_{mid} &= \frac{\alpha(m) + \alpha(m - 1)}{2} \\ i(m) &= 1 + \frac{X_1 + \alpha_{mid} \cdot (X_2 - X_1) - X_{plane}(1)}{d_x} \\ j(m) &= 1 + \frac{Y_1 + \alpha_{mid} \cdot (Y_2 - Y_1) - Y_{plane}(1)}{d_y}\end{aligned}\tag{3.10}$$

Knowing the pixels and the ray lengths for each of them makes the application of the radiological path equation (Equation 3.1) trivial. From another perspective, Siddon's algorithm produces an even more important piece of information. One gets total geometric knowledge of the tomographic assembly. If matrix form, this is called the system matrix, and it is an essential part of the application of any iterative algorithm.

Figure ?? aims to graphically explain the formation of this matrix. Each line in the matrix can be thought of as a flattened matrix of the same size as the tomographic image to reconstruct. There are as many of these lines as there are rays in the tomographic assembly. Each element of the matrix contains the length of the ray corresponding to each line, as it is calculated (through the application of Siddon's algorithm) for the corresponding pixel of the aforementioned flattened matrix.

3.1.1.1 Exit Point Calculation

Figure 3.4 is a schematic snapshot of a point in which the drone is taking a spectrum in one of its stops. Here, the drone's position (P_1) is given by the distance D and the angle β . The gimbal is pointing at a direction at an angular distance of γ from line $0P_1$. Point

P_2 , which is not known, is at the intersection between the trajectory's circumference and line P_1P_2 . Now, any point on this line can be expressed parametrically, with the sum of a point and a vector; while to say a point is on a circumference is the same as saying the distance between that point and the centre of this circumference is equal to its radius. The situation can be described by the expressions in Equation 3.11.

$$\begin{aligned} X &= P_1 + t \cdot (P_2 - P_1) \\ |P_2| &= D^2 \end{aligned} \quad (3.11)$$

Unravelling these expressions, and making use of the algebraic property that says that $|A|^2 = A \cdot A$, the expression becomes a second degree equation, as stated in Equation 3.12, writing $P_2 - P_1$ as V .

$$t^2 V^2 + 2 \cdot V \cdot P_1 \cdot t + P_1^2 - D^2 = 0 \quad (3.12)$$

If line P_1P_2 non-tangentially intersects the circumference, solving Equation 3.12 renders two values for t (which correspond to P_1 and P_2). Selection is made by determining the returned value of t which maximises the euclidean distance between the produced point and P_1 .

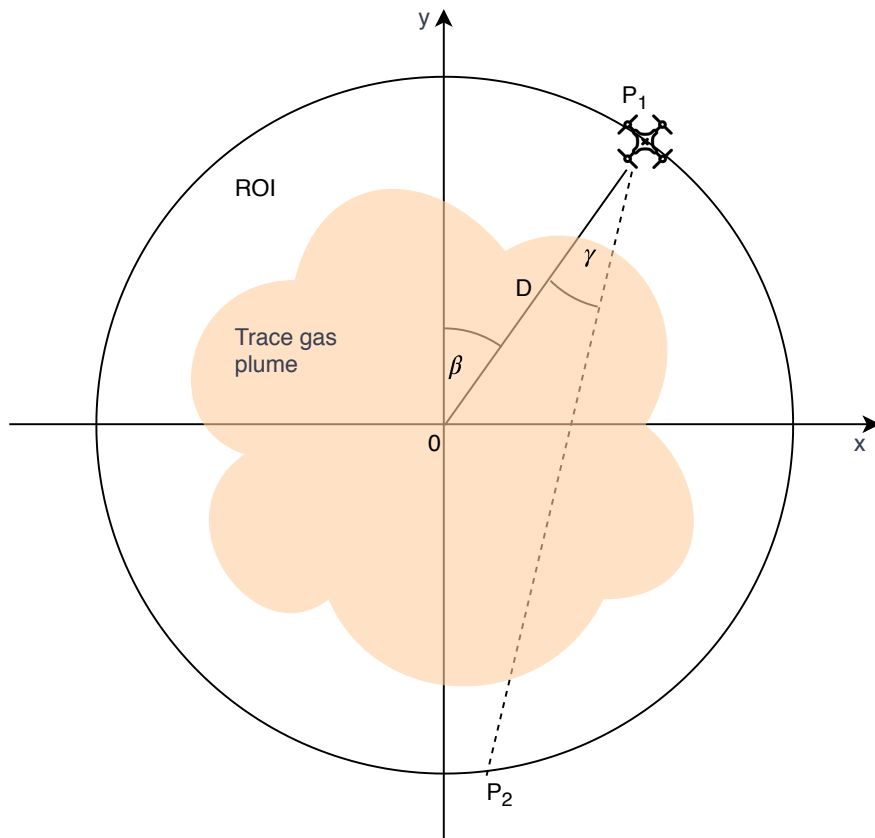


Figure 3.4: P_2 Calculation. The software uses the position of the drone, as defined by the vertical angle, β , and the distance between the drone and the centre of the trajectory, D , to determine P_2 through the solution of a second degree equation.

3.1.2 Phantoms

A phantom is a device that represents the human body or some of its parts. They have been used in medical physics since the beginning of the field. In medical imaging, for instance, phantoms started being used in the late nineteenth century and early twentieth century. At the time, it was very difficult to find volunteers for any kind of experiment that involved radiation, due to the common effects that were rapidly reported by the first people subject to this kind of intervention [26]. In spite of this difficulty, scientists and researchers still had to determine the dosimetry properties and physical limitations of their radiative devices, so medical physicists had to develop their own test models, or phantoms, for this effect. More recently, phantoms have been designed to develop computed tomography applications and algorithms. These phantoms mimic the body's attenuation properties in the X-Ray section of the electromagnetic spectrum, for instance.

Although the system that I propose does not aim at measuring or using the human body (or any other animal's), the concept still stands. To evaluate our reconstruction methods and the validity of our data gathering strategies, I needed an atmospheric phantom.

The distribution of gases in the atmosphere is completely different from biological tissue. Therefore, medical imaging phantoms were not adequate. The design that I have created is based on the premise that a two-dimensional Gaussian peak is more appropriate to describe the smoother nature of gaseous distribution [78]. This in contrast with the crisply defined edges of a medical tomography phantom such as Shepp-Logan's head phantom [75].

To design the phantom itself, I used a library called TomoPhantom [49], a tomographic phantom generator that provides a Python [Application Programming Interface \(API\)](#), making it trivial to include in the Tomosim simulator. The new phantom is comprised of 5 Gaussian profiles, depicting a static gas mixture. An ellipse is also in the phantom, near one of the corners. This serves mainly as a reference point for reconstruction, given its more solid and crisp nature. The new phantom can be seen in Figure 3.5 and its features are stated in Table 3.1.

Table 3.1: Table summarising the new phantom's construction details, as a sum of 5 Gaussian profiles and an ellipse designed using TomoPhantom. In this table, Co is the object's amplitude, Xo and Yo are its center coordinates, and a and b are the objects half-widths. The table is constructed using TomoPhantom's particular syntax and more information can be obtained at [49].

Type	Co	Xo	Yo	a	b	Angle
Gaussian	1	-0,1	-0,1	0,25	0,5	-45
Gaussian	1	0,6	0	0,65	0,45	-45
Gaussian	1	-0,6	-0,4	0,8	0,8	0
Gaussian	1	-0,4	0,8	0,7	0,7	0
Ellipse	1	0,4	-0,8	0,3	0,15	0

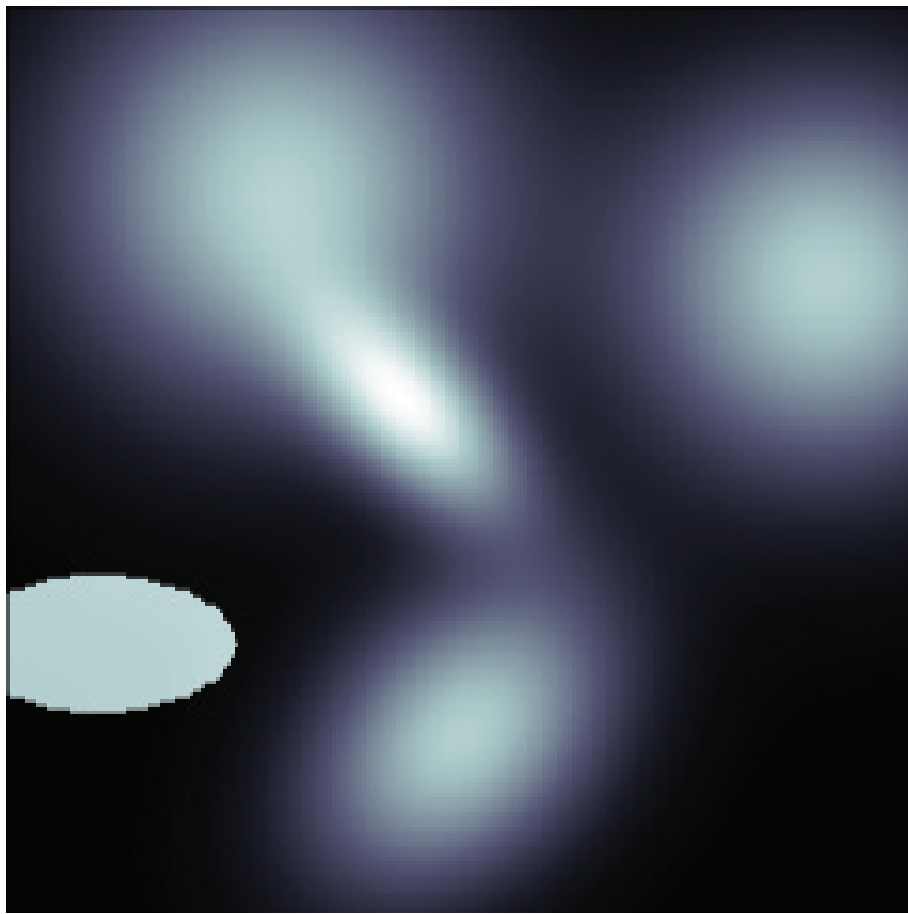


Figure 3.5: A graphical representation of the new spectral phantom, custom built for the TomoSim application.

3.1.3 Error Estimation

Error sources for the Tomosim simulator come in four different natures: time errors, geometric errors, spectroscopic errors and reconstruction errors.

Time errors come from the fact that there are two moments of measurement. In a dynamic system, the time that passes between the two is enough for concentrations to change significantly. Tomosim does not address these errors, because they can be eliminated by the introduction of a second drone carrying the same type of equipment, which would eliminate said time difference.

Geometric errors exist due to the drone not being able to situate itself perfectly. There is always a positioning error, no matter how sophisticated the onboard equipment is. This type of error is addressed in the simulation through a Monte Carlo like approach.

Positioning and pointing errors are assumed to have normal distributions. Each time a point is calculated by the drone, a normally distributed random number, with a mean of 0 and a standard deviation equal to the nominal error of the positioning system. This number is then added to the theoretical point. Figure 3.6 is a graphical representation of the reasoning behind the calculation of the geometric error. The image deals with two types of error. One comes from the [Real Time Kinematic Global](#)

Positioning System (RTK GPS) positioning system (the positioning error, ϵ_p); and the other that comes from the gimbal (the pointing error, ϵ_γ). The two ϵ values are the nominal error for the positioning and the pointing devices. The error is introduced in the simulation through the values of β and D (see Figure 3.4) while calculating P_2 . Given the very low nominal error for the gimbal, the small angle approximation is valid ($\sin \theta = \theta$). This is used to determine the theoretical value of P_2 , located on the device's circular trajectory. Finally, the software adds the positioning error, using the same process as in P_1 's case. The error depiction in Figure 3.6 is extremely exaggerated for visibility.

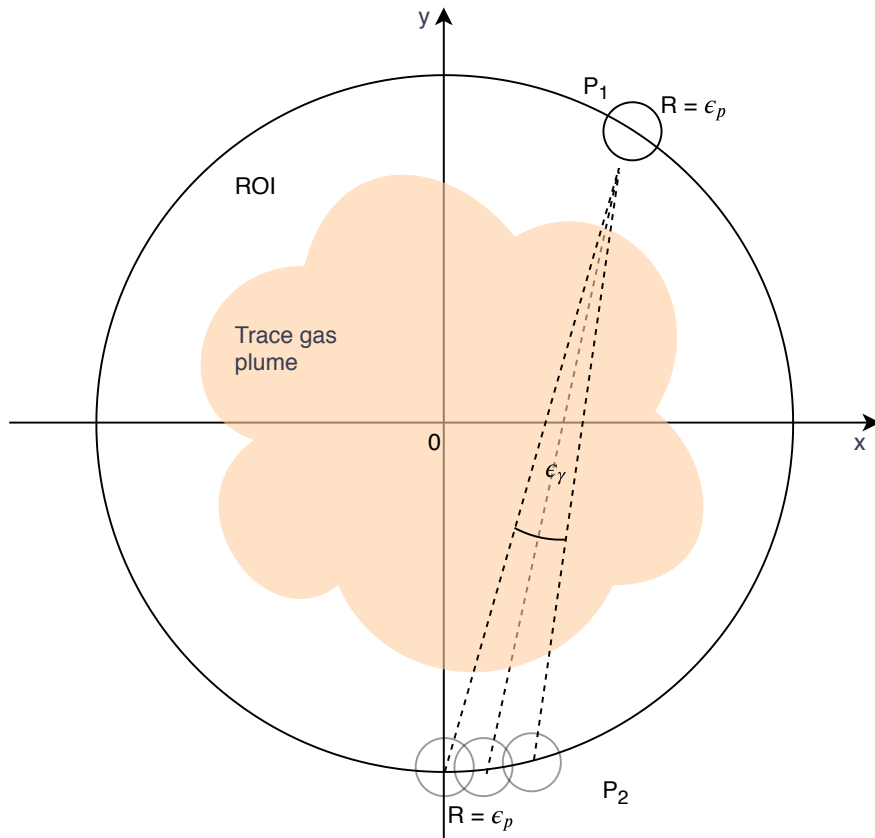


Figure 3.6: Error estimation graphical representation. Note errors are extremely exaggerated for visualisation purposes.

The third type of error are the spectroscopic errors. These come from the spectroscopic equipment that is used to gather projections. To take this noise into account, the simulator adds a Gaussian noise spectrum to each measurement, which is configurable through its standard deviation, as was previously done in [79]. This is a valid approach, insofar as the captured spectra are perfectly calibrated regarding spectral shift and squeeze. Since this is a simulation software, this is an acceptable assumption.

The final type of error that the system needs to contend with is the reconstruction error. In tomographic inversion problems, it is common to use techniques such as the **Mean Squared Error (MSE)** as a metric for an algorithm's performance. Tomosim was also evaluated in this light and in two separate ways. The first was to calculate the **MSE** for each pixel of the whole image. This information can still be viewed as an

image (it is a two-dimensional grid of values) and paints an immediate picture of the general behaviour of the reconstruction algorithm. Moreover, it can tell the viewer if there are any types of shapes or areas in which the algorithm has more difficulties. The second way of using MSE to evaluate the reconstruction is to calculate a score through Equation 3.13. In this equation, and with respect to this simulator, f is the original image and g the one reconstructed from projections.

$$E = \sqrt{\frac{\sum |g(x, y) - f(x, y)|^2}{\sum |f(x, y)|^2}} \quad (3.13)$$

3.1.4 Reconstruction Results

Until now, this section was dedicated to explaining the theoretical and computational aspects of the TomoSim software program. In this subsection, I will focus on the results that it produced, namely in what concerns the tomographic reconstruction of an image based on the concentration of selected atmospheric trace gases.

In TomoSim, a projection is the sum of the pixel lengths (the lengths of the rays that traverse each pixel) for each ray and for the grid mentioned in Section 3.1. Unlike a real life situation, the contents of the ROI are completely known and correspond to the phantoms also described in Section 3.1 multiplied by a given maximum number of molecules. Siddon's algorithm is used in this process, and the final results of its application are the sinogram and the system matrix. Figure 3.7 contains some examples of these matrices, before and after the resorting operation described in the last lines of Section 2.4.

Images corresponding to the trace gas distribution within the ROI were reconstructed using iterative and analytical methods. In Figure 3.8, one can see the reconstruction results for the three tested methods when applied to the new spectral phantom; Figure 3.9 shows the graphical representation of the reconstruction errors for the spectral phantom and is accompanied by Table 3.2; and in Figure 3.10, a comparison between reconstructions with different Δ values is presented, also for the new spectral phantom.

Table 3.2: Reconstruction error table for the new spectral phantom at several projection intervals. The MLEM routine used pure fan-beam data while the other two used resorted parallel information. Errors presented were calculated using the Root Mean Square Errors, normalised to the range of the reconstructed image.

Algorithm	Projection Intervals				
	1	2	3	4	5
FBP	0,2365	0,2408	0,2609	0,2948	0,3465
SART	0,2225	0,2278	0,2771	0,3537	0,3302
MLEM	0,8705	0,9723	0,9986	0,9744	0,9890

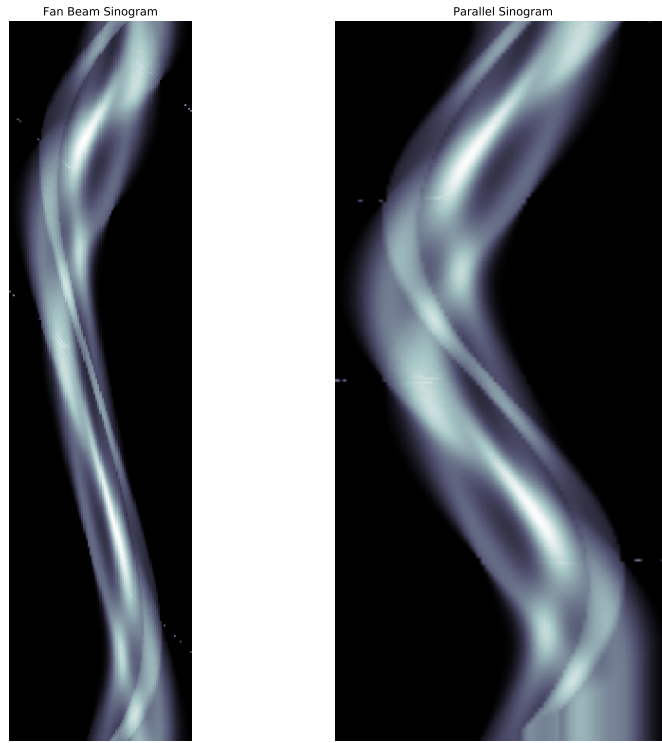


Figure 3.7: Sinogram examples: the new spectral phantom projection data at a projection interval of 1 degree. On the left, the projection data before resorting; on the right, the parallel projection data obtained after resorting the fan-beam line integrals.

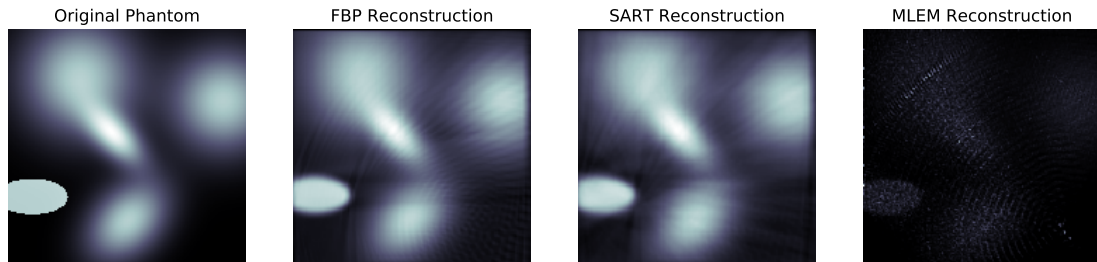


Figure 3.8: Tomographic reconstruction results, projection interval of 1 degree. From left to right: original phantom, FBP reconstruction, SART reconstruction, MLEM reconstruction

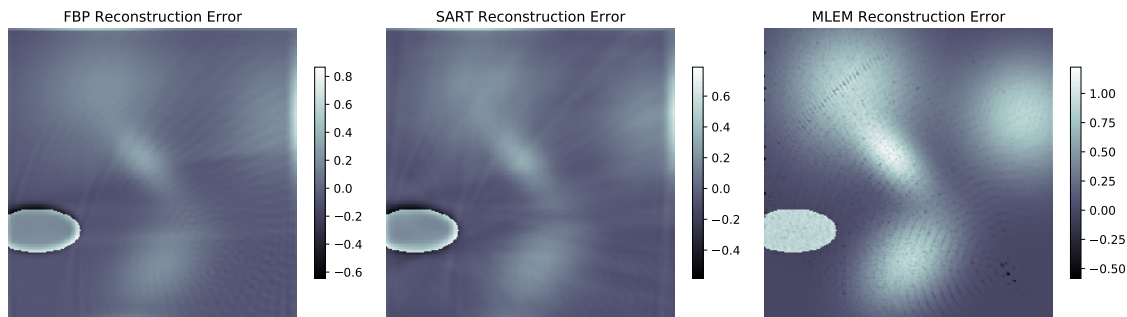


Figure 3.9: Tomographic reconstruction errors. Each one of these images was constructed by subtracting the respective reconstruction matrix, displayed in Figure 3.8, from the original phantom matrix. Error value is normalised to the pixel values, i.e., 32 bit floating point numbers with values between 0 and 1.



Figure 3.10: Reconstruction degradation: the projection interval was crucial for reconstruction. Note the image degradation going from a projection interval of 1 degree to 5 degrees (left to right). Images reconstructed using the FBP algorithm.

3.2 The Experiment

As stated in this chapter's introductory notes, this thesis main body of work revolves around two base assumptions, our hypothesis. The first one, about the information capturing by the idealised system, was addressed in Subsection 3.1.1. The second, more physical in nature, is the subject matter of this section. Our hypothesis states that the light absorption between points A and B (let's call it A_{AB}) should be equal to the difference of the absorptions in A and B . We can write this, in a *Lambertian* manner as in Equation 3.14.

$$I_B = I_A \cdot \exp \left[-AB \cdot \sum_i \sigma_{ABi} \cdot c_{ABi} \right] \quad (3.14)$$

This is to say that the light intensity reaching point B is given by the intensity reaching A , exponentially decreased by the absorbers at interval AB . The intensities at A and B are written as in Equation 3.15.

$$\begin{aligned} I_B &= I_0 \cdot \exp \left[-L_B \cdot \sum_i \sigma_{Bi} \cdot c_{Bi} \right] \\ I_A &= I_0 \cdot \exp \left[-L_A \cdot \sum_i \sigma_{Ai} \cdot c_{Ai} \right] \end{aligned} \quad (3.15)$$

If we join all this information in the same expression, the equation is transformed into its final form, presented in Equation 3.16.

$$I_0 \cdot \exp \left[-L_B \cdot \sum_i \sigma_{Bi} \cdot c_{Bi} \right] = I_0 \cdot \exp \left[-L_A \cdot \sum_i \sigma_{Ai} \cdot c_{Ai} \right] \cdot \left[-AB \cdot \sum_i \sigma_{ABi} \cdot c_{ABi} \right] \quad (3.16)$$

Equation 3.16 can be greatly simplified: we take the natural logarithm of both sides and we state that $\sum_i \sigma_{Xi} \cdot c_{Xi} = S_i$. These operations result in the simplified form of Equation 3.17.

$$L_B \cdot S_B = L_A \cdot S_A + L_{AB} \cdot S_{AB} \quad (3.17)$$

Now, $L_X \cdot S_X$ can be thought of as the wavelength dependent light absorption in path X . In this case, the wavelength interval is always the same. We can therefore conclude that, theoretically, our hypothesis is valid: light absorption between points A and B can be expressed in terms of the absorption on both these points and corresponds to their difference.

Although mathematically this seems clear-cut, in the real world things can become more problematic, since we have to deal with the imperfections that characterise a real physical system. Noise, instrumental limitations, adverse environmental effects, etc.. The experiment we describe in the next few paragraphs aimed at determining target trace gas concentration in a set analysis field. This field is dimension-wise compatible with those that would be employed in the final working system. This experiment is represented in Figure 3.11.

The goal of the experiment was to compare passive and active DOAS measurements performed with a very short time difference between them. The passive measurement

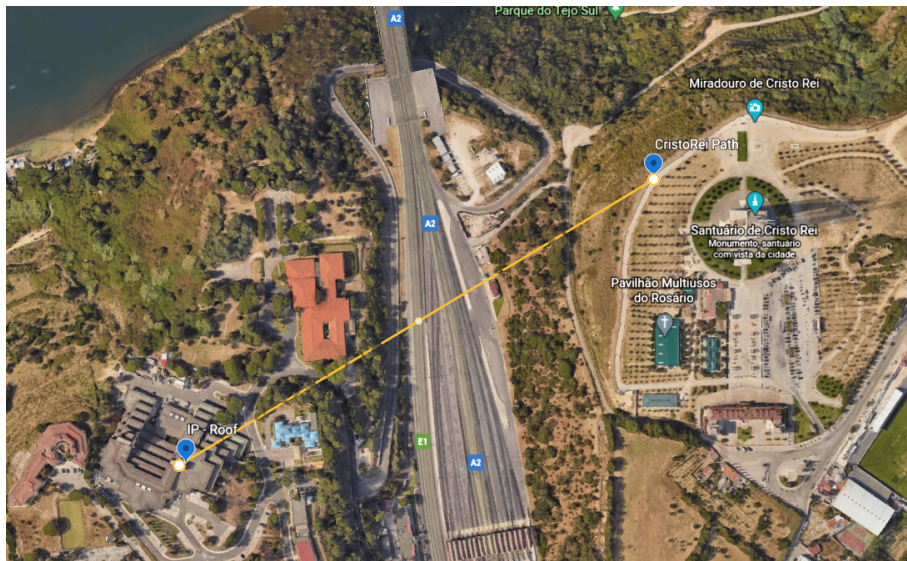


Figure 3.11: Location of observer points for the physical experiment.

would employ the same acquisition strategy as the drone is expected to use. This comparison will be used to test our second hypothesis.

Finding two appropriate experiment sites proved to be the first difficulty: both telescopes should see sky on the back of the other telescope. Otherwise, the contribution from the terrain's reflection would have to be taken into account and the experiment conditions would be very different from the ones the drone will have. There are not many site pairs that provide this, and most of the ones that exist are private and authorisations are not easy to obtain. In the end, we managed to run the experiment in the facilities of *InfraEstruturas de Portugal (IEP)* and the *Cristo-Rei* sanctuary, near our own base.

3.2.1 Protocol and conduction

The experiment involved two different optical assemblies, which are summarised in Table 3.3. Both assemblies play two roles, which reflect the comparison between active and passive that is the entire aim of the test. To simplify, we will address the two as West Bank and East Bank. The West Bank is, as the name implies, the assembly that is placed further West, i.e., the one that is installed on IEP's roof. By exclusion, the East Bank assembly is the one placed on the sanctuary. The West Bank assembly is comprised of a telescope and tripod, a spectrometer (with the necessary fibre optics attached) and a laptop.

The East Bank assembly has exactly the same parts, but in addition to them, it features a hand-held torch that sports an XHP50.2 CREE LED. The manufacturer states that this torch is capable of illuminating by itself up to a distance of 300 m and produces luminous flux of at least 1500 lm. By fitting this torch on the telescope's eyepiece channel, we are able to further collimate the light that it produces, making it reach much further distances than originally stated, and being easily picked up by the other telescope. This is plain to see in Figure 3.14. The light spectrum that pertains to the CREE LED in use is published in this device's datasheet, and presented in

CHAPTER 3. METHODS

Figure 3.12, which largely corroborates the spectrum in Figure 3.13, taken by the same spectrometers that were used in the experiment, at a distance of approximately 50 m from the torchlight.

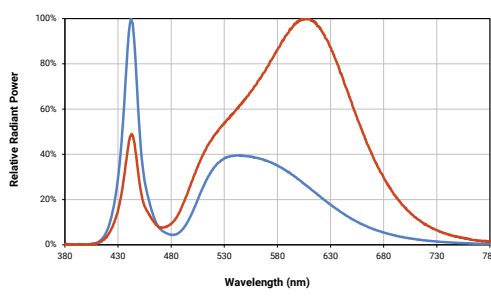


Figure 3.12: Published spectrum of the CREE XHP50.2 LED light. The LED that was used in this experiment corresponds to the blue line [21].

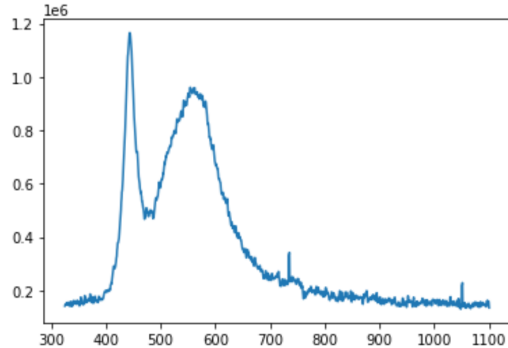


Figure 3.13: Spectrum measured with the experiment spectrometers, at a distance of approximately 50 m from the torchlight.

Table 3.3: Summary table for the two experiment assemblies. Note the difference in terms of material, due to the two different roles both assemblies play during the experiment. This is translated into not having the need of an artificial light source in the West Bank's assembly.

	West Bank	East Bank
Spectrometer	Avantes USB 2048 channels	Avantes USB 2048 channels
Telescope	Meade ET90	Meade ET90
Artificial Light Source	N/A	Goobay CREE XHP50.2 torch
Laptop	Windows 10 laptop	Windows 10 laptop
Software	AvaSoft 8.11	AvaSoft 8.11

The experiment itself is scheduled to start at around 06:00 A.M.. It consists in capturing spectral measurements in both modes (active and passive) periodically, with the least amount of time possible between measurements in the same capture. In this case, I am calling capture to a particular group of actions that are defined in Table 3.4. Captures are defined according to the time at which they are run, and are summarised in Table 3.5. Closing time for this experiment was set on 11:00 A.M.. This time window ensures measurements are taken during sunrise and until after the morning rush hour is over.

As displayed in Table 3.3, the spectrometers are both the same model, manufactured by Avantes and with 2048 channels, powered through the same [Universal Serial Bus \(USB\)](#) cable that is used for data transfer. The spectra are acquired through Avantes' own collection software, AvaSoft 8. The spectrometer are configured to have an integration time of 20ms and immediately store every measurement on an [American Standard Code for Information Interchange \(ASCII\)](#) file. With the kind of lighting conditions that we are dealing with, this integration time allows us not to worry about saturation. However, to build usable spectra we need to sum the collected files. This

Table 3.4: Actions are the indivisible unit upon which each capture is built. The prescribed actions for this experiment are described in this table.

Action ID	Action	Description
A	Active trace gas concentration determination	With the two telescopes facing each other, we collect spectra for two minutes with the light source turned off and another 2 min with the light source turned on.
B	Passive trace gas concentration determination	With the two telescopes aligned and approximately facing West, we collect spectra for 2 minutes.
C	Passive reference collection	The West telescope points upwards and collects data for 2 minutes.

Table 3.5: Captures are particular sets of actions that are conducted according to a specific order, depending on the time of day on which the capture is run. This table describes the prescribed captures on which this experiment consisted.

Time Frame	Period	Action
05:00 - Sunrise	15 minutes	A
Sunrise	Once	C
Sunrise - 11:00	15 minutes	A and B

is valid because given the very little time it takes to make a measurement (2 minutes), the sun can be considered a constant light source, and therefore we can consider the photons to have a Poissonian statistic distribution [31].

3.2.2 First Run

The first attempt at running this experiment took place on June 7th 2021. Weather conditions were optimal for this kind of measurement, with no wind, clear sky and very low optical density, as can be testified by Figure 3.14. The experiment started with a small delay, caused by a problem on the charger of the East bank laptop. Besides this delay, this was not a problem for the experiment itself. It was the other laptop's battery that did not hold enough charge for the experiment to reach its determined end, and there was no means to charge it on IEP's roof. Given this circumstance, we were able to retrieve spectral measurements from around 06:20 A.M. to 08:20 A.M., in a total of 6 measurements which are produced in Table 3.6.

On the one hand, it is clear from Table 3.6 that we do not have data on the active baseline spectra ³ (likely due to some operation error); on the other hand, we have too few data points to make any claim of validation or refutation of the principle we were to measure. It was thus clear that another run was necessary to get satisfactory results.

³In this case, the baseline spectrum is one taken in the exact same direction and approximately simultaneously, with the light turned off to allow removal of solar contribution.

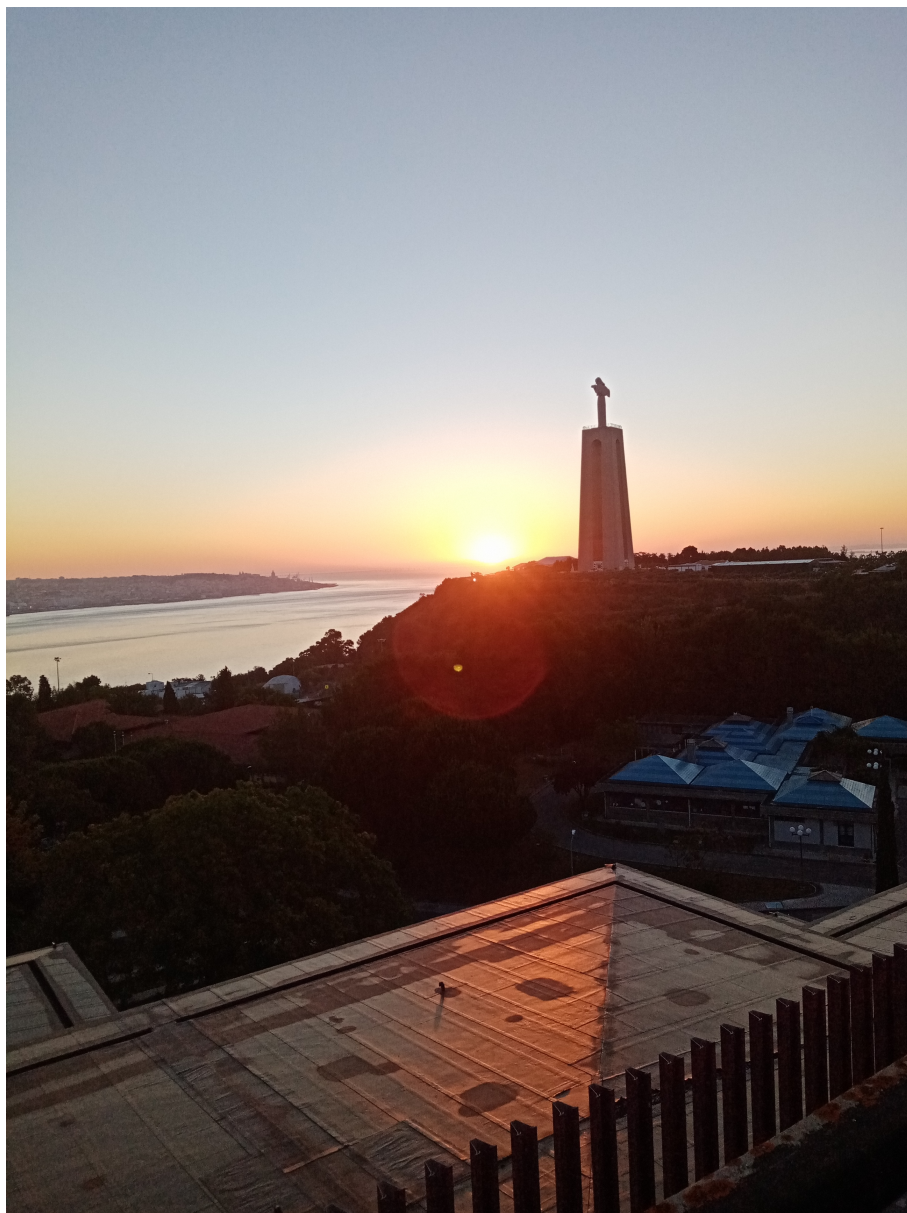


Figure 3.14: View from West Bank assembly at sunrise during the first run of the experiment. Note that even with the sun appearing in the back, the light from the torch is perfectly visible at this distance.

Table 3.6: First run: measurement table.

#	Passive meas.	Passive ref.	Active mean.	Active ref.
1	06:20	06:23	06:15	—
2	06:46	06:50	06:41	—
3	07:04	07:07	07:00	—
4	07:25	07:27	07:21	—
5	07:48	07:50	07:45	—
6	08:10	08:12	08:06	08:08

Although the collected data did not allow to make any claims whatsoever, they were of good individual quality and allowed for a partial analysis to be run, namely the passive DOAS side. Using the first measurement as the reference spectrum, it was possible to calculate the NO₂ concentration. The fits that generated these concentration values are presented in Figure 3.15 and Figure 3.16, respectively, for the West and East assemblies. The molecular density values for NO₂ are presented in Figure 3.17. The DOAS parameters for this run of the experiment are presented in Table 3.7

Table 3.7: Parameters for the DOAS measurements relative to the first run of the experiment.

Parameter	Value
Analysis Window	[430, 455] nm
Order of Filtering Polynomial	2
Spectral Resolution	2.4 nm

3.2.3 Second run

The second run of this experiment took place on the 23rd of June. The weather was not as perfect as it had been in the first day, with a few scattered clouds dotting the sky, and a lot more wind. These clouds were on a completely different azimuth than the field of study, so they had no influence whatsoever on the results. The exact spot of the experiment also changed slightly. On the first run, the East bank assembly was closer to the western limit of the sanctuary. This run was conducted putting the East bank assembly farther to the East. This change improved (but also made more difficult) the artificial light measurements, by providing a better background. It also improved operational conditions, decreasing human error probability. This position difference is illustrated in Figure 3.18.

Unlike the first run, the second run started without any logistic hiccup, on time, and we were able to continue measuring until 10:00. The total number of measurements reached 12. This was slightly under the 16 target measurements, but much better than what we had achieved in the previous day. Table 3.8 contains the time for each of the performed spectral collections.

Spectroscopically, the collected data were of good quality. Unfortunately, in terms of the experiment itself, some had to be discarded. This is chiefly true with regard to the artificial light portion of the experiment. With the change in position described in the previous paragraph, the light came to fill a much smaller visual slice than in the first run. This meant that it was much more difficult to pick up the torch with the telescope on the West bank. Although I have tried to align both telescopes in order to only capture the light that I was interested in, in more than one occasion, this alignment was (probably by the wind) destroyed. Since the light was so small in comparison with the field of vision, the final resulting spectrum is one of the background instead of the torch. In the end, only 8 measurements were viable. Analytical parameters are found in Table 3.9. Figure 3.19 and Figures 3.20 are plots of the measured concentration

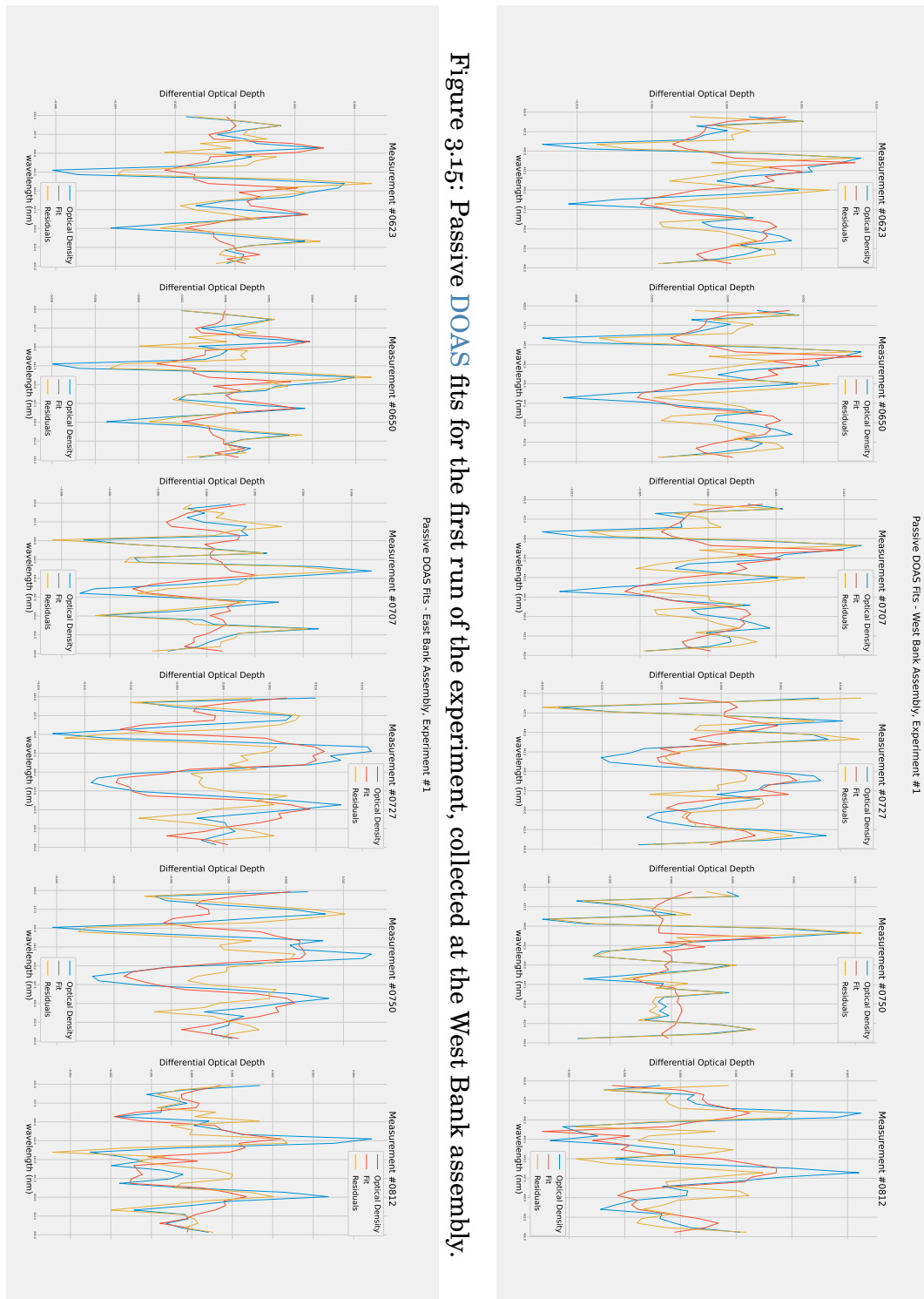


Figure 3.15: Passive DOAS fits for the first run of the experiment, collected at the West Bank assembly.

Figure 3.16: Passive DOAS fits for the first run of the experiment, collected at the East Bank assembly.

Passive DOAS - NO₂ Molecular Density

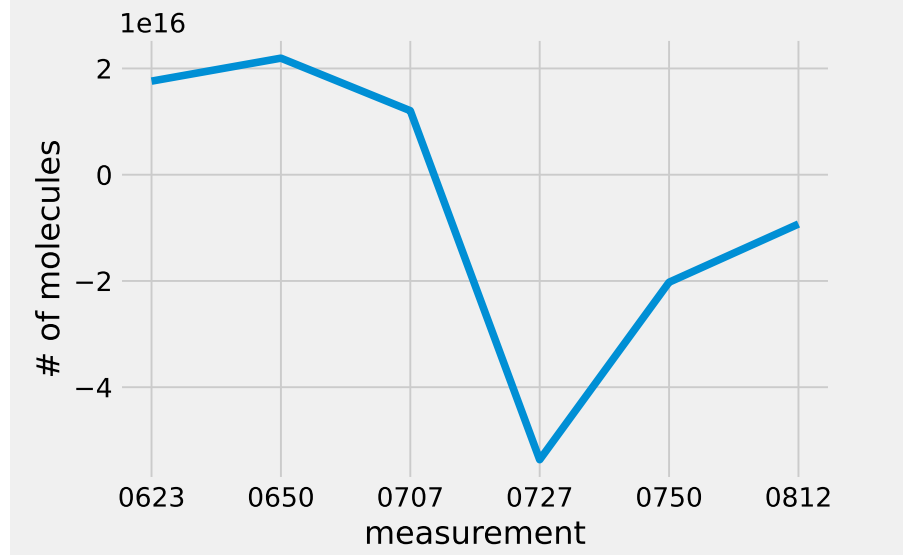


Figure 3.17: NO₂ density values, in number of molecules, for the first run of the experiment. Note that the calculated value is the subtraction between the density found for the East Bank and the density found at the West Bank.

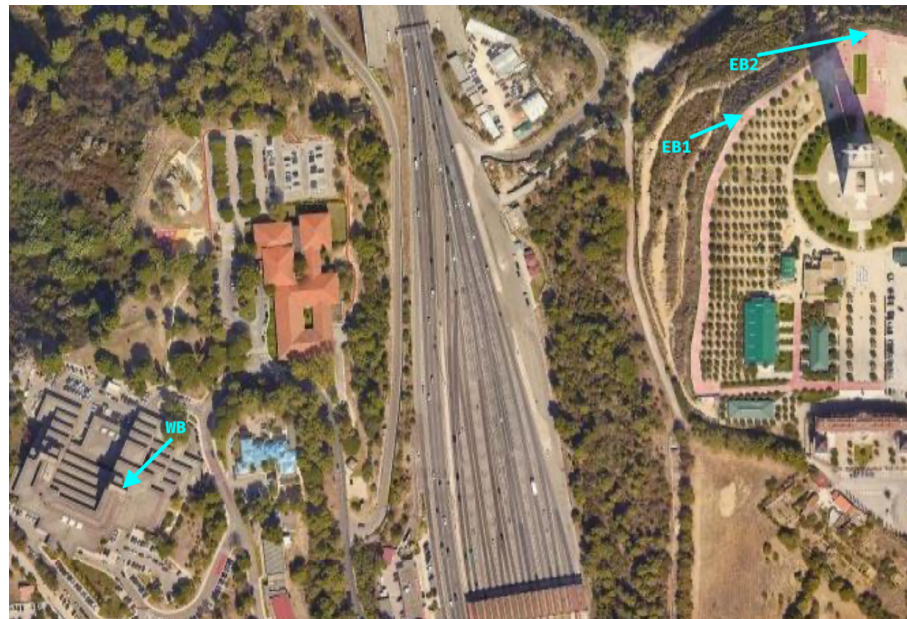


Figure 3.18: This image, built using Google Maps, illustrates the East Bank relocation that took place in the second leg of the experiment. The first location is presented as EB1, while the second is naturally EB2. The West Bank is also presented for some geographic reference, and identified by WB.

Table 3.8: Second run: time of measurements table.

#	Active DOAS	Active DOAS Reference	West Bank Passive DOAS	East Bank Passive DOAS	Comments
1	06:07	05:57	06:14	06:12	BAD
2	06:35	06:30	06:40	06:40	BAD
3	06:50		06:50	07:00	BAD
4	07:10	07:15	07:00	07:27	
5	07:50	07:40	07:10		
6	08:08	08:03	07:25	07:52	
7	08:18	08:21	07:53		
8	08:35	08:30	08:35	08:36	
9	09:00	08:53	09:02	09:00	
10	09:45	09:50	09:24	09:20	
11	10:00	10:05	09:53	09:48	

of NO_2 . Figures 3.21, Figure 3.22 and Figure 3.23 are the plots showing the actual DOAS fits.

Table 3.9: Parameters for the DOAS measurements relative to the second run of the experiment.

Parameter	Value
Analysis Window - Active Experiment	[400, 450] nm
Analysis Window - Passive Experiment	[430, 455] nm
Order of Filtering Polynomial	2
Spectral Resolution	2.4 nm

3.2.4 Data Processing

While the rest of this section is dedicated to the gathering of spectral data and even the results that it returns, it is important to mention and to provide a (brief, high level) description of what is being done to said data.

AvaSoft, Avantes' spectrometer handling software application, allows one to store collected data in several formats. Most of these formats are binary in nature. These are more compact in terms of occupied disk space and are commonly used in this kind of application because spectra are most likely being collected for later processing through another computer program. However, they are not good if one needs to quickly check if the data are being correctly gathered or to see if there was any kind of operation error in the collection process, since they are completely unintelligible for humans. For this purpose, Avantes make the Avantes ASCII file format available. This is, as its name might imply, an ASCII formatted file that can be quickly inspected by anyone that can read the English language and understand the Latin characters. The files have a particular structure which is illustrated by Figure 3.24.

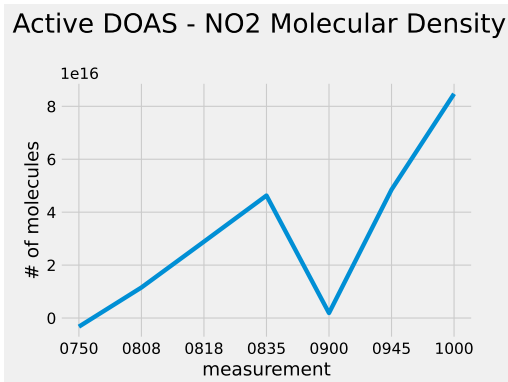


Figure 3.19: Active DOAS molecular density for NO_2 , varying with the measurement number.

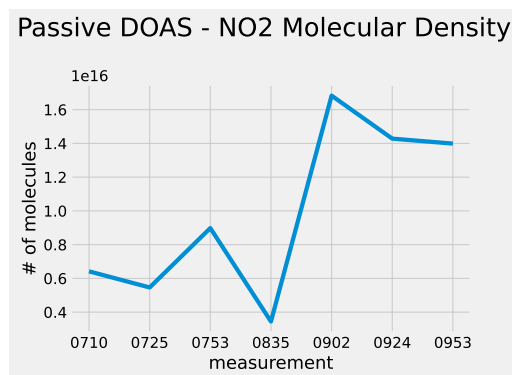


Figure 3.20: Passive DOAS molecular density for NO_2 , varying with the measurement number. Note that this is the difference between the density obtained at the two experiment assemblies, as per hypothesis 2 (see 4.2).

Some light string parsing operations are the compromise that is required to use this kind of file format in analytical software. In the case of this thesis' application, the files are opened and parsed using an OOP approach that takes advantage of the organisational structure of the several files involved in the process. Each file originates an AvantesASCII object, which loads the data, parses its values and stores them in a Pandas DataFrame internal object ⁴. For each folder that contains this kind of file, the parsing library creates an AvantesASCIIFolder object, which loads all files inside that folder and runs global data operations such as summation and integration-time-normalisation. A general schematic of this approach is provided in Figure 3.25, while a flowchart for the file loading routine is presented in Figure 3.26 and the folder loading process is illustrated by Figure 3.27.

3.2.5 The DOAS Library

The DOAS software library is a Python package developed specifically for this thesis data processing operations. It was, as other components, designed using an OOP approach and following the SOLID principles of Object Oriented Programming. This piece of software was written in response to the initial research that I undertook and that returned no usable results in terms of modular, compact Python libraries for DOAS applications, that I could use in my work. It is, as far as I know, the only DOAS solving application with this kind of structure.

The library (Unified Modelling Language (UML)) diagram presented in Figure 3.28) models a DOAS application through the instrumentation lens. A DOAS application is always parametrised through its spectrometer's physical features and limitations, which in turn determine the structure of the analysed spectral data, and even the differential cross sections of the trace gases that are to be studied. Of course, this library is much more limited in its capabilities than some specific programs that have

⁴Pandas is a data processing library used in Python that provides a very efficient way to access and manipulate tabular data by leveraging the use of C code through Python commands.

CHAPTER 3. METHODS

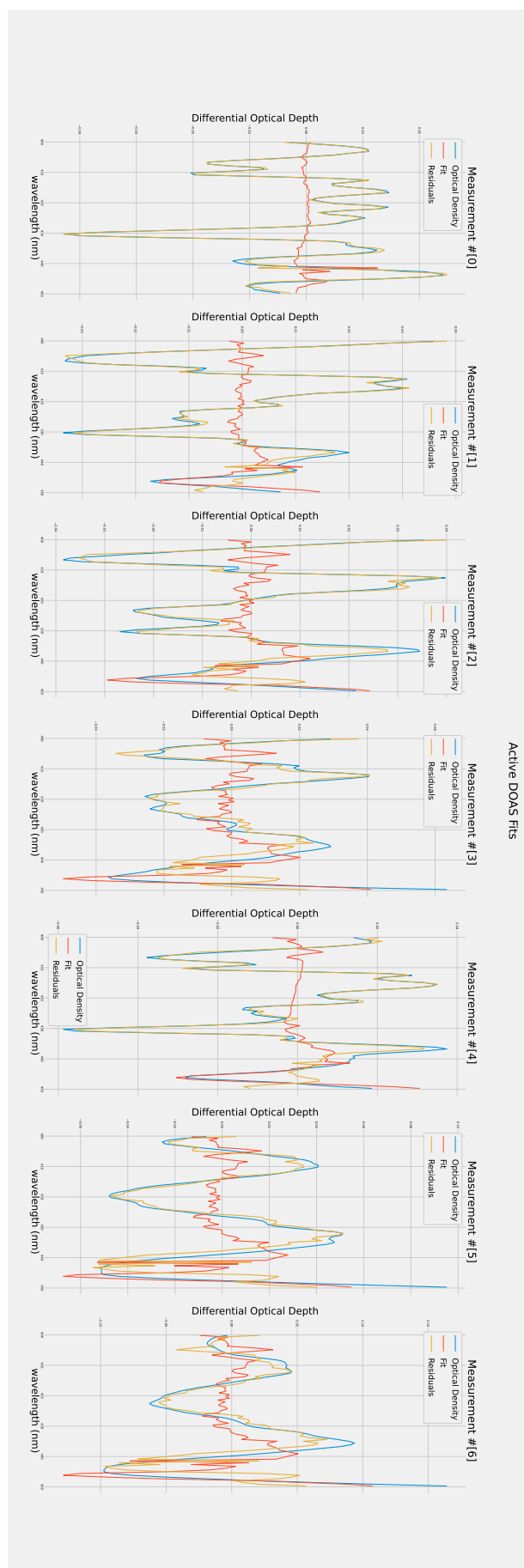


Figure 3-21: Active DOAS fit results. Each plot corresponds to one measurement moment.

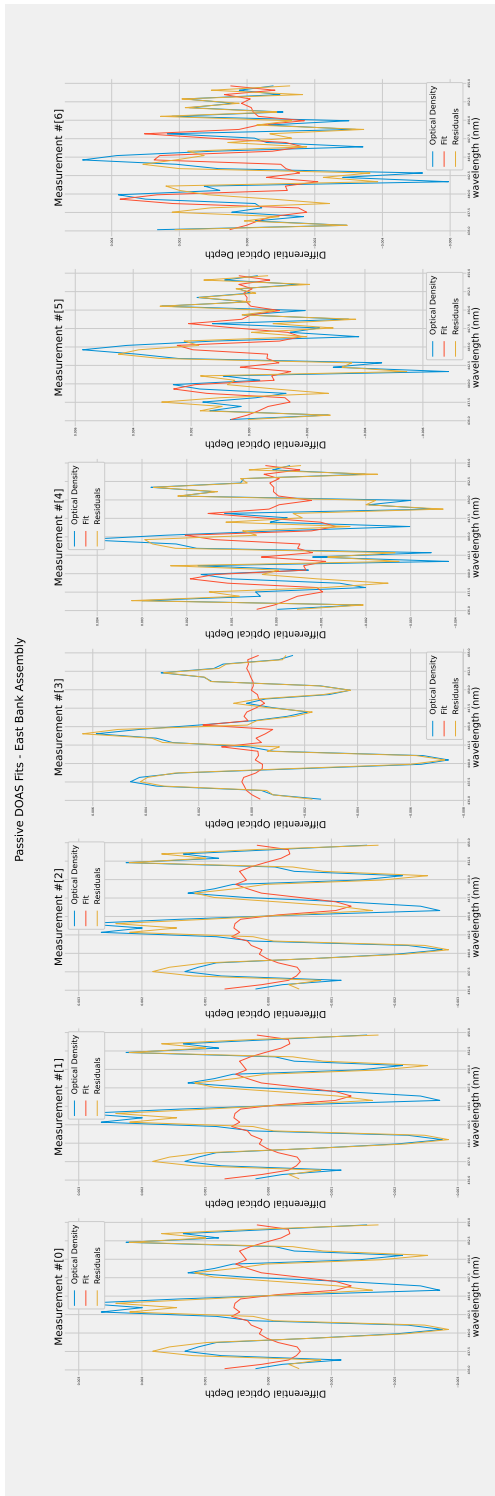


Figure 3.22: Passive DOAS fit results, from the system on the East Bank. Each plot corresponds to one measurement moment.

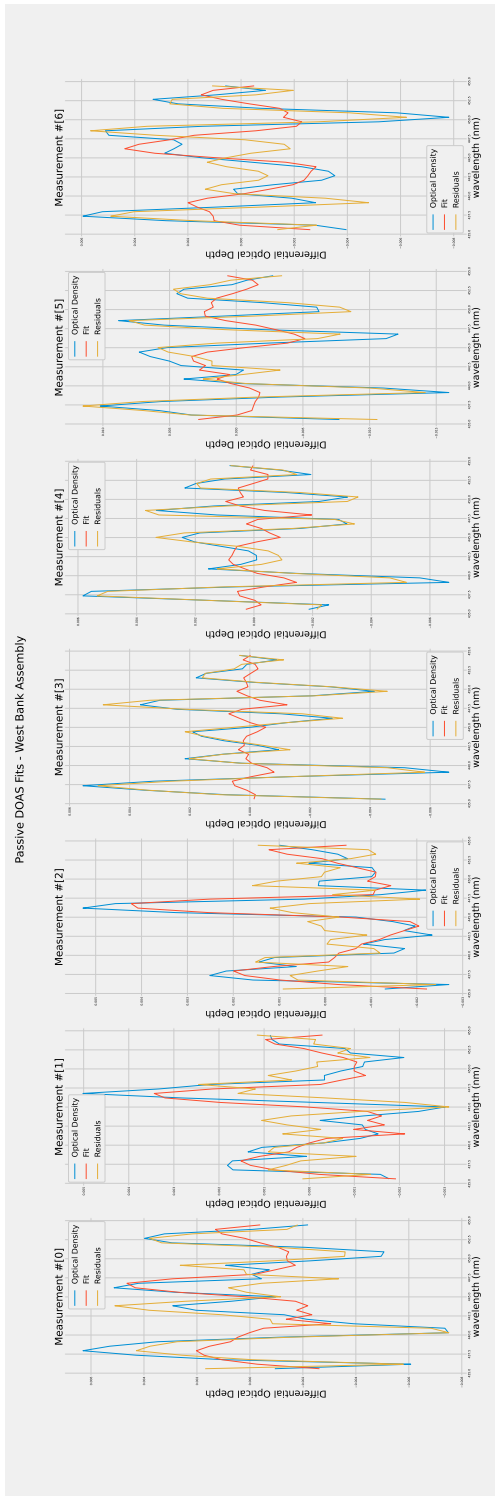
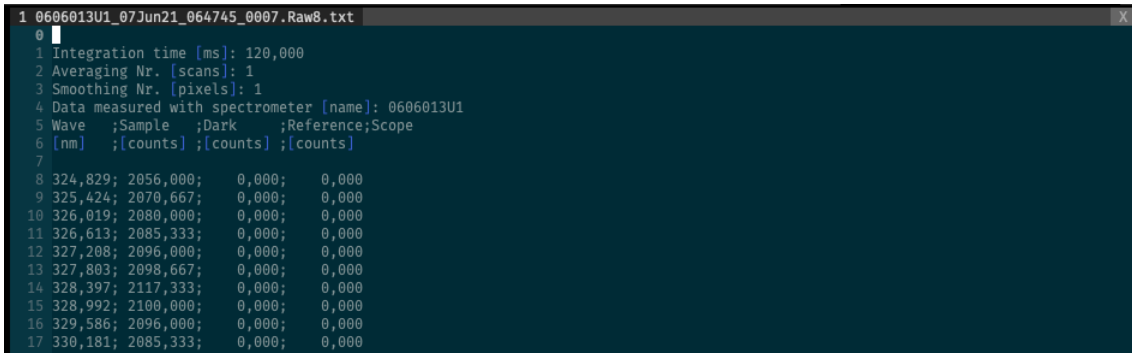


Figure 3.23: Passive DOAS fit results, from the system on the West Bank. Each plot corresponds to one measurement moment.

CHAPTER 3. METHODS



```
1 0606013U1_07Jun21_064745_0007.Raw8.txt
0
1 Integration time [ms]: 120,000
2 Averaging Nr. [scans]: 1
3 Smoothing Nr. [pixels]: 1
4 Data measured with spectrometer [name]: 0606013U1
5 Wave ;Sample ;Dark ;Reference;Scope
6 [nm] ;[counts] ;[counts] ;[counts]
7
8 324,829; 2056,000; 0,000; 0,000
9 325,424; 2070,667; 0,000; 0,000
10 326,019; 2080,000; 0,000; 0,000
11 326,613; 2085,333; 0,000; 0,000
12 327,208; 2096,000; 0,000; 0,000
13 327,803; 2098,667; 0,000; 0,000
14 328,397; 2117,333; 0,000; 0,000
15 328,992; 2100,000; 0,000; 0,000
16 329,586; 2096,000; 0,000; 0,000
17 330,181; 2085,333; 0,000; 0,000
```

Figure 3.24: The Avantes ASCII file format. This is a screenshot of a file of this type opened in the VIM text editor. Note its particular structure, around which the file / folder parsing objects described by Figure 3.26 and Figure 3.27 are constructed.

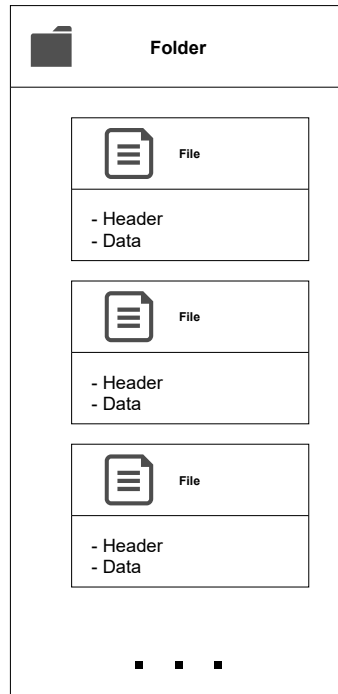


Figure 3.25: The Data processing. The **OOP** approach that was taken attempts to take advantage of the organisational structure of the spectral data, by modelling it into Python objects.

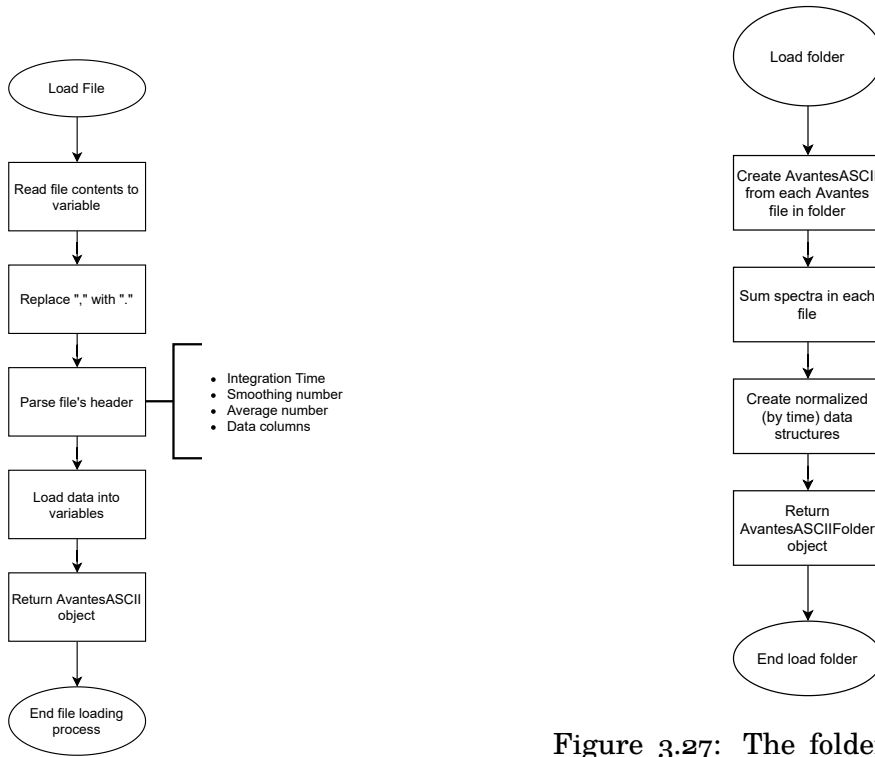


Figure 3.26: The file loading process. An Avantes ASCII file originates an AvantesASCII object, which besides a series of string-parsing operations stores the data in a Pandas DataFrame, for easy access and control.

Figure 3.27: The folder loading process. Each folder can have many files. The way in which the data is gathered (described in Subsection 3.2.2) requires some global operations performed on groups of files, like summation and normalisation (with reference to the integration time). The AvantesASCIIFolder object provides such operations.

become commonplace in this kind of application, such as QDOAS [22], but the fact that it can be operated through a Python program and that one can manipulate the data through such tools as Pandas DataFrames more than make up for this lack. Moreover, since it is in effect a software library, it is also as flexible as one is willing to expand it.

An important side note that attests to this library’s relevance is that it has been fully integrated in FutureCompta’s Bee2Fire software, with further developments being conducted through this team’s efforts. This is the first commercially applicable result provided by the work in this thesis.

CHAPTER 3. METHODS

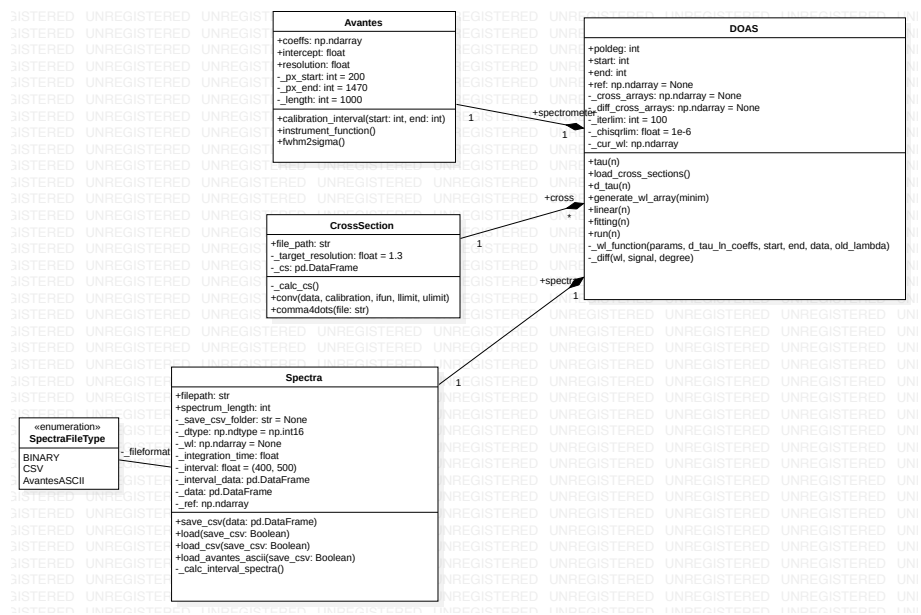


Figure 3.28: UML diagram for the DOAS library. The OOP approach that was followed allows for an instrument-oriented experiment parametrisation, which is not available in any other software

DISCUSSION

4.1 First Hypothesis

Results presented in Section 3.1 raise a series of pertinent observations that should be addressed in discussion. The first remark goes to the fact that the number of projections used seemed adequate to perform the tomographic reconstruction in adequate fashion, although there are tomographic applications with many more projections (orders of magnitude more projections). This was not an unexpected result, as there are already several examples of studies in which a considerably lower number of projections was used, still producing satisfactory results [69]. Moreover, and since the simulation software automatically includes errors in the calculations, this number also proves that geometric error plays a very limited role in changing the result of the reconstruction due to the difference in size between the drone's trajectory and the geometric error, this was also a predicted result.

Even with the relatively low number of projections produced by the drone's trajectory and measurement strategy, all reconstruction algorithms were able to produce a reconstructed image that resembled the phantom that generated it. Δ , the angular interval between projections, revealed itself to be crucial. This was expected as the number of captured projections is obtained by dividing 360 by Δ . This is, also as expected, confirmed by the upward trend of the error when increasing the value of the angular projection interval, as can be seen numerically in Table 3.2 and qualitatively in Figure 3.10. With respect to the algorithms used, the custom-made MLEM routine produces clearly outlier results, which are not on par with the other two reconstruction methods used. This is plain to see both in Figure 3.8 and in Table 3.2, in which this algorithm's NRMSE is almost four times the second best result (FBP) for the smallest projection interval. This difference could to some extent be expected. SART and FBP algorithms were implemented using some of the most relevant and consistently used Python libraries (SciPy, for instance [88]). Given the amount of attention these libraries get from the scientific programming community, levels of optimisation are extremely high. Although it is nowhere near the other two approaches, the MLEM routine is still useful, as it is the only truly geometry-independent algorithm in this study (SART is also geometry independent, but this particular implementation expects a parallel projection sinogram as input).

As stated in Section 3.1.3, three different kinds of error influence the reconstruction

results: geometric, spectroscopic and reconstruction errors. The first kind of error is directly included in projection calculations, through the application of a Monte Carlo-like method to the geometry described in the same section. The second kind of uncertainty comes from the spectrum acquisition process itself, which is not perfect. If one considers there are no systematic errors present in the results, which is an acceptable premise in a simulation, then these errors can be simulated by the inclusion of Gaussian noise in the spectral measurements. This approach is based on the one used in [79], in which a Gaussian noise spectrum is added to the spectrum of interest in order to simulate how the error behaves with a degraded signal. Finally, reconstruction errors come from the finite precision of the calculations that render the images. These errors were presented in Subsection 3.1.4.

The three methods were also evaluated as to how they perform computationally, by measuring the time it took to produce the images in Figure 3.8 using a Paperspace P4000 cloud computing instance. In this regard, the fastest method was FBP, which took around 3 seconds to reconstruct. The second was MLEM, with around 50 seconds for 1000 iterations, and finally came SART, with 1 minute and 50 seconds for 1 iteration. One relevant observation comes from the fact that MLEM was significantly faster than SART, even taking into account the difference in optimisation, which was not an expected result and may indicate some reconstruction enhancing technique on SART's side, as the literature seems to indicate that this technique is faster than MLEM [25].

All things considered, the FBP algorithm produces a very good reconstruction, equivalent to SART's, while being more than 10 times faster, indicating that for this kind of application and with this kind of projection information, it is the best reconstruction algorithm.

4.2 Second Hypothesis

The proposed hypothesis was, as explained in Section 1.5, that one could obtain a trace gas' column density between two points by determining this value on both said points and then subtracting them one from another. Moreover, this was achievable with the kind of distances that the proposed monitoring system would be designed to use. To test this, I have setup an experiment comprising two spectroscopic assemblies. With them, I was able to test my approach against an active DOAS system. The expected results included similar levels of detected molecules for the passive and the active systems.

I defined the protocol and divided into measurements, which are comprised of sets of unitary actions. These actions included not only the measurements themselves, but also the collection of reference data for each measurement moment. In order to guide the conduction of the experiment, both on my behalf and on the volunteer's, a written protocol was created and made available to participants. This protocol constitutes an important part of Appendix D.

The experiment was conducted in two "runs". The first run took place on 07/06/2021. A slight logistics-related delay complicated matters. The first measurement was taken at 06:20, some minutes after sunrise. Although meteorological conditions were optimal and there were no hassles, work was interrupted at around 08:20, when the battery

of one of the laptops that were being used ran out. Although not enough to make claims, it was possible to produce some results from these data, namely concerning passive DOAS. These were presented in Figure 3.17 and their fits in Figure 3.16 and Figure 3.15.

The fits themselves show a lot of signal being measured, although NO_2 has less expression than O_4 in most of the measurements. For the reader's reference, a cross section of NO_2 and O_4 is included in Figure 4.2 and Figure 4.3, already cut to the analysis wavelength window. This weak fit expression coincides with the trends displayed on the NO_2 density plot.

QualAR, a Portuguese public initiative to monitor the territory's air quality, makes its data public and available for consultation at the initiative's website [3]. The QualAR chart for the concentration of NO_2 in the closest monitoring station to the experiment's site is presented in Figure 4.1. By comparing the chart's data and the experiment's data, one can see that they seem to approximately agree.

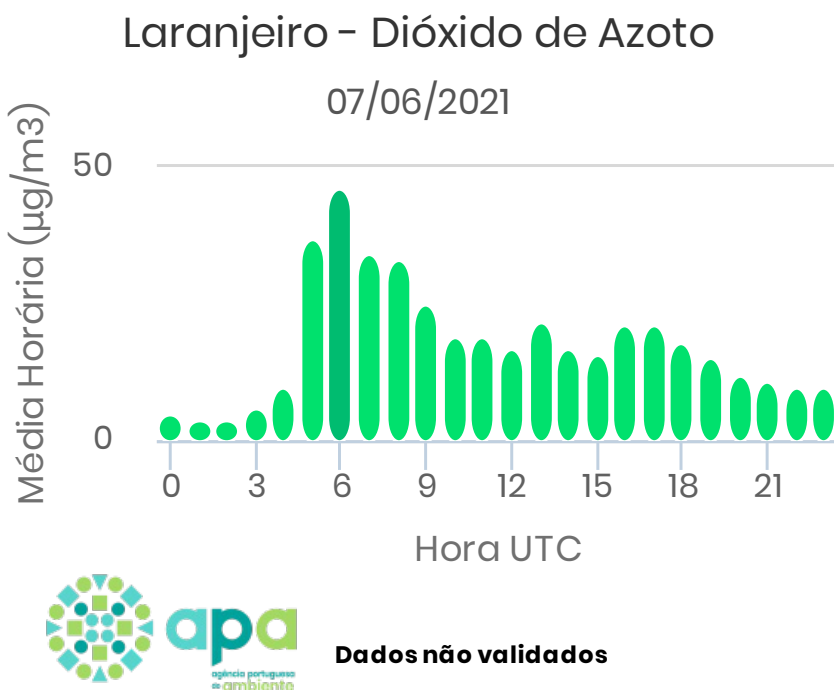


Figure 4.1: QualAR chart for the NO_2 concentration at the closest monitoring station from the experiment site [3]. 07 June 2021.

The second run of the experiment happened later in the same month, on the 23rd. The assembly on the East Bank was relocated around 100m, in an attempt to improve the spectral measurements. However, this introduced a new challenge. Since the assembly was positioned farther from the West Bank than in the previous run, the light source occupied a smaller fraction of the telescope's field of view. Moreover, in this day we had worse conditions than in the first day, with wind making the alignment of the two telescopes even more difficult. In the end, three out of the eleven possible measurements were discarded due to alignment issues. Coincidentally, the first three. A relocation schematic is included in Figure 3.18. There were no logistical problems

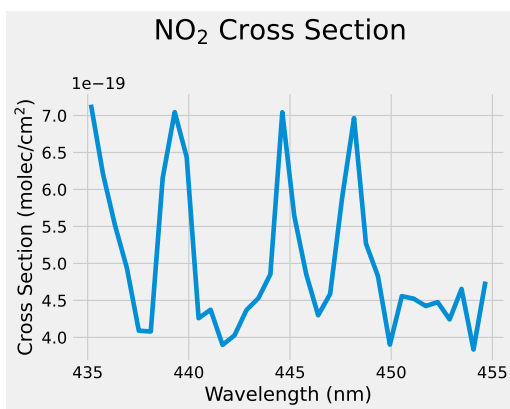


Figure 4.2: Cross section for NO_2 , cut to the analysis window described in Table 3.7.

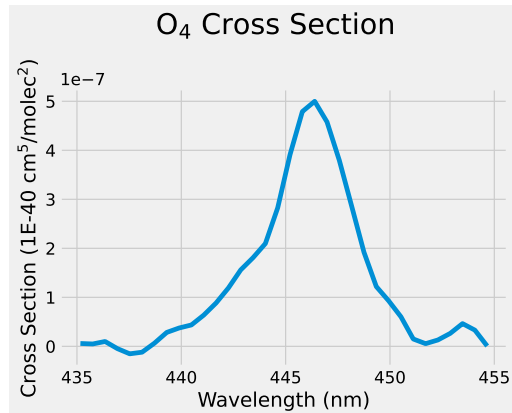


Figure 4.3: Cross section for O_4 , cut to the analysis window described in Table 3.7.

this time, and the use of external UPS ensured the laptops would have sufficient battery to run this experiment until 10:00, half an hour before the opening of the sanctuary for visitors.

Again we can analyse the data from two angles:

Internal analysis: did the experiment confirm or deny the hypothesis it was meant to test (see Section 4.2)?

External analysis: are the collected data comparable in any way with the official data coming from QualAR?

With regards to the first level of analysis, one might initially be tempted to consider the hypothesis validated if looking only at the shape of the two plots, Figure 3.19 and Figure 3.20. They are in fact quite similar in terms of trend, and they share the same order of magnitude in the scale, but the values displayed from one to another are quite different. Not so different as to making the hypothesis implausible, but unfortunately, not close enough to confirm it directly. As to the fit plots, Figure 3.21, Figure 3.22 and Figure 3.23, the fit line is much closer to the signal being fitted (differential optical density) in the passive experiment than in the active experiment. However, the values of the fit are one order of magnitude higher in the latter. In every fit, the line is clearly above noise level, which was one of the most important concerns in the beginning.

Regarding the second level of analysis, the official QualAR data are presented in the chart of Figure 4.4. Although this chart has a low resolution, it is safe to say that the peak value for NO_2 concentration was measured between 07:00 and 08:00. This contradicts the data collected in the second run of the experiment, which detected a growing trend for NO_2 at least until 10:00. These differences might be explained with some local effects due to the proximity of the highway (QualAR's measuring station is near, but in a completely different surrounding, in the middle of a primary school) or from some alignment-related instability.

Alignment issues are in fact the single most important threat for the validity of this experiment. As detailed in Section 3.2, the experiment was mainly a manual process, that relied in the sensibility of the two necessarily human operators to produce the

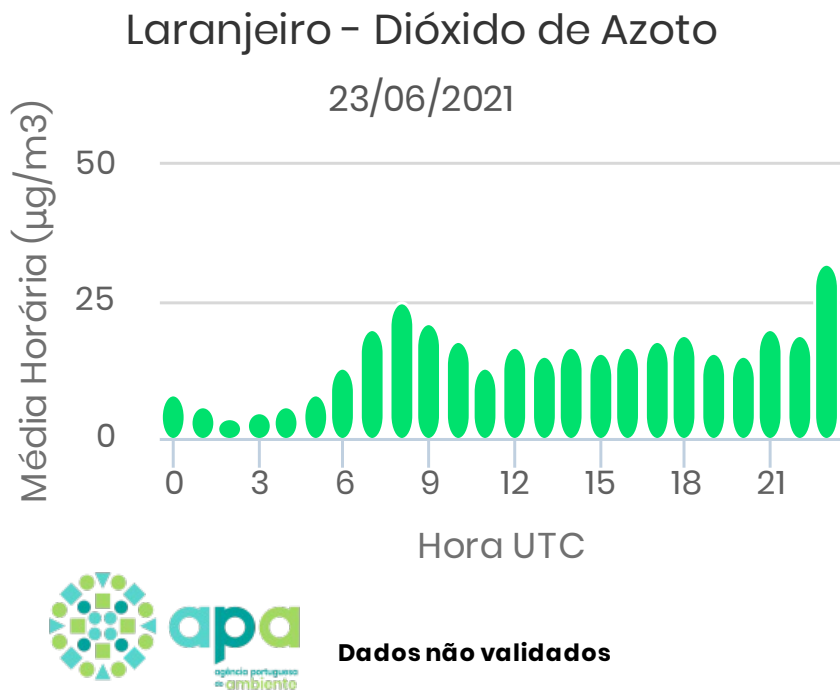


Figure 4.4: QualAR chart for the NO_2 concentration at the closest monitoring station from the experiment site [3]. 23 June 2021.

most correct data possible. Given the small size of the artificial light in the field of view of the telescope, and the presence of moderately strong winds, this experiment may have been too tall an order. It is impossible to reach a definite conclusion without the development of some kind of automatic alignment and measurement process, that mimics what would be performed by the autonomous UAV.

CONCLUSIONS

5.1 TomoSim

The initial goal of the TomoSim software project was to develop a simulation platform with which to recreate the tomographic reconstruction of the column density distribution for a number of target atmospheric trace gases.

The software program was written using the Python language and some numeric calculation libraries, such as NumPy and SciPy. Using these two libraries had two main effects: on the one hand, it enabled the programmers to easily create and manipulate matrices and vectors (images, for instance), and on the other, they greatly improved the running speed of the code, since their core is written in lower level languages (namely C).

The simulations that the software performs prove that, if the final device is programmed to comply to trajectory and acquisition requirements, reconstruction is perfectly achievable, even with relatively low projection numbers (comparing with medical imaging procedures). This brings another significant conclusion which is that the devised acquisition definitions, which produce a set of fan beam arrays, provide sufficient projection information to run the reconstruction and achieve plausible results.

TomoSim runs three algorithms on the projection data in order to produce the spectral mapping of the target pollutants: FBP (analytical), SART and MLEM (both algebraic). SART offered the best results, at the expense of time. The analytical algorithm produced very nearly the same results, but took a fraction of the time when comparing with either SART or MLEM. The MLEM algorithm cannot be directly compared to the SART algorithm, due to differences in the optimisation levels of both routines, but had nonetheless a reasonable time performance altogether, although producing the poorest reconstruction results.

Regarding future developments, there are three main avenues that should be explored:

Other phantoms: Presently, TomoSim only includes tomographic reconstruction for two different phantoms. While this is sufficient for simulation, it would be desirable to have some more phantoms, which could mimic other concentration distributions of interest.

Paradigm shift: This simulation software was developed under the passive DOAS

analysis model. Active measurements are much more versatile and accurate, and it would be interesting to develop this same technique using an artificial light source. Of course this would require many adaptations, namely regarding equipment and trajectory (probably even algorithms and interpolations).

Threedimensional reconstruction: TomoSim was developed to produce the reconstruction of a twodimensional image corresponding to the spatial distribution of an array of target trace gases. It would be much more interesting to have a threedimensional equivalent. As far as simulation goes, this is one of the most immediate developments for this project. On a more tangible level, the additional dimensional would make the problem much more complex, mainly because of trajectory and battery logistics.

5.2 Lambertian Absorption Experiment

The experiment described in Section 3.2 and discussed in Section 4.2 was designed to verify if one could, with currently commercially available equipment, perform DOAS measurements for small distances, as an autonomous UAV would perform. If this hypothesis was confirmed, the atmospheric monitoring system that I proposed in this thesis would be pretty much completed. Although this is not directly the case, I have reasons to be optimistic. Namely that the density values obtained for both the active and the passive DOAS measurements were in the same order of magnitude and displayed the same trends. One would not be realistic if expecting the measurements to be overlappable, and the fact that they seem to have similar behaviour is very positive. Moreover, I have identified an important imperfection in this experiment, which is the fact that the alignment can be very complicated to ensure in a less than perfect day. The two together make it impossible to produce definite conclusions without further study, namely with an automatically aligned system, but they also leave some good room to consider my hypothesis very plausible. This is highlighted even more when considering that the comparison with the official public data returns two very different results for the two runs of the experiment: on the first run (when the weather was perfect and there was no wind at all), my results are similar to the ones obtained from QualAR; on the second run (when the day was quite windy), they do not agree at all.

With regards to future developments for this side of the project, I think it is imperative to develop the necessary adaptations for this system to operate autonomously, so that we can solve the question of alignment once and for all.

5.3 Research Questions Summary

Table 5.1: Summary table for the research questions presented in Section 1.4.

Research Question	Status	Description
RQ 1.1	Partially Verified	The Lambertian hypothesis of Section 4.2 would allow for the coverage of the target geographical area with an autonomous UAV. This hypothesis was only partially verified and needs further studies with more sophisticated equipment.
RQ 1.2	Verified / Published	Described in Appendix C.
RQ 1.3	Verified / Published	By performing a series of spectroscopic measurements with a particularly defined trajectory, it will be possible to gather fanbeam projection data for the target geographical region.
RQ 1.4	Verified / Published	Described in Section 3.1

BIBLIOGRAPHY

- [1] 2 Degrees Institute. *CO₂ Levels*. 2020. URL: <https://www.co2levels.org/> (visited on 04/14/2020) (cit. on p. 22).
- [2] U. S. D. of Agriculture. *Early History of the NCRS*. 2012. URL: <https://www.nrcs.usda.gov/wps/portal/nrcs/detail/national/about/history/?cid=stelprdb1049437> (visited on 04/11/2020) (cit. on p. 19).
- [3] A. P. do Ambiente. *QualAR*. 2019. URL: <https://qualar.apambiente.pt/> (visited on) (cit. on pp. 79, 81).
- [4] M. N. Asl and A. Sadremomtaz. “Analytical image reconstruction methods in emission tomography”. In: *Journal of Biomedical Science and Engineering* 06.01 (2013), pp. 100–107. ISSN: 1937-6871. DOI: 10.4236/jbise.2013.61013. URL: <http://www.scirp.org/journal/doi.aspx?DOI=10.4236/jbise.2013.61013> (cit. on p. 42).
- [5] C. Beekman. “Differential Optical Absorption Spectroscopy of Trace Gas Species and Aerosols in the Upper Ohio River Valley”. PhD thesis. Ohio State University, 2010 (cit. on pp. 37, 38).
- [6] M. L. Bell, D. L. Davis, and T. Fletcher. “A retrospective assessment of mortality from the london smog episode of 1952: The role of influenza and pollution”. In: *Urban Ecology: An International Perspective on the Interaction Between Humans and Nature* 6.1 (2008), pp. 263–268. DOI: 10.1007/978-0-387-73412-5_15 (cit. on p. 10).
- [7] G. P. Bishop, J. L. E. Flack, and M. Campbell. *Sensor Systems for Environmental Monitoring, Volume 2*. 1996. ISBN: 9789401065337 (cit. on p. 27).
- [8] T. Bourdrel et al. “Cardiovascular effects of air pollution”. In: *Archives of Cardiovascular Diseases* 110.11 (Nov. 2017), pp. 634–642. ISSN: 18752136. DOI: 10.1016/j.acvd.2017.05.003. URL: <https://linkinghub.elsevier.com/retrieve/pii/S1875213617301304> (cit. on p. 14).
- [9] R. T. Brinkmann. “Rotational Raman scattering in planetary atmospheres”. In: *Astrophys J* 154 (1968), pp. 1087–1093. ISSN: 0004-637X. DOI: 10.1086/149827 (cit. on p. 30).
- [10] R. D. Brook. “Cardiovascular effects of air pollution”. In: *Clinical Science* 115.5-6 (2008), pp. 175–187. ISSN: 01435221. DOI: 10.1042/CS20070444 (cit. on p. 13).

BIBLIOGRAPHY

- [11] P. P. Bruyant. “Analytic and iterative reconstruction algorithms in SPECT.” In: *Journal of nuclear medicine : official publication, Society of Nuclear Medicine* 43.10 (2002), pp. 1343–58. ISSN: 0161-5505. URL: <http://jnm.snmjournals.org/cgi/content/abstract/43/10/1343%5Cnhttp://jnm.snmjournals.org/cgi/content/full/43/10/1343%5Cnhttp://www.ncbi.nlm.nih.gov/pubmed/12368373> (cit. on pp. 3, 40).
- [12] M. Buchwitz et al. “Global carbon monoxide as retrieved from SCIAMACHY by WFM-DOAS”. In: *Atmospheric Chemistry and Physics* 4.7 (Sept. 2004), pp. 1945–1960. ISSN: 16807316. DOI: [10.5194/acp-4-1945-2004](https://doi.org/10.5194/acp-4-1945-2004). URL: [www.atmos-chem-phys.org/acp/4/1945/](http://atmos-chem-phys.org/acp/4/1945/) (cit. on pp. 34, 35).
- [13] M. Buchwitz, V. V. Rozanov, and J. P. Burrows. “A near-infrared optimized DOAS method for the fast global retrieval of atmospheric CH₄, CO, CO₂, H₂O, and N₂O total column amounts from SCIAMACHY Envisat-1 nadir radiances”. In: *Journal of Geophysical Research: Atmospheres* 105.D12 (June 2000), pp. 15231–15245. ISSN: 01480227. DOI: [10.1029/2000JD900191](https://doi.org/10.1029/2000JD900191). URL: <http://doi.wiley.com/10.1029/2000JD900191> (cit. on pp. 34, 35).
- [14] R. L. Byer and L. A. Shepp. “Two-dimensional remote air-pollution monitoring via tomography”. In: *Optics Letters* 4.3 (Mar. 1979), p. 75. ISSN: 0146-9592. DOI: [10.1364/OL.4.000075](https://doi.org/10.1364/OL.4.000075). URL: <https://www.osapublishing.org/abstract.cfm?URI=ol-4-3-75> (cit. on pp. 5, 45).
- [15] CABI. *Air Pollution: Sources, Impacts and Controls*. Ed. by P. Saxena and V. Naik. 1st. Vol. 53. 9. Oxfordshire, UK: CAB International, 2019, pp. 1689–1699. ISBN: 9781786393890 (cit. on pp. 6, 13, 22–25).
- [16] L. Calderón-Garcidueñas et al. “Air pollution and detrimental effects on children’s brain. The need for a multidisciplinary approach to the issue complexity and challenges”. In: *Frontiers in Human Neuroscience* 8.AUG (2014), pp. 1–7. ISSN: 16625161. DOI: [10.3389/fnhum.2014.00613](https://doi.org/10.3389/fnhum.2014.00613) (cit. on p. 16).
- [17] N. Casaballe et al. “Comparison Between Regularized Optimization Algorithms for Tomographic Reconstruction of Plume Cross Sections in the Atmosphere”. In: *Earth and Space Science* 4.12 (Dec. 2017), pp. 723–736. ISSN: 23335084. DOI: [10.1002/2017EA000341](https://doi.org/10.1002/2017EA000341). URL: <http://doi.wiley.com/10.1002/2017EA000341> (cit. on p. 8).
- [18] CE Delft. *Health impacts and costs of diesel emissions in the EU*. Tech. rep. Delft: CE Delft, 2018, p. 72. URL: www.cedelft.eu (cit. on p. 3).
- [19] K. Chance and R. L. Kurucz. “An improved high-resolution solar reference spectrum for earth’s atmosphere measurements in the ultraviolet, visible, and near infrared”. In: *Journal of Quantitative Spectroscopy and Radiative Transfer* 111.9 (2010), pp. 1289–1295. ISSN: 00224073. DOI: [10.1016/j.jqsrt.2010.01.036](https://doi.org/10.1016/j.jqsrt.2010.01.036). URL: <http://dx.doi.org/10.1016/j.jqsrt.2010.01.036> (cit. on p. 39).
- [20] A. G. Clark. *Industrial Air Pollution Monitoring*. 1997. ISBN: 9789401071437. DOI: [10.1007/978-94-009-1435-3](https://doi.org/10.1007/978-94-009-1435-3) (cit. on pp. 27, 28).
- [21] Cree. *XLamp® XHP50.2 LEDs Datasheet*. 2021 (cit. on p. 64).

- [22] T. Danckaert et al. *QDOAS*. 2015. URL: <http://uv-vis.aeronomie.be/software/QDOAS/> (cit. on pp. 30, 37, 75).
- [23] L. De Chiffre et al. “Industrial applications of computed tomography”. In: *CIRP Annals - Manufacturing Technology* 63.2 (2014), pp. 655–677. ISSN: 17260604. DOI: [10.1016/j.cirp.2014.05.011](https://doi.org/10.1016/j.cirp.2014.05.011). URL: <http://dx.doi.org/10.1016/j.cirp.2014.05.011> (cit. on p. 3).
- [24] P. de Prado Bert et al. “The Effects of Air Pollution on the Brain: a Review of Studies Interfacing Environmental Epidemiology and Neuroimaging”. In: *Current environmental health reports* 5.3 (2018), pp. 351–364. ISSN: 21965412. DOI: [10.1007/s40572-018-0209-9](https://doi.org/10.1007/s40572-018-0209-9) (cit. on pp. 16, 17).
- [25] M. Defrise, P. E. Kinahan, and C. J. Michel. *Positron Emission Tomography*. Ed. by D. L. Baley et al. London: Springer London, 2005, pp. 63–91 (cit. on pp. 3, 40, 78).
- [26] L. A. Dewerd and M. Kissick. *The Phantoms of Medical and Health Physics*. Ed. by L. A. DeWerd and M. Kissick. Biological and Medical Physics, Biomedical Engineering. New York, NY: Springer New York, 2014, p. 286. ISBN: 978-1-4614-8303-8. DOI: [10.1007/978-1-4614-8304-5](https://doi.org/10.1007/978-1-4614-8304-5). URL: <http://www.springer.com/series/3740%20http://link.springer.com/10.1007/978-1-4614-8304-5> (cit. on p. 56).
- [27] EEA. *Air pollution in Europe 1990–2004*. Tech. rep. 2. 2007 (cit. on p. 11).
- [28] EEA. *Air quality in Europe*. Tech. rep. 28. 2016, p. 83. DOI: [10.2800/80982](https://doi.org/10.2800/80982) (cit. on pp. 11, 13).
- [29] EEA. *European Environmental Agency*. 2019. URL: <https://www.eea.europa.eu> (visited on 09/23/2019) (cit. on pp. 25, 26).
- [30] D. M. Etheridge et al. *Historical CO₂ record from the Law Dome DE08, DE08-2 and DSS ice cores*. Tech. rep. Aspendale, Victoria, Australia: Division of Atmospheric Research, CSIRO. URL: <http://cdiac.ornl.gov/ftp/trends/co2/lawdome.combined.dat> (cit. on p. 22).
- [31] M. Fox. *Quantum optics*. Oxford, UK: Oxford University Press, 2006. ISBN: 9780198566724 (cit. on p. 65).
- [32] P. Frank and M. A. Ottoboni. *The Dose Makes The Poison: A Plain Language Guide to Toxicology*. 3rd Editio. Hoboken, New Jersey: John Wiley & Sons, Inc, 2011. ISBN: 9780470381120 (cit. on p. 11).
- [33] E. Frins et al. “Tomographic multiaxis-differential optical absorption spectroscopy observations of Sun-illuminated targets: a technique providing well-defined absorption paths in the boundary layer.” In: *Appl. Opt.* 45.24 (2006), pp. 6227–6240. ISSN: 0003-6935. DOI: [10.1364/AO.45.006227](https://doi.org/10.1364/AO.45.006227) (cit. on pp. 6, 8, 33, 47, 48).
- [34] S. Genc et al. “The adverse effects of air pollution on the nervous system”. In: *Journal of Toxicology* 2012 (2012). ISSN: 16878191. DOI: [10.1155/2012/782462](https://doi.org/10.1155/2012/782462) (cit. on pp. 16, 17).

BIBLIOGRAPHY

- [35] F. C. Goldizen, P. D. Sly, and L. D. Knibbs. “Respiratory effects of air pollution on children”. In: *Pediatric pulmonology* 51.1 (2016), pp. 94–108. ISSN: 10990496. DOI: [10.1002/ppul.23262](https://doi.org/10.1002/ppul.23262) (cit. on p. 13).
- [36] J. F. GRAINGER and J. RING. “Anomalous Fraunhofer Line Profiles”. In: *Nature* 193.4817 (Feb. 1962), pp. 762–762. ISSN: 0028-0836. DOI: [10.1038/193762a0](https://doi.org/10.1038/193762a0). URL: <http://www.nature.com/doifinder/10.1038/193762a0> (cit. on p. 30).
- [37] C. Guerreiro, J. Soares, and A. G. Ortiz. *Air quality in Europe — 2019 report*. 5. Luxembourg: Publications Office of the European Union, 2019. ISBN: 9789294800886. DOI: [10.2800/822355](https://doi.org/10.2800/822355). URL: papers2://publication/uuid/1D25F41B-C673-4FDA-AB71-CC5A2AD97FDD (cit. on p. 3).
- [38] R. Gunderman. *Essential Radiology: Clinical Presentation, Pathophysiology, Imaging*, 2nd ed. 2nd ed. Thieme, 2006. ISBN: 9781588900821 (cit. on pp. 3, 39).
- [39] A. Hartl, B. C. Song, and I. Pundt. “Atmospheric Chemistry and Physics 2-D reconstruction of atmospheric concentration peaks from horizontal long path DOAS tomographic measurements: parametrisation and geometry within a discrete approach”. In: *Atmos. Chem. Phys* 6.3 (Mar. 2006), pp. 847–861. ISSN: 1680-7324. DOI: [10.5194/acpd-5-11781-2005](https://doi.org/10.5194/acpd-5-11781-2005). URL: <http://www.atmos-chem-phys.net/6/847/2006/> (cit. on p. 45).
- [40] A. Hartl et al. “2d tomographic reconstruction of trace gas distributions from long-path DOAS measurements: General approach, validation and outlook on an experiment on an urban site”. In: *Proceedings, 31st International Symposium on Remote Sensing of Environment, ISRSE 2005: Global Monitoring for Sustainability and Security* 2 (2005) (cit. on p. 45).
- [41] G. T. Herman. “Image Reconstruction From Projections”. In: *Real-Time Imaging* 1.1 (1995), pp. 3–18. ISSN: 10772014. DOI: [10.1006/rtim.1995.1002](https://doi.org/10.1006/rtim.1995.1002) (cit. on pp. 3, 40).
- [42] G. T. Herman. *Fundamentals of Computerized Tomography. Advances in Pattern Recognition*. London: Springer London, 2009. ISBN: 978-1-85233-617-2. DOI: [10.1007/978-1-84628-723-7](https://doi.org/10.1007/978-1-84628-723-7). URL: <http://link.springer.com/10.1007/978-1-84628-723-7> (cit. on pp. 3, 4, 40).
- [43] G. T. Herman, A. Lent, and S. W. Rowland. “ART: Mathematics and applications. A report on the mathematical foundations and on the applicability to real data of the algebraic reconstruction techniques”. In: *Journal of Theoretical Biology* 42.1 (1973). ISSN: 10958541. DOI: [10.1016/0022-5193\(73\)90145-8](https://doi.org/10.1016/0022-5193(73)90145-8) (cit. on pp. 3, 40, 43).
- [44] IEA. *Data & Statistics - International Energy Agency*. URL: [https://www.iea.org/data-and-statistics?country=World&fuel=Energy&20supply%5C&indicator=Total%20primary%20energy%20supply%20\(TPES\)%20by%20source](https://www.iea.org/data-and-statistics?country=World&fuel=Energy&20supply%5C&indicator=Total%20primary%20energy%20supply%20(TPES)%20by%20source) (visited on 04/17/2020) (cit. on p. 24).
- [45] International Agency for Research on Cancer. *Outdoor Air Pollution. IARC Monograph 109*. Vol. 109. 2016, p. 454. ISBN: 9789283201755 (cit. on p. 22).

- [46] M. Johansson et al. “Tomographic reconstruction of gas plumes using scanning DOAS”. In: *Bulletin of Volcanology* 71.10 (Dec. 2009), pp. 1169–1178. ISSN: 0258-8900. DOI: 10.1007/s00445-009-0292-8. URL: <http://link.springer.com/10.1007/s00445-009-0292-8> (cit. on pp. 8, 47).
- [47] A. Kak and M. Slaney. *Principles of Computerized Tomographic Imaging*. Society of Industrial and Applied Mathematics, 2001 (cit. on pp. 3, 4, 39, 40, 43, 44).
- [48] A. C. Kak and M. Slaney. *Principles of Computerized Tomographic Imaging*. 1. Society for Industrial and Applied Mathematics, Jan. 2001, pp. 49–112. ISBN: 978-0-89871-494-4. DOI: 10.1137/1.9780898719277. URL: <http://pubs.siam.org/doi/book/10.1137/1.9780898719277> (cit. on pp. 41, 44).
- [49] D. Kazantsev et al. “TomoPhantom, a software package to generate 2D–4D analytical phantoms for CT image reconstruction algorithm benchmarks”. In: *SoftwareX* 7 (Jan. 2018), pp. 150–155. ISSN: 2352-7110. DOI: 10.1016/J.SOFTX.2018.05.003. URL: <https://www.sciencedirect.com/science/article/pii/S2352711018300335?via%5C3Dihub> (cit. on p. 56).
- [50] B. Kitchenham and S. Charters. “Guidelines for performing Systematic Literature reviews in Software Engineering Version 2.3”. In: *Engineering* 45.4ve (2007), p. 1051. ISSN: 00010782. DOI: 10.1145/1134285.1134500. arXiv: 1304.1186. URL: <http://scholar.google.com/scholar?hl=en&btnG=Search%5C&q=intitle:Guidelines+for+performing+Systematic+Literature+Reviews+in+Software+Engineering#0%5C5Cnhttp://www.dur.ac.uk/ebse/resources/Systematic-reviews-5-8.pdf> (cit. on pp. 45, 46).
- [51] B. Kitchenham et al. “Systematic literature reviews in software engineering - A systematic literature review”. In: *Information and Software Technology* 51.1 (2009), pp. 7–15. ISSN: 09505849. DOI: 10.1016/j.infsof.2008.09.009. URL: <http://dx.doi.org/10.1016/j.infsof.2008.09.009> (cit. on p. 45).
- [52] T. Laepple et al. “Longpath DOAS tomography on a motorway exhaust gas plume: numerical studies and application to data from the BAB II campaign”. In: *Atmospheric Chemistry and Physics Discussions* 4.3 (May 2004), pp. 2435–2484. ISSN: 1680-7375. DOI: 10.5194/acpd-4-2435-2004. URL: www.atmos-chem-phys.org/acp/4/1323/%20http://www.atmos-chem-phys-discuss.net/4/2435/2004/ (cit. on pp. 6, 45).
- [53] LevelFiveSupplies. *LevelFiveSupplies*. 2021. (Visited on 06/21/2021) (cit. on p. 50).
- [54] S. Li et al. “Effect of ambient air pollution on premature SGA in Changzhou city, 2013-2016: A retrospective study”. In: *BMC Public Health* 19.1 (2019), pp. 1–10. ISSN: 14712458. DOI: 10.1186/s12889-019-7055-z (cit. on p. 14).
- [55] G. M. Lovett et al. “Effects of Air Pollution on Ecosystems and Biological Diversity in the Eastern United States”. In: *Annals of the New York Academy of Sciences* 1162.1 (Apr. 2009), pp. 99–135. ISSN: 00778923. DOI: 10.1111/j.1749-6632.2009.04153.x. URL: <http://doi.wiley.com/10.1111/j.1749-6632.2009.04153.x> (cit. on p. 18).

BIBLIOGRAPHY

- [56] A. Merlaud. "Development and use of compact instruments for tropospheric investigations based on optical spectroscopy from mobile platforms". PhD Thesis. Louvain: Faculté des Sciences - Université Catholique de Louvain, 2013. ISBN: 978-2-87558-128-0. URL: <http://books.google.com/books?hl=en&lr=%5C&id=inXVSyR82zwc%5C&oi=fnd%5C&pg=PR3%5C&dq=Development+and+use+of+compact+instruments+for+tropospheric+investigations+based+on+optical+spectroscopy+from+mobile+platforms+sciences%5C&ots=VdebeDBQMc%5C&sig=4G0eVEvthJXuqd8WI3IWjjVXuXc> (cit. on pp. 5, 29–31, 33, 36).
- [57] K. U. Mettendorf, A. Hartl, and I. Pundt. "An indoor test campaign of the tomography long path differential optical absorption spectroscopy technique". In: (2005). DOI: [10.1039/b511337g](https://doi.org/10.1039/b511337g) (cit. on p. 45).
- [58] J. G. Murphy, S. O'Driscoll, and N. J. Smith. "Multipath DOAS for tomographic measurements". In: *Opto-Ireland 2002: Optics and Photonics Technologies and Applications*. Ed. by T. J. Glynn. Vol. 4876. Mar. 2003, p. 875. DOI: [10.1117/12.463960](https://doi.org/10.1117/12.463960). URL: <http://proceedings.spiedigitallibrary.org/proceeding.aspx?doi=10.1117/12.463960> (cit. on p. 47).
- [59] G. E. Nilsson. *Respiratory Physiology of Vertebrates Life with and without oxygen*. Ed. by G. E. Nilsson. Oslo, Norway: Cambridge University Press, 2010. ISBN: 9780521878548 (cit. on pp. 11, 12).
- [60] S. O'Driscoll, J. G. Murphy, and N. J. Smith. "Computed tomography of air pollutants in street canyons". In: *Spie 4876* (2003), pp. 958–967. DOI: [10.1117/12.463985](https://doi.org/10.1117/12.463985) (cit. on p. 47).
- [61] S. O'Driscoll, J. G. Murphy, and N. J. Smith. "Computed tomography of air pollutants in street canyons". In: ed. by T. J. Glynn. Mar. 2003, p. 958. DOI: [10.1117/12.463985](https://doi.org/10.1117/12.463985). URL: <http://proceedings.spiedigitallibrary.org/proceeding.aspx?doi=10.1117/12.463985> (cit. on p. 47).
- [62] M. Office. *The Great Smog of 1952*. 2019. URL: <https://www.metoffice.gov.uk/weather/learn-about/weather/case-studies/great-smog> (visited on 09/23/2019) (cit. on p. 10).
- [63] D. Olsson, I. Mogren, and B. Forsberg. "Air pollution exposure in early pregnancy and adverse pregnancy outcomes: A register-based cohort study". In: *BMJ Open* 3.2 (2013), pp. 1–8. ISSN: 20446055. DOI: [10.1136/bmjopen-2012-001955](https://doi.org/10.1136/bmjopen-2012-001955) (cit. on p. 15).
- [64] Oxford Press. *Lexico English Dictionary*. 2020. URL: <https://www.lexico.com/> (visited on 02/27/2020) (cit. on p. 17).
- [65] D. Perner et al. "OH - Radicals in the lower troposphere". In: *Geophysical Research Letters* 3.8 (Aug. 1976), pp. 466–468. ISSN: 00948276. DOI: [10.1029/GL003i008p00466](https://doi.wiley.com/10.1029/GL003i008p00466). URL: <http://doi.wiley.com/10.1029/GL003i008p00466> (cit. on p. 5).
- [66] U. Platt and J. Stutz. *Differential Optical Absorption Spectroscopy - Principles and Applications*. Ed. by R. Guzzi et al. Heidelberg, Germany: Springer-Verlag Heidelberg Berlin, 2008. ISBN: 9783540211938 (cit. on pp. 5, 10, 11, 28, 29, 31–34, 45).

- [67] W. H. Press et al. *Numerical Recipes: The Art of Scientific Computing*. 3rd Editio. 2007. ISBN: 9788578110796. arXiv: [arXiv:1011.1669v3](https://arxiv.org/abs/1011.1669v3) (cit. on p. 31).
- [68] D. /. ProTeste. *Radão: perigo que se esconde no granito*. 2003. URL: <https://www.deco.proteste.pt/institucionalemedia/imprensa/comunicados/2003/radao-perigo-que-se-esconde-no-granito> (visited on 04/11/2020) (cit. on p. 21).
- [69] I. Pundt et al. “Mapping of tropospheric trace gas concentration distributions from ground and aircraft by DOAS-tomography (Tom-DOAS)”. In: () (cit. on pp. 5, 45, 77).
- [70] I. Pundt et al. “Measurements of trace gas distributions using Long-path DOAS-Tomography during the motorway campaign BAB II: Experimental setup and results for NO₂”. In: *Atmospheric Environment* 39.5 (2005), pp. 967–975. ISSN: 13522310. DOI: [10.1016/j.atmosenv.2004.07.035](https://doi.org/10.1016/j.atmosenv.2004.07.035) (cit. on pp. 45, 46).
- [71] I. Pundt. “DOAS tomography for the localisation and quantification of anthropogenic air pollution”. In: *Analytical and Bioanalytical Chemistry* 385.1 (Apr. 2006), pp. 18–21. ISSN: 1618-2642. DOI: [10.1007/s00216-005-0205-4](https://doi.org/10.1007/s00216-005-0205-4). URL: <http://link.springer.com/10.1007/s00216-005-0205-4> (cit. on p. 45).
- [72] J. Radon. “On the determination of functions from their integral values along certain manifolds”. In: *IEEE Transactions on Medical Imaging* 5.4 (Dec. 1986), pp. 170–176. ISSN: 0278-0062. DOI: [10.1109/TMI.1986.4307775](https://doi.org/10.1109/TMI.1986.4307775). URL: <http://ieeexplore.ieee.org/document/4307775/> (cit. on p. 39).
- [73] R. Reis. *The Dust Bowl*. 1st ed. New York, New York, USA: Chelsea House, 2008. ISBN: 978-0-7910-9737-3 (cit. on pp. 19, 21).
- [74] V. Rozanov et al. “Sciatran - a new radiative transfer model for geophysical applications in the 240–2400 NM spectral region: the pseudo-spherical version”. In: *Advances in Space Research* 29.11 (June 2002), pp. 1831–1835. ISSN: 02731177. DOI: [10.1016/S0273-1177\(02\)00095-9](https://doi.org/10.1016/S0273-1177(02)00095-9). URL: <https://linkinghub.elsevier.com/retrieve/pii/S0273117702000959> (cit. on p. 35).
- [75] L. A. Shepp and B. F. Logan. “The Fourier reconstruction of a head section”. In: *IEEE Transactions on Nuclear Science* 21.3 (June 1974), pp. 21–43. ISSN: 0018-9499. DOI: [10.1109/TNS.1974.6499235](https://doi.org/10.1109/TNS.1974.6499235). URL: <http://ieeexplore.ieee.org/document/6499235/> (cit. on p. 56).
- [76] R. L. Siddon. “Fast calculation of the exact radiological path for a three-dimensional CT array”. In: *Medical Physics* 12.2 (Mar. 1985), pp. 252–255. ISSN: 00942405. DOI: [10.1118/1.595715](https://doi.org/10.1118/1.595715). URL: <http://doi.wiley.com/10.1118/1.595715> (cit. on pp. 51, 52).
- [77] E. Souza, A. Moreira, and M. Goulão. “Deriving Architectural Models from Requirements Specifications: a Systematic Mapping Study”. In: *Information and Software Technology* (Jan. 2019). ISSN: 09505849. DOI: [10.1016/j.infsof.2019.01.004](https://doi.org/10.1016/j.infsof.2019.01.004). URL: <https://linkinghub.elsevier.com/retrieve/pii/S0950584919300035> (cit. on p. 45).

BIBLIOGRAPHY

- [78] C. Stachniss, C. Plagemann, and A. J. Lilienthal. “Learning gas distribution models using sparse Gaussian process mixtures”. In: *Autonomous Robots* 26.2-3 (Apr. 2009), pp. 187–202. ISSN: 0929-5593. DOI: 10.1007/s10514-009-9111-5. URL: <http://link.springer.com/10.1007/s10514-009-9111-5> (cit. on p. 56).
- [79] J. Stutz and U. Platt. “Numerical analysis and estimation of the statistical error of differential optical absorption spectroscopy measurements with least-squares methods”. In: *Applied Optics* 35.30 (1996), p. 6041. ISSN: 0003-6935. DOI: 10.1364/ao.35.006041 (cit. on pp. 58, 78).
- [80] J. Stutz et al. “A novel dual-LED based long-path DOAS instrument for the measurement of aromatic hydrocarbons”. In: *Atmospheric Environment* 147 (Dec. 2016), pp. 121–132. ISSN: 13522310. DOI: 10.1016/j.atmosenv.2016.09.054. URL: <http://linkinghub.elsevier.com/retrieve/pii/S1352231016307713> (cit. on pp. 6, 46, 47).
- [81] P. Tans et al. *Atmospheric CO₂ concentrations (ppm) derived from in situ air measurements at Mauna Loa Observatory, Hawaii*. Tech. rep. Mauna Loa, Hawaii, USA: NOAA/ESRL and Scripps Institution of Oceanography. URL: ftp://aftp.cmdl.noaa.gov/products/trends/co2/co2_annmean_mlo.txt (cit. on p. 22).
- [82] TSF and Lusa. *Erupção do Vulcão dos Capelinhos foi há 60 anos*. 2017. URL: <https://www.tsf.pt/sociedade/foi-ha-60-anos-a-erupcao-do-vulcao-dos-capelinhos-8798755.html> (visited on 04/11/2020) (cit. on pp. 19, 20).
- [83] UNICEF. “Levels & Trends in Child Mortality: Report 2013-Estimates developed by the UN Inter-agency Group for Child Mortality Estimation”. In: *Unicef/Who/Wb/Un* (2013), pp. 1–32. ISSN: 19326203. DOI: 10.1371/journal.pone.0144443 (cit. on p. 13).
- [84] R. Valente de Almeida and P. Vieira. “Forest Fire Finder – DOAS application to long-range forest fire detection”. In: *Atmospheric Measurement Techniques* 10.6 (June 2017), pp. 2299–2311. ISSN: 1867-8548. DOI: 10.5194/amt-10-2299-2017. URL: <https://www.atmos-meas-tech.net/10/2299/2017/> (cit. on pp. 2, 28, 31).
- [85] D. Vallero. *Fundamentals of air pollution*. 5th ed. Oxford, UK: Academic Press - Elsevier, 2014. ISBN: 9780124017337 (cit. on pp. 10–16, 18, 19, 21, 27).
- [86] P. Vieira and J. Matos. *System for Automatic Detection of Forest Fires Through Optical Spectroscopy*. 2008 (cit. on p. 2).
- [87] P. Vieira, J. Matos, and M. Mendes. *Sistema para a detecção automática de incêndios florestais por espectroscopia óptica*. 2007 (cit. on p. 2).
- [88] P. Virtanen et al. “SciPy 1.0: fundamental algorithms for scientific computing in Python”. In: *Nature Methods* 17.3 (Mar. 2020), pp. 261–272. ISSN: 1548-7091. DOI: 10.1038/s41592-019-0686-2. URL: <http://www.nature.com/articles/s41592-019-0686-2> (cit. on p. 77).
- [89] H. A. de Wit, J. P. Hettelingh, and H. Harmens. *ICP Waters Report 125/2015: trends in ecosystem and health responses to long-range transported atmospheric pollutants*. Tech. rep. 6946-2015. 2015 (cit. on p. 17).

BIBLIOGRAPHY

- [90] World Bank. *World Bank Datasets*. URL: data.worldbank.org (visited on 04/17/2020) (cit. on p. 24).
- [91] World Health Organization. *Radon and Health*. 2016. URL: <https://www.who.int/news-room/fact-sheets/detail/radon-and-health> (visited on 04/11/2020) (cit. on p. 21).
- [92] J.-M. Zhang and J. An. “Cytokines, Inflammation, and Pain”. In: *International Anesthesiology Clinics* 45.2 (2007), pp. 27–37. ISSN: 0020-5907. DOI: [10.1097/AIA.0b013e318034194e](https://doi.org/10.1097/AIA.0b013e318034194e). URL: <http://journals.lww.com/00004311-200704520-00004> (cit. on p. 17).

A

SYSTEMATIC REVIEW OF DOAS TOMOGRAPHY

Tomographic DOAS - a Systematic Mapping Study on its technological status

Rui Valente de Almeida^{a,c,*}, Ana Moreira^b, João Araújo^b, Vasco Amaral^b,
Pedro Vieira^a

^a*Physics Department, FCT NOVA, Campus da Caparica, 2829-416 Caparica*

^b*Computer Science Department, FCT NOVA, Campus da Caparica, 2829-416 Caparica*

^c*Compta, S.A.; Alameda Fernão Lopes, 12, 10th floor, 1495-190 Algés*

Abstract

In atmospheric chemistry and physics, DOAS is one of the most commonly used analytical techniques. The method allows the application of tomographic reconstruction procedures for 2D or 3D mapping of target trace gases' concentrations.

Tomographic DOAS applications have been documented for at least 20 years. The number of articles detailing its implementation, however, is low, and literature is sparse. This paper aims to catalogue publications on this subject, painting a quick picture of the field's technological landscape.

Our search has found that there is a great prevalence of active DOAS systems in Tomographic DOAS research activities, since we were unable to find a passive application. We can also infer that there is no current commercial application using this technology and while it is true that there are similarities between different groups' apparatus, there is still no uniform application.

Our initial search has rendered more than 700 articles. However, the application of our inclusion and exclusion criteria resulted in a final set of 8 papers detailing the tomographic equipment, reconstruction algorithm and software. From them, we were able to identify some common practices and possible research gaps.

Keywords: DOAS, Tomography, Systematic Mapping Study

*Corresponding Author

Email address: rf.almeida@campus.fct.unl.pt (Rui Valente de Almeida)

1. Introduction

Differential Optical Absorption Spectroscopy (DOAS) is one of the most prominent methods for analysing and quantifying atmospheric chemistry, namely in what concerns trace gas concentrations. The technique, developed during the 70s by Perner and Platt [20], was popularised in the following decades by its use in detecting Ozone, Nitrogen Oxydes and studies of cloud radiative transport. DOAS is a type of absorption spectroscopy, which uses a clever mathematical and physical observation to overcome the difficulties of spectral measurement in the open atmosphere.

Through the setting of very careful geometric considerations, it is possible to combine DOAS with tomographic reconstruction methods in order to assemble a map of the gaseous concentrations in a given geographic region. Tomography is the process of reconstructing an image through projections obtained by subjecting a given target (in our case, the atmosphere) to being traversed by any kind of penetrating or reflecting wave, which in our case is visible light.

With this study, we have intended to capture the current literary landscape surrounding the usage of tomographic DOAS, assessing this technique's technological status. For this purpose, we have employed a review methodology originary from Evidence Based Medicine. This method, which has migrated to engineering through Software Engineering, is called a Systematic Mapping Study (MS). It provides a framework that allows researchers to produce detailed and systematic search protocols, which are used to catalogue literature information and identify research gaps within a determined subject.

The search procedure that we have defined was carefully engineered to cover all tomographic DOAS research relevant to urban, rural or industrial environments. Through it, we were able to find several different applications, all pertaining to scientific research, which are similar regarding physical principle, but differ in equipment assembly, algorithms, software, and geometry.

The rest of this paper has the following structure: Section 2 presents the context within which this study was written; Section 3 describes how we have planned to perform the study and the methods we have used in doing it; Section 4 describes the application of the said methods in the pursuit of our goals and presents the results we have obtained, as well as our evaluation of our processes; Section 5 shows our conclusions and what we think might be retained from reading this paper.

2. Background

2.1. Differential Optical Absorption Spectroscopy

Absorption Spectroscopy is the term used to identify all techniques that use radiation absorption by matter to assess and quantify elements or molecules in a given spectroscopic sample. It had, and still has, a very important role in the study of the Earth's atmosphere [22].

It is, as many other spectroscopic techniques, based on Lambert-Beer's law, which states that 'in a medium of uniform transparency the light remaining in a collimated beam is an exponential function of the length of the path in the medium', as described originally by Pierre Bouguer in 1729, and can be written [22]:

$$I(\lambda) = I_0(\lambda) \cdot \exp[-L \cdot \sigma(\lambda) \cdot c] \quad (1)$$

In Equation 1, I is the light intensity as measured by the spectrometer, I_0 the original light intensity at the source, L is the optical path in which the sample is exposed to the light, σ is the optical cross section of the sampled element or molecule and c is the sample's concentration. λ is the radiation's wavelength.

Lambert-Beer's equation, while valid in a laboratory setting, is generally not enough to determine gaseous concentrations in an open atmosphere experiment. I_0 determination would require any absorbant from the medium, which is impossible. Besides, in this medium, there are many factors that influence measurements: Rayleigh's scattering, Mie's scattering, thermal variations, turbulence and instrumental transmissivities. All these play an important part in altering atmospheric light [22, 16].

Differential Optical Absorption Spectroscopy (DOAS) overcomes these difficulties by capitalising on cross section's differences between interfering phenomena (normally broad spectral features) and certain trace gases (usually narrow spectral structure). The mathematical formulations behind the technique are well beyond the scope of this article, but suffice it to say that the broad structures are removed through subtraction of a fitted low order polynomial, and a fitting algorithm (such as Levenberg-Marquardt) is used to retrieve concentrations. Detailed presentations of these procedures are presented in [22] and [16].

In [22], the authors split the DOAS method into two fundamental families: passive and active. The passive family is characterised by being designed to capture and analyse natural light, whether from the Sun, the Moon or any other celestial body. This kind of measurement has the advantage of being simple to assemble, but natural light usage implies an additional technical effort for the retrieval of atmospheric concentrations. Active DOAS

applications, on the other hand, use artificial light sources to make their measurements. This has been used extensively in the identification of several atmospheric components. Its concentration extraction procedure is simpler, at the expense of a more complex assembly.

DOAS has had a number of applications throughout the years. The technique was first applied in the 1970s. At that time, Perner used an active setup with a laser light source to identify the OH radical in the atmosphere [20]. More recently, researchers around the world have been employing broadband sources (such as Xenon lamps) to measure trace gases like Ozone, Nitrogen Dioxide or Sulphur Dioxide. Almost simultaneously, passive systems have been used to study stratospheric chemistry and radiative transport in clouds [22].

2.2. Multi-Axis DOAS

Multi-Axis DOAS (MAX-DOAS) is one of the more recent applications of the DOAS technique. It represents a significant progress regarding zenith scattered sunlight measurements, a well established atmospheric analysis technique. It performs a series of passive DOAS measurements in several telescope elevations (typically 4 to 10) [11], either in sequence or simultaneously.

MAX-DOAS stems from another set of techniques called *off-axis*, which in this case means that the telescope is pointed at another angle than the zenith. Off-axis DOAS was first employed in 1993 when Sanders et al. [25] used it to assess OCIO in Antarctica. During this experiment, the team concluded that the off-axis geometry greatly improves sensitivity for tropospheric species, but does not change the system's ability to quantify stratospheric absorbers.

By evaluating several directions, the technique allows researchers to measure not only stratospheric contributors, as zenith sky assemblies, but also to detect absorbers at ground level, as an active DOAS instrument would.

We mention MAX-DOAS in this paper because one could argue that these systems would be able to be adapted to perform tomographic measurements, if more than one system would analyse the same region from more than the same number of observation angles. MAX-DOAS tomography is a special case, and would probably deserve to be investigated fully. However, since this was not the object of our study, we chose not to specifically target this method in our search.

2.3. Imaging DOAS

Imaging DOAS combines spectral and spatial information by combining an imaging spectrometer with a scanning system. The resulting data clearly resembles that of a hyperspectrum ??.

The method, developed by Bobrowsky et al. [2], employs a 2D CCD detector. One dimension measures spectral information, while the other

contains spatial information for one direction. The other spatial direction is obtained by scanning the field of view with the pushbroom method.

DOAS is used to yield slant column density values for the absorbers for each pixel. The values are colour coded and produce an image describing the gas distribution.

Mention to this technique is included in this paper because it exists in order to produce a two-dimensional image from spectral information. This image, however, does not come from a tomographic reconstruction procedure, nor is spatial information recovered from projections, but instead comes directly from the acquisition method. Hence, we did not include articles on this method in this study.

2.4. Tomography

Tomography refers to the set of techniques that aim to produce a cross sectioning image from data collected by exposing a given target body to some kind of penetrating or reflecting wave from many different directions [9, 13].

The initial theories that gave rise to tomography were laid out by Johannes Radon in 1917, with a mathematical operation that would later be known as the Radon transform. This process maps a function f , defined in the plane, to the function Rf , comprised of the values of the line integrals of f , taken in θ directions. In practice, this formulation allows the reconstruction of an image by its projections, which are nothing more than line integrals [4].

Tomographic image reconstruction can be achieved by running one of several algorithms through a computer program. The presentation of these algorithms is completely beyond the scope of this article, but a good starting point for learning about these operations is *The Mathematics of Medical Imaging*, by Timothy Freeman [4]. It is in the scope of this article, however, to make a small introduction to a particular set of reconstruction methods. The reason for this being the prevalence of these methods in the field of DOAS tomography, which is the main subject of this study. These techniques are thus:

Algebraic Reconstruction Techniques (ART) Proposed in 1970 by Gordon and Herman [10], these techniques are based on successive approximations between the actual projection data and the sum of the reconstruction elements which represent it [5]. The process is conducted line by line, until a satisfactory convergence condition is met.

Simultaneous ART Simultaneous ART is very similar to the ART algorithm. The difference being that the iterative changes occur for all lines at the same time, instead of in only one.

Simultaneous Iterative Reconstruction Techniques (SIRT) The main difference between SIRT and SART is that in the former, cell changes are not reflected immediately after one calculation. Updates occur at the end of each iteration. At this point, the change for each cell is the average correction calculated for it taking all equations into account [12].

During the second half of the twentieth century, tomographic processes have had a revolutionary influence in many fields of study, but especially in medicine. Computational tomography scanners allow doctors to see their patients interior in a highly detailed and extremely safe fashion. At first, tomographic imaging was performed only with X-Rays. Their attenuation throughout the patient's body being used as a projection. Nowadays, there are much more methods of image retrieval, such as radioisotopes, ultrasound or particle annihilation [13, 4, 9].

Although it was the field of medicine was more influenced by tomographic procedures than any other, the applications of these methods are not restricted to it. One can find numerous industrial and research applications [1, 6, 3]. One of which is the application to atmospheric research, namely in conjunction with DOAS. In recent years, scientists have been working on tomographic methods for measuring atmospheric trace gas concentration values. The field is interesting because it allows for 2D or even 3D mapping of a given region, with respect to those trace gases. This article aims to make an assessment of the status of this tomographic application, by analysing current literature on the subject.

2.5. Mapping Study

A Systematic Mapping Study (MS) is a type of secondary study designed to determine the general features of the research landscape in the subject they are addressing [14, 21].

An MS is driven by broad (and often multiple) research questions and applies an also broad data extraction protocol. This is in line with the fact that this kind of study aims to summarise its findings, answering the research questions, and in-depth analysis is not required. It is common for an MS to be a precursor to a Systematic Literature Review (SLR), which is a much deeper kind of systematic study. Guidelines for performing studies of both kinds can be found in a report made by Kitchenham and Charters in 2007 [14]. In this document, the authors establish the 3 stages which all MS and SLR generally have:

Planning This stage includes all preliminary considerations regarding the MS or SLR in the making. All protocols, from search to evaluation, through data extraction, are devised;

Conduction During this staged, researchers apply what they have planned in the previous phase. Protocols are *actually* run, and data is synthesised;

Reporting In this phase, the team has to define their dissemination strategy, and implement it. It is in this stage that a final report is written and evaluated.

Although it is logical (and fundamentally correct) to assume that these steps are sequential, this may not be, and usually is not, accurate. Many of these stages and their intermediate steps require iteration. For instance, some inclusion or exclusion criteria may only be found necessary once the search protocol is implemented.

3. Methods

In the elaboration of this article, we took the three normal stages of SLR conduction: planning, conduction and reporting. The first stage involves making the decisions that guide the rest of the process; the conduction phase is comprised of the actual gathering of data, using the protocol defined in the first stage. The final section of the study is basically the writing and the publishing of the results. In this section, we present the methods used in the study and their rationale, which roughly corresponds to the planning stage.

3.1. Objectives

An MS always aims to answer its research questions in a broad but definite way. It is a way of understanding a given field of research, and being able to systematise how this understanding is achieved.

As stated before, this is an MS aimed at characterising DOAS tomography general status. In doing this, we pretend to get a clearer image of what has been done and what should be attempted next, hopefully managing a sort of roadmap for future research contributions.

3.2. Research Questions

We have begun by defining the goals for our study, and structuring them with a PICOC (Population, Intervention, Context, Outcome and Comparison) analysis, which is summarised in Table 1. This analysis led us to our research goal: *to assess the technological status of the DOAS tomography technique*.

We used this goal statement as a primer to our research question, which was then formulated as: **what is the current status of the technology used in tomographic DOAS?**

Table 1: *PICO analysis.*

Population	DOAS research in general.
Intervention	The papers must address tomographic DOAS.
Outcome	Status assessment for DOAS tomography .
Context	Research papers.

Table 2: *Research question slicing*

Original	What is the current status of the technology used in tomographic DOAS?
RQ1	Is there a typical hardware setup used in tomographic DOAS studies?
RQ2	Is there a standard software used to perform these analysis?
RQ3	What are the algorithms more commonly used?

Now, this question is too vague to pursue in a systematic fashion, so we had to slice it into smaller and more objective chunks. This sectioning is presented in Table 2.

The research question is one of the most important steps in planning a Systematic Literature Review, but it cannot be entered into a library's search box. Therefore, we have to define our search terms before we can make any effort of answering our questions.

3.3. Search Query Definition, Library Selection and Filter Definition

In the case of this study, the search terms were selected in order to purposefully maintain a broad scope, so that we could retrieve a high number of relevant studies. The selected search terms were: **DOAS atmospher*** **tomography**¹. The search query was entered into 5 academic search engines, as shown in Table 3.

Table 3: *Electronic libraries used in this study.*

Library	URL
Google Scholar (GS)	https://scholar.google.com/
Web of Knowledge (WoK)	https://webofknowledge.com
Science Direct (SD)	https://www.sciencedirect.com
IEEE	http://ieeexplore.ieee.org/
AGU Publications (AGU)	http://agupubs.onlinelibrary.wiley.com/hub/

¹The asterisk acts as a wildcard.

After setting Table 3 libraries, it was time to define our article selection criteria, which are summarised in Table 4. We began with 2 Inclusion Criteria (IC) and 3 Exclusion Criteria. The IC determined that our selected papers would have to be journal articles (thus excluding thesis, white papers, patents and other documents) and that these articles should be on the topic of Tomographic DOAS. The EC dictated that no selected paper should include volcanology studies or satellite data analysis (these have particularities which we do not want to approach in this study) and that no other language than English will be accepted.

During the course of the search, however, we had to include another two EC. The first was included in the Google Scholar search, where we understood that papers from a certain publisher were not accessible. The second came in the subsequent searches, when it became clear that most papers had already been retrieved by the GS search.

Table 4: Selection filters in use for this study's search.

Criterium Definition		
Exc. Criteria	EC1	Duplicate in Scholar
	EC2	Non English articles are not accepted
	EC3	Volcanology papers are not accepted
	EC4	Satellite data papers are not accepted
	EC5	CNKI published articles are not accepted
Inc. Criteria	IC1	Results must be articles
	IC2	Results must be about Tomographic DOAS

3.4. Data Extraction Strategy

The data extraction process is a key part of any systematic review, whether an SLR or an MS. It determines how each article is approached with regard to its content, before any information is retrieved. In our case, our strategy took place in two separate moments: an initial screening, in which we would assess contents as expressed by the articles' abstract; and a second moment, in which we performed a full article read. Special attention was given to explicit sections covering our target topics (equipment, algorithm and software).

3.5. Quality Assessment

It is very difficult to assess a paper's quality, and to rank it accordingly. However, for this review in particular, we have decided to follow Souza's

Table 5: *Quality assessment criteria presentation.*

Criterium Type	Criterium (Weight)	Decision Factor	Score
General Criteria	Contribution to this SLR (0,2)	cited in study: more than three times	1
		cited in study: three times	0,75
		cited in study: twice	0,5
		cited in study: once or less	0,25
		Detailed	1
Specific Criteria	Algorithm description (0,6)	Semi-Detailed	0,4
		Mentioned	0,2
		None	0
		Detailed	1
	Instrument description (0,2)	Semi-Detailed	0,4
		Mentioned	0,2
		None	0
		Mentioned	1
	Software Description (0,1)	None	0

approach [26] and adopt a similar evaluation method. Table 5 contains the used criteria.

In our evaluation model, we took into account both general and specific criteria. The former addresses an article's contributions to our particular SLR; the latter targets the actual content of that article.

In order to measure the contribution of each individual paper to our study (our general criterium), we have assessed its number of citations in all the other selected papers. This is a valid measurement of a paper's impact in the study, but it might become difficult to implement if a high number of articles are selected for the final stage. Contentwise (specific criteria), we have defined our scoring model according to the Research Question separation explained in Subsection 3.2.

In our study's case, distinction between Specific and General was not sufficient to adequately separate scores according to importance. It was necessary to introduce scoring weights for that end. These weights are also shown in Table 5 and were set according to the goals of our SLR, meaning

that the tomographic element is the most important.

In the end, a paper's total score comes from the formula described by Equation 2.

$$TotalScore = \sum_i w_i \cdot S_i \quad (2)$$

Where S_i and w_i are a paper's score and weight for a given criterium, respectively.

Finally, we shall discuss the different weights given to each criterium and the different ways in which they are evaluated. The most important aspect that we are trying to assess is the algorithm, which defines the whole tomographic process and the results achievable by the studies.

A detailed algorithmic description includes the mathematical basis as well as a complete description of required adaptations, both on the mathematical level and on a conceptual method.

Instrument description is also an important criterium, since it is with it that scientists retrieve the information they will afterwards process tomographically, through the algorithm.

It is sometimes difficult to establish how good an instrument description is. A too detailed description can be just as bad as a non-sufficient one, if the equipment options are not correctly presented.

That being said, we have considered a detailed description one that includes explicit mention to the composition of the optical system and its assembly details, together with the analysing hardware (e.g. spectrometers) configuration and capabilities.

The least important of the technical features under evaluation is the software. This is because theoretically, results would be the same independently of the software in use. We have included this feature in the study as a way of identifying if there was some kind of software prevalence in the community. In this study, software is binarily assessed: either the scrutinised study mentions it or not.

Finally, we evaluate the contribution of each article to this study. Since DOAS tomography is a field with a relatively low number of players, it can be expected that there are many cross citations. We have introduced this as a method of measuring an article's relative importance within this mapping study, simply by counting the number of times a cross citation occurs.

4. Conduction

4.1. The Search

SLR guideline literature [14, 28] recommend that the first stage of any Systematic Literature Review be the search for previous literature of this kind, since a recent systematic study may render the execution of a new study disencourageable. In our case, none of the several libraries used appeared to have any article of the sort.

The search terms, derived in Subsection 3.2, were run in all libraries found in Subsection 3.3. The Google Scholar search had the particularity of being run through a specialised software called *Publish or Perish*[8], which allowed the search results to be exported to a comma separated values file, which made the process a lot easier, since it was then possible to work the data directly in a spreadsheet program (Microsoft Excel, in this particular case).

The conduction phase of our study followed the flowchart illustrated by Figure 1. Notice that Google Scholar is the first library to be searched. This is motivated by the fact that the vast majority of the articles were retrieved by Google's academic search engine. In fact, GS-retrieved articles were so predominant that we had to create a special EC, as described in Subsection 3.3.

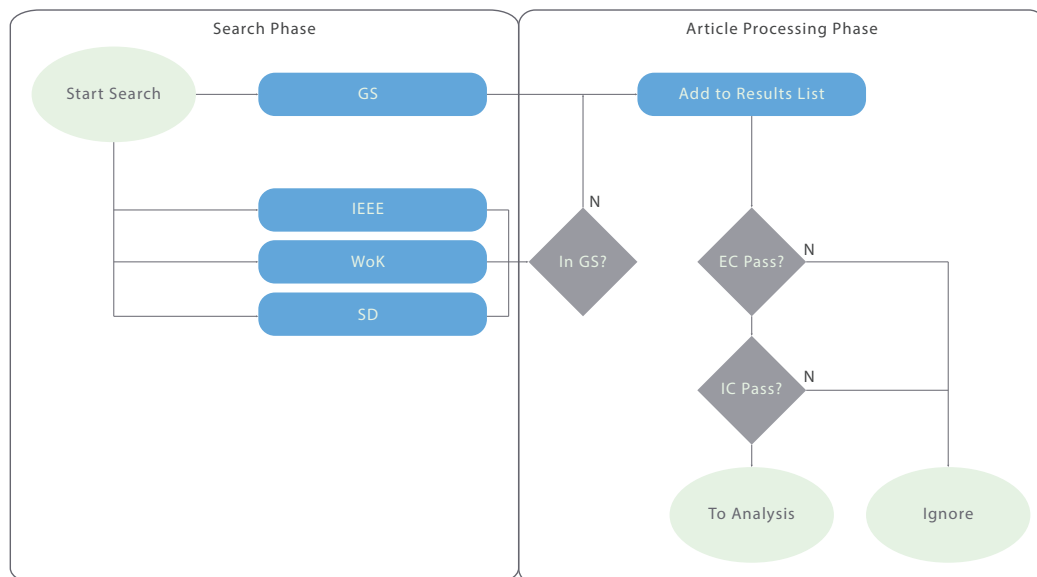


Figure 1: Conduction stage flowchart. Notice Google Scholar's prevalence.

4.2. Results and Discussion

4.2.1. Presentation and analysis

Our search returned 732 results, of which 709 were distinct ($\approx 97\%$). Of these, 601 were journal articles ($\approx 82\%$). The vast majority of the results came from GS ($\approx 80\%$, see Figure 2). Selection criteria (Inclusion and Exclusion) application resulted in the exclusion of 701 results ($\approx 99\%$), thus leaving 8 articles reaching the content analysis stage (the attempt to answer the Research Question). A summary of these findings can be seen in Table 6.

Table 6: Search results. For a paper to reach the rightmost column, which means it is selected, it must verify both IC1 and IC2 as well as none of the EC, ranging from EC1 to EC5.

Articles which trigger criteria									
Source	# Articles	IC1	IC2	EC1	EC2	EC3	EC4	EC5	Rem. Articles
GS	576	455	142	-	25	82	53	18	8
IEEE	116	116	1	0	0	1	1	0	0
WoK	14	14	6	13	0	1	1	0	0
SD	10	0	0	0	0	0	0	0	0
AGU	16	1	1	1	1	1	1	0	1
TOTAL									9

Library	# Results	Percentage
GS	576	78.7%
IEEE	116	15.8%
WoK	14	1.9%
SD	10	1.4%
AGU	16	2.2%

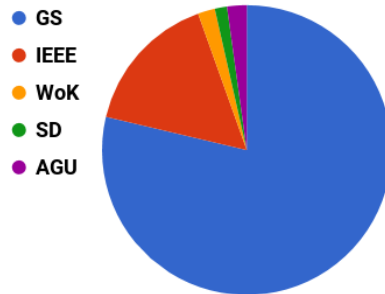


Figure 2: Results distribution by library.

Table 7 presents the 8 selected articles. It categorises them with respect to their covered topics and whether they are empirical or theoretical in nature. The same table summarises article scores according to the criteria defined in Subsection 3.5, and presents the keys with which we will refer to each article from this point forward.

The 8 papers averaged a score of 0,48 and a median score of 0,6. There is a strong difference between the average and the median suggesting that there are some outliers or some kind of clustering. Although this is actually the case, it is statistically irrelevant, given the small size of the sample.

Table 7: Scoring results for the selected articles. In the second column, a T means the article is theoretical and an E means the article is empirical.

Key	Type	Alg.	Inst.	Soft.	Cit.	Score
Hartl2006 [7]	T	1	0,4	0	0,5	0,73
Laeapple2004 [15]	T	1	0	0	1	0,70
Mettendorf2006 [17]	E	0,4	1	1	0,25	0,57
ODriscoll2003 [18]	T	1	0	0	0,25	0,63
Olaguer2017 [19]	E	0	0,2	0	0,25	0,07
Poehler (unpub) [23]	E	0	0,4	0	0,25	0,11
Pundt2005 [24]	E	0,4	1	1	1	0,64
Stutz2016 [27]	E	0	1	1	0,25	0,33

4.3. Discussion

In this subsection, we will use the 8 articles that were selected in order to try and answer the Research Questions. For clarity, we will approach with respect to the instrument, algorithm and software in a separate manner.

Different articles present data in different ways, and with different levels of detail. This has been taken into account in designing our evaluation method, and it should also be observed when discussing results. Therefore, our general approach in this subsection will be to address the more detailed articles first and then complement that information with what we can gather from the less detailed papers.

4.3.1. Instrument

Instrumentation description is present in 7 of the 8 ([7, 15, 17, 19, 23, 24, 27]) selected articles. Stutz2016 [27], Pundt2005 [24] and Mettendorf2006 [17] present the highest level of detail.

In Stutz2016 [27], the authors used a newly developed Long Path DOAS instrument for the study of atmospheric concentration of Benzene, Toluene and Xylenes. This instrument's main innovation is its light source, which consists in a double LED (255nm and 265nm) assembly. This system's telescope is a homebuilt telescope with a focal length of 120 cm and a 12 inch diameter aluminum coated main mirror, mounted on a high accuracy motorised pan and tilt unit from Newark Systems. The telescope is used both

as emitter and receiver, therefore the system needs a reflector. Stutz used a quartz corner cube reflector array, with an individual reflector diameter of 57 mm and the number of reflector ranging from 10 to 25 (depending on the path length). For detection, the system relied on a UV-enhanced PIXIS 256 CCD detector from Princeton Instruments on an Acton spectrometer with 300 grating and ≈ 0.3 nm spectral resolution, which was stabilised to -35°C.

Pundt2005 [24] was conducted during the BAB II motorway campaign. The team was working with the goal of performing a tomographic measurement of vehicle pollution along a certain motorway between Heidelberg and Mannheim. For that, they used an assembly of two telescopes and eight reflectors, rendering a total of 16 light paths, then used to perform a tomographic reconstruction of the trace gas detection in that region. The telescopes used had a focal length of 150 and 80 cm, with respective diameters of 300 and 200 mm. Both assemblies used Acton spectrometers. One used the Acton 500, with 0.5 nm spectral resolution in the range between 295 and 375 nm; the other used an Acton 300, with 0.4 nm spectral resolution between 295 and 355 nm. In both cases, the sensor used was a 1024 pixel Photo Diode Array (PDA), thermally stabilised at -15°C. The telescopes were pointed towards two towers which bore the reflectors, set at heights of 10, 20, 30 and 40 m from the ground.

In Mettendorf2006 [17], the authors validated two-dimensional LP-DOAS tomography through an indoor experiment. To this end, they have used three multibeam instruments, which consisted in a telescope with a focal length of 1.5 m and 300 mm in diameter, which was also used as emitter and receiver. The system used a broad spectrum Xenon lamp as light source, though no details are given. The experiment assembly included the careful positioning of plane mirrors and 6 cm diameter corner cube reflectors, used to create a total of 39 light paths (13 for each multibeam instrument).

As for the other 4 less detailed instrument description, three (Hartl2006 [7], Poehler [23] and Laepple2004 [15]) are from the same group as Pundt2005 [24] and Mettendorf2006 [17], and therefore use the same or similar hardware. Olaguer2017 [19], on the other hand, is the companion paper of Stutz2016 [27], and therefore gives a description of the same instrumentation, though in a less detailed manner.

4.3.2. Algorithm

The reconstruction algorithm is the most important part of our study, as we already demonstrated by the weight it is given in our quality evaluation model (see Subsection 3.5). Algorithm descriptions are present in 6 of the 8 selected articles: [7, 15, 17, 18, 19, 24]. The most complete descriptions are featured in Hartl2006 [7], Laepple2004 [15] and ODriscoll2003 [18]. Mettendorf2006 [17],

Olaguer2017 [19] and Pundt2005 [24] approach the reconstruction algorithms with less emphasis or in a less detailed way.

In Hartl2006 [7], the research team describe their discretisation process, reconstruction methods, grid translation methods and error estimation and quality assessment, with the greatest level of detail being given to the latter.

The paper also focuses in the comparison SIRT and ART results for the test samples, which consisted in up to four Gaussian concentration profiles, which were randomly arranged in a 100x100 (a.u.) test field, in six different geometries and with up to 36 known light paths.

Furthermore, Hartl2006 [7] discusses how the choice of the reconstruction grid affects both the reconstruction error and reconstruction area integrals, the possibility of the existence of background concentration influencing equation constraints and reconstruction results, and how the whole system would behave were its geometry any different, namely regarding light paths and number of telescopes.

The next algorithm-oriented paper is Laepple2004 [15]. In this article, the group discussed several discretisation approaches, their drawbacks and advantages. Still on discretisation, they approach the problem of resolution, and the necessary balance between physical accuracy and the need for *a priori* information which arises from increasing it. Afterwards, the group presents some strategies for solving the linear system that results from discretising the concentration field and how to take error into account.

For their reconstructions, the group chose to adapt ART, SIRT, and SART (see Subsection 2.4). These adaptations were described and detailed in the article's third section, before the error estimation procedures adopted in their case. Finally, the team presents how they chose to optimise reconstruction in several aspects, including the generation of test plumes and optimisation for the BABII campaign, which was the parent project of this article.

O'Driscoll2003 [18] also covers the algorithm extensively. While this paper is considerably shorter than the previous two, it provides a detailed (on an iteration basis) description for ART and SIRT (see Subsection 2.4). In addition, and perhaps of greater interest, the paper's authors suggest a different approach to solving the reconstruction matrix, different from the algebraic methods already presented: an evolutionary algorithm.

An evolutionary algorithm is a mathematical method of solving complex problems, which mimics or is in any form based on the process of natural selection. These algorithms have, according to the paper's authors and their references, been shown to be extraordinarily powerful.

The research team have applied a Differential Evolution algorithm to the reconstruction process and provide a detailed description of how they have done this.

The other two articles which mention the algorithm are Mettendorf2006 [17] and Pundt2005 [24]. Both these studies were conducted under the same project as Laepple2004 [15] and Hartl2006 [7] and therefore their algorithm descriptions and methods draw heavily on these two studies.

4.3.3. Software

Of the 8 selected articles, only 3 mention the software used. Even these, do not go into any detail of the reasons that led to that specific usage.

In Mettendorf2006 [17], the team used TOMOLAB for the calculation of the modelled column densities of their experiment. In Pundt2005 [24], spectral analysis was performed using the *MFC Software*. Finally, Stutz2016 [27] used the DOASIS software for control and automation purposes, and does not explicitly mention its use for spectral analysis purposes, although this is likely.

4.3.4. General Observations

While this is not a part of the discussion *per se*, we believe it makes sense to make some general observations about the data which we had to analyse.

The first important mention is the BABII campaign. This study, which ran in 2001 and aimed to quantify pollution from the A656 motorway between Heidelberg and Mannheim produced a significant part of the literature which we analysed.

Another point which should be addressed is that all DOAS tomography efforts detected in this search were based on active DOAS technology. This only means that the DOAS systems all employed an artificial light as a light source.

A final remark is due to the prevalence of algebraic methods for solving the discretisation and reconstruction problem, namely ART, SART and SIRT.

4.4. Validity Threats

When writing an MS or an SLR, authors always have to analyse their findings and methods in order to mitigate potential sources of error or lack of validity. This is called a validity threat analysis.

There are two main families of validity threats. They can be internal, i.e., they come from the methods employed used in conducting the study; or external, which means that the threat comes from the applicability (or lack thereof) of the effects observed in the study, outside of its scope.

On the level of internal validity of our study, two main observations come to mind:

Relevant papers left out The very low number of found studies could be an indication that our inclusion and exclusion filters were set in a too restrictive manner.

It could also happen that some relevant papers were not found due to being written in such a way that the libraries' search engines did not find them with our search phrase. This same problem would also occur if for some reason, an important library was left out of the study, and therefore not searched.

We mitigate all these risks by selecting a purposefully broad search phrase, by using powerful general search engines (eg. Google Scholar) and by running several undocumented test-runs with other search phrases.

A common strategy used for tackling this kind of threat is to extend the study through snowballing. In our case, we have opted to not perform this operation because of the very high cross-reference pattern between the found studies.

Quality of selected papers While it is true that we do not have any control over the quality of the articles rendered by the search engines, and there is no standard regarding it, we must address the issue that it entails. We have tried to mitigate this risk, as far as we can, by using strict and strong selection criteria in systematic fashion (see Section 3).

On the external threat plane, we contend with the applicability of our findings outside our study. We have tackled this issue by trying to remain focused only to the technologic aspect of the Tomographic DOAS technique, both in respect to its instrumentation and to the mathematical methods involved.

With this in mind, and even if the internal validity threats were all verifiably concerning, this study's finding are of great use to anyone wanting to understand how the field is working or wishing to design and build an analysis system.

5. Conclusions

The essential goal of this MS was to assess the technological status of the tomographic DOAS technique as described in the relevant academic literature.

By performing a systematic search using the phrases and libraries enumerated in Section 3, we have retrieved more than 700 articles. The elimination process took place through the application of inclusion and exclusion criteria, as described in full in Subsection 3.3.

In the end, 8 articles were identified as relevant. There are several possible justifications for such a low number of retrieved articles. Some of those reasons are addressed in Subsection 4.4. Mostly, we believe that DOAS tomography

is a relatively new field of study, which has not yet been sufficiently explored, and that results in a small *corpus* of literature.

Our analysis was performed on three distinct levels: **algorithms**, **hardware** and **software**. We have found that, while there are commonalities amongst almost all papers (such as the fact that they are all active DOAS applications), on the hardware and software planes, there is no *standard model* for the used devices. On the algorithm level, however, and due to data quantity restrictions related to the low number of used projections (several tens), iterative reconstruction methods (namely ART) are almost universal.

6. Acknowledgments

This study was funded by the FCT grant PDE/BDE/114549/2016 and by the ATMOS Project (PORLisboa FEDER 3491).

References

- [1] Industrial Tomography - Systems and Applications. In M. Wang, editor, *Industrial Tomography*, volume 4. Elsevier. ISBN 9781782421184. doi: 10.1016/B978-1-78242-118-4.12001-5. URL <http://linkinghub.elsevier.com/retrieve/pii/B9781782421184120015>.
- [2] N. Bobrowski, G. Hönninger, F. Lohberger, and U. Platt. IDOAS: A new monitoring technique to study the 2D distribution of volcanic gas emissions. 150(4):329–338. ISSN 03770273. doi: 10.1016/j.jvolgeores.2005.05.004.
- [3] R. L. Byer and L. A. Shepp. Two-dimensional remote air-pollution monitoring via tomography. 4(3):75–77. ISSN 0146-9592. doi: 10.1364/OL.4.000075. URL <http://eutils.ncbi.nlm.nih.gov/entrez/eutils/elink.fcgi?dbfrom=pubmed&id=19687805&retmode=ref&cmd=prlinks>.
- [4] T. G. Feeman. *The Mathematics of Medical Imaging*. Springer Undergraduate Texts in Mathematics and Technology. Springer New York. ISBN 978-0-387-92711-4. doi: 10.1007/978-0-387-92712-1. URL <http://link.springer.com/10.1007/978-0-387-92712-1>.
- [5] R. Gordon. A tutorial on art (algebraic reconstruction techniques). 21(3):78–93. ISSN 0018-9499. doi: 10.1109/TNS.1974.6499238. URL <http://ieeexplore.ieee.org/document/6499238/>.

- [6] C. Haisch. Optical Tomography. 5(1):57–77. ISSN 1936-1327. doi: 10.1146/annurev-anchem-062011-143138. URL <http://www.annualreviews.org/doi/10.1146/annurev-anchem-062011-143138>.
- [7] A. Hartl, B. C. Song, and I. Pundt. Atmospheric Chemistry and Physics 2-D reconstruction of atmospheric concentration peaks from horizontal long path DOAS tomographic measurements: parametrisation and geometry within a discrete approach. 6(3):847–861. ISSN 1680-7324. doi: 10.5194/acpd-5-11781-2005. URL <http://www.atmos-chem-phys.net/6/847/2006/www.atmos-chem-phys.net/6/847/2006/>.
- [8] A. Harzing. Publish or Perish. URL <http://www.harzing.com/pop.htm>.
- [9] G. T. Herman. *Fundamentals of Computerized Tomography*. Advances in Pattern Recognition. Springer London. ISBN 978-1-85233-617-2. doi: 10.1007/978-1-84628-723-7. URL <http://link.springer.com/10.1007/978-1-84628-723-7>.
- [10] G. T. Herman, A. Lent, and S. W. Rowland. ART: Mathematics and applications. A report on the mathematical foundations and on the applicability to real data of the algebraic reconstruction techniques. 42(1). ISSN 10958541. doi: 10.1016/0022-5193(73)90145-8.
- [11] G. Hönniger, C. von Friedeburg, and U. Platt. Multi Axis Differential Optical Absorption Spectroscopy (MAX-DOAS). (4):231–254. URL www.atmos-chem-phys.org/acp/4/231/.
- [12] A. C. Kak. Algebraic Reconstruction Algorithms. In *Computerized Tomographic Imaging*, pages 275–296. ISBN 978-0-89871-494-4. doi: 10.1137/1.9780898719277.ch7.
- [13] A. C. Kak and M. Slaney. *Principles of Computerized Tomographic Imaging*. Number 1. Society for Industrial and Applied Mathematics. ISBN 978-0-89871-494-4. doi: 10.1137/1.9780898719277. URL <http://epubs.siam.org/doi/book/10.1137/1.9780898719277>.
- [14] B. Kitchenham and S. Charters. Guidelines for performing Systematic Literature reviews in Software Engineering Version 2.3. 45(4ve):1051. ISSN 00010782. doi: 10.1145/1134285.1134500. URL <http://scholar.google.com/scholar?hl=en&btnG=Search&q=intitle:Guidelines+for+performing+Systematic+Literature+Reviews+in+Software+Engineering%20%Cnhttp://www.dur.ac.uk/ebse/resources/Systematic-reviews-5-8.pdf>.

- [15] T. Laepple, V. Knab, K.-U. Mettendorf, and I. Pundt. Long-path DOAS tomography on a motorway exhaust gas plume: numerical studies and application to data from the BAB II campaign. 4(3):2435–2484. ISSN 1680-7375. doi: 10.5194/acpd-4-2435-2004. URL www.atmos-chem-phys.org/acp/4/1323/ <http://www.atmos-chem-phys-discuss.net/4/2435/2004/>.
- [16] A. Merlaud. Development and use of compact instruments for tropospheric investigations based on optical spectroscopy from mobile platforms. URL <http://books.google.com/books?hl=en&lr=&id=inXVSyR82zwC&oi=fnd&pg=PR3&dq=Development+and+use+of+compact+instruments+for+tropospheric+investigations+based+on+optical+spectroscopy+from+mobile+platforms+sciences&ots=VdebeDBQMc&sig=4G0eVEvthJXuqd8WI3IWjjVXuXc>.
- [17] K. U. Mettendorf, A. Hartl, and I. Pundt. An indoor test campaign of the tomography long path differential optical absorption spectroscopy technique. 8(2):279–287. ISSN 1464-0325. doi: 10.1039/B511337G. URL <http://xlink.rsc.org/?DOI=B511337G>.
- [18] S. O'Driscoll, J. G. Murphy, and N. J. Smith. Computed tomography of air pollutants in street canyons. 4876:958–967. doi: 10.1111/12.463985.
- [19] E. P. Olaguer, J. Stutz, M. H. Erickson, S. C. Hurlock, R. Cheung, C. Tsai, S. F. Colosimo, J. Festa, A. Wijesinghe, and B. S. Neish. Real time measurement of transient event emissions of air toxics by tomographic remote sensing in tandem with mobile monitoring. 150:220–228. ISSN 13522310. doi: 10.1016/j.atmosenv.2016.11.058. URL <http://linkinghub.elsevier.com/retrieve/pii/S1352231016309487>.
- [20] D. Perner, D. H. Ehhalt, H. W. Pätz, U. Platt, E. P. Röth, and A. Volz. OH - Radicals in the lower troposphere. 3(8):466–468. ISSN 00948276. doi: 10.1029/GL003i008p00466. URL <http://doi.wiley.com/10.1029/GL003i008p00466>.
- [21] K. Petersen, R. Feldt, S. Mujtaba, and M. Mattsson. Systematic Mapping Studies in Software engineering. pages 1–10. doi: citeulike-article-id: 3955889.
- [22] U. Platt and J. Stutz. *Differential Optical Absorption Spectroscopy*. Springer. ISBN 9783540211938.

- [23] D. Poehler, B. Rippel, A. Stelzer, K. U. Mettendorf, A. Hartl, U. Platt, and I. Pundt. Instrumental setup and measurement configuration for 2D tomographic DOAS measurements of trace gas distributions over an area of a few square km.
- [24] I. Pundt, K. U. Mettendorf, T. Laepple, V. Knab, P. Xie, J. Lösch, C. V. Friedeburg, U. Platt, and T. Wagner. Measurements of trace gas distributions using Long-path DOAS-Tomography during the motorway campaign BAB II: Experimental setup and results for NO 2. 39(5): 967–975. ISSN 13522310. doi: 10.1016/j.atmosenv.2004.07.035.
- [25] R. W. Sanders, S. Solomon, J. P. Smith, L. Perliski, H. L. Miller, G. H. Mount, J. G. Keys, and A. L. Schmeltekopf. Visible and near-ultraviolet spectroscopy at McMurdo Station, Antarctica: 9. Observations of OCIO from April to October 1991. 98(D4):7219–7228. ISSN 01480227. doi: 10.1029/93JD00042. URL <http://doi.wiley.com/10.1029/93JD00042>.
- [26] E. Souza, A. Moreira, and M. Goulão. Deriving Architectural Models from Requirements Specifications: a Systematic Mapping Study. ISSN 09505849. doi: 10.1016/j.infsof.2019.01.004. URL <https://linkinghub.elsevier.com/retrieve/pii/S0950584919300035>.
- [27] J. Stutz, S. C. Hurlock, S. F. Colosimo, C. Tsai, R. Cheung, J. Festa, O. Pikelnaya, S. Alvarez, J. H. Flynn, M. H. Erickson, and E. P. Olaguer. A novel dual-LED based long-path DOAS instrument for the measurement of aromatic hydrocarbons. 147:121–132. ISSN 13522310. doi: 10.1016/j.atmosenv.2016.09.054. URL <http://linkinghub.elsevier.com/retrieve/pii/S1352231016307713>.
- [28] E. Tacconelli. *Systematic reviews: CRD's guidance for undertaking reviews in health care*, volume 10. ISBN 1900640473. doi: 10.1016/S1473-3099(10)70065-7. URL <http://linkinghub.elsevier.com/retrieve/pii/S1473309910700657>.

B

**FOREST FIRE FINDER: DOAS
APPLICATION TO LONG-RANGE FOREST
FIRE DETECTION**



Forest Fire Finder – DOAS application to long-range forest fire detection

Rui Valente de Almeida^{1,2} and Pedro Vieira^{1,2}

¹NGNS, Ingenious Solutions, Rua Cidade de Évora, 11, 2660-022 Loures, Portugal

²Faculty of Science and Technology, NOVA University of Lisbon, Caparica Campus, 2829-516 Caparica, Portugal

Correspondence to: Pedro Vieira (pedro.vieira@ngns-is.com)

Received: 23 September 2016 – Discussion started: 14 November 2016

Revised: 11 April 2017 – Accepted: 8 May 2017 – Published: 22 June 2017

Abstract. Fires are an important factor in shaping Earth's ecosystems. Plant and animal life, in almost every land habitat, are at least partially dependent on the effects of fire. However, their destructive force, which has often proven uncontrollable, is one of our greatest concerns, effectively resulting in several policies in the most important industrialised regions of the globe.

This paper aims to comprehensively characterise the Forest Fire Finder (FFF), a forest fire detection system based mainly upon a spectroscopic technique called differential optical absorption spectroscopy (DOAS). The system is designed and configured with the goal of detecting higher-than-the-horizon smoke columns by measuring and comparing scattered sunlight spectra. The article covers hardware and software, as well as their interactions and specific algorithms for day mode operation. An analysis of data retrieved from several installations deployed in the course of the last 5 years is also presented.

Finally, this paper features a discussion on the most prominent future improvements planned for the system, as well as its ramifications and adaptations, such as a thermal imaging system for short-range fire seeking or environmental quality control.

1 Introduction

Fire is a process by which elements chemically combine with oxygen, releasing energy (as heat and light) and smoke into the surrounding environment. Fires are an important factor in shaping Earth's ecosystems. Plant and animal life, in many

land habitats, are at least partially dependent on the effects of fire (Food and Agriculture Organisation , FAO).

The use of fire by hominids predates civilisation by thousands of years and, in today's society, there are almost no areas of technology or scientific knowledge that do not involve fire in one way or another. However, fire's destructive power is undeniable.

Forest fires are among the great concerns of the present day in industrialised countries. Research regarding wildfires has been targeted by many countries and unions worldwide in an effort to minimise the negative impact these events imply.

According to the Intergovernmental Panel on Climate Change (IPCC), climate change is expected to increase global temperatures and change rainfall patterns, leading to an increased risk of fire (IPCC, 2012). This means that the number of registered fires throughout the world is expected to increase, a phenomenon the world must be ready to address.

In the European Union, the Horizon2020 research programme states that there must be a union-wide investment in research concerning forest protection and recovery from fires. In the past, the FP7 programme had sponsored the development of an automatic forest fire detection system called FireSense, an investment of over EUR 2.5 million (European Comission, 2012).

The United States Forest Service acknowledge the importance of understanding wildland fire dynamics, running a network of research centres solely dedicated to the study of this subject. Research endeavours take 6 % of the service's annual budget, which is currently directed primarily towards fire suppression (United States Forest Department, 2015).

Australia is another geographic region where wildfires have had a great impact. As a response, its government has created the Bushfire and Natural Hazards Cooperative Research Centre. The institution builds upon more than 10 years of experience dealing with Australian bushfires and aims to produce internationally recognised research regarding the study and modelling of wildfires in Australia and New Zealand (BNHCRC, 2016).

In spite of this global investigation effort regarding fires and their behaviour, every year, material losses as a result of fires ascend to billions of dollars and thousands of lives are lost in the same way. This leads to a strong increase in the size of the fire protection market, including passive and active detection platforms, which is expected to grow at a cumulative aggregate growth rate of 11.53 % from 2014 to 2020 (Research and Markets, 2016).

2 State of the art

In recent years, several methods have been developed in an attempt to automatically and reliably detect forest fires. These systems differ primarily in their strategic approach to the issue at hand, creating three main categories:

- Satellite monitoring techniques: satellite data have been used for fire monitoring purposes since the late 20th century. The MODIS (MODerate resolution Imaging Spectroradiometer) and AVHRR (Advanced Very High Resolution Radiometer) sensors, deployed respectively in the Aqua/Terra and NOAA satellites, have had extensive use in this regard. However, their low temporal resolution (2 and 4 times per 24 h, respectively) make them poor candidates for fire detection uses. Geostationary satellites overcome this difficulty by continuously scanning a single, very large geographic region. They have, nevertheless, a low spatial resolution of 1 km, which means that small fires are difficult for them to detect (Manyangadze, 2009).
- Wireless network sensing: the wireless sensor network approach to fire detection is completely different from the other two categories. Instead of having a single device patrolling the target region, these systems are designed on the capabilities of a high number of extremely small battery-operated sensor boards that can communicate among themselves (Alkhatib, 2014; Liyang et al., 2005).

The sensor boards are equipped with several sensors, from temperature and humidity to luminance detectors. In spite of their great fire detection capabilities, these networks present various drawbacks, such as their very limited individual range of detection and their 2-year lifetime or the fact that their remains might imply an environmental issue (Alkhatib, 2014).

- Large-area remote sensing: this family of systems is designed with the goal of minimising the number of deployed devices in a given target region. Their architecture implies the use of an optical principle in order to detect smoke or flames, whether optical cameras or spectrometers.

There are already several commercially available systems, such as the Forest Fire Finder (FFF; the main subject of this paper), FireWatch, ForestWatch, AlarmEYE or EyeFi SPARC. Although these are commercial products, the available information is sparse and many times outdated, so a true comparison not only is beyond the scope of the article but also would require more research efforts. Nevertheless, it is important to briefly describe the operating principles of the more prominent systems.

- ForestWatch, developed in South Africa by EnviroVision Solutions, uses optical object recognition software, coupled to a very specific camera system. It detects smoke during the day and the flame glow during the night, at a maximum distance of 24 km in every direction, in a semi-automatic fashion. It is probably the most commercially successful system, with more than 300 currently operating towers (Envirovision Solutions, 2015; Hough, 2007).
- FireWatch is a commercial system operated and sold by IQ Wireless GmbH, in Germany. The system uses optical sensors and object recognition algorithms to detect smoke at a maximum distance of 15 km. It is important to mention that the FireWatch system is not a fully automatic fire detection platform, requiring a control room to operate correctly (IQ-Wireless, 2016).
- The FFF was developed in Lisbon, in a partnership between the NOVA University of Lisbon and NGNS-IS, Ltd., in 2006. This patented system uses a spectroscopic technique to assess the atmosphere and detect smoke columns (NGNS-IS, 2016). During the night, the system changes its operation mode and relies solely on image processing to detect a fire's glow. Its maximum rate detection range is of 15 km, and it acts with complete autonomy, requiring minimal human intervention (see Fig. 1).

The FFF's most significant advantage over its rivals is its low number of false alarms (typically one or two per week). This comes from the fact that the system's smoke-detection capabilities do not rely on image processing. This in turn means that reliable detections can be achieved by a smaller number of deployed devices (only one, three for triangulation). However, more reliable alarms imply less human intervention, which translates into less financial expenditure over time.

The FFF system is the only one to use an optical spectroscopy technique to detect fire through smoke presence in

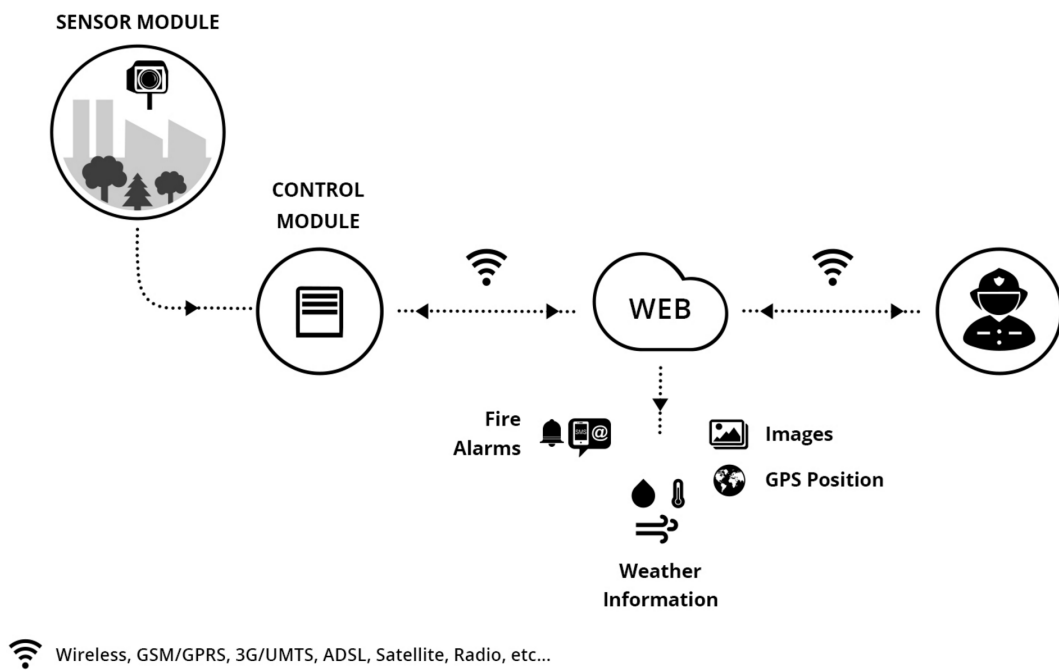


Figure 1. The Forest Fire Finder system (NGNS-IS, 2016).

real time. Since the analysis is carried out in an outdoor scenario, the process is not as straightforward as in laboratory experiments. This article addresses only the spectroscopic techniques used in the system's daytime operation mode.

3 The technique

The FFF system makes use of a spectroscopic technique called differential optical absorption spectroscopy (DOAS). This is a well-established and widely used technique in the field of atmospheric studies (Platt and Stutz, 2007).

There are two main categories of DOAS experiment assemblies, with different goals and capabilities:

- Active systems, of which a simple illustration is presented in Fig. 2, are characterised by relying on an artificial light source for their measurements. A spectrometer at the end of the light path performs spectroscopic detection. Active DOAS techniques are very similar to traditional in-lab absorption spectroscopy techniques (Platt and Stutz, 2007);
- Passive DOAS techniques, illustrated in Fig. 3, use natural light sources, such as the Sun and the moon, in their measurement process. An optical system is pointed in certain elevation and azimuth angles and sends the captured light into a spectrometer, connected to a computer. The system returns the total value of the light absorption in its path (Platt and Stutz, 2007; Merlaud, 2013). Since the FFF system is basically a passive DOAS sys-

tem, we will centre our discussion on this category from this point forward.

DOAS itself is based on Lambert–Beer's law, which can be written as (Platt and Stutz, 2007)

$$I(\lambda) = I_0(\lambda) \cdot \exp(-\sigma(\lambda) \cdot c \cdot L), \quad (1)$$

where λ is the wavelength of the emitted light; $I(\lambda)$ is the light intensity as measured by the system; $I_0(\lambda)$ is the intensity of the light as emitted by the source; and $\sigma(\lambda)$ is the absorption cross section of absorber, which is wavelength dependent; c is the concentration of the absorber we want to measure.

This law allows the definition of optical thickness (τ) (Platt and Stutz, 2007):

$$\tau(\lambda) = \ln\left(\frac{I_0(\lambda)}{I(\lambda)}\right) = \sigma(\lambda) \cdot c \cdot L. \quad (2)$$

In a laboratory setting, Eq. (1) or (2) can be used to directly calculate an absorber's concentration, provided there is knowledge of its cross section. In the open atmosphere, however, absorption spectroscopy techniques are far more complex. On one hand, $I_0(\lambda)$ is not accessible since we measure from inside the medium we want to measure. On the other hand, there are several environmental and instrumental effects that influence measurement results. These effects include the following (Platt and Stutz, 2007).

- Rayleigh scattering is due to small molecules present in the atmosphere and is heavily influenced by wavelength (hence the blue colour of the sky).

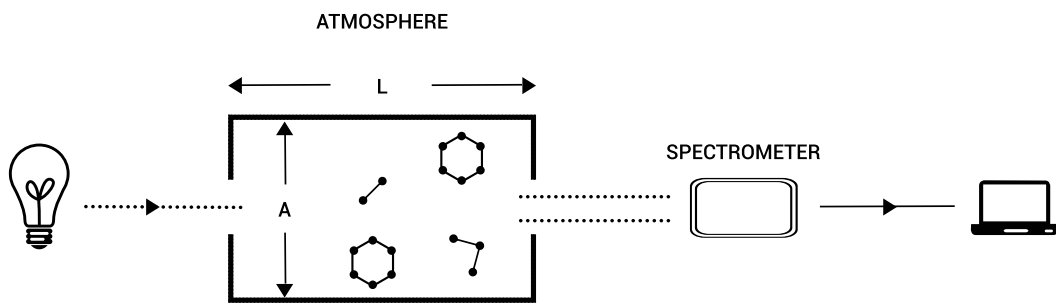


Figure 2. Active DOAS schematic.

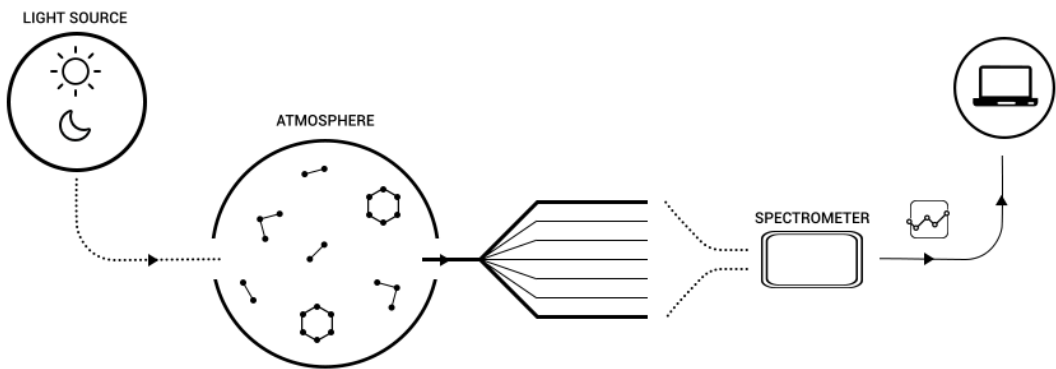


Figure 3. Passive DOAS schematic.

- Mie scattering is caused by particles and larger molecules suspended in the atmosphere and is not very dependent on the wavelength (hence the white colour of clouds).
- Instrumental and turbulence effects are the instrument's transmissivity and atmospheric turbulence in the optical path also limit light intensity.

In addition, we also have to take into account that, in the atmosphere, there are a number of trace gases that interfere with passing light.

Another aspect worth mentioning is that our device is never pointed directly at the light source (the Sun) but always processes light that has been scattered at some unknown point in the optical path. This means that the light that reaches our detector is only the scattered fraction of the sunlight, depending on the system's position and geometry, as well as wavelength.

The expansion of Lambert–Beer's equation to include all these effects results in Eq. (3).

$$I(\lambda) = I_0(\lambda) \cdot A(\lambda, \dots) \cdot S(\lambda) \cdot \exp \left[- \int \left[\left(\sum_i \sigma_i(\lambda, s) \cdot c_i(s) \right) + \epsilon_M(\lambda, s) \right] ds \right],$$

$$+ \epsilon_R(\lambda, s) \right] ds \Big], \quad (3)$$

where $A(\lambda, \dots)$ is the fraction of scattered light that reaches the device, $S(\lambda)$ represents instrumental and turbulence effects, $\sigma_i(\lambda, s)$ is the absorption cross section of absorber i , c_i is the concentration of absorber i , $\epsilon_R(\lambda)$ represents Rayleigh's extinction coefficient and $\epsilon_M(\lambda)$ represents Mie's extinction coefficient.

The interest of this equation lies within the retrieval of c_i , a given absorber's concentration. Since the integral is taken along the total atmospheric path of the measured photons, and considering that their cross sections do not vary significantly in atmospheric conditions, it is possible to define the concept of slant column, which is of great importance (Merlaud, 2013).

$$\text{SC}_i = \int c_i(s) ds \quad (4)$$

This quantity, as Eq. (4) shows, equals the integral of an individual absorber's concentration along the atmospheric optical path of relevance.

Now, without knowledge of $I_0(\lambda)$, these equations cannot give us absolute concentration values. We can, however, use another scattered light spectrum as reference in Eq. (2). Instead of absolute densities, this will yield relative changes in the atmosphere. We thus arrive at Eq. (5).

$$\begin{aligned} \ln\left(\frac{I_{\text{ref}}}{I}(\lambda)\right) &= \ln\left(\frac{A_{\text{ref}}}{A}(\lambda, \dots)\right) + \ln\left(\frac{S_{\text{ref}}}{S}(\lambda)\right) \\ &+ \sum_i (\sigma_i(\lambda) \cdot \Delta SC_i(\lambda)) + \Delta \tau_M(\lambda) \\ &+ \Delta \tau_R(\lambda), \end{aligned} \quad (5)$$

where ΔSC_i is the relative slant column of absorber i ; $\Delta \tau_M$ is the relative Mie scattering term, integrated to its optical thickness; and $\Delta \tau_R$ is the relative Rayleigh scattering term, integrated to its optical thickness.

This is where the principle of DOAS is applied. Instrument features, scattering and other atmospheric effects have broad absorption spectral profiles, which vary slowly with wavelength. Several trace absorbers have narrow and rapidly varying spectral signatures in at least a small section of the spectrum. By using Eq. (6), we can separate these contributions (Danckaert et al., 2015).

$$\sigma(\lambda) = \sigma'(\lambda) + \sigma_0(\lambda) \quad (6)$$

Here, the broad part of the optical thickness ($\sigma_0(\lambda)$) can be separated from the narrow part ($\sigma'(\lambda)$ – differential) by approximating it by a low-order polynomial, resulting in Eq. (7).

$$\ln\left(\frac{I_{\text{ref}}}{I}(\lambda)\right) = \sum_{i=1}^n \sigma'_i(\lambda) \cdot \Delta SC_i + \sum_{j=0}^m a_j \cdot \lambda^j, \quad (7)$$

where $\sum_{i=1}^n \sigma'_i(\lambda) \cdot \Delta SC_i$ is the differential part (narrow-band, rapidly varying with wavelength) and $\sum_{j=0}^m a_j \cdot \lambda^j$ is a low-order polynomial, used to remove the broadband spectral features resulting from atmospheric and instrumental phenomena.

In practice, the mathematical solving of Eq. (7) is not enough since it does not account for the Ring effect or the non-linearities that result from stray light and wavelength shift in measured and cross-section spectra.

The Ring effect is a consequence of rotational Raman scattering: molecules in the atmosphere do not absorb photons in a purely elastic (Rayleigh scattering) fashion. A small portion of the light–matter interaction is in fact inelastic (Brinkmann, 1968; Merlaud, 2013). This changes the light source frequencies as seen from the detector. This phenomenon was first noticed by Grainger and Ring in 1962. At the time, they noticed that the well-known Fraunhofer lines would slightly change when one observed them by using moonlight instead of scattered daylight (Grainger and Ring, 1962).

From the occurrence of these phenomena, it results that the mathematical procedure for DOAS measurements consists in solving a linear and a non-linear problem. The linear problem is solved by writing Eq. (7) in its matrix form:

$$\boldsymbol{\tau} = \mathbf{A} \cdot \mathbf{X}. \quad (8)$$

\mathbf{A} is an $m \times n$ matrix, with its columns being the differential cross sections $\sigma'_i(\lambda)$ and the wavelength powers taking the polynomial $P(\lambda) = \sum_{j=0}^m a_j \cdot \lambda^j$ into account. Since the number of lines in \mathbf{A} is much larger than the number of columns, the system is overdetermined and, in this case, we must use methods to numerically approximate a solution. It is common to use the least-squares approach, in which the best solution is the one that minimises $\chi^2 = [\boldsymbol{\tau} - \mathbf{A} \cdot \mathbf{X}] \cdot [\boldsymbol{\tau} - \mathbf{A} \cdot \mathbf{X}]^T$.

While the Ring effect is treated as a pseudo-absorber, a synthetically produced (Chance and Spurr, 1997) cross section that is fitted just like any other absorber, non-linearities are addressed by applying Levenberg–Marquardt's approach to non-linear fitting problems to Eq. (9) (Merlaud, 2013; Bevington and Robinson, 2003):

$$\begin{aligned} \ln\left(\frac{I_{\text{ref}}(\lambda)}{I(\lambda + \text{shift}) + \text{offset}}\right) &= \sum_{i=1}^n \sigma'_i(\lambda) \cdot \Delta SC_i \\ &+ \sum_{j=0}^m a_j \cdot \lambda^j, \end{aligned} \quad (9)$$

where shift and offset, which represent spectral wavelength shifts and stray light offsets, respectively, are responsible for the non-linear character of the problem.

The FFF system and its algorithm are based on the Passive DOAS technique by making scattered sunlight spectral measurements. Our algorithm differs from the original method mainly because of its very particular goal – fire detection through smoke. This objective is very different from the precise quantification of a certain trace gas concentration levels and means that both hardware and software must be adapted to the task at hand, as described in Sect. 4.

4 The device

The Forest Fire Finder (see Fig. 4) is a remote sensing system that has the goal of detecting forest fires. It is a sophisticated piece of equipment with many features and customisation possibilities. Its complexity and the fact that it is meant to operate 24 h per day create a need for control electronics and instrumentation. These devices are out of scope for this paper and will be revisited for another article that will include a detailed description of the FFF control software. This section aims to give a brief and basic hardware/software presentation for daytime spectroscopic operation and fire detection.

The FFF scans the horizon for the presence of a column of smoke by performing sequential spectroscopic measurements of its surrounding environment using only the Sun as a light source, as illustrated by Fig. 5. Sunlight is captured with a Maksutov–Cassegrain telescope and guided through an optical fiber cable into a spectrometer, which will transform it into an electric signal.

The system has to cover wide areas, which is why the telescope is mounted on an ENEO VPT-501 pan and tilt unit



Figure 4. The Forest Fire Finder system in one of its deployment locations in the north of Portugal.

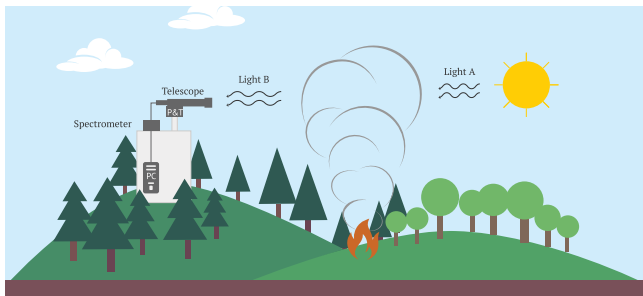


Figure 5. FFF illustration. The system continuously scans the horizon, in search of a smoke column.

that ensures the device's movement. The pan and tilt head unit assembly also includes a full-HD camera, which is used primarily for the optical alignment of the system and for human validation and supervision. During the night, this camera is also used for fire detection purposes; however, that is not within the scope of this paper and will be approached in another publication.

The Maksutov–Cassegrain telescope design uses the folded tube of the Cassegrain types and the spherical shape of primary mirror, secondary mirror and corrector lens of the Maksutov. In the FFF case, the chosen 90 mm aperture and 13.8 *f* ratio telescope, with a field of view of 1.4°, represents the best compromise between size, magnification and amount of captured light. In addition, it is also a cost-effective solution for the task at hand.

The AvaSpec 2048 is a popular 2048-pixel CCD photo array spectrometer. It can be customised with several slit sizes and gratings in order to suit the application it is intended for. In the case of the FFF system, a 50 µm slit is used in conjunction with a 300 lines mm⁻¹ grating, which ensures a wavelength range of 800 nm, from 300 to 1100 nm at a spectral resolution of 2.4 nm.

The spectrometer is connected to a computer, which is responsible for data processing and fire detection. It runs a custom-made software, developed in MathWorks' MATLAB development suite and C#. This software is deployed as a Microsoft Windows Service, as part of the FFF software suite.

5 Automatic smoke detection

The Forest Fire Finder is an electronic device that performs a spectroscopic analysis of the sky above the horizon, with the aim of detecting the presence of a smoke column. Smoke detection depends on the fire's emissions, which influence the composition of the atmosphere and on the system's spectroscopic algorithms, which allow those changes to be detected.

5.1 Forest fire emissions and DOAS

Forest fire smoke is a complex mixture of gases and aerosols that considerably changes the atmosphere (Urbanski et al., 2008). Among its key components are carbon oxides (CO and CO₂), methane (CH₄), non-methane hydrocarbons, volatile organic components, nitrous oxides (NO_x) and particulate matter (Van Der Werf et al., 2010; Ward and Hardy, 1991; Spichtinger et al., 2004). Trace gases in smoke have a definite impact on the atmosphere's optical properties since some absorb light in the visible region of the electromagnetic spectrum. In addition to this, and depending on the combustion process, fire gives rise to the formation and emission of solid particles (Ward and Hardy, 1991). Given their size, these particles become aerosols, which influence light in all wavelengths due to Mie's scattering.

In contrast, fire emissions also alter the balance between the perceived column densities of water (H₂O), oxygen (O₂), ozone (O₃) and the oxygen dimer (O₄). All of these chemicals' cross sections are significant in the visible part of the spectrum.

Passive DOAS measurements are commonly used to retrieve the atmospheric column densities of several chemical compounds. Smoke columns, however, present themselves as sudden and localised changes in atmospheric concentrations. If one were to use this technique and analyse their absolute concentration values per se, it would be very difficult to infer the presence of smoke.

This does not mean passive DOAS cannot be used in this context. In fact, this method is very effective in detecting smoke if we put a "smoky" spectrum as I and a "normal" spectrum as I_0 in Eq. (2), resulting in a signal as displayed in Fig. (7). Thus, by continuously acquiring spectra in a set of fixed azimuths and comparing the retrieved DOAS signals in pairs by azimuth, a narrow change such as the one produced by a forest fire becomes discernible in time. The FFF algorithm, presented in Sect. 5.2, does precisely this. These alterations are often difficult for the human eye to see, but there are some artificial intelligence algorithms that

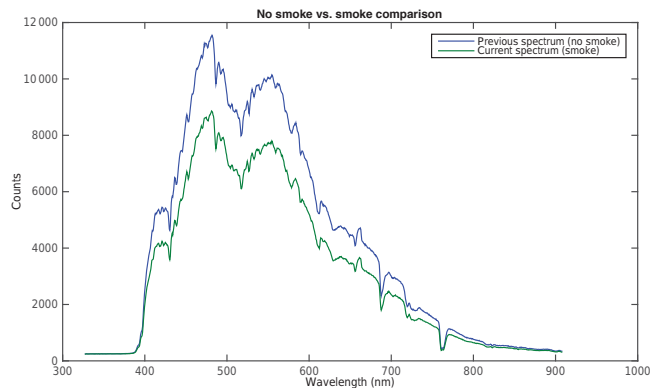


Figure 6. This plot shows how a smoke column can influence a spectral measurement. Both these spectra were acquired on 29 December 2014, with a time difference of approximately 5 min and no azimuth difference.

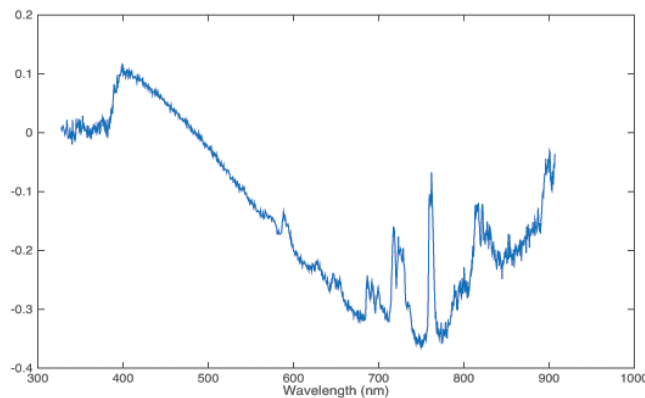


Figure 7. Example of a signal obtained by dividing two consecutive spectra of the same azimuth and calculating the logarithm of this division, the differential optical thickness. It is this signal that is fitted through Eq. (9).

have been shown to be effective in separating the sky from a smoke column event and which we will discuss in Sect. 5.2.2.

5.2 The FFF algorithm

The FFF algorithm uses the mathematical ingenuity behind DOAS measurements to attempt the detection of forest fire smoke columns. It is important to bear in mind that this device is meant for real-time automatic detection of a forest fire. This creates strict time and memory constraints that the algorithm must adapt to in order to accomplish its function.

The system relies on its continuous movement at constant speed to provide spatially accurate detections. The spectrometer acquires 2 spectra s^{-1} , which are all analysed by the computer. Spectral integration time varies from 60 ms to 450 ms and is typically 210 ms. DOAS calculations are currently taking between 250 ms and 350 ms in the industrial computers powered by Intel i5 we use on the system. This

means that the software is almost always lagging behind the hardware. The system is designed to cope with this delay, and does so with great robustness, but in larger scans this lag becomes sufficiently significant as to compromise real-time fire detection.

These limits are reflected in several steps in the DOAS calculation process, such as the non-inclusion of stretch effects in the non-linear DOAS problem or the consideration that there are no atmospheric temperature fluctuations over the optical path. This approach would not be valid if we wanted to make a precise quantification of a certain compound's atmospheric column, but it works given the fact that we only want to distinguish between a smoky spectrum and non-smoky spectrum.

The algorithm is divided into two separate phases. The first phase, which is run in real time as soon as the spectrum arrives, is the chemical phase, described in Sect. 5.2.1. Results from this stage are stored in memory and accessed at the end of each scan by the second phase, which performs the classification of the analysis as a detection or a non-detection. This phase is described in Sect. 5.2.2.

5.2.1 The chemical phase

This algorithm section happens immediately after spectral acquisition. It corresponds to a passive DOAS analysis (see Sect. 3) of the spectrum in two different conceptual levels, as illustrated in Fig. 10. The first level uses the same azimuth spectrum of the previous scan as a reference spectrum in the DOAS calculations. The second level uses the mean of the ten spectra immediately to the left and to the right of the analysed spectrum for the same purpose. This processing level was created in an empirical way, after observing that in the presence of strong winds, smoke columns move horizontally. Both levels are calculated using literature spectra, compiled in Table 1. In practice, these two processing levels represent three possible ways of applying Eq. (2): considering I_0 as the previous spectra acquired with the same azimuth; considering I_0 as the average of the ten immediate spectra to the left of current azimuth; and considering I_0 as the average of the ten immediate spectra to the right of current azimuth (this last method implies delayed processing of the current spectrum).

In this stage, the algorithm proceeds to retrieve column density values for NO_2 , H_2O , O_2 , O_3 and O_4 , using Eq. (9) and the Levenberg–Marquardt algorithm. Figures 8 and 9 show actual retrieved column densities for one of the Peneda-Gerês FFF systems, taken on 26 December 2014. The charts were produced using the QDOAS software (Danckaert et al., 2015). These plots are all relative to the first level of processing, as described above. In parallel to the column density retrieval, short- and long-wavelength energy contribution and signal-to-noise ratio (SNR) are also computed for the analysed spectrum optical density (with relation to the previous spectrum of the same azimuth). All the processed data are

stored in a single matrix, which will be used by the second stage of the FFF algorithm, described in Sect. 5.2.2.

As stated, in the first level of processing the FFF uses the same azimuth spectrum of the previous scan as a reference. This means that between the spectrum of interest and the reference there is only an approximately 5 min difference. This in turn implies that, when plotted, the fitting signal is almost always negligible for non-smoky spectra (see the top of Figs. 8 and 9). However, smoky spectra have higher column density differences, which produce fitting plots with somewhat more-pronounced signals (see bottom of Figs. 8 and 9).

At this point, it is important to note two things. First and foremost, this kind of measurements produce results that are near the limit of the FFF's detection capabilities, which can still be numerically used to train a detection algorithm. Second, it should be highlighted that smoke-detection patterns were not manually defined. It would be extremely hard for a human to consider all the subtle changes in the millions of spectra acquired by the FFF systems and find a discerning pattern with that information. Instead, and as will be shown in Sect. 5.2.2, a machine learning algorithm was used to perform this task.

5.2.2 The classification phase

The classification stage runs at the end of each scan and goes through the chemical data gathered and stored in the previous algorithmic stage. It is divided into two levels, which are sequentially run. The first level acts as a filter for the second level, which is comprised of a support vector machine (SVM) classifier, an artificial intelligence supervised learning algorithm.

The first level starts by assembling two signals from the gathered data: one is comprised of the SNR value for each spectrum in the scan and the other is assembled by calculating an average signal energy per pixel, by dividing the sum of the square of each spectrum and by the number of its pixels and sequentially storing this result in an array.

The algorithm then applies a peak detection routine to the second artificial signal. For each detected peak, the system evaluates the SNR of the corresponding spectrum and compares it to a fixed threshold value, which is set in a configuration file. If this value is higher than said threshold, the spectrum is marked to be further analysed.

The next step involves the calculation of column density ratios between O₂, O₄, NO₂, H₂O and O₃ for the marked spectra. These ratios are then fed to the SVM, which returns a binary classification result (1 or 0).

An SVM is an algorithmic approach to the problem of classification in the context of supervised learning (Press et al., 2007). Introduced in 1992, by Boser et al. (1992), this method has since proved itself of great usefulness by providing relatively straightforward solutions to previously complicated classification applications. SVMs are generally easier to implement and understand, and this has also contributed

Table 1. Literature spectra used for the FFF's passive DOAS calculations. All cross sections are downloaded from the MPI-Mainz UV/VIS Spectral Atlas of Gaseous Molecules of Atmospheric Interest (Keller-Rudek et al., 2013).

Compound	Interval used (nm)	Reference key	Year
Oxygen (O ₂)	600–800	Bogumil et al. (2003)	2003
Ozone (O ₃)	500–650	Bogumil et al. (2003)	2003
Oxygen dimmer (O ₄)	400–800	Hermans (2011)	2011
Water vapour (H ₂ O)	400–500	Coheur et al. (2002)	2002
Nitrogen dioxide (NO ₂)	400–500	Vandaele (2002)	2002

for their fast spread. The general concept behind the SVM methodology is to find and define the hyperplane that better separates data into two classes (Press et al., 2007).

Like all supervised learning techniques, SVMs need to be trained prior to being used. In the case of the FFF classification algorithm, SVMs were trained in successive generations, with each generation built upon the results of the previous.

The first FFF SVM generation was built using data from 60 different moments in 2014 (fire and non-fire), in 13 different locations in the Peneda-Gerês National Park (PNPG). A specially designed software tool was used to manually search and store fire data from 30 different events and 30 non-fire moments in said year and an SVM was trained with the resulting information. Another custom-made software was used to classify data of several months with the created SVM. The second-generation SVM was created by repeating the process, taking the results of the first-generation SVM into account and testing against a new set of data.

One downside of using this kind of classifier is that, after training and application, the classification becomes opaque. It is not feasible to understand what caused a false detection. This raises the problem of how to improve the detection capabilities of the FFF system. There are two fundamental approaches to this issue: focusing on the SVM or adding more information to the decision process.

The current line of thought concerning this situation is that, in normal circumstances, the classifier's performance is quite satisfactory. Still, some peculiar events cause the system to issue wrong detections. These events are many times of systematic nature, such as particular kind of cloud that only appears in the early morning or emissions from local industrial facilities. These interferences can be detected themselves, without altering the smoke column detection algorithm, which is where the majority of improvement efforts will be made in the near future (see Sect. 7).

Finally the algorithm reaches the final point, at which it has to say whether the data that were run correspond to a smoke column in the horizon. The spectral information entered to the SVM includes the results from the two chemical processing levels debated in Sect. 5.2.1 and originates three classification possibilities:

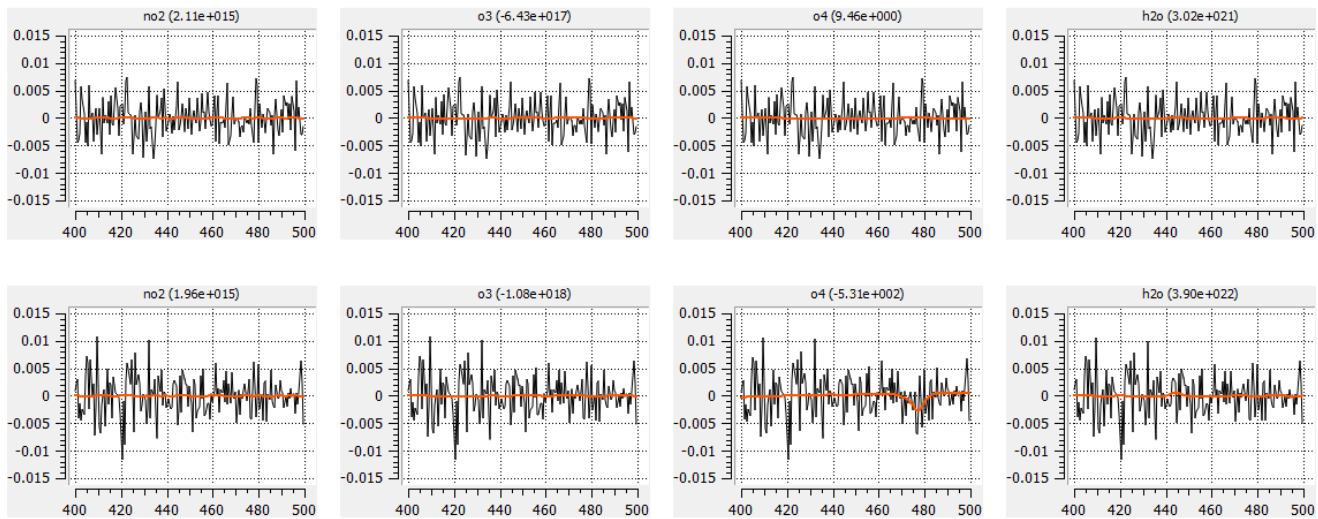


Figure 8. Column densities for NO₂, O₃, O₄ and H₂O, retrieved between 400 and 500 nm. The plots below correspond to a smoke column detection. In these plots, the horizontal axis corresponds to wavelength in nm and the vertical axis to the differential optical thickness.

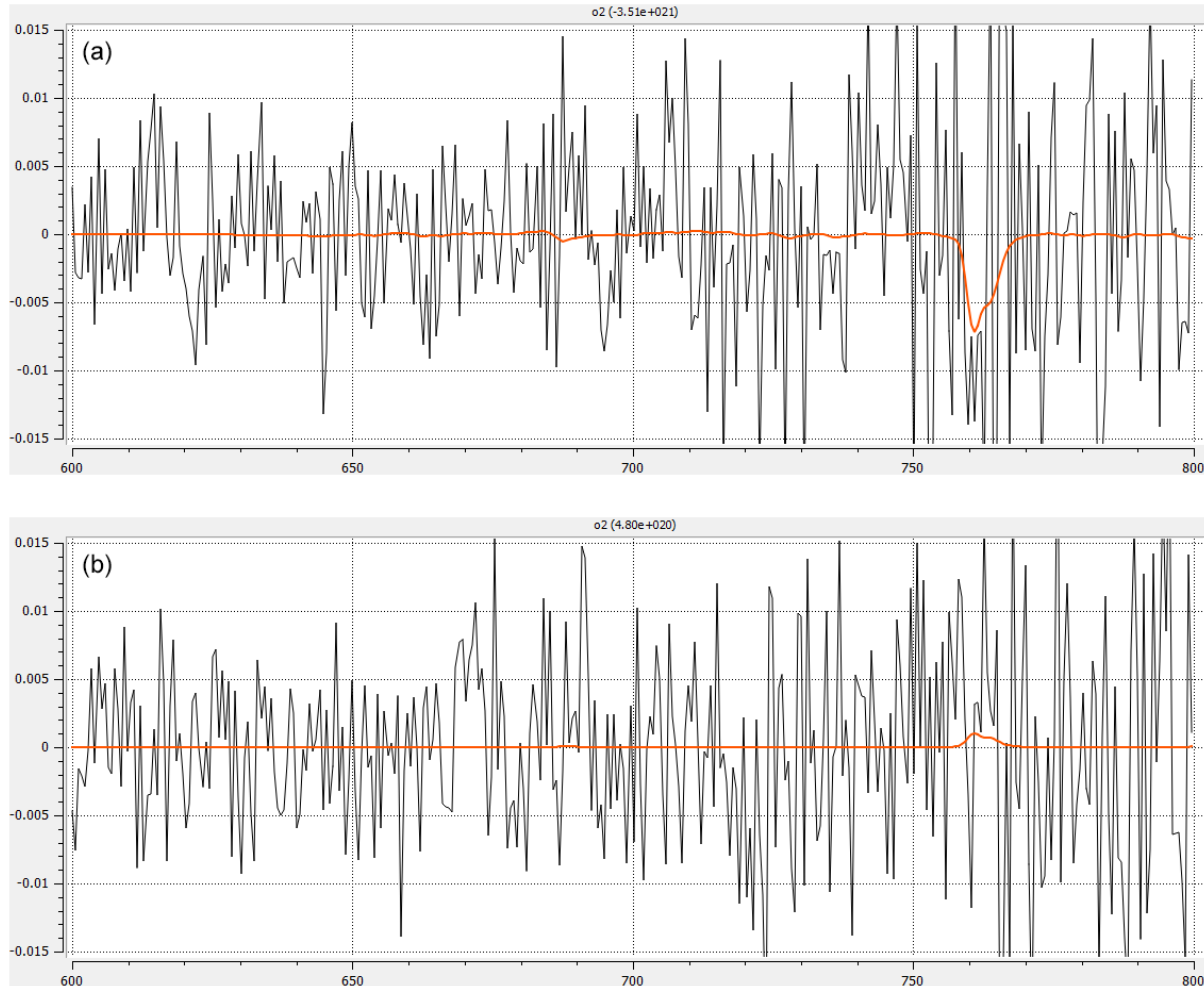


Figure 9. Column density for O₂, retrieved between 600 and 800 nm. The plot below corresponds to a smoke column detection. In these plots, the horizontal axis corresponds to wavelength in nm and the vertical axis to the differential optical thickness.

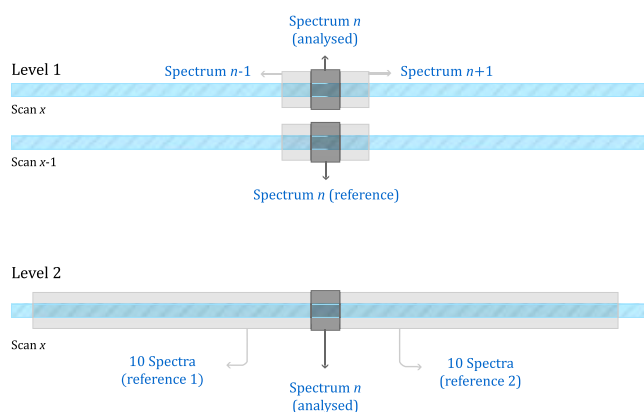


Figure 10. Illustration of FFF's two processing levels in the chemical stage of the algorithm.

- smoke column detected between previous and current scan;
- smoke column detected on the left of analysed spectrum;
- smoke column detected on the right of analysed spectrum.

If two of these classification results are positive, the system issues an alarm.

6 Results and discussion

In 2013, 13 FFF devices were deployed in the PNPG, in the north of Portugal. Their placement reflected topography, local accessibility and fire protection needs.

In 2015, FFF data were gathered and compared to official data from the Portuguese National Authority of Civil Protection (ANPC), the country's institution responsible for forest fire protection and management.

Table 2 shows said data and comparison. In it, a confirmed detection occurs when a smoke column is sensed by an FFF device and the detection is validated by a human operator. This is different from a registered fire event (RFE), which is a fire that was inserted into ANPC's database.

Official statistics count 132 fire events in 2015 within PNPG. During the same period, the FFF network issued 578 detections, of which 369 were false detections, and 209 confirmed events, of which 53 were coincident with RFEs.

Although the false detections may seem to be high in comparison to confirmed detection, it is important to bear in mind that each system has an average working period of 12 h per day. At two spectra per second, this means an average of 86 400 analysed spectra per system per day. Since each and every one of these analysis can trigger an alarm by itself, false detections reach only 0.0000833 % in all systems. In addition, there have been some events that were wrongly

Table 2. FFF statistics for 2015 in the Peneda-Gerês National Park.

Registered fire events	132
Total fire detections	578
False events	369
Confirmed detections	209
Estimated network	56 940
Operation time (h)	
Estimated analysis	409 968 000
False detection %	0.0000900
False alarms per system/day	0.07776607

marked as false detections due to misunderstandings on how the system is to be handled by humans. These events correspond mainly to small fires and prescribed burns, large enough to be detected. Security issues, regarding the Portuguese Civil Protection Authority, prevent the exact quantification of human errors, but they amount to a significant percentage of false alarms.

Although the presented numbers are enough to paint a general picture of the FFF system's behaviour, the available data do not allow a thorough quantification of the system's performance, since there is no correct gold standard regarding forest fires due to fire registry procedures not being clearly established. This becomes exceedingly apparent when comparing the number of RFEs and the number of confirmed detections: every confirmed detection was deemed relevant by a human operator, yet there are only 132 RFEs for the 209 confirmed detections.

Another important result that becomes noticeable in Table 2 is the fact that false positives and true detections vary in similar ways. This can be explained by the fact that the FFF is a spectroscopic system at its heart. Fire releases chemical components into the atmosphere, which in turn are detected by the system. If there are many fires in a small geographic region, such as the PNPG, it is possible that an FFF is able to sense it, without the presence of a visible smoke column in its patrol path. We have also noticed a trend for false alarms on specific cloudy days. We believe this is due to pollutant particles carried by the clouds. Light scattering by these particular clouds sometimes breaches through the system's energy and SNR filters (see Sect. 5.2.1) and is incorrectly classified as a smoke column.

7 Future developments

The FFF has been an ongoing development for NGNS-IS, Ltd. Since 2006, the device has undergone two complete redesign processes, motivated by hardware improvements. The current version is without a doubt the most robust and reliable design ever, achieving uptimes of 99 %. There will always be room for improvement regarding hardware, but given the operating level of the current version these will not be a priority in the near future.

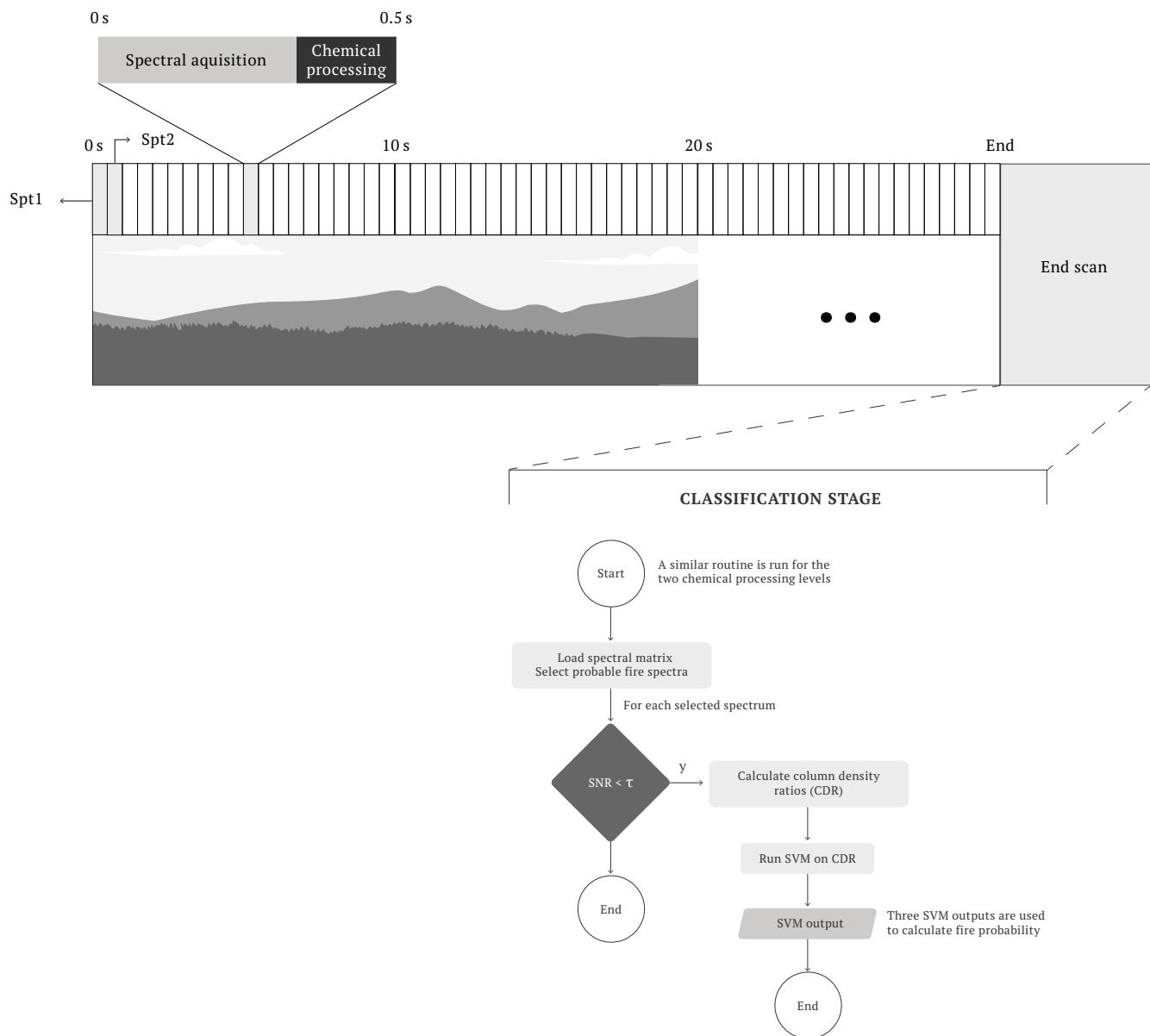


Figure 11. FFF algorithm simplified work-flow diagram.

The software architecture selected for the system allows total freedom for future development needs, with minimal integration efforts. As stated in Sect. 4, this was a requirement because most customers need some level of customisation.

As mentioned in Sect. 5, the FFF is subject to a number of strict time constraints, mostly related to the real-time nature of the system. As a consequence, one of our ever-present goals is algorithm optimisation. Currently, the spectral algorithms are being rewritten, with the inclusion of more features in less processing time. It is also true that as computers become more powerful, it is possible to add more details to the algorithms.

Another line of research currently being pursued is the study of false positives and their relation to the presence of aerosols in the atmosphere. These developments are, however, entirely dependent on the optimisation, since it is currently not possible to add this functionality without sacrificing real-time operation.

DOAS (see Sect. 3) is a widely used atmospheric analysis technique, with much broader uses than just fire sensing. In fact, the technique is used for urban air pollution monitoring (OPSIS, 2016), almost-real-time volcanic plumes monitoring for aviation control (Brenot et al., 2014) and quantification of volcanic gases (Galle et al., 2010). The experience attained while developing FFF allowed the creation of another

project, called Project ATMOS, designed to monitor and control air pollution, crop maturity, water stress and agricultural plagues. This project started in April 2016 and is expected to conclude in September 2019.

8 Conclusions

Life on Earth is greatly influenced and shaped by fire events. Humans in particular depend on fire to maintain their technology and way of life. However, forest fires are a global menace that cause concern all over the world. Several industrialised countries have allocated a great deal of resources to researching wildfires and their behavioural dynamics.

It is this concern that generates a very large market for remote sensing equipment for early forest fire detection, a market which is expected to grow 11.53 % by 2020.

This article addresses one of such equipments. The FFF was developed in Lisbon in 2006 by NGNS-IS, Ltd. and is the only one that is based on optical spectroscopy, particularly differential optical absorption spectroscopy.

In 2013, a 14-element network of FFF devices was installed in the Peneda-Gerês National Park. In 2015, this network was able to detect a confirmed 209 fire events, a number significantly higher than the officially registered 132 fire occurrences in the same region.

For the same period the system has issued 369 false detections, but it is worth considering that confirmed and false detections have similar trends. This is due to the fact that fires pollute the atmosphere with the chemicals that the system aims to detect and is in agreement with the device's operating physical principle, optical spectroscopy.

Evaluation of a fire detection system is a very difficult task. There is no formal definition of how large a forest fire must be to be considered an event and this means there is no perfect classification model (a gold standard) to compare the system's performance to.

The FFF is an automatic forest fire detection system which has proven itself to be effective and detected a great number of forest fires (see Table 2 in Sect. 6). In addition, the system's current hardware and software configuration has resulted in extremely high uptime levels, contributing for an adequate fire detection coverage and, consequently, optimal levels of fire protection.

Data availability. The data used in this paper are not publicly available nor are we authorised to make them so.

Competing interests. The authors are affiliated with NGNS, which developed the Forest Fire Finder system and may be affected by the research reported in the enclosed paper.

Acknowledgements. The authors would like to thank the NGNS team for their support, especially Hélia Pinto, for the numerous drawings and diagrams. This work was funded in part by the FCT PhD grant PD/BDE/114549/2016 and by the FEDER-3491 project, through Lisbon's Operational Program LISBOA2020.

Edited by: M. Van Roozendael
Reviewed by: two anonymous referees

References

- Alkhatib, A. A. A.: A review on forest fire detection techniques, International Journal of Distributed Sensor Networks, 2014, 597368, <https://doi.org/10.1155/2014/597368>, 2014.
- Bevington, P. R. and Robinson, D. K.: Data Reduction and Error Analysis for the Physical Sciences, 2003.
- BNHCRC: Bushfire & Natural Hazards CRC, available at: <http://www.bnhcrc.com.au/home>, last access: 10 May 2016.
- Bogumil, K., Orphal, J., Homann, T., Voigt, S., Spietz, P., Fleischmann, O., Vogel, A., Hartmann, M., Kromminga, H., Bovensmann, H., Frerick, J., and Burrows, J.: Measurements of molecular absorption spectra with the SCIAMACHY pre-flight model: instrument characterization and reference data for atmospheric remote-sensing in the 230–2380 nm region, J. Photoch. Photobio. A, 157, 167–184, [https://doi.org/10.1016/S1010-6030\(03\)00062-5](https://doi.org/10.1016/S1010-6030(03)00062-5), 2003.
- Boser, B. E., Guyon, I. M., and Vapnik, V. N.: A training algorithm for optimal margin classifiers, in: Proceedings of the fifth annual workshop on Computational learning theory – COLT '92, ACM Press, New York, New York, USA, 144–152, <https://doi.org/10.1145/130385.130401>, 1992.
- Brenot, H., Theys, N., Clarisse, L., van Geffen, J., van Gent, J., Van Roozendael, M., van der A, R., Hurtmans, D., Coheur, P.-F., Clerbaux, C., Valks, P., Hedelt, P., Prata, F., Rasson, O., Sievers, K., and Zehner, C.: Support to Aviation Control Service (SACS): an online service for near-real-time satellite monitoring of volcanic plumes, Nat. Hazards Earth Syst. Sci., 14, 1099–1123, <https://doi.org/10.5194/nhess-14-1099-2014>, 2014.
- Brinkmann, R. T.: Rotational Raman scattering in planetary atmospheres, Astrophys. J., 154, 1087–1093, <https://doi.org/10.1086/149827>, 1968.
- Chance, K. V. and Spurr, R. J. D.: Ring effect studies: Rayleigh scattering, including molecular parameters for rotational Raman scattering, and the Fraunhofer spectrum, Appl. Opt., 36, 5224, <https://doi.org/10.1364/AO.36.005224>, 1997.
- Coheur, P.-F., Fally, S., Carleer, M., Clerbaux, C., Colin, R., Jenouvrier, A., Mérienne, M.-F., Hermans, C., and Vandaele, A. C.: New water vapor line parameters in the 26000-region, J. Quant. Spectrosc. Ra., 74, 493–510, [https://doi.org/10.1016/S0022-4073\(01\)00269-2](https://doi.org/10.1016/S0022-4073(01)00269-2), 2002.
- Danckaert, T., Fayt, C., Van Roozendael, M., de Smedt, I., Letocart, V., Merlaud, A., and Pinardi, G.: QDOAS, available at: <http://uv-vis.aeronomie.be/software/QDOAS/> (last access: 12 June 2017), 2015.
- Envirovision Solutions: Forestwatch by EnviroVision Solutions, EVS, 4th Wildfire Detection Workshop, 11–12 March 2015, Edmonton, Alberta, Canada, 2015.

- European Comission: Catalogue of EU funded projects in Environmental research, 0, 2012.
- Food and Agriculture Organisation (FAO): Fire management – global assessment 2006, FAO Forestry Paper 151, 135 pp., available at: <http://www.fao.org/docrep/009/a0969e/a0969e00.htm> (last access: 12 June 2017), 2007.
- Galle, B., Johansson, M., Rivera, C., Zhang, Y., Kihlman, M., Kern, C., Lehmann, T., Platt, U., Arellano, S., and Hidalgo, S.: Network for Observation of Volcanic and Atmospheric Change (NOVAC) – A global network for volcanic gas monitoring: Network layout and instrument description, *J. Geophys. Res.-Atmos.*, 115, 1–19, <https://doi.org/10.1029/2009JD011823>, 2010.
- Grainger, J. F. and Ring, J.: Anomalous Fraunhofer Line Profiles, *Nature*, 193, 762–762, <https://doi.org/10.1038/193762a0>, 1962.
- Hermans, C.: Collisionally induced absorption spectrum of oxygen attributed to the oxygen dimer (O₂)₂, Tech. rep., BIRA-IASB Spectroscopy Lab, available at: <http://spectrolab.aeronomie.be/index.htm> (last access: 12 June 2017), 2011.
- Hough, G.: Vision Systems for Wide Area Surveillance: ForestWatch – a long-range outdoor wildfire detection system, in: TASSIE FIRE Conference Proceedings, <https://doi.org/10.1017/CBO9781107415324.004>, 2007.
- IPCC: Managing the risks of extreme events and disasters to advance climate change adaptation, <https://doi.org/10.1596/978-0-8213-8845-7>, 2012.
- IQ-Wireless: FireWatch, available at: <http://www.fire-watch.de/>, last access: 19 May 2016.
- Keller-Rudek, H., Moortgat, G. K., Sander, R., and S'renzen, R.: The MPI-Mainz UV/VIS Spectral Atlas of Gaseous Molecules of Atmospheric Interest, *Earth Syst. Sci. Data*, 5, 365–373, <https://doi.org/10.5194/essd-5-365-2013>, 2013.
- Liyang, Y., Wang, N., and Meng, X.: Real-time forest fire detection with wireless sensor networks, in: Proceedings, 2005 International Conference on Wireless Communications, Networking and Mobile Computing, 2, 1214–1217, <https://doi.org/10.1109/WCNM.2005.1544272>, 2005.
- Manyangadze, T.: Forest fire detection for near real-timemonitoring using geostationary satellites, International Institute for Geo-Information Science and Earth Observation, MSc, 80, 2009.
- Merlaud, A.: Development and use of compact instruments for tropospheric investigations based on optical spectroscopy from mobile platforms, Books.Google.Com, 2013.
- NGNS-IS, L.: Long range fire detection exclusive solution, available at: <http://www.ngns-is.com/products/ngns-all-over/forest-fire-finder>, last access: 10 May 2016.
- OPSIS: Opsiis, availabel at: <http://www.opsis.se/Aboutus/tabid/996/Default.aspx>, last access: 19 May 2016.
- Platt, U. and Stutz, J.: Differential Optical Absorption Spectroscopy, Springer, Heidelberg, Germany, 2007.
- Press, W. H., Teukolsky, S. A., Vetterling, W. T., and Flannery, B. P.: Numerical Recipes: The Art of Scientific Computing, 3rd Edn., 2007.
- Research and Markets: Fire Protection Systems Market by Technology (Active, Passive), Product (Fire Detection (Sensors & Detectors, RFID), Management (Fire Sprinklers, Extinguishers), Fire Analysis & Response), Service, Vertical, and Geography – Global Forecast to 2022, Tech. rep., Research And Markets, avaible at: <http://www.researchandmarkets.com/reports/3696148/fire-protection-systems-market-by-technology> (last access: 12 June 2017), 2016.
- Spichtinger, N., Damoah, R., Eckhardt, S., Forster, C., James, P., Beirle, S., Marbach, T., Wagner, T., Novelli, P. C., and Stohl, A.: Boreal forest fires in 1997 and 1998: a seasonal comparison using transport model simulations and measurement data, *Atmos. Chem. Phys.*, 4, 1857–1868, <https://doi.org/10.5194/acp-4-1857-2004>, 2004.
- United States Forest Department: The Rising Cost of Fire Operations: Effects on the Forest Service's Non-Fire Work, United States Department of Agriculture, 13 pp., available at: <http://www.fs.fed.us/sites/default/files/media/2014/34/nr-firecostimpact-082014.pdf> (last access: 12 June 2017), 2015.
- Urbanski, S. P., Hao, W. M., and Baker, S.: Chapter 4 Chemical Composition of Wildland Fire Emissions, *Develop. Environ. Sci.*, 8, 79–107, [https://doi.org/10.1016/S1474-8177\(08\)00004-1](https://doi.org/10.1016/S1474-8177(08)00004-1), 2008.
- van der Werf, G. R., Randerson, J. T., Giglio, L., Collatz, G. J., Mu, M., Kasibhatla, P. S., Morton, D. C., DeFries, R. S., Jin, Y., and van Leeuwen, T. T.: Global fire emissions and the contribution of deforestation, savanna, forest, agricultural, and peat fires (1997–2009), *Atmos. Chem. Phys.*, 10, 11707–11735, <https://doi.org/10.5194/acp-10-11707-2010>, 2010.
- Vandaele, A. C.: High-resolution Fourier transform measurement of the NO₂ visible and near-infrared absorption cross sections: Temperature and pressure effects, *J. Geophys. Res.*, 107, 4348, <https://doi.org/10.1029/2001JD000971>, 2002.
- Ward, D. E. and Hardy, C. C.: Smoke emissions from wildland fires, *Environment International*, 17, 117–134, [https://doi.org/10.1016/0160-4120\(91\)90095-8](https://doi.org/10.1016/0160-4120(91)90095-8), 1991.

C

**TOMOSIM: A TOMOGRAPHIC SIMULATOR
FOR DIFFERENTIAL OPTICAL ABSORPTION
SPECTROSCOPY**

Article

TomoSim: A Tomographic Simulator for Differential Optical Absorption Spectroscopy

Rui Valente de Almeida ^{1,2,*}, Nuno Matela ³ and Pedro Vieira ¹

¹ Physics Department, FCT NOVA, NOVA University of Lisbon, 2829-516 Caparica, Portugal; pmv@fct.unl.pt

² FutureCompta SA, 1495-190 Algés, Portugal

³ Biomedical Engineering and Biophysics Institute, University of Lisbon, 1749-016 Lisbon, Portugal; nmatela@fc.ul.pt

* Correspondence: rf.almeida@campus.fct.unl.pt

Abstract: TomoSim comes as part of project ATMOS, a miniaturised Differential Optical Absorption Spectroscopy (DOAS) tomographic atmospheric evaluation device, designed to fit a small drone. During the development of the project, it became necessary to write a simulation tool for system validation. TomoSim is the answer to this problem. The software has two main goals: to mathematically validate the tomographic acquisition method; and to allow some adjustments to the system before reaching final product stages. This measurement strategy was based on a drone performing a sequential trajectory and gathering projections arranged in fan beams, before using some classical tomographic methods to reconstruct a spectral image. The team tested three different reconstruction algorithms, all of which were able to produce an image, validating the team's initial assumptions regarding the trajectory and acquisition strategy. All algorithms were assessed on their computational performance and their ability for reconstructing spectral "images", using two phantoms, one of which custom made for this purpose. In the end, the team was also able to uncover certain limitations of the TomoSim approach that should be addressed before the final stages of the system.

Keywords: atmospheric monitoring; DOAS; tomography; UAV; drone



Citation: Valente de Almeida, R.; Matela, N.; Vieira, P. TomoSim: A Tomographic Simulator for Differential Optical Absorption Spectroscopy. *Drones* **2021**, *5*, 3. <https://doi.org/10.3390/drones5010003>

Received: 13 November 2020

Accepted: 21 December 2020

Published: 29 December 2020

Publisher's Note: MDPI stays neutral with regard to jurisdictional claims in published maps and institutional affiliations.



Copyright: © 2020 by the authors. Licensee MDPI, Basel, Switzerland. This article is an open access article distributed under the terms and conditions of the Creative Commons Attribution (CC BY) license (<https://creativecommons.org/licenses/by/4.0/>).

1. Introduction

1.1. Background and Motivation

This article details the construction of TomoSim, which is the software simulation package used in the ATMOS project, a Portuguese European Union (EU) funded initiative that aimed at creating a miniaturised spectroscopy platform for atmospheric monitoring and trace gas mapping. The project was a joint effort from Compta, S.A., one of the oldest IT groups in Portugal; and FCT NOVA, from the NOVA University of Lisbon, also one of the largest and most important science schools in the country.

The idea of using a tomographically capable drone with spectroscopic equipment for mapping trace gas concentrations in defined geographical regions made the need for a simulation tool evident from a very early stage. Any monitoring device that depends on drones for the actual measurements must take into account a number of restrictions, of both physical and logistical order (weight, battery life, etc.). These considerations are even more important if the measurements themselves depend on the ability of the drone to move and position itself a certain way and the precision with which it can do so. For the ATMOS project, they were paramount. Simulation is a simple and inexpensive way of determining the technical feasibility of the project and the mathematical validity of the reconstruction strategy.

This strategy is based on two premises:

- A custom-equipped drone should be able to measure trace gas column density in a carefully programmed sequence;

- One can then organise these measurements into an array.

These column density values could then be used as projections in a tomographic reconstruction. The resulting image would correspond to the geographic distribution of the target trace gases.

The simulator, built in Python [1] and using NumPy [2], uses the system's premise and applies three algorithms for reconstruction: fan beam Filtered BackProjection (FBP), Simultaneous algebraic Reconstruction Technique (SART) and Maximum Likelihood Expectation Maximisation (MLEM). Algorithm verification and analysis was performed using a custom-designed phantom for DOAS spectral measurements. All three mathematical algorithms managed to reconstruct the image. FBP was shown to be significantly more computationally cost-effective than the other two. The custom coded MLEM routine was not on-par with the other two solutions, which were plugged directly from the SciPy library.

Besides runtime and other significant software engineering considerations, the development of TomoSim concluded that the assumptions of the team regarding the acquisition strategy for spectral geographic images were correct, but lifted the veil on some limitations that should be addressed before building the final system.

The paper is structured as follows: the section after this introduction, Section 1, targets the theoretical background with which the paper was built; Section 2 describes the design, the rationale behind it and the technical choices that have been taken in the making of TomoSim; in Section 3 there is a description of the results that were obtained through the simulator, including reconstructions, running times and Section 5 is dedicated to the conclusions that were taken using this piece of software, as well as some foreseeable future developments.

1.2. Differential Optical Absorption Spectroscopy (DOAS)

DOAS is a widely used atmospheric analysis technique, developed in the late 1960s. Fundamentally, it is an absorption spectroscopy technique, therefore based on Lambert-Beer's law. This law was actually first formulated by Pierre Bouguer in 1729. At the time, he wrote that "in a medium of uniform transparency, the light remaining in a collimated beam is an exponential function of the length of the path in the medium" [3]. This theory can thus be written as in Equation (1).

$$I(\lambda) = I_0(\lambda) \cdot \exp(-\sigma(\lambda) \cdot c \cdot L). \quad (1)$$

$I_0(\lambda)$ is the source intensity of a light beam, $I(\lambda)$ the intensity of the light that reaches the detector, σ is the absorption cross-section of the chemical compound being measured, c its concentration and L the optical path of the light (the length of the path that is traversed by the ray of light). Finally, λ is the wavelength of the radiation.

The rearrangement of Equation (1) gives us the concentration, and more importantly, allows us the creation of a new quantity, τ , which is called *optical depth*. This is explicit in Equation (2) [4,5].

$$c = \frac{\ln\left(\frac{I_0(\lambda)}{I(\lambda)}\right)}{\sigma(\lambda) \cdot L} = \frac{\tau}{\sigma(\lambda) \cdot L}. \quad (2)$$

In the laboratory, this equation can be (and is) used directly and with few obstacles, since there are very few uncontrolled variables, and that which exists is controlled for. In the open atmosphere, this is not the case at all.

There are many factors that influence the degree to which we can apply Lambert-Beer's rule in atmospheric measurements. The most important one is the fact that in order to know the source intensity ($I_0(\lambda)$), one would have to remove any and every absorber from optical path, and this is clearly infeasible in the great majority of circumstances. To surpass this problem, DOAS measures differences between absorption structures at many different wavelengths [5].

There are many different DOAS systems, but the single greatest distinction among them is whether they are active or passive. Active systems use artificial light sources such

as a Xenon lamp to measure chemicals in the air. Passive systems use natural sources, such as the Sun or the Moon (or other celestial bodies). This paper will focus on passive systems, since the ATMOS project is a scattered sunlight DOAS system, and thus passive.

Scattered sunlight DOAS systems have their own specific particularities and special properties. For instance, the optical path is unknown as the last scattering event cannot be determined. Scattering also implies that there is a fraction of the source's light that does not reach the detector. Moreover, one must account for all the other passive DOAS common effects, such as the fact that there are many absorbers that have spectral structures overlapping the target species; that there are Fraunhofer lines, Mie and Rayleigh scattering, turbulence and instrumental effects, and so forth [5,6].

All these influential effects mean that, in the open atmosphere, Equation (3) is a more plausible model than that presented in Equation (1).

$$I(\lambda) = I_0(\lambda) \cdot A(\lambda, \dots) \cdot \exp \left[- \int_s \left(\sum_i \sigma_i(\lambda, s) \cdot c_i + \epsilon_M(\lambda, s) + \epsilon_R(\lambda, s) \right) ds \right]. \quad (3)$$

In Equation (3), there is more than one absorber, which is denoted by index i in the sum. $A(\lambda, \dots)$ denotes the fraction of light that gets scattered into the detector, ϵ_M and ϵ_R are Mie and Rayleigh scattering coefficients, and the integral is performed on the whole optical path, s .

Typically, we measure a trace gas's atmospheric contribution by its total column. This quantity is essentially the integral of the compound's number density, in molecules/cm³, over a column that goes from the ground to the Top Of the Atmosphere (TOA). In Equation (4), the number density for molecule x is denoted c_x .

$$C_x = \int_0^{TOA} c_x(z) dz. \quad (4)$$

One can look again at Equation (3) with the interest of quantifying only the trace gas contribution. This contribution should be somehow related to the total column, since the only real difference between what the DOAS instruments see and the total column is the dependence on the optical path of the former. In fact, we can separate the integral to get the trace absorbers optical density expression, displayed in Equation (5). Since we can consider the cross-section to be fairly constant with the optical path, it is possible to separate this integral, and we arrive at the very important value of the slant column, SC_i , which is the integral of the gas's number density along the optical path.

$$SC_i = \int_s c_i(s) ds. \quad (5)$$

If we integrate the absorption coefficients inside the exponential term of Equation (3) to their optical densities, we arrive at the expression in Equation (6). This equation cannot be solved without some very seldomly available data, such as the original light source I_0 . DOAS allows us to overcome this problem by making relative measurements (hence the differential in the name of the technique), using another scattered light spectrum as reference and by observing that most interesting trace gases have very narrow spectral structures, while effects like Mie and Rayleigh scattering have broad spectral features.

$$\ln \left(\frac{I_{ref}}{I} (\lambda) \right) = \ln \left(\frac{A_{ref}}{A} \right) + \sum_i \sigma_i(\lambda) \cdot \Delta SC_i + \tau_R(\lambda) + \tau_M(\lambda). \quad (6)$$

I_{ref} and A_{ref} are, respectively, the reference light intensity and reference scattered light ratio and τ_R and τ_M the integrated optical depth of the Rayleigh and Mie scattering phenomena. It is thus possible to separate the original optical depth in two parts, a differential part, which is comprised of the narrowband contributions coming mainly from trace gases; and the “continuous” part, which contains the slow-variation, broadband contributions

in Equation (3). The latter can be approximated by fitting a low order polynomial to the original optical depth signal. If one subtracts this polynomial from the optical depth, the result is the narrowband signal that constitutes the differential part. Target absorbers column densities can then be found by fitting their cross-sections to the differential signal, using a numerical algorithm such as Levenberg-Marquardt's [7].

This small introduction to the topic of DOAS is more than enough to explain and understand the rest of this article regarding the spectroscopic procedures. References [5,6] contain a more thorough coverage of the topic, both with reference to the technique's physics and instrumental considerations.

1.3. The Tomography Problem

1.3.1. Introduction

Tomography is the cross-sectional imaging of an object through the use of transmitted or reflected waves, collected by the object exposure to the waves from a set of known angles. Tomography has many different applications in science, industry, and in particular, medicine. Since the invention of the Computed Tomography (CT) machine, in 1972 by Hounsfield [8], tomographic imaging techniques have had a revolutionary impact, allowing doctors to see inside their patients without having to subject them to surgical interventions. Examples of tomographic applications for scientific and industrial purposes include radio-astronomy and certain kinds of tomographic non-destructive test techniques [9].

Tomography has had its mathematical basis set by Johannes Radon, a German mathematician that proved that it is possible to represent a function in \mathbf{R} (the domain of the real numbers) in the space of straight lines L through its line integrals. In the tomographic case, these integrals represent a measurement on a ray that is traversing the field of analysis. Each set of line integrals (rays), characterised by a given projection angle, is called a projection. The set of all projections, arranged in matrix form by projection angle and detector is called a sinogram. All reconstruction methods revolve around this matrix [9–11].

1.3.2. Discretisation

Siddon's algorithm [12], published in 1985, is one of the most common and most studied ways to go from the naturally analogical presentation of the real world into computer-operable discrete geometric fields of vectors, in the field of tomography. The algorithm considers each pixel to be the intersection area of orthogonal sets of equally spaced parallel planes. With this in mind, it is possible to parametrise a ray of light, with the ray being written (in two dimensions):

$$\begin{aligned} X(\alpha) &= X_1 + \alpha(X_2 - X_1) \\ Y(\alpha) &= Y_1 + \alpha(Y_2 - Y_1). \end{aligned} \quad (7)$$

In Equation (7), X_1 and Y_1 are the coordinates for the entry point (of the ray in the analysis field) and X_2 and Y_2 are the exit point coordinates. α is the parametric value. If the ray is totally contained within the field of analysis, this value varies between 0 and 1; otherwise, it has its minimum at the entry point and maximum at the exit.

The parametrical representation of the line integral, allows one to recursively calculate all intersections between the ray and the grid defined by the orthogonal lines described above. The differences between intersection points render the lengths of each ray contained within each pixel. The sum of all the lengths for one ray yields the total value of the line integral, which corresponds to a projection. The algorithm steps are presented in Algorithm 1 [12,13].

1.3.3. Geometry

The application of analytical algorithms such as FBP depends on the type of geometric arrangement of the tomographic problem. TomoSim uses two tomographic geometries in its reconstructions: parallel and fan beam.

Algorithm 1: Siddon's algorithm's procedural steps. After running this algorithm, one is able to represent any continuous ray through the analysis field as a sum of discrete lengths

Result: Discretised Region of Interest(ROI).

- calculate range of parametric values;
 - calculate range of pixel indices;
 - calculate parametric sets;
 - merge sets;
 - calculate pixel(or voxel) lengths;
 - calculate pixel indices;
-

Parallel Projection geometry (see Figure 1) is the most basic assembly. In this arrangement, each projection is a set of parallel line integrals, as can be seen in Figure 1. The radiation sources can be assembled in a linear array, facing detectors in the same number on the opposite side of the target object, or, in alternative, a single source can move in a linear trajectory, directing its rays onto an array of detectors, linearly arranged on the opposite side of the target object. Projections of this sort are characterised by the projection angle, which is the angle each ray makes with the vertical axis. The other relevant geometric assembly is the fan beam arrangement (see Figure 1). In this projection mode, all radiation in the projection comes from a single source, with rays being directed outwards onto a set of detectors, which may be arranged on a circumference arc (equiangular rays) or on a straight line (equally spaced rays) [9].

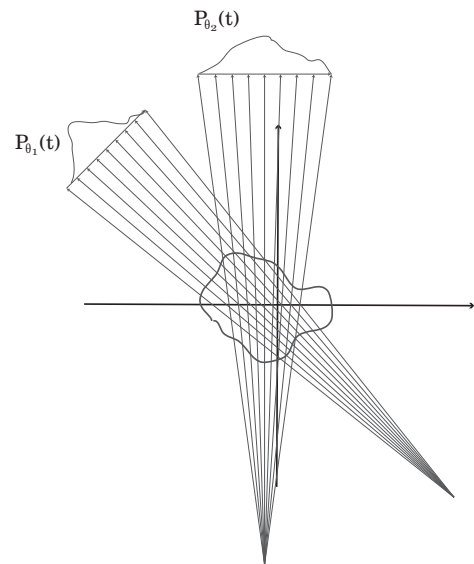


Figure 1. *Cont.*

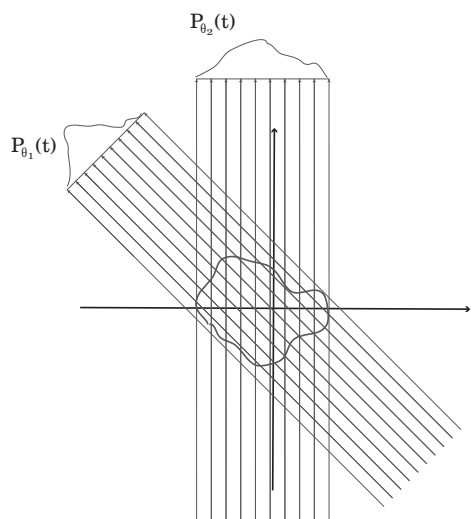


Figure 1. Fanbeam and Parallel geometric assemblies for a tomographic experiment (respectively, left to right). Note that the figures are only meant to exemplify how these assemblies are widely different, and therefore do not have scales or any angular data.

1.3.4. Reconstruction

The overarching division between tomographic reconstruction algorithms is on the level of their nature, which can be analytical or algebraic (iterative). Other subdivisions come from the geometry and the type of technology used for the particular application on which reconstruction is being run. In medical imaging, the most common analytical method is the Filtered BackProjection algorithm (FBP). FBP is based on Fourier's Slice Theorem, which states that the one dimensional Fourier Transform (FT) of a projection at a given angle is the two dimensional FT of the reconstructed image through that same angle [9,14]. If a sufficient number of projections is gathered, one can create a good estimate of the image by performing a 1D FT of the projections, and inverting them in 2D, before summing them in the image space. It so happens that this direct inversion process produces heavily distorted images due to the fact that calculation errors are typically larger the higher the frequency of the image component [9]. This is overcome in FBP by the application of a weighing filter before the inversion process.

This sequence of steps is sufficient for parallel projection reconstruction, but for fan beam projections, the FBP can only be applied after a series of somewhat cumbersome geometric transformations. If this is not acceptable, for some reason, there is an alternate solution: the fan beam sinogram can be reorganised, based on the observation that a ray in a fan beam is equal to a ray in a parallel projection in another given angle. Of course this resorting operation will not render a perfect sinogram for this new parallel projection (since not every fan ray has a direct parallel ray correspondent), but imperfections can be normally corrected through interpolation. After this procedure is run, one can proceed as if the geometry were parallel [9,11,15].

Iterative algorithms are based on simpler premises, but require a different mindset. The set of projections can be thought of as a matrix, called sinogram, as has been introduced in this same section. In this matrix, the lines refer to the projection number, and the columns deal with the detectors (for instance, the first line of this matrix corresponds to all detections in the first projection). The image can also be thought of as a matrix, in which each pixel has a given value, which gives it its intensity (and/or colour). Finally, there is the system matrix, which is the matrix that contains the lengths of every ray in each projection contained in each one of the image's pixels, lengths which are obtained, in this case, through Siddon's algorithm, already presented. Iterative algorithms, in general, attempt to solve Equation (8). In it, $\mathbf{g} \in \mathbb{R}^{m,1}$ is the column vector sinogram, $\mathbf{a} \in \mathbb{R}^{m,n}$ is the system matrix and $\mathbf{f} \in \mathbb{R}^{n,1}$ is the column vector image. m is the number of measurements (projections times detectors)

and n is the number of pixels in the image. As their designation implies, iterative algorithms produce an estimation for \mathbf{f} which is updated in the direction of error minimisation in every iteration [9,10].

$$\mathbf{g} = \mathbf{a} \cdot \mathbf{f}. \quad (8)$$

The popularity of algebraic reconstruction methods has not remained constant throughout the years. For a long time, they have been considered too computationally intensive to use in a clinical setting (paradoxically, Hounsfield's machine used this kind of algorithm). This was in direct opposition to the fact that researchers know that these methods are better able to model reconstruction since Shepp and Vardi published the maximum likelihood tracer estimation in 1982. Nowadays, and since the mid nineties, these algorithms are the first choice whenever the reconstruction dataset is not too large to process using the available computational capabilities [15].

The general goal of iterative reconstruction algorithms is to solve Equation (8) [10]. In principle, any method that solves it can be used for image reconstruction in tomography. In reality, however, only a few are currently in use by the community. Of these, TomoSim uses two of the most prominent: Simultaneous Algebraic Reconstruction Technique (SART) and Maximum Likelihood Expectation Maximisation (MLEM).

SART was presented in 1984 by Andersen and Kak [16] and the global idea is that the estimated image is corrected for all projections at the same time (in opposition to the original algebraic Reconstruction Technique, in which corrections were applied for each single projection). Iterations in SART change the estimated image according to Equation (9), iterating on k .

$$\mathbf{g}_i^{(k+1)} = \mathbf{g}_i^{(k)} + \frac{\sum_j \left[\mathbf{a}_{ij} \cdot \frac{p_j - \mathbf{a}_j^T \cdot \mathbf{g}^{(k)}}{\sum_{i=1}^n \mathbf{a}_{ij}} \right]}{\sum_j \mathbf{a}_{ij}}. \quad (9)$$

MLEM algorithms were first published in the medical imaging community in 1982, by Shepp and Vardi [17]. With this algorithm, image corrections are ruled by Equation (10), which also iterates over k .

$$\mathbf{f}_j^{k+1} = \frac{\mathbf{f}_j^k}{\sum_{i=1}^n \mathbf{a}_{ij}} \sum_{i=1}^n \frac{\mathbf{g}_i}{\sum_{j'=1}^m \mathbf{a}_{ij'} \mathbf{f}_{j'}^k}. \quad (10)$$

This equation is very easy to implement computationally, if one observes that the sums of the second multiplication term expand neatly onto matrix products. In the end, this equation is the equivalent of writing Equation (11), as explained in Reference [10], in which $\text{IMG}^{(k)}$ is the estimated image in the k th iteration, NBP is the Normalised Backprojection operation, RSNG the real sinogram (as in coming from the detector hardware) and SSNG the simulated sinogram, calculated through the previous iteration.

$$\text{IMG}^{(k+1)} = \text{IMG}^{(k)} \times \text{NBP} \left(\frac{\text{RSNG}}{\text{SSNG}^{(k)}} \right). \quad (11)$$

1.4. DOAS Tomography

DOAS tomography is a relatively new field of study within DOAS. It involves, as the name implies, the application of tomographic techniques to the atmospheric studies that are normally conducted through DOAS. The concentration values retrieved through the spectroscopic technique are essentially line integrals in themselves. Therefore, they can be almost immediately considered projections. If one gathers enough of these integrals from a sufficient number of angles, any tomographic algorithm is able to reconstruct an image, which corresponds to a map of concentrations of the target trace gas in the study.

One of the first suggestions of a technique which could be adapted to the DOAS procedures was made in 1979 [18]. However, the first study that applied tomography to DOAS in a significant manner was the BAB-II campaign [19,20]. This was a research

initiative that involved people from the Heidelberg DOAS group and intended to study the temporal evolution of the NO₂ concentration in a bi-dimensional way, along the motorway that connects Heidelberg to Mannheim, in Germany. This campaign led to several publications and is to this day the main “contributor” to tomographic studies with DOAS. More recently, in 2016, Stutz and his team have built and used a similar set-up to study the atmospheric profiles of aromatic hydrocarbons near an refinery plant, in Texas. Their system was composed of a dual-light emitting diode light source, a telescope which acted as emitter and receiver of light and retro-reflector arrays, positioned strategically in the geographic region that was being studied. Although this study was not as extensive as the previously mentioned Heidelberg study, it is also very important, as it proves the practical applicability of the technique to real world problems [21]. Finally, it is worth to mention the paper by Erna Frins, who in 2006 used sun-illuminated targets to perform a tomographic analysis of the region in which her system was positioned, which coincidentally is also Heidelberg. This study is important because it is one of the few that uses scattered sunlight with this technique. Moreover, it also features a very good description of the physics and mathematical approximations that are inherent to the experiments at hand [22].

These studies and more are addressed in another paper, which should be submitted shortly, and in which the authors have conducted a deeper and more systematic literature review on the subject.

2. Materials and Methods

2.1. Device Description

TomoSim is a simulation platform for a drone-mounted atmospheric monitoring system based on DOAS. Although the physical device has not yet been assembled, the team has already compiled a final (or very close) design, which is schematically represented in Figure 2. The reasoning behind the custom design was to increase the maximum payload and allow longer flight times. The team chose to use a DJI S900 frame (hexacopter), manufactured by DJI in China, with custom-made 368 mm carbon fibre arms, longer and lighter than the original. The increased empty space allows the replacement of the default propellers by 17" carbon fibre units, coupled to 6 E1200 motors. This propeller-motor configuration is not only significantly more powerful than the default assembly, but also more efficient. According to the manufacturer [23], this configuration is able to lift and work with payloads exceeding 8 kg, which is much more than we need for data acquisition platform, comprised of the gimbal, a Celera SSIN-06 [24] unit with a maximum pointing error of 2 arcseconds; the telescope, an Omegon MightyMak [25]; and an Avantes Mini spectrometer with 2048 spectral channels [26].

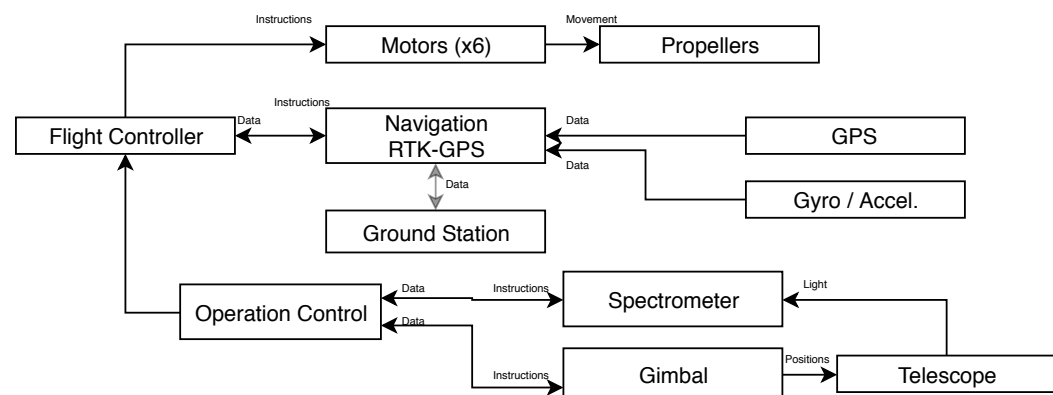


Figure 2. Drone system schematic representation, with component relations.

A Pixhawk flight controller is used to handle and manage aerial dynamics, and also to gather every sensor output in the device. The controller comes with integrated gyroscopes, magnetometers and barometers. The only external sensor that needs to be adapted and purchased separately is the navigation (GPS) unit. The Pixhawk supports Real Time Kinematic GPS (RTK-GPS), a combination of inertial sensors and satellite navigational data that can grant the UAV a positioning precision under 20 cm [27,28]. The flight controller is in permanent communication with the operation controller, which is a Raspberry Pi 0 (or similar) single board computer. This computer stores the flight program and directs the flight controller to each necessary position, and also controls data acquisition through a USB connection to the spectrometer. The device's trajectory will be planned using Arducopter's Python libraries and their Software In The Loop (SITL) simulation platform.

2.2. Data Acquisition

The simulated drone is to describe an unobstructed horizontal circular trajectory with a maximum diameter of 1 km at the intended measurement height, the interior of which is the Region Of Interest (ROI). There are two moments to the data gathering process. Figure 3 attempts to illustrate both.

- **First moment** While flying in this circle, the device stops in a series of positions at a given fixed angular interval (Δ) from each other. The number of stops is defined by Δ and by fan beam information requirements (see Reference [9]) At each one of these stops, the gimbal turns towards the trajectory's interior and points in a series of angular directions that describe an arc. For procedural simplicity, the angle between these directions is also Δ . At each one of these angles, the device's operational controller instructs the spectrometer to acquire a given number of spectra, which depends on configuration and conditions. Besides spectral data, the system algebraically calculates and stores the point in which the light will exit the ROI (see Appendix A).
- **Second moment** The device positions itself in each of the points in which light has exited the ROI in the first moment and the gimbal is pointed towards the entrance point, effectively aiming in the opposite direction to which a spectral measurement took place in the 1st moment. Light that comes from the sun is scattered somewhere in the atmosphere and enters the ROI (at a given angle) in point A. It then traverses the distance AB and leaves the ROI in point B. At these distances and with this kind of geometry, light scattering can be considered negligible [22,29,30] and therefore light extinction will primarily be due to absorption by components between A and B [5]. It should then be possible to apply Lambert-Beer's law to extract trace gases concentrations in the ROI, by considering light at point A as the source intensity (I_0 in Equation (1)) and light at B the final intensity (I in Equation (1)). When the 2nd moment is complete, the system has a set of fan beam distributed spectra, which can be equated to projections in a tomography problem.

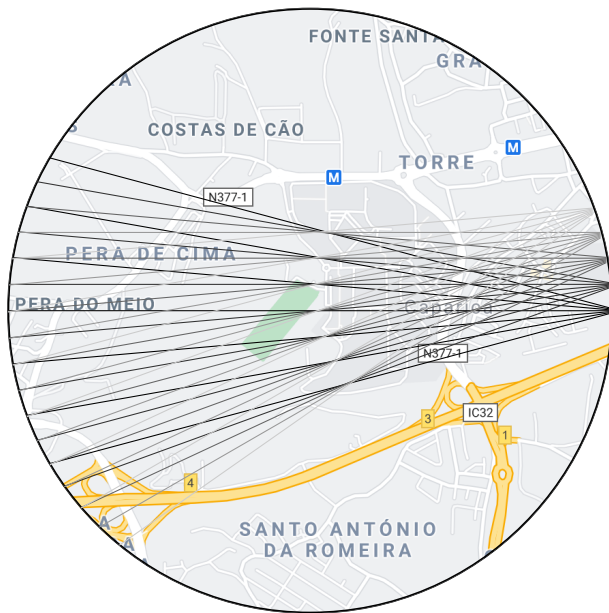


Figure 3. Simplified schematic representation of the first five fans acquired by the drone over the circular trajectory. The drone stops at the vertex of each fan, represented on the right. These points correspond to point A in the explanation of the two measurement moments in Section 2.2. Each line in the drawing represents a ray within a fan, i.e., a direction, in which a projection is taken. The “exit points” of each ray from the ROI correspond to point B, and are represented on the left. In the second measurement moment, the drone moves to each of these points and takes another spectrum in the same direction as the ray itself. Here, both fans and rays are separated by an angular interval of 5 degrees, and there are only 3 rays within each fan, for graphical simplicity. Both values are customisable at runtime. The map, included for example purposes, was retrieved from Google Maps in 2019 ©Google.

2.3. Phantoms

In medicine, a phantom is a model that emulates certain properties of human or animal tissue. Researchers use these models to evaluate therapeutic or diagnostic methods. In the imaging field, phantoms are known matrices with a given size that were designed to mimic the types of bodies that are to be reconstructed with the technique or algorithm being tested. Most phantoms described in the literature were constructed specifically for medical imaging, since this is clearly the most prominent application field for tomographic methods. Computed Tomography phantoms, for instance, intend to mimic the X-ray absorption of the human body, or of part of the human body. Since the distribution of gases in the atmosphere is entirely different from biological tissue's, these phantoms are not adequate for TomoSim. This implied the design of a new phantom, based on the idea that a two-dimensional (in this case) Gaussian peak is more appropriate to describe the smoother nature of the distribution of a gas than a series of sharply defined ellipses [31]. The new phantom, designed with TomoPhantom [32], is comprised of 5 bivariate Gaussian profiles, depicting a static gas mixture, and an ellipse near one corner of the image, which serves as a reference point. This new spectral phantom can be seen in Figure 4, and a descriptive summary is provided in Table 1.

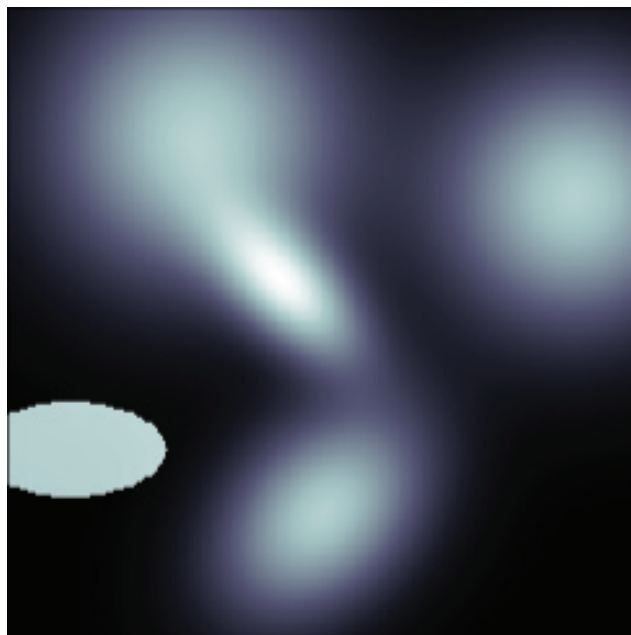


Figure 4. A graphical representation of the new spectral phantom, custom built for the TomoSim application.

Table 1. Table summarising the new phantom's construction details, as a sum of 5 Gaussian profiles and an ellipse designed using TomoPhantom. In this table, C0 is the object's amplitude, X0 and Y0 are its center coordinates, and a and b are the objects half-widths. The table is constructed using TomoPhantom's particular syntax and more information can be obtained in Reference [32].

Type	C0	X0	Y0	a	b	Angle
Gaussian	1	-0.1	-0.1	0.25	0.5	-45
Gaussian	1	0.6	0	0.65	0.45	-45
Gaussian	1	-0.6	-0.4	0.8	0.8	0
Gaussian	1	-0.4	0.8	0.7	0.7	0
Ellipse	1	0.4	-0.8	0.3	0.15	0

During simulation, a phantom is totally contained within the ROI. A gaussian filter (kernel size 5, auto standard deviation) is applied to the phantom image to simulate noise. The phantom shares the same grid as the discretised ROI and each pixel has a value comprehended between 0 and 255. This value is linearly correlated with the number of molecules of the target trace gases in the ROI. Software configuration allows the definition of the maximum number of molecules per pixel. Default value for NO₂, the test case presented in Section 3 is 1×10^{15} molecules.

2.4. Reconstruction

Any tomographic reconstruction requires the previous and detailed knowledge of the ray geometry of the problem. This implies that the space being reconstructed is discretised, so that it can be addressed through computational routines. In this case, the discretisation consists in overlaying a 100×100 pixel grid (10 m square pixels, considering a 1 km diameter circular drone trajectory). By applying Siddon's algorithm to this geometry, the lengths that each ray traverse in each pixel of the grid are retrieved, assembling the system matrix. The system matrix is a complete description of the problem's geometric properties, and is therefore characteristic of each experiment, depending on the angular intervals between projections (Δ in this case) and on the size and number of the pixels in the discretisation grid.

TomoSim then performs a resorting operation on the sinogram, in order to transform the fan beam projections into parallel projections, greatly simplifying image reconstruction.

Since the angular interval between the fans and the rays within the fans is the same (Δ), resorting is greatly simplified [9]. After discretisation and the necessary resorting steps are taken, the software reconstructs the images with three different algorithms—MLEM, FBP and SART.

Finally, after the images are calculated, the simulator must convert the pixel values back into molecule numbers. For this, the software runs Siddon algorithm on the reconstructed images for a selected number of angles. Resulting projection values are then compared with the projection values of the original images in order to find a converting parameter that allows the presentation of accurate concentration values.

2.5. Error Estimation

There are three major error sources in TomoSim—geometric errors, spectroscopic errors and reconstruction errors. Geometric errors come from the fact that the device's positioning has an associated error: the drone is not where it thinks it is, nor does it point to where it thinks it points. TomoSim addresses this kind of error in a Monte Carlo like fashion. Positioning and pointing errors are assumed to be normal. Each time a point is calculated, the software generates a normally distributed 0 mean random number, with a standard deviation equal to the rated error of the positioning system and sums it to the intended point (error calculations illustrated in Appendix A). Given the ratios between the linear distances involved in the trajectory and the positioning errors, geometric errors have a very small contribution towards the end results.

On the spectroscopic level, errors come from the instruments used for capturing the data. TomoSim takes this noise into account by adding Gaussian noise spectra to each measurement, for which the magnitude is configurable via its standard deviation, a method previously followed in Reference [33]. This approach is only valid insofar as the captured spectra are perfectly calibrated regarding spectral shift and squeeze, which is an acceptable assumption for a simulation.

Finally, the software has to deal with the reconstruction errors. In image reconstruction from projections, it is common to use techniques such as Mean Squared Error (MSE) as a metric with which to assess the algorithm's performance. This simulator was also evaluated in this light, in two different ways. First, the MSE for the whole reconstructed image was calculated. This enables the possibility to look at the reconstruction as a whole and visually tell where it is lacking and where it is better performing. Secondly, a score was calculated according to Equation (12). In this equation, and with reference to this simulator, f is the original image and g is the reconstructed image.

$$E = \sqrt{\frac{\sum |g(x, y) - f(x, y)|^2}{\sum |f(x, y)|^2}}. \quad (12)$$

Finally, there is an additional source of error that was not explored in this simulation. It is the temporal error that comes from the difference in time between measurement moments (see Section 2.2), which can introduce a larger error than those considered above. In the real world, this can be easily mitigated by the introduction of a second vehicle, which would only conduct 2nd moment measurements. In the simulation, it was considered that there were no changes in the field of measurement with time.

3. Results

This section presents, analyses and discusses results obtained by the application of the techniques and methods described in the previous two sections, that is, the tomographic reconstruction of the phantoms which were also presented in Section 2.

3.1. Projection Calculations

In TomoSim, a projection is the sum of the pixel lengths (the lengths of the rays that traverse each pixel) for each ray and for the grid mentioned in Section 2. Unlike a real life situation, the contents of the ROI are completely known and correspond to the phantoms also described in Section 2 multiplied by a given maximum number of molecules. Siddon's algorithm is used in this process, and the final results of its application are the sinogram and the system matrix. Figure 5 contains some examples of these matrices, before and after the resorting operation described in Section 2.4.

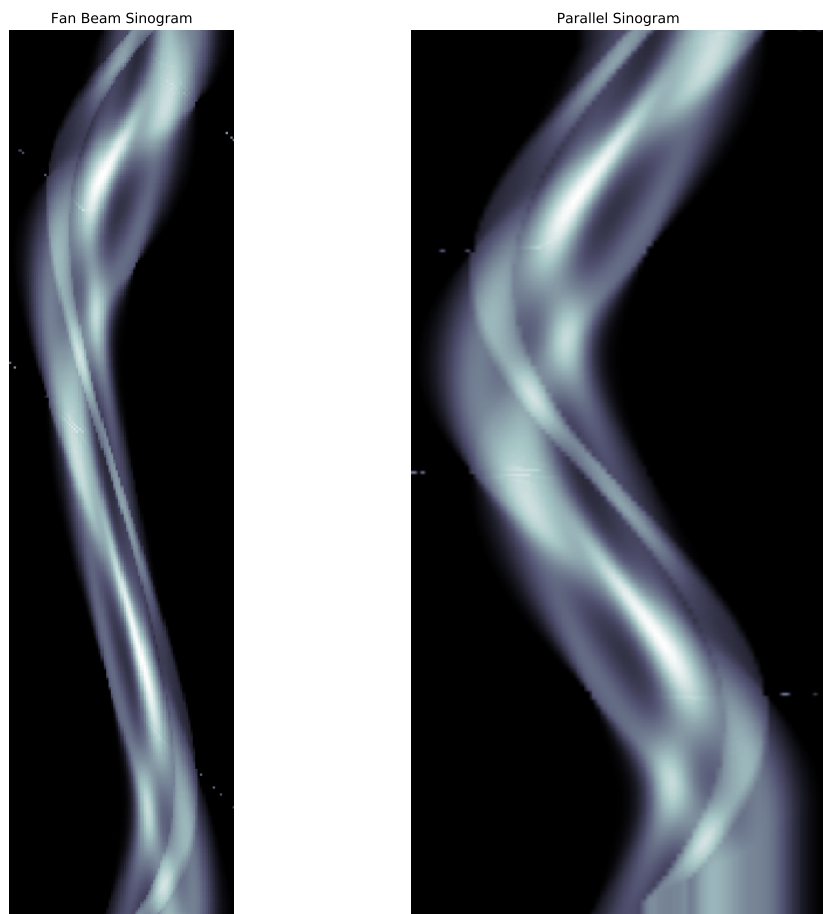


Figure 5. Sinogram examples: the new spectral phantom projection data at a projection interval of 1 degree. On the **left**, the projection data before resorting; on the **right**, the parallel projection data obtained after resorting the fan-beam line integrals.

3.2. Reconstruction Results

Images corresponding to the trace gas distribution within the ROI were reconstructed using iterative and analytical methods. In Figure 6, one can see the reconstruction results for the three tested methods when applied to the new spectral phantom; Figure 7 shows the graphical representation of the reconstruction errors for the spectral phantom and is accompanied by Table 2; and in Figure 8, a comparison between reconstructions with different Δ values is presented, also for the new spectral phantom.

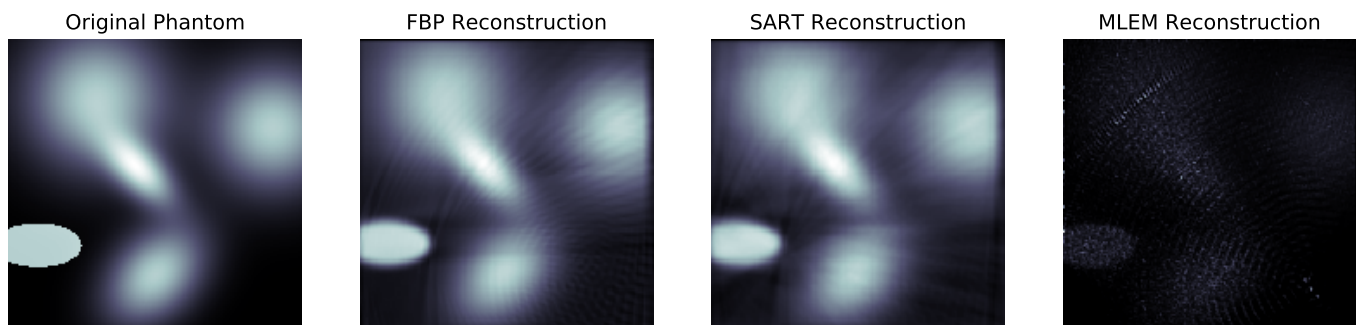


Figure 6. Tomographic reconstruction results, projection interval of 1 degree. From **left** to **right**: original phantom, Filtered BackProjection algorithm (FBP) reconstruction, Simultaneous Algebraic Reconstruction Technique (SART) reconstruction, Maximum Likelihood Expectation Maximisation (MLEM) reconstruction

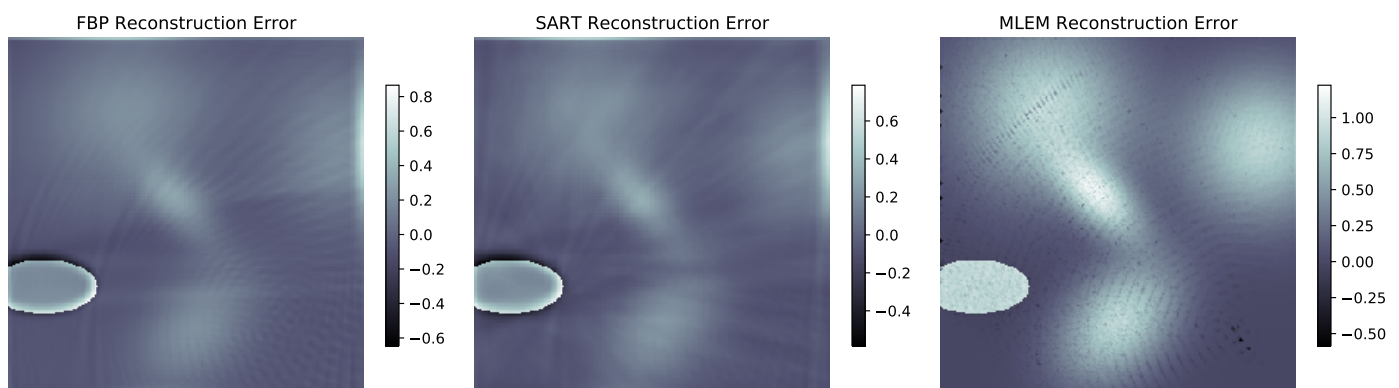


Figure 7. Tomographic reconstruction errors. Each one of these images was constructed by subtracting the respective reconstruction matrix, displayed in Figure 6, from the original phantom matrix. Error value is normalised to the pixel values, i.e., 32 bit floating point numbers with values between 0 and 1.



Figure 8. Reconstruction degradation: the projection interval was crucial for reconstruction. Note the image degradation going from a projection interval of 1 degree to 5 degrees (**left** to **right**). Images reconstructed using the FBP algorithm.

Table 2. Reconstruction error table for the new spectral phantom at several projection intervals. The MLEM routine used pure fan-beam data while the other two used resorted parallel information. Errors presented were calculated using the Root Mean Square Errors, normalised to the range of the reconstructed image.

Algorithm	Projection Intervals				
	1	2	3	4	5
FBP	0.2365	0.2408	0.2609	0.2948	0.3465
SART	0.2225	0.2278	0.2771	0.3537	0.3302
MLEM	0.8705	0.9723	0.9986	0.9744	0.9890

4. Discussion

The results presented in the previous subsection raise a series of pertinent observations that should be addressed in discussion. The first remark goes to the fact that the number of projections used was adequate to perform the tomographic reconstruction in adequate fashion, as expected. There are already several examples of studies in which a considerably lower number of projections was used, still producing satisfactory results [20]. Moreover, and since the simulation software automatically includes errors in the calculations, this figure also proves that geometric error plays a very limited role in changing the result of the reconstruction. Given the difference in size between the drone's trajectory and the geometric error, this was also a predicted result.

Even with the relatively low number of projections produced by the drone's trajectory and measurement strategy, all reconstruction algorithms were able to produce a reconstructed image that resembled the phantom that generated it. Δ , the angular interval between projections, revealed itself to be crucial. This was expected as the number of captured projections is obtained by dividing 360 by Δ . This is, also as expected, confirmed by the upward trend of the error when increasing the value of the angular projection interval, as can be seen numerically in Table 2 and qualitatively in Figure 8. With respect to the algorithms used, the custom-made MLEM routine produces clearly outlier results, which are not on par with the other two reconstruction methods used. This is plain to see both in Figure 6 and in Table 2, in which this algorithm's NRMSE is almost four times the second best result (FBP) for the smallest projection interval. This difference could to some extent be expected. SART and FBP algorithms were implemented using some of the most relevant and consistently used Python libraries (SciPy, for instance [2]). Given the amount of attention these libraries get from the scientific programming community, levels of optimisation are extremely high. Although it is nowhere near the other two approaches, the MLEM routine is still useful, as it is the only truly geometry-independent algorithm in this study (SART is also geometry independent, but this particular implementation expects a parallel projection sinogram as an input).

As stated in Section 2.5, three different kinds of error influence the reconstruction results: geometric, spectroscopic and reconstruction errors. The first kind of error is directly included in projection calculations, through the application of a Monte Carlo-like method to the geometry described in Appendix A. The second kind of uncertainty comes from the spectrum acquisition process itself, which is not perfect. If one considers there are no systematic errors present in the results, which is an acceptable premise in a simulation, then these errors can be simulated by the inclusion of Gaussian noise in the spectral measurements. This approach is based on the one used in Reference [33], in which a Gaussian noise spectrum is added to the spectrum of interest in order to simulate how the error behaves with a degraded signal. Finally, reconstruction errors come from the finite precision of the calculations that render the images. These errors were presented in Section 3.

The three methods were also evaluated as to how they perform computationally, by measuring the time it took to produce the images in Figure 6 using a Paperspace P4000 cloud computing instance. In this regard, the fastest method was FBP, which took around 3 s to reconstruct. The second was MLEM, with around 50 s for 1000 iterations, and finally came SART, with 1 min and 50 s for 1 iteration. One relevant observation comes from the fact that MLEM was significantly faster than SART, even taking into account the difference in optimisation, which was not an expected result and may indicate some reconstruction enhancing technique on SART's side, as the literature seems to indicate that this technique is faster than MLEM [15].

All things considered, the FBP algorithm produces a very good reconstruction, equivalent to SART's, while being more than 10 times faster, indicating that for this kind of application and with this kind of projection information, it is the best reconstruction algorithm.

5. Conclusions

The initial goal of the TomoSim software project was to develop a simulation platform to create the tomographic reconstruction of the column density distribution for a number of target atmospheric trace gases.

The software program was written using the Python language and some numeric calculation libraries, such as NumPy and SciPy. Using these two libraries had two main effects: on the one hand, it enabled the programmers to easily create and manipulate matrices and vectors (images, for instance), and on the other, they greatly improved the running speed of the code, since their core is written in lower level languages (namely C).

The simulations that the software performs prove that, if the final device is programmed to comply to trajectory and acquisition requirements, reconstruction is perfectly achievable, even with relatively low projection numbers (comparing with medical imaging procedures). This brings another significant conclusion which is that the devised acquisition definitions, which produce a set of fan beam arrays, provide sufficient projection information to run the reconstruction and achieve plausible results.

TomoSim runs three algorithms on the projection data in order to produce the spectral mapping of the target pollutants—FBP (analytical), SART and MLEM (both algebraic). SART offered the best results, at the expense of time. The analytical algorithm produced very nearly the same results, but took a fraction of the time when comparing with either SART or MLEM. The MLEM algorithm cannot be directly compared to the SART algorithm, due to differences in the optimisation levels of both routines, but had nonetheless a reasonable time performance altogether, although producing the poorest reconstruction results.

Regarding future developments, there are three main avenues that should be explored:

- **Other phantoms:** Presently, TomoSim only includes tomographic reconstruction for two different phantoms. While this is sufficient for simulation, it would be desirable to have some more phantoms, which could mimic other concentration distributions of interest.
- **Paradigm shift:** This simulation software was developed under the passive DOAS analysis model. Active measurements are much more versatile and accurate, and it would be interesting to develop this same technique using an artificial light source. Of course this would require many adaptations, namely regarding equipment and trajectory (probably even algorithms and interpolations).
- **Three-dimensional reconstruction:** TomoSim was developed to produce the reconstruction of a two dimensional image corresponding to the spatial distribution of an array of target trace gases. It would be much more interesting to have a three dimensional equivalent. As far as simulation goes, this is one of the most immediate developments for this project. On a more tangible level, the additional dimension would make the problem much more complex, mainly because of trajectory and battery logistics.

Author Contributions: Conceptualization, R.V.d.A., N.M. and P.V.; Investigation, R.V.d.A.; Methodology, R.V.d.A. and P.V.; Project administration, P.V.; Software, R.V.d.A.; Supervision, P.V.; Validation, N.M.; Writing—original draft, R.V.d.A.; Writing—review & editing, N.M. and P.V. All authors have read and agreed to the published version of the manuscript.

Funding: This work was funded by Fundação para a Ciência e Tecnologia, grant number PDE/BDE/114549/2016 and UIDB/00645/2020.

Conflicts of Interest: The authors declare no conflict of interest.

Appendix A. Geometric Calculations

Appendix A.1. Light ROI Exit Point (P_2) Determination

Figure A1 is a schematic snapshot of a point in which the drone is taking a spectrum in one of its stops. Here, the drone's position, P_1 , is given by the distance D and the angle β , while the gimbal is pointing at a direction at an angular distance of γ from line $0P_1$.

Point P_2 , which is not known, is at the intersection between the trajectory's circumference and line P_1P_2 . Parametrically, any point in this line can be expressed as $P_1 + t \cdot (P_2 - P_1)$, with t being a scalar. Moreover, to say a point X is on this circumference is the same as writing $X - Q = D$. Here, Q is the centre of the trajectory and can therefore be eliminated from the equation. If one is to expand these equations, the situation can be accurately described by Equation (A1).

$$\begin{aligned} P_2 &= P_1 + t \cdot (P_2 - P_1) \\ |P_2| &= D^2 \end{aligned} \quad (\text{A1})$$

Unravelling the expressions in Equation (A1), and making use of the algebraic property that says $|A|^2 = A \cdot A$, the expression becomes a two degree equation, as stated in Equation (A2), if one writes $P_2 - P_1$ as V .

$$t^2 V^2 + 2 \cdot V \cdot P_1 \cdot t + P_1^2 - D^2 = 0 \quad (\text{A2})$$

If line P_1P_2 non-tangentially intersects the circumference, solving Equation (A2) renders two values for t (which correspond to P_1 and P_2). Selection is made by determining the returned value of t that maximises the euclidean distance between the produced point and P_1 .

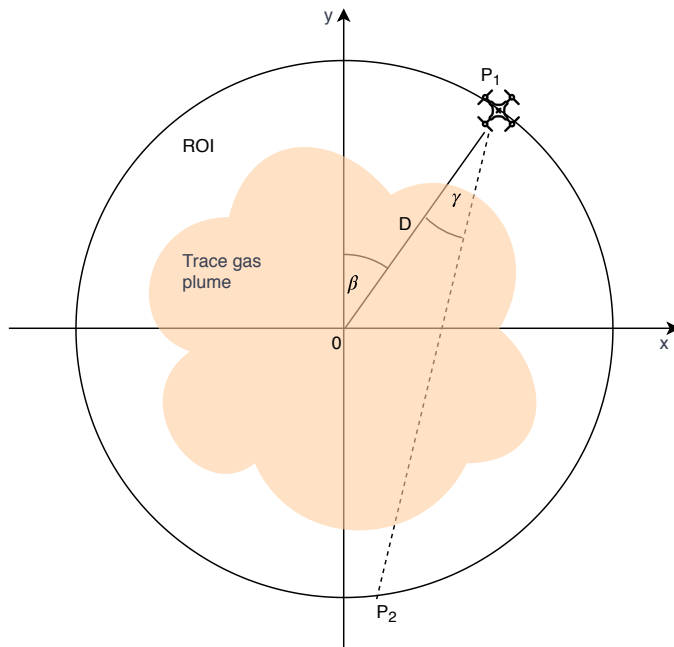


Figure A1. P_2 Calculation.

Appendix A.2. Geometric Error Determination

Figure A2 is a graphical representation for the reasoning behind the geometric error estimation. There are two types of error in this image: the ones that come from the RTK-GPS system (positioning error, denoted ϵ_p) and the ones that come from the gimbal (pointing error, denoted ϵ_γ). TomoSim considers these errors to be normally distributed, and the two ϵ values correspond to their standard deviation. To introduce the error into the simulation, the software calculates the theoretical P_1 from the β and D values (see Figure A1) and then adds a normally distributed random number that respects ϵ_p , retrieving the true P_1 . This new point is used to draw the theoretical line P_1P_2 and the pointing error is added using the same process as in P_1 . Given the very low gimbal error, the small angles approximation ($\sin \theta = \theta$) is used to determine the theoretical value of P_2 , on the drone's circular trajectory. Finally, the software adds again the positioning error, in the same

manner as it had on P_1 . As a finishing remark, it is important to note that in Figure A2, all errors are extremely exaggerated as they would not be visible otherwise, due to the huge size difference between them and the trajectory.

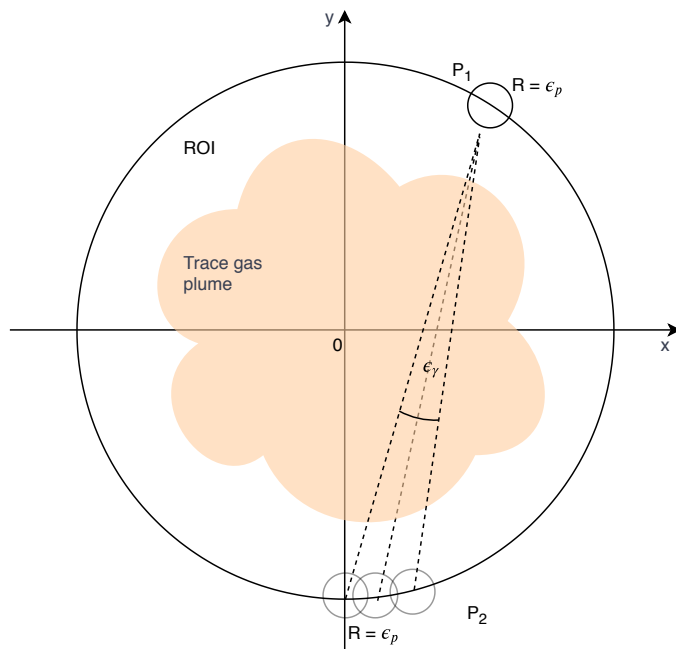


Figure A2. Error estimation graphical representation. Note errors are extremely exaggerated for visualisation purposes.

Appendix B. Simulation Data Characterization

As stated in Section 2, the simulation uses a phantom matrix to perform its reconstructions. However, this is not purely the input to the simulator routine. Some transforms, introducing random variation, are run beforehand.

As described in Figure A3, the simulator starts by loading the phantom data. This is a 300 by 300 pixels image, which is created by running the TomoPhantom [32] software. This matrix, which is parametrically stored, is always the same. The data it contains are 64 bit floating point numbers, ranging from 0 to 1 (0 is black; 1 is white). This image is then normalised to range between 0 and 255, and its data type is changed to unsigned 8 bit integers.

The extremes of concentration values are randomly taken from a uniform distribution between 1×10^{15} and 1×10^{17} , rendering `min_val` and `max_val`. These two values will be used as concentration limits for the phantom matrix, with `min_val` representing the baseline (0 in the phantom matrix) and `max_val` representing the maximum value in the ROI (255 in the phantom matrix).

The projection operator which geometrically describes the projection system is applied to the phantom matrix, rendering the sinogram. Before reconstruction, the program adds poissonian noise to this matrix.

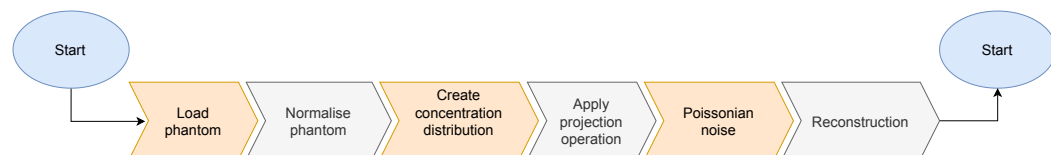


Figure A3. The data flowchart of the simulation routine. The phantom is entered to the routine as a fixed matrix, but is transformed so that each time the program runs, the reconstruction is randomly different and more in line with what happens in nature.

References

- Perez, F.; Granger, B.E. IPython: A System for Interactive Scientific Computing. *Comput. Sci. Eng.* **2007**, *9*, 21–29. [[CrossRef](#)]
- Oliphant, T.E. Python for Scientific Computing. *Comput. Sci. Eng.* **2007**, *9*, 10–20. [[CrossRef](#)]
- APS. August 15, 1758: Death of Pierre Bouguer. *Am. Phys. Soc. News* **2011**, *20*, 2.
- Struve, W.S. *Fundamentals of Molecular Spectroscopy*; Wiley-Interscience: Hoboken, NJ, USA, 1989.
- Platt, U.; Stutz, J. *Differential Optical Absorption Spectroscopy—Principles and Applications*; Springer: Berlin/Heidelberg, Germany, 2007.
- Merlaud, A. Development and Use of Compact Instruments for Tropospheric Investigations Based on Optical Spectroscopy from Mobile Platforms. Ph.D. Thesis, Faculté des Sciences—Université Catholique de Louvain, Louvain, Belgium, 2013.
- Press, W.H.; Teukolsky, S.A.; Vetterling, W.T.; Flannery, B.P. *Numerical Recipes: The Art of Scientific Computing*, 3rd ed.; Cambridge University Press: Cambridge, UK, 2007.
- Gunderman, R. *Essential Radiology: Clinical Presentation, Pathophysiology, Imaging*, 2nd ed.; Thieme: New York, NY, USA, 2006.
- Kak, A.; Slaney, M. *Principles of Computerized Tomographic Imaging*; Society of Industrial and Applied Mathematics: Philadelphia, PA, USA, 2001.
- Bruyant, P.P. Analytic and iterative reconstruction algorithms in SPECT. *J. Nucl. Med. Off. Publ. Soc. Nucl. Med.* **2002**, *43*, 1343–1358.
- Herman, G.T. Image Reconstruction From Projections. *Real-Time Imaging* **1995**, *1*, 3–18. [[CrossRef](#)]
- Siddon, R.L. Fast calculation of the exact radiological path for a three-dimensional CT array. *Med. Phys.* **1985**, *12*, 252–255. [[CrossRef](#)] [[PubMed](#)]
- Gao, H. Fast parallel algorithms for the x-ray transform and its adjoint. *Med. Phys.* **2012**, *39*, 7110–7120. [[CrossRef](#)]
- Herman, G.T. *Fundamentals of Computerized Tomography: Advances in Pattern Recognition*; Springer: London, UK, 2009. [[CrossRef](#)]
- Defrise, M.; Kinahan, P.E.; Michel, C.J. *Positron Emission Tomography*; Springer: London, UK, 2005; pp. 63–91.
- Andersen, A. Simultaneous Algebraic Reconstruction Technique (SART): A superior implementation of the ART algorithm. *Ultrason. Imaging* **1984**, *6*, 81–94. [[CrossRef](#)]
- Shepp, L.A.; Vardi, Y. Maximum Likelihood Reconstruction for Emission Tomography. *IEEE Trans. Med Imaging* **1982**, *1*, 113–122. [[CrossRef](#)] [[PubMed](#)]
- Byer, R.L.; Shepp, L.A. Two-dimensional remote air-pollution monitoring via tomography. *Opt. Lett.* **1979**, *4*, 75. [[CrossRef](#)] [[PubMed](#)]
- Laepple, T.; Knab, V.; Mettendorf, K.U.; Pundt, I. Longpath DOAS tomography on a motorway exhaust gas plume: Numerical studies and application to data from the BAB II campaign. *Atmos. Chem. Phys. Discuss.* **2004**, *4*, 2435–2484. [[CrossRef](#)]
- Pundt, I.; Mettendorf, K.U.; Laepple, T.; Knab, V.; Xie, P.; Lösch, J.; Friedeburg, C.V.; Platt, U.; Wagner, T. Measurements of trace gas distributions using Long-path DOAS-Tomography during the motorway campaign BAB II: Experimental setup and results for NO₂. *Atmos. Environ.* **2005**, *39*, 967–975. [[CrossRef](#)]
- Stutz, J.; Hurlock, S.C.; Colosimo, S.F.; Tsai, C.; Cheung, R.; Festa, J.; Pikelnaya, O.; Alvarez, S.; Flynn, J.H.; Erickson, M.H.; et al. A novel dual-LED based long-path DOAS instrument for the measurement of aromatic hydrocarbons. *Atmos. Environ.* **2016**, *147*, 121–132. [[CrossRef](#)]
- Frins, E.; Bobrowski, N.; Platt, U.; Wagner, T. Tomographic multiaxis-differential optical absorption spectroscopy observations of Sun-illuminated targets: A technique providing well-defined absorption paths in the boundary layer. *Appl. Opt.* **2006**, *45*, 6227–6240. [[CrossRef](#)] [[PubMed](#)]
- DJI. DJI E1200 Pro Tuned Propulsion System. 2015. Available online: <https://www.dji.com/pt/e1200> (accessed on 28 December 2020).
- Celera. UAV Gimbal. Available online: <https://www.celeramotion.com/applications/satcom-uav/uav-gimbal/> (accessed on 28 December 2020).
- Omegon. MightyMak 60 Specifications. Available online: https://www.omegon.eu/telescopes/omegon-maksutov-telescope-mightymak-60/p,46442#tab_bar_1_select (accessed on 28 December 2020).
- Avantes. AvaSpec-Mini: Small and Powerful OEM Spectrometer. Available online: <https://www.avantes.com/products/spectrometers/compactline/avantes-spectrometer-mini-2048cl/> (accessed on 28 December 2020).
- Triantafyllou, D.; Aspragathos, N.A. *Intelligent Robotics and Applications—Lecture Notes in Computer Science*; Springer: Berlin/Heidelberg, Germany, 2011; Volume 7101, pp. 509–519. [[CrossRef](#)]
- Zimmermann, F.; Eling, C.; Klingbeil, L.; Kuhlmann, H. Precise Positioning of Uavs—Dealing with Challenging Rtk-Gps Measurement Conditions during Automated Uav Flights. *ISPRS Ann. Photogramm. Remote Sens. Spat. Inf. Sci.* **2017**, *4*, 95–102. [[CrossRef](#)]
- Casaballe, N.; Osorio, M.; Di Martino, M.; Frins, E. Comparison Between Regularized Optimization Algorithms for Tomographic Reconstruction of Plume Cross Sections in the Atmosphere. *Earth Space Sci.* **2017**, *4*, 723–736. [[CrossRef](#)]
- Kern, C.; Deutschmann, T.; Vogel, L.; Wöhrbach, M.; Wagner, T.; Platt, U. Radiative transfer corrections for accurate spectroscopic measurements of volcanic gas emissions. *Bull. Volcanol.* **2010**, *72*, 233–247. [[CrossRef](#)]
- Stachniss, C.; Plagemann, C.; Lilienthal, A.J. Learning gas distribution models using sparse Gaussian process mixtures. *Auton. Robot.* **2009**, *26*, 187–202. [[CrossRef](#)]

32. Kazantsev, D.; Pickalov, V.; Nagella, S.; Pasca, E.; Withers, P.J. TomoPhantom, a software package to generate 2D–4D analytical phantoms for CT image reconstruction algorithm benchmarks. *SoftwareX* **2018**, *7*, 150–155. [[CrossRef](#)]
33. Stutz, J.; Platt, U. Numerical analysis and estimation of the statistical error of differential optical absorption spectroscopy measurements with least-squares methods. *Appl. Opt.* **1996**, *35*, 6041. [[CrossRef](#)] [[PubMed](#)]

D

TESTING LAMBERTIAN ABSORPTION -
HANDOUT PROTOCOL FOR THE
EXPERIMENT OF SECTION 3.2

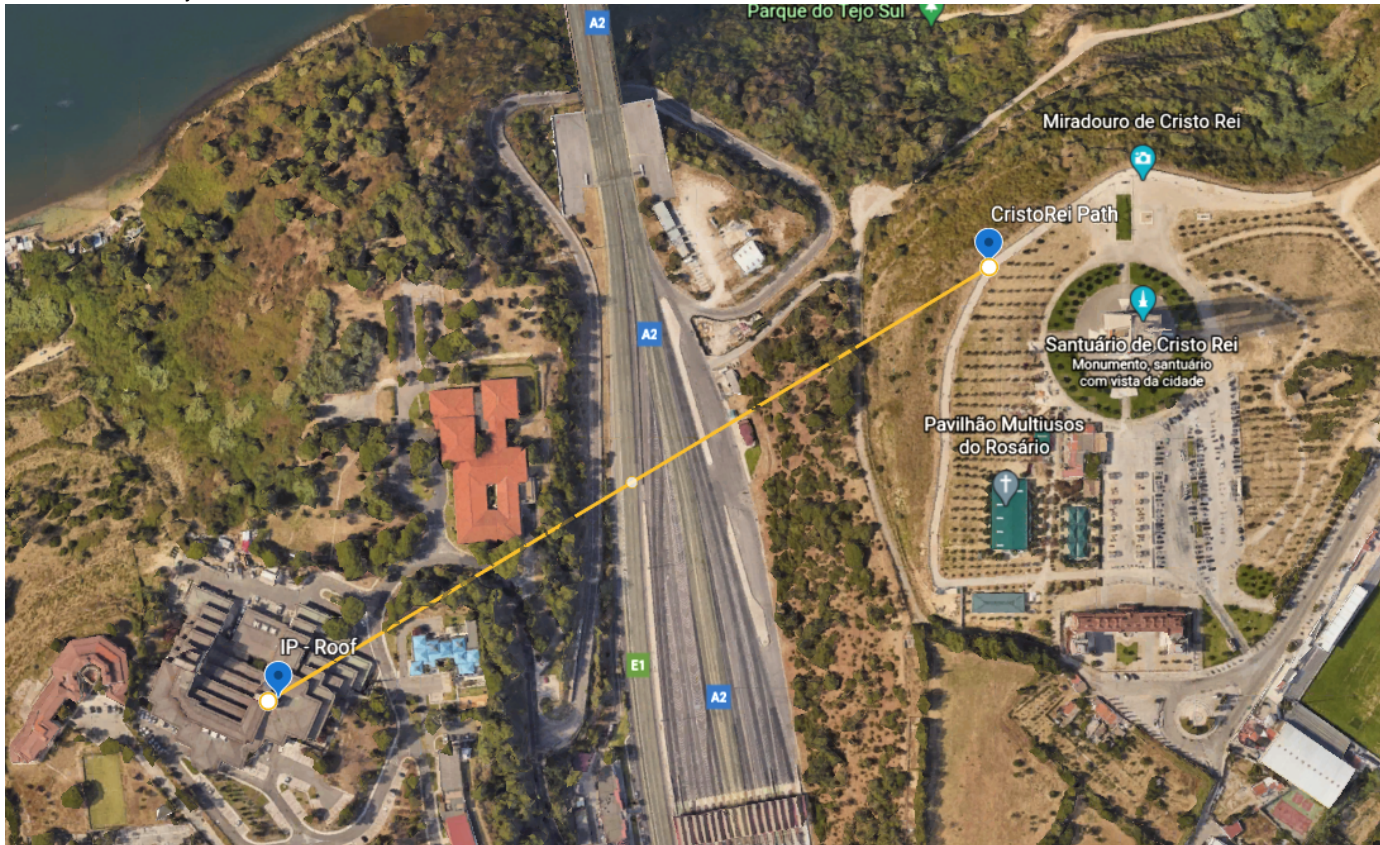
Testing Lambertian Absorption

Experiment plan and results	This experiment is designed to prove that we can use the lambertian notion that light absorption depends on the optical path and that we can use this to determine a projection in a tomographic imaging system.
Experiment owner	@ Rui Almeida
Jira ticket(s)	https://rfa123c.atlassian.net/browse/PHD-3
Status	DONE
On this page	<ul style="list-style-type: none">• Experiment planning• Results• Conclusions

Experiment planning

Overview

The experiment was designed to validate that we are able to measure trace gas concentrations with our current instruments and using passive DOAS for an optical path of around 1km. We will assemble a telescope on the roof of the IEP building and another one in a specific point of the Cristo Rei sanctuary.

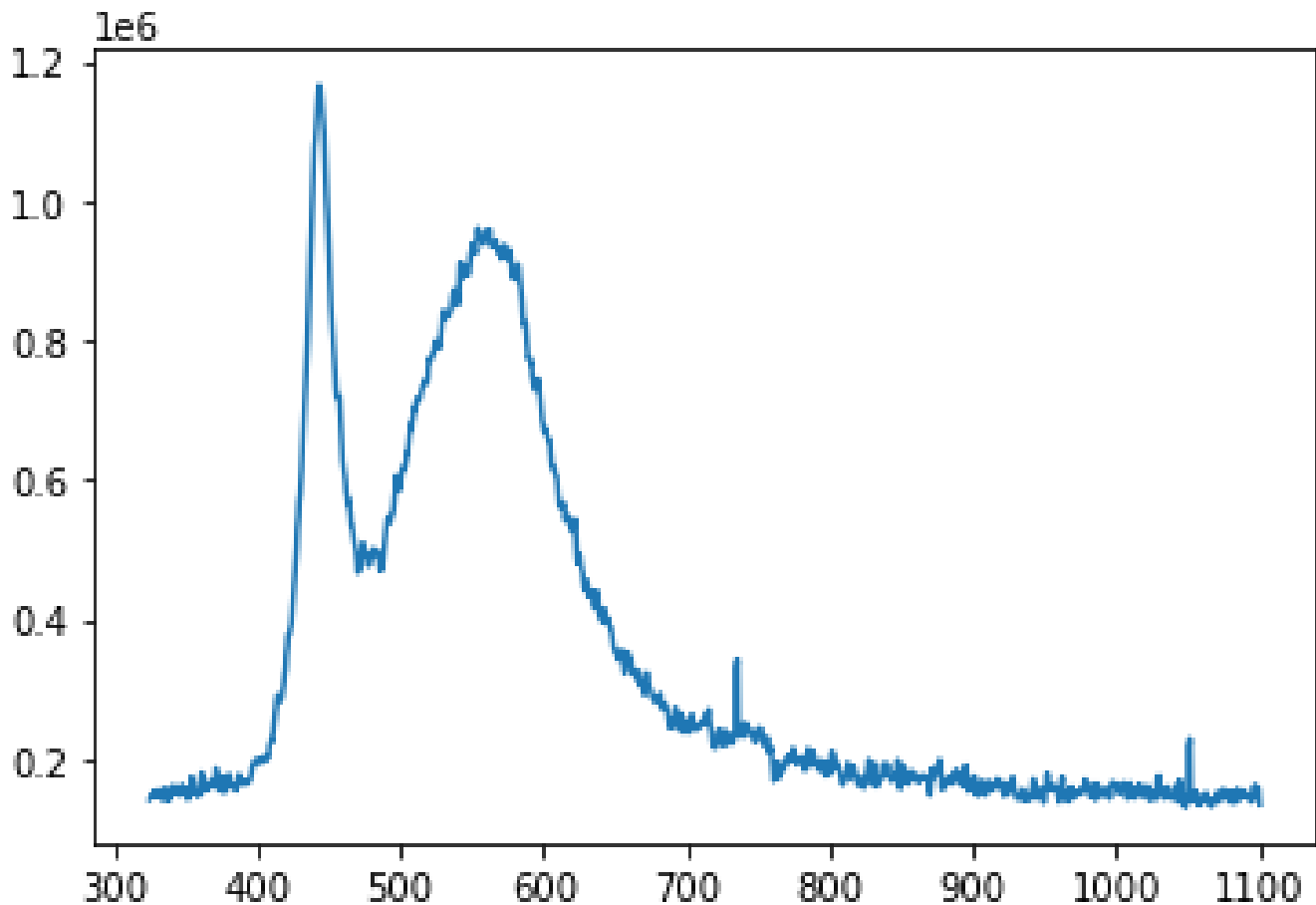


Both points are located in Pragal - Almada, Portugal. They are, however, on opposite banks of the valley created by the A2 motorway, which is one of the country's busiest roads, especially during rush hour.



In addition to the telescopes, we will use a collimated light source pointing from one telescope to the other. An artificial light source will give us a baseline with which to compare our target data, the passive DOAS trace gas concentrations.

The selected light source is a bright 20W XP50.2 LED lamp collimated through the telescope located at the sanctuary. The relative spectrum of this white lamp is presented in the figure below.



Hypothesis

We hypothesize that light absorption between points A and B will be equal to the difference in absorptions in A and B and we can measure this difference with our equipment.

Actions

Action ID	Action	Description
A	Active trace gas concentration determination	With the two telescopes facing each other, we collect spectra for two minutes with the light source turned off and another 2 min with the light source turned on.
B	Passive trace gas concentration determination	With the two telescopes aligned and approximately facing East, we collect spectra for 2 minutes.
C	Passive reference collection	With the two telescopes pointed upwards, we collect spectra for 2 minutes.

Experiment day

When we get to the sites of the experiment, we must start by preparing the equipment for operation. This will entail:

1. Mount the tripods and the telescope on it;
2. Point the telescope in the general direction of the other experiment site;
3. Connect all fiber optics to the spectrometer and the optical adapter on the telescope;
4. Connect the spectrometer to the USB port and check AVASOFT detects it;
5. Finish pointing the device and focus telescope and take note of its geographical position (LAT LON).

Additional Material

The experiment starts in the dead of the night and goes on for 6 hours. Bring:

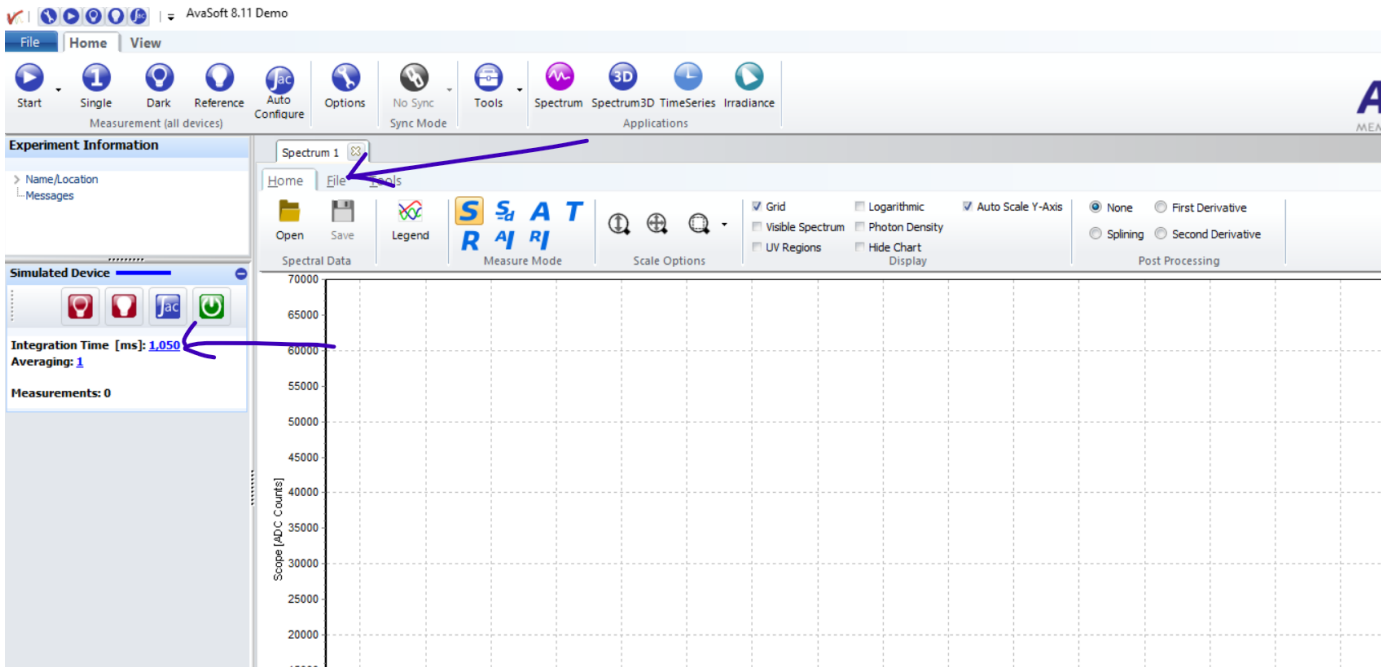
- warm clothes;
- food;
- water;
- something to pass the time (most of the time there will be nothing to do for the experiment);

The following table presents the list of prescribed actions and their periodicity. Note that only the IEP telescope moves (natural light exclusive).

Time Frame	Period	Action
05:00 - Sunrise	15 minutes	A
Sunrise	Once	C
Sunrise - 11:00	15 min	A and B

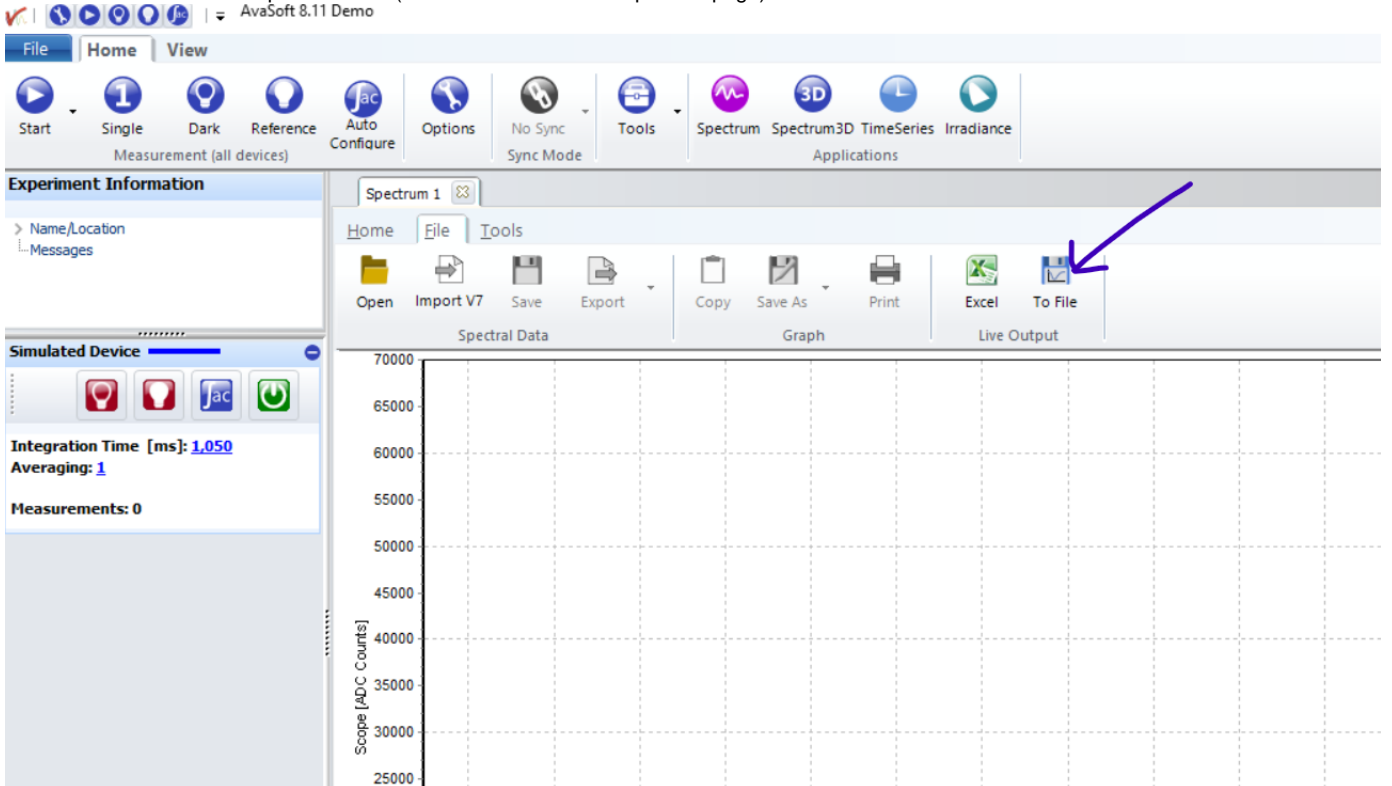
Spectrometer Software Settings

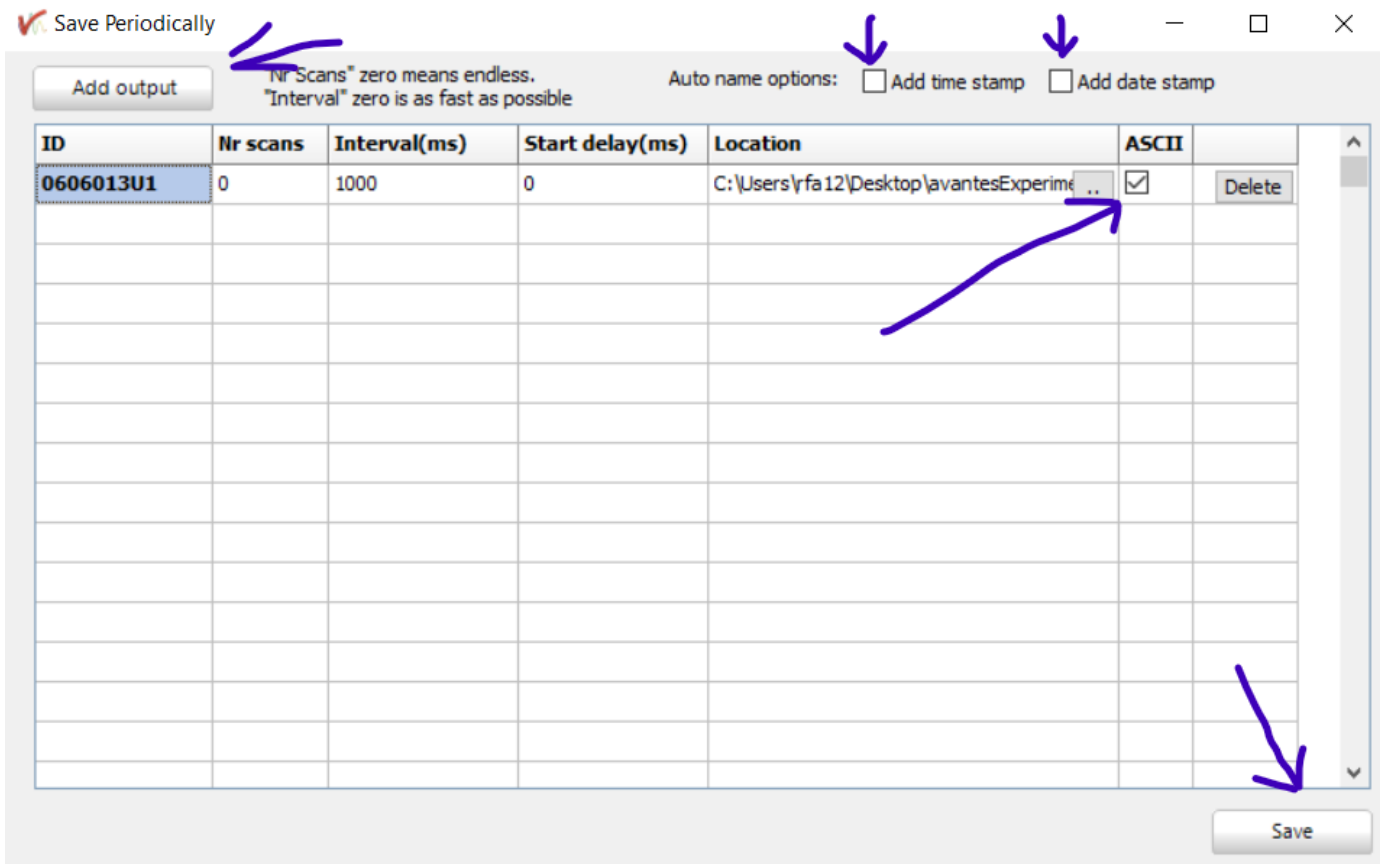
Calibration Coefficients	From spectrometer's memory (no action required)
Integration Time	500 ms
Number of measurements	-1 (non stop)
Reference Spectrum	None



File saving settings

At the start of the experiment, setup file saving in the AvaSoft software to save a file to disk each second from the spectrometer output. Check that both time and datestamps are active (two checkboxes in the top of the page).





Results

1st experiment run

Experiment start	07 Jun 2021
Conclusion	INCONCLUSIVE

The first attempt at the experiment was run on Jun 7 2021. All weather conditions were optimal for the kind of data acquisition we were conducting. The experiment started with a small delay, caused by last minute conditions due to not having a laptop battery charger (on the sanctuary side). This lack of a charger came to not influence the results, since it was the other laptop (on IEP's roof) that failed first, closing the experiment for this day.

The acquisition table follows:

#	Passive meas.	Passive ref.	Active mean.	Active ref.
1	06:20	06:23	06:15	--
2	06:46	06:50	06:41	--
3	07:04	07:07	07:00	--
4	07:25	07:27	07:21	--
5	07:48	07:50	07:45	--
6	08:10	08:12	08:06	08:08

On the one hand, it is clear from this table that we do not have data on the active reference spectra (likely due to some operation error on my part); on the other hand, we have too few data points to make any claim of validation or refutation of the principle we were to measure.

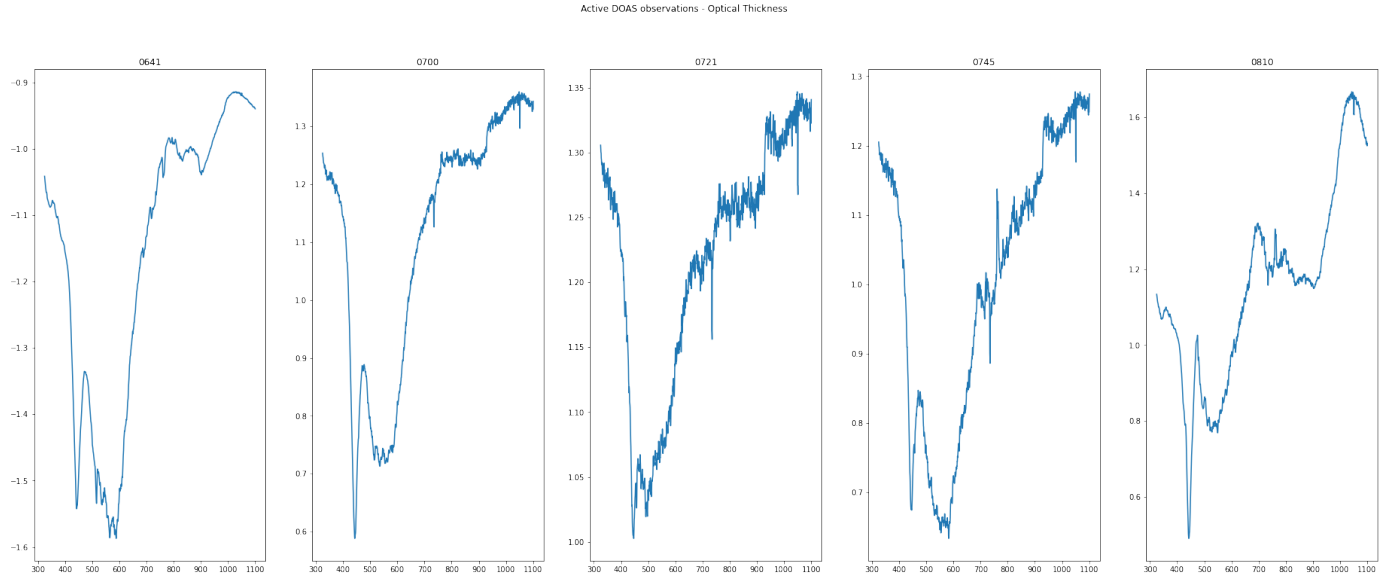
The acquired data makes it clear that we need to take another go at the experiment, from the top. Logistically, this is already being prepared (UPS and authorizations).

Preliminary results - data analysis

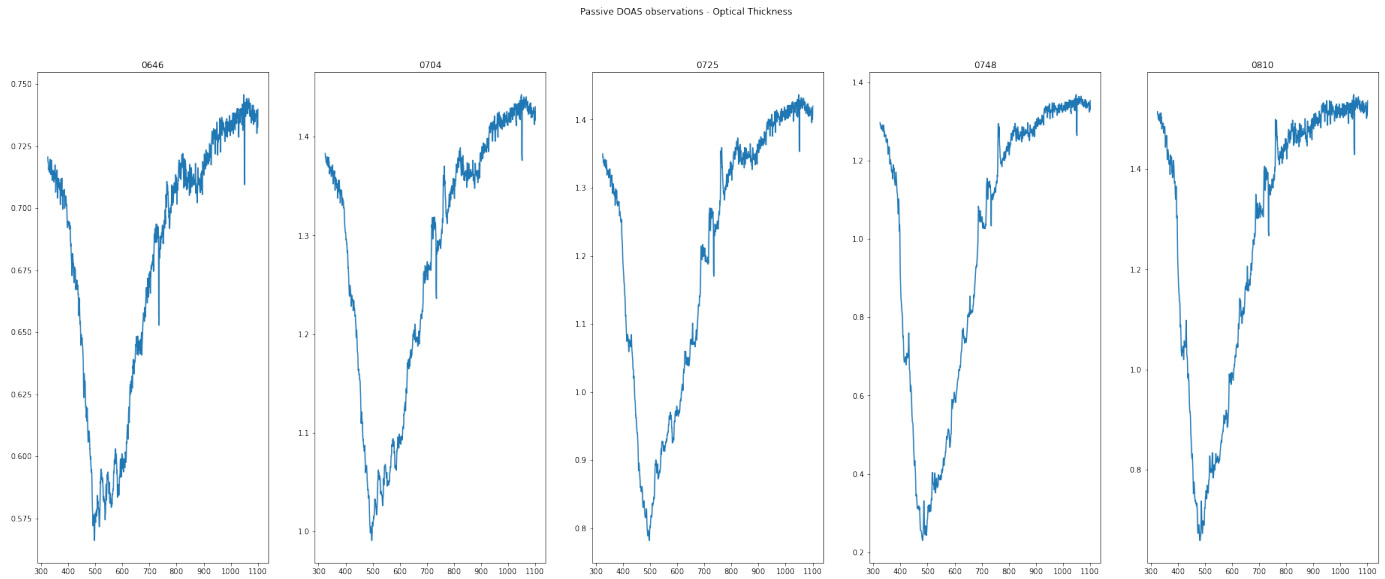
Although there is insufficient data to produce a convincing conclusion at this point, the data that was collected was of good quality and allowed some interesting analysis.

The collected spectra were correctly displayed, having the expected shape. In terms of optical density, here are the charts for the produced signals:

Active DOAS



Passive DOAS

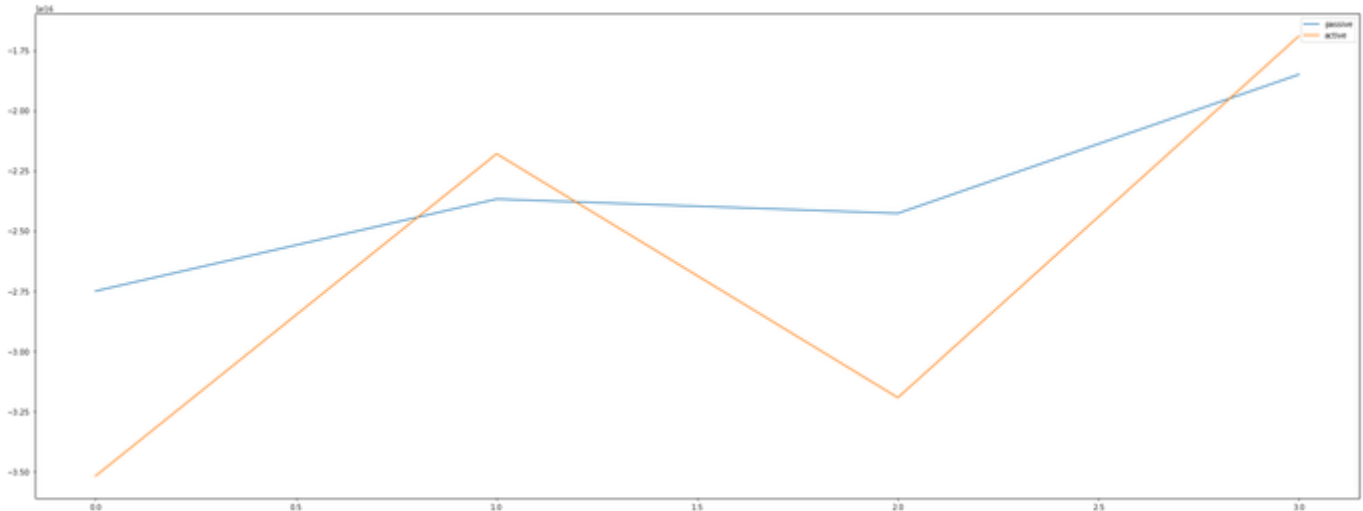


NO₂ Concentration

NO₂ concentration results were a bit surprising, but this is probably due to a lack of reference or some contamination in the spectra, so it's not a definitive conclusion.

The first datapoint, at around 0620, is decisively the highest. This is quite surprising, given that the number of cars that were on the road at that time was minute, compared with what came next. To add to the confusion, the second datapoint is the lowest of the dataset, and after this, measurements behave as they should (rising).

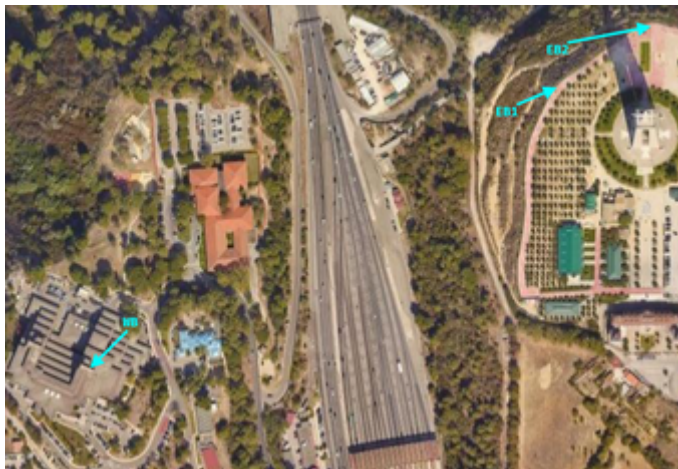
A good result was that in any case, both passive and active measurements seem to have a good agreement, indicating that our premise is valid, as it should. The following chart demonstrates this point.



2nd experiment run

Experiment start	22 Jun 2021
Conclusion	PLAUSIBLE

The second run of the experiment took place on the 23rd of June. The weather was not as good as during the first run, namely because of the wind. The East Bank assembly was moved behind a few meters. This improved the measurements but made them more difficult. The figure shows how the East Bank was relocated.



We were able to make many more measurements, that are presented in the following table.

#	Active	Active Reference	Passive
1	06:07	05:57	06:14
2	06:35	06:30	06:40
3	06:50		06:50
4	07:10	07:15	07:00
5	07:50	07:40	07:10
6	08:08	08:03	07:25
7	08:18	08:21	07:53
8	08:35	08:30	08:35
9	09:00	08:53	09:02
10	09:45	09:50	09:24

11

10:00

10:05

09:53

DOAS analysis of the collected spectra produced the following charts:



passive_densitie...converted-to.pdf



active_densities...converted-to.pdf

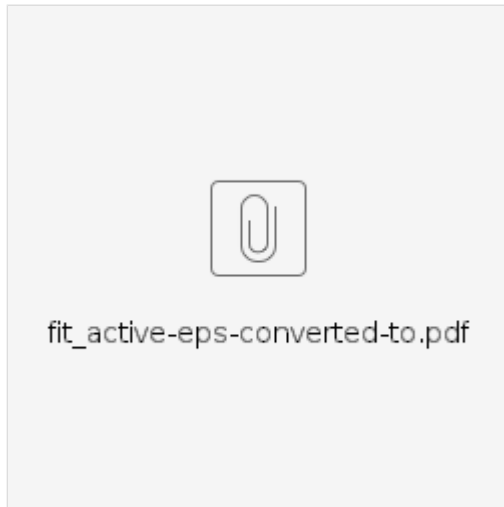
These density values were obtained from the following fits:



fit_passive_fron...converted-to.pdf



fit_passive_back...converted-to.pdf



fit_active-eps-converted-to.pdf

⭐ Conclusions

- Good quality measurements produced coherent results (passive vs active) that disagree with the official numbers.

- In the field, we did see an increase in the number of cars that were passing the bridge, but we don't know if that would be enough to produce these changes.
- The fits are good, particularly the ones obtained in the West Bank, indicating that we were in fact measuring what we thought we were measuring, thus confirming the densities in the previous plots.
- The fact that this is a manual procedure makes it very difficult to ensure proper alignments, so it is possible that this error played some part in the disagreement between the two sources.
- The wind also played a role in destroying alignments.

Results do disagree with the official concentrations, but are quite coherent within themselves. The hypothesis in test can be considered plausible, but without improving the acquisition process (at least making it automatic) it is difficult to assert that it is verified.

